Ultra-wideband antenna systems for in-band full-duplex applications

Hadi Hijazi

DOCTORAT BRETAGNE LOIRE / MATHSTIC

ENSTA Bretagne

UBO Université de Bretagne Occidentale

THÈSE DE DOCTORAT DE

L'ÉCOLE NATIONALE SUPÉRIEURE
DE TECHNIQUES AVANCÉES BRETAGNE et
L'UNIVERSITÉ DE BRETAGNE OCCIDENTALE

ÉCOLE DOCTORALE N° 601
Mathématiques et Sciences et Technologies de l'Information et de la Communication
Spécialité : *Électronique*

Par

Hadi HIJAZI

Ultra-Wideband Antenna Systems for In-Band Full-Duplex Applications

Thèse présentée et soutenue à Brest, le 20/05/2021

Unité de recherche : Lab-STICC

Rapporteurs avant soutenance :

Bernard Jarry	Professeur, XLIM Limoges
Fabien Ferrero	Professeur, LEAT Sophia Antipolis

Composition du Jury :

	Bernard Jarry	Professeur, XLIM Limoges
	Fabien Ferrero	Professeur, LEAT Sophia Antipolis
	Nathalie Raveu	Professeur, ENSEEIHT Toulouse
	Mohamad Rammal	Professeur, Université Libanaise
Dir. de thèse :	André Pérennec	Maître de conférences HDR, Université de Bretagne Occidentale
Co-encadrants :	Marc Le Roy	Maître de Conférences, Université de Bretagne Occidentale
	Raafat Lababidi	Enseignant-Chercheur, ENSTA Bretagne
	Denis Le Jeune	Ingénieur de Recherche, ENSTA Bretagne

Invité(s) :

Rémy Vauché	Maître de Conférences, Université d'Aix-Marseille
Stéphane Rioual	Maître de Conférences HDR, Université de Bretagne Occidentale

Acknowledgments

At the end of the three years of my doctoral journey I would like to take a moment to thank all those who contributed to my work and made it possible to achieve.

First, I would like to express my deep gratitude for my wonderful supervisors: Andre Pérennec, Marc Le Roy, Raafat Lababidi, and Denis Le Jeune. Thank you, first, for giving me the opportunity to be a Ph.D. student in your research team, and, second, for your continuous guidance, remarkable assistance, endless patience, and invaluable support during those years of my doctoral work.

Secondly, I would like also to thank Prof. Bernard Jarry, from XLIM Limoges research institute, and Prof. Fabien Ferrero, from LEAT Sophia Antipolis, for accepting to be the reviewers of my thesis manuscript. I would like to equally thank Prof. Nathalie Raveu, from ENSEEIHT Toulouse, and Dr. Mohamad Rammal, from the Lebanese University in Beirut, for giving me the pleasure of taking the role of the examiners in my thesis defense. And, also, I would like to thank Mr. Rémy Vauché, from Université d'Aix-Marseille, and Mr. Stéphane Rioual, from Université de Bretagne Occidentale, for honoring us by accepting to be invited guests to my defense.

For the colleagues whom I shared the office with: Saadou, Ihsan, and Allan, thanks for all the casual and formal moments that we have been through in every day of office work, and for the help that you offered me in both my personal and professional lives. Also thanks for all other colleagues in our department in particular Hassan and Julian for their technical input and for the long scientific discussions about the different aspects of my work.

Special thanks to Mrs. Annaig Martin-Guennou and Mr. Alain Escabasse for providing access to the simulation cluster and for their technical intervention in software-related problems. Also, special thanks to Mrs. Bernadette Grisart, Mr. Vincent Laur, and Mr. Charles Cannaf for their technical assistance and for providing the necessary supplies and tools to conduct our measurements.

I would also like to thank some members of the administrative staff who took care of the administrative procedures needed to complete my work: Mrs. Annick Billon-Coat, the dean of MathSTIC doctoral school, Mrs. Anne Le Roux, secretary of the electronics department at UBO, and Mrs. Catherine Debay from human resources at ENSTA Bretagne.

Table of Contents

List of Figures

List of Tables

General Introduction

Thesis Context:

It has been long held that radio systems cannot transmit and receive on the same frequency at the same time, as the higher powered transmit signal would be unavoidably coupled to the receiver circuitry, which results in a comparatively strong self-interference (SI), thereby obscuring the weaker receive signal and preventing its reception. In fact, radio systems typically transmit signal powers which are many orders of magnitude higher than the received signals from other radios (often by over 100 dB), this is mainly due to the high path loss between the local receiver and the distant transmitter which weakens the received signal. Nonetheless, for any two radios, achieving a full-duplex communication, where both radios can transmit and receive simultaneously, is vital for many applications, in particular for mobile telephony. Until now, radio systems have achieved full-duplex operation by simply circumventing self-interference using the conventional out-of-band full-duplex (OBFD) techniques, such as Time Division Duplexing (TDD) and Frequency Division Duplexing (FDD), which utilizes orthogonal resources such as time or frequency to separate the transmit and receive signals in the time domain or in the frequency domain.

In fact, the available time and frequency resources are limited, and the demand for additional wireless services continues to expand as the population increases, thus the limited spectral resources in a licensed frequency band are becoming scarcer, and soon the conventional out-of-band full-duplex techniques will become inefficient and might fail to serve the demand. This requires finding new approaches to increase the spectral efficiency of the available bands. Recently, in-band full-duplex (IBFD) emerged as a promising solution for this problem. In-band full-duplex does much more than trying to avoid self-interference, as it reuses the same frequency spectrum for simultaneously transmitting and receiving by employing various methods to reduce and cancel the self-interference, in order to suppress it to below the receiver noise floor, such that it does not significantly impact the receiver signal-to-noise ratio. In essence, cancellation is simple: the transmitted signal is known, and therefore it can be subtracted at the receiver. However, in reality, it is far from easy because the "known" transmit signal will be corrupted by noise and non-linearities in the transmitter, and also because circuit imperfections in the cancellation hardware will limit its effectiveness.

Every radio system requires at least one antenna, this being the interface between the electrical signals in the radio circuits, and the radio waves propagating in space.

Therefore, when designing in-band full-duplex transceivers to isolate the receiver from the transmitter, the antenna domain is an obvious place to start, although cancellation can be performed at other stages of the front-end in the analog and digital domains. Indeed, a substantial amount of transmit-to-receive (Tx-Rx) isolation is required prior to the receiver input, in order to prevent the high powered transmit signal from overloading (or even destroying) the receiver front-end, and to provide adequate suppression of non-linearities and noise components. Depending on the design, antenna-based techniques alone may not provide the necessary levels of isolation, and it is common for in-band full-duplex transceivers to deploy additional self-interference cancellation circuitry at the analog and digital stages.

The simultaneous transmit-receive property of in-band full-duplex technology can enable the introduction of novel and efficient multiple access techniques, physical layer security protocols, relaying solutions, and can reduce air interface delay. Also, it might benefit radar systems, radio-frequency identification (RFID) tags, cognitive radios (CR), and multiple-input multiple output (MIMO) arrays. Considering their appealing advantages, it is highly desirable to implement full-duplex systems over wide bandwidths for multi-standard applications, such as radars or cognitive radios. A wideband full-duplex front-end can be considered as a general-purpose tool that can serve many applications and eliminates the necessity to design multiple front-ends for different standards. However, available publications on self-interference cancellation techniques were focused on achieving high levels of cancellation over a narrow bandwidth, and little work was done to extend their performances over a wide bandwidth, hence more effort needs to be invested in that domain.

Thesis Objectives:

The aim of this work is to provide a solid evidence of the capability of implementing in-band full-duplex systems for wideband applications, while maintaining an acceptable level of self-interference cancellation throughout the band. This is achieved by investigating the different self-interference cancellation techniques and choosing the one(s) that might have a wideband potential, and then by designing and fabricating the wideband devices needed to implement those techniques. However, recent works on wideband full-duplex systems indicate that achieving high levels of self-interference cancellation over a relatively wide bandwidth is possible at the antenna level, but the analog and digital parts fall far behind with achieving wideband cancellation, mainly, due to circuitry bandwidth limitations, complexity, and cost. Although it might not be feasible or possible to implement a fully-developed wideband full-duplex front-end, with wideband analog and digital cancellation, but at least it is good to have a wideband full-duplex antenna system as a first step, which in turn can be used in multiple applications while the analog and digital parts can be tailored several times based on the application requirements. In the light of this, in this work, we mainly focus on implementing a wideband full-duplex antenna system that can provide a high level of self-interference cancellation, good gain, relatively compact size, and that can transmit and receive in the same direction.

Thesis Organization:

Based on the above, Chapter 1 will discuss the state-of-the-art of in-band full-duplex technology starting by a brief demonstration of some traditional techniques that were used to solve the spectrum congestion problem, and how in-band full-duplex technology can be superior to those techniques in enhancing spectrum efficiency. After that, it will present the basic concepts of in-band full-duplex like how it works, what the components of self-interference signals are, the requirements that a full-duplex system should achieve, advantages and disadvantages, and then a global overview of a full-duplex system circuitry. After that, the chapter will introduce our frame of work and what are the specifications that we are looking for. This will be followed by a wide survey on the different techniques to achieve self-interference cancellation at the antenna level and which techniques could be qualified to operate over a wide bandwidth with a decent level of self-interference cancellation. Finally, the chapter concludes that near-field cancellation is the self-interference cancellation technique that is best suitable to build a wideband "bistatic" in-band full-duplex system and it requires at least four wideband antennas and two 180° out-of-phase power dividers (or baluns), which will be discussed in Chapter 2.

So, Chapter 2 will describe the different devices necessary for the implementation of the full-duplex antenna systems and it will be divided into two parts: the first part will discuss the different ways to implement 180° out-of-phase power dividers and the second part will discuss the different types of wideband antennas. In fact, out-of-phase power dividers can be built as 180°-hybrids or by connecting an in-phase power divider to a 180° phase shifter or a phase inverter. Thus, a broad literature review on wideband in-phase power dividers, phase shifters, phase inverters, and hybrids will be presented first, then the different implementations of wideband out-of-phase power dividers will be presented after. From this literature review we will pick an out-of-phase power divider based on wideband microstrip-to-slotline transitions. The theory of microstrip-to-slotline transition will be demonstrated and will be followed by a parametric analysis to optimize the transition and maximize its bandwidth. Then the out-of-phase power divider will be introduced with its performance, and an enhanced power divider with better isolation between the output ports will be presented next. Following this, this chapter will show a brief summary of the available wideband antennas and we will choose and design the Vivaldi antenna which can satisfy our specifications. Finally, the chapter will end by showing the fabricated antenna with its performance and will pave the way for Chapter 3 which deals with the whole full-duplex system implementation.

Chapter 3 will discuss the different implementations of ultra-wideband full-duplex antenna system, and it will commence by showing the first system implementation using the printed-circuit board (PCB) components that were designed and built in Chapter 2. The principle of system operation will be described mathematically first, then will be followed by a description of the system assembly and performance while pointing to the major defects and drawbacks that the system suffers from. The major weakness of the PCB system will be the mechanical fragility especially of the antennas. Thus, Chapter 3 moves to demonstrate a new antenna system with the same configuration but with thicker antennas which are built from metallized 3D-printed parts. The 3D-printed system overcomes the mechanical fragility problem but shares a common drawback with the PCB system which is the presence of two significant grating lobes alongside the main lobe of

radiation, the grating lobes are related to the minimum separation distance between the antennas which is limited by the antenna size, so, we will demonstrate an approach based on partial size reduction for the antennas to reduce the grating lobe level without degrading the antenna performance.

After that, Chapter 3 will discuss the implementation of a dual-polarized full-duplex array, which can transmit and receive simultaneously two orthogonal linear polarizations while operating in full-duplex mode. The design of a dual-polarized Vivaldi antenna with a novel feeding technique will be presented first and will be compared to the conventional way of feeding, then the implementation of the full-duplex array will be presented after with its feeding network. The novel dual-polarized Vivaldi antenna suffers from asymmetry in its radiation pattern, where more energy is radiated toward one side of the antenna, thus we propose another way of feeding of the antenna that balances the antenna and restores symmetry to the radiation pattern. At the end, Chapter 3 will propose a new figure of merit dedicated to wideband full-duplex systems to evaluate and compare their performances. The proposed figure of merit takes into consideration the system bandwidth, gain, level of self-interference cancellation, and the system of the size. The introduction of the new figure of merit will be followed by a table that compares our designed systems to other works in the literature.

Finally, this dissertation will be wrapped up with some general conclusions and perspectives for future work, and with our publications in national and international conferences and journals that resulted from our work.

Chapter 1

State of the Art

Contents

1.1 Introduction

Estimates of future mobile traffic indicate that the global number of mobile subscriptions could be 13.8 billion in 2025 and 17.1 billion in 2030, whereas this number has reached 6.7 billion in 2013 [1]. The increase in the number of mobile users creates an increased demand on mobile services which in turn leads to spectrum congestion problems and spectral resources scarcity and elevates the pressure on the available mobile infrastructure. To keep up with the increased demand on mobile services and serve the population, these problems need to be mitigated, thus a new approach is required to find more spectrum resources by exploiting traditional spectrum sharing techniques or harnessing new ones: for instance, new frequency bands are being licensed for commercial use, however, this requires the modification of available mobile devices and infrastructure to be able to operate in the newly licensed bands, which might not be feasible or might be costly. Another approach exploits intensively the concepts of cell division and frequency reuse in mobile networks: by reducing the cell size, a smaller number of mobile users per cell is obtained, which reduces the quantity of spectrum resources needed. Yet, this approach requires increasing the number of base transceiver stations (BTSs) and limiting their emitted powers, which might also become costly and complex.

One other approach that has been long used to increase the spectral resources is based on multiple access techniques which permit multiple users to access a shared communication medium and transmit or receive their data simultaneously. Traditionally, multiple access techniques utilize orthogonal resources such as frequency, time, or code, which are becoming scarcer with increased number of mobile users, this led to the development of non-orthogonal multiple access (NOMA) [2] as an alternative for the traditionally used orthogonal multiple access (OMA) techniques such as frequency division multiple access (FDMA), time division multiple access (TDMA), and code division multiple access (CDMA). The basic NOMA scheme is called the power-domain NOMA, and it allows multiple users to share the same resources (time, frequency, or code) by controlling the transmitted power of each user and implementing successive interference cancellation techniques. The power-domain NOMA scheme allocates less power to users with good channel conditions (termed as NOMA strong users) and higher power to users that have poor channel conditions (termed weak users). NOMA strong users can decode their own signals by removing the signals intended to NOMA weak users using successive interference cancellation. On the contrary, NOMA weak users, which experience poor channel conditions, are lightly affected by the interference caused by NOMA strong users, as such, the reception ability of the weak users is not affected. NOMA is still underdeveloped and suffers greatly with increased number of simultaneous users, and it can, also, pose a security risk as all users can access all the transmitted signals.

In addition to all the above approaches, cognitive radios (CR) [3] were also introduced to allow an unlicensed user (or the secondary user) to use a certain frequency band if it is not occupied by a licensed user (or the primary user), or if the unlicensed user can respect some interference constraints while the licensed user is transmitting. In general, a cognitive period consists of two phases: spectrum sensing and cognitive transmission. In the spectrum sensing phase, unlicensed users sense the radio environment and collect spectrum information (e.g., occupation status, traffic, energy), and in the cognitive transmission phase, unlicensed users select the best spectrum bands and

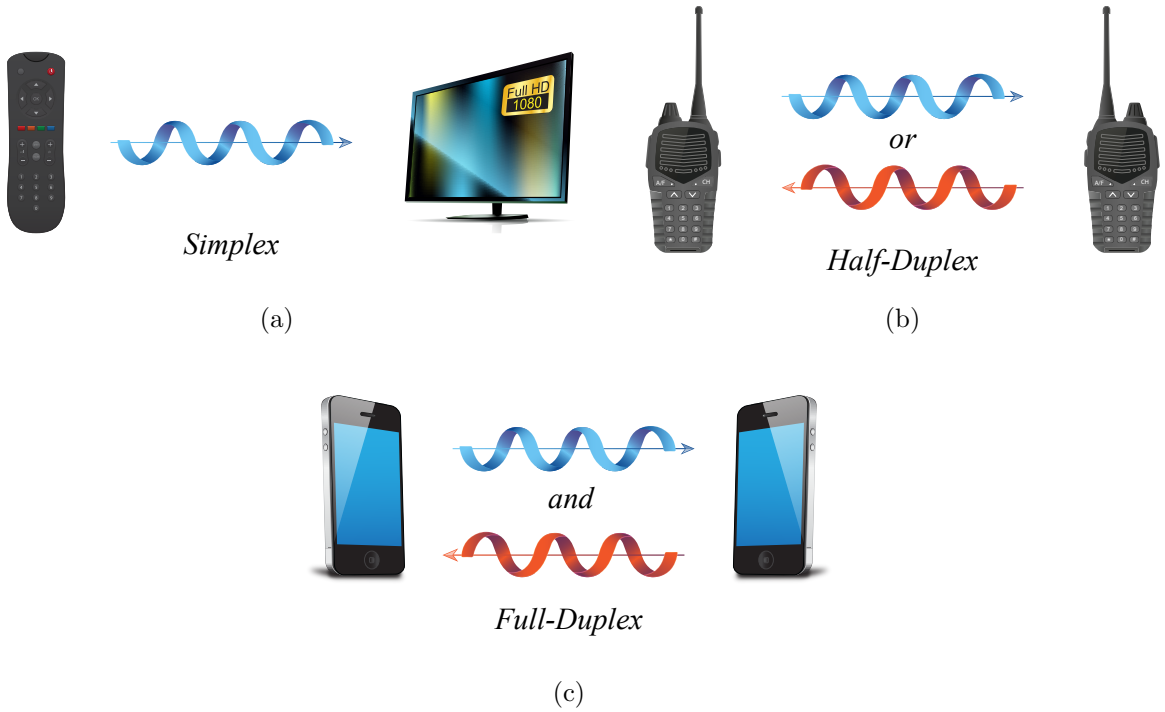

Figure 1.1: Illustration of (a) simplex, (b) half-duplex, and (c) full-duplex notions.

adapt transmissions according to the collected spectrum information [4]. Nonetheless, conducting cognitive operations in unlicensed bands requires the approval of the band owner, or, in worst cases, a lease which increases the cost of the system. Moreover, cognitive nodes need to adopt complex coordination procedures with neighboring cognitive nodes to prevent transmission on similar bands, which might become more complex with the increase in the number of simultaneous users. And, finally, cognitive transmission takes double the time needed for regular transmissions, because cognitive systems spend half the time sensing the spectrum.

Recently, in-band full-duplex (IBFD) technology emerged as a promising solution to mitigate spectrum congestion and spectral resources scarcity. This technology challenges a long-held axiom which claims that "it is generally not possible for radios to receive and transmit on the same frequency band due to the interference that results [5]." To better understand this point, few things need to be put in context first. In modern wireless telecommunication technology, there exist three modes of transmission between two communicating nodes or devices: simplex, half-duplex, and full-duplex (Figure 1.1). In simplex mode only one device can transmit a signal, on a certain frequency, to the other device but can never receive a signal, that is, the communication is unidirectional, like in a remote-control device (RCD). However, in half-duplex mode both devices can transmit and receive on the same frequency but not at the same time, a device in such mode needs to wait until the other device ends its transmission in order to transmit its own signal, that is, the communication is now bidirectional but not simultaneous, like in walkie talkies. And, finally, in full-duplex mode both devices can transmit and receive at the same time, that is, the communication is now bidirectional and simultaneous, like in mobile phones.

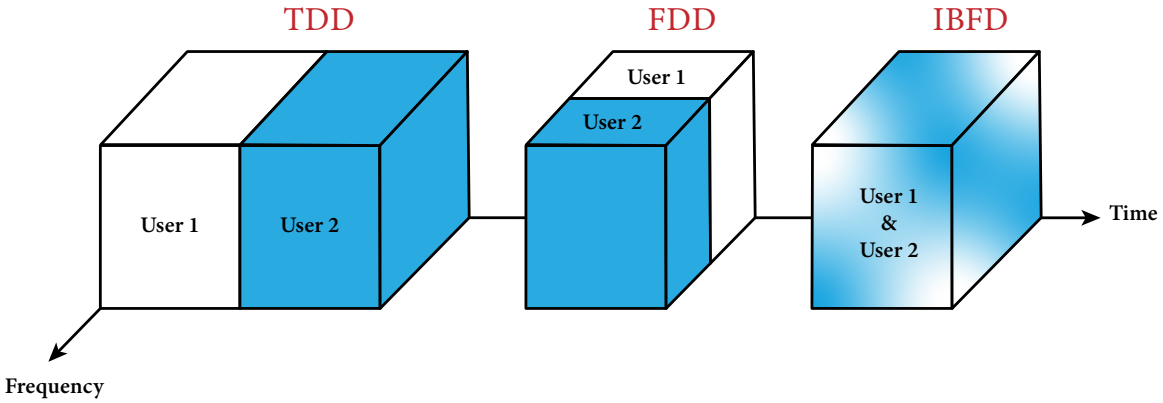

Figure 1.2: Frequency and time resources allocation for time-division duplexing (TDD), frequency division duplexing (FDD), and in-band full-duplex (IBFD).

Full duplex is the preferred mode of transmission for mobile communications and is conventionally implemented using two techniques: Frequency Division Duplexing (FDD) and Time Division Duplexing (TDD). In Frequency Division Duplexing, two frequencies are allocated for a device, one frequency is used for transmission and the second is used for reception, that is, both transmission and reception are happening simultaneously in the time domain, yet they are separated in the frequency domain, of course, this technique requires the availability of sufficient number of frequencies in order to serve all the users. In Time Division Duplexing, transmission and reception may use the same frequency but they occur at different time slots, that is, they are happening simultaneously in the frequency domain but separately in the time domain. A time slot at a certain frequency is called a communication channel. Usually, both Time Division Duplexing and Frequency Division Duplexing are used to generate the maximum number of communication channels possible in a licensed spectrum. The full-duplex mode implemented using Frequency Division Duplexing or Time Division Duplexing is called out-of-band full-duplex (OBFD) because a device transmits and receives data signals utilizing orthogonal resources (time or frequency).

To enhance the effectiveness of full-duplex it is highly desirable to be able to transmit and receive simultaneously in time and frequency domains. In this case, the full-duplex mode is called in-band full-duplex (IBFD) because a device uses the same resources to transmit and receive, which might, theoretically, double the available spectral resources in a certain frequency band. One might wonder why, originally, no attempts were made to achieve simultaneous transmission and reception using similar resources instead of orthogonal resources, and why the previously mentioned axiom assumes that radios cannot simultaneously transmit and receive. The answer can be extracted from Figure 1.3. If two nodes attempt to communicate simultaneously at the same frequency and the same time slot, the power coupled from the transmitter of one node to its own receiver will be much greater than the power received from the other node. This power coupling between the transmitter and the receiver of the same node is usually referred to as self-interference (SI), and basically it saturates the node's receiver and jams the signal transmitted by the other node. The level of self-interference depends basically on the transmitted power, which might be a few milli-Watts or a couple of Watts for short-range and indoor applications,

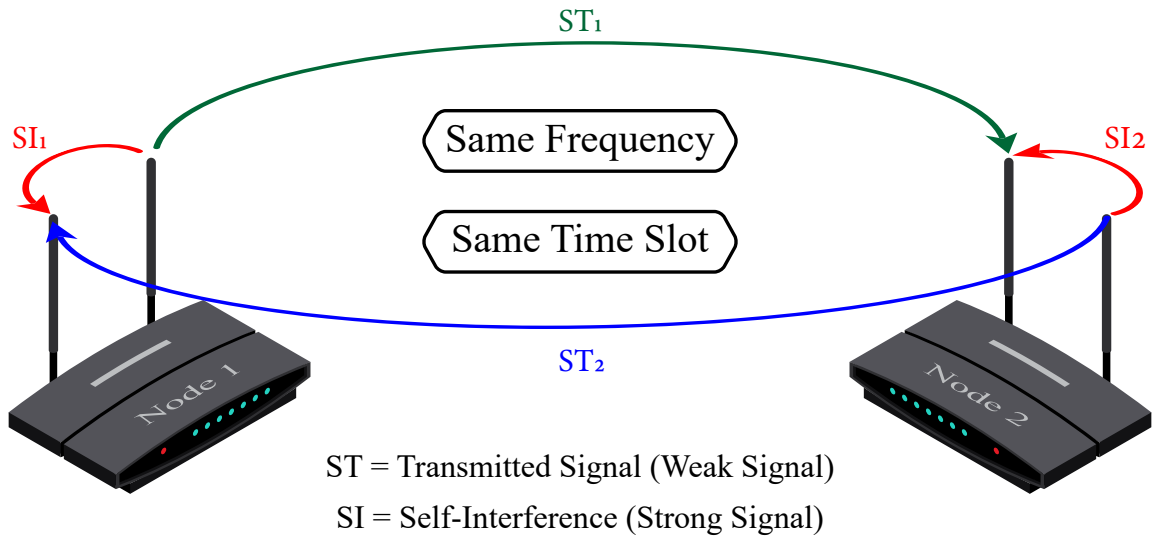

Figure 1.3: The case for in-band full-duplex.

such as mobile phones and WiFi, and might reach tens and hundreds of Watts for long-range outdoor applications, such as radars and base transceiver stations (BTSs).

In order to implement an in-band full-duplex system it is necessary to totally cancel self-interference signals by reducing their level below the noise floor of the receiver, where, typically, the noise floor of most radios is between -70 dBm and -110 dBm. So, if we take as an example the mobile phone that can transmit a maximum power of 33 dBm (2 Watts) [6] depending on how far it is from the base station, with a -90 dBm noise floor (as in many references, here the "noise floor" refers to the noise power in the bandwidth under consideration), then the required level of self-interference cancellation would be about 123 dB. Similarly, for WiFi applications, the average level of self-interference cancellation is about 110 dB [7]. Note that it is not sufficient just to reduce the level of self-interference by 80% or 90% for example, because although the residual self-interference will not saturate the receiver, yet it will act as additional noise in the system and will degrade its signal-to-noise ratio (SNR), which will, consequently, degrade its demodulation and throughput, and, in this case, it is better to operate in the traditional out-of-band full-duplex mode rather than the in-band mode.

1.2 In-Band Full-Duplex Systems: Challenges and Requirements

In essence, the self-interference cancellation mechanism is straightforward and direct: the transmitted signal is known, and therefore it can be subtracted at the receiver. However, in practice, it is not an easy task. In fact, when we think about how the front-end of the radio prepares the data for transmission, we would assume that the digital baseband signal is first converted to analog, then used to modulate the carrier signal, and after that it gets amplified and transmitted. Thus, we naively assume that the radio front-end maintains the baseband signal without distortion before transmission, except for amplitude scaling

and phase shifting. Also, we might tend to think that the transmitted signal remains the same when traveling between the transmitter and the receiver. Nonetheless, in practice, the signal gets significantly distorted (in amplitude, frequency, or phase) as it passes through the different components of the front-end and as it travels through air (or any desired propagation medium). Various imperfections in the transmit chain can cause noise and distortion; all of the components will contribute thermal noise, the digital-to-analog converter (DAC) will add quantization noise, and the local oscillator (LO) will introduce phase noise. Furthermore, many components, in particular the power amplifier (PA), will introduce non-linear distortions.

1.2.1 Self-Interference Components

It is important to distinguish between the different distortion types to identify the different components of the self-interference signals, and accordingly, we can plan and design the circuitry required to deal with each component. The main components of the self-interference signals can be classified into three major categories:

1. Linear Components: this corresponds to the actual signal intended for transmission, which travels through the direct path between the transmitter and the receiver, and its replicas, which are generated by the multipath reflections from the surrounding environment. These signals can be expressed as a linear combination of delayed copies of the original signal. Note that the direct path signal is much stronger, in terms of power, than the replicas and all the other components of the self-interference signals, and more effort is needed to suppress it.

2. Non-Linear Components: digitally modulated signals, after passing through the non-linear components of the radio front-end such as the amplifiers and the mixers, will produce spurious signals through a phenomenon called "Spectral Regrowth". The different frequencies constituting the modulated signal will interact together to form other components at harmonic frequencies (integer multiples), at the sum and difference frequencies of the original frequencies, and at the sums and differences of multiples of those frequencies. These non-linear components might be, typically, 30 dB below the transmitted power, and some of them might reside inside the frequency band of the modulated signal, while the rest might fall outside this band. The in-band components will contribute directly to the self-interference signals while the out-of-band components will interfere with other radios operating in the adjacent frequency bands. Both components need to be reduced, however, the main concern of in-band full-duplex systems is the in-band components.

3. Transmitter Noise: is mainly predominated by the thermal noise that is generated in each component of the transmit chain, and then amplified by the power amplifier. However, its value remains flat over an extremely wide bandwidth, which is, typically, 50-60 dB below the transmitted power level, and thus, it is usually called the broadband noise.

1.2.2 Requirements for Self-Interference Cancellation

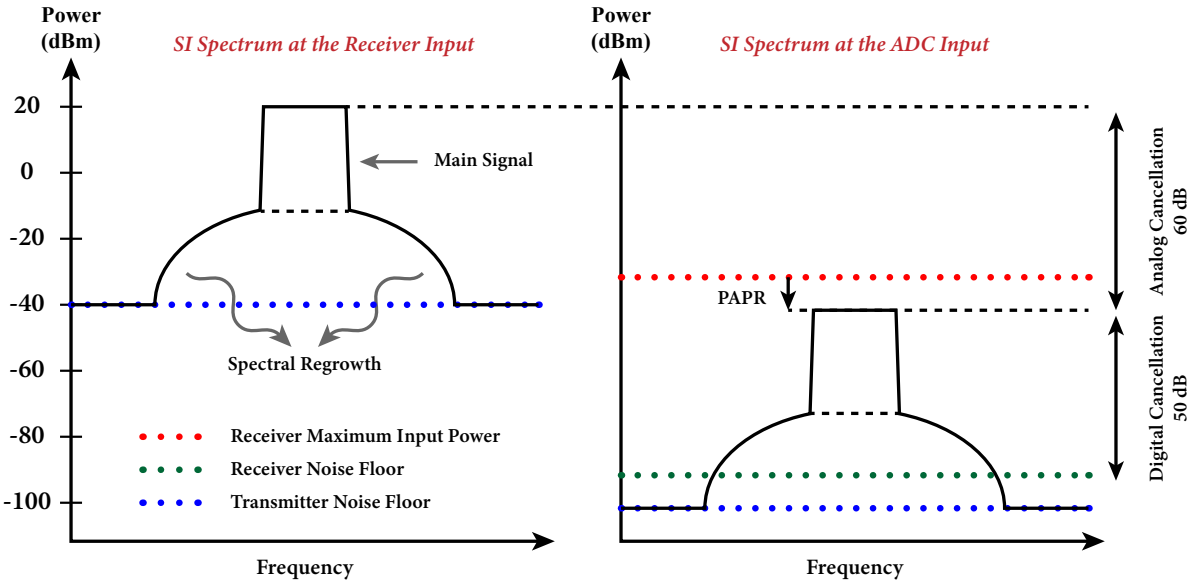

Figure 1.4: Typical self-interference signals' spectra of an in-band full-duplex system: at the input of the receiver and then at the input of the analog-to-digital converter (ADC).

Now, after indicating the different components of the self-interference signals, we can say that to implement an in-band full-duplex system it is necessary to cancel all these components, especially the main signal which has the highest power level. The different components need to be mitigated at the different stages of the front-end (as we will see in the next section): at the antenna(s), in the analog domain, and in the digital domain. Several requirements need to be considered, at each stage, when dealing with each individual component or the self-interference signals as a whole:

- It is required to bring all the self-interference signals below the receiver noise floor, in particular the linear component(s) which is(are) the strongest among all. So, if we consider for example a radio that can transmit an average power of 20 dBm with a receiver noise floor of -90 dBm, then the strongest transmitted signal power (the main signal) will be 110 dB higher than the receiver noise floor, and hence 110 dB of **linear self-interference cancellation** is needed.

- The non-linear components will be 30 dB below the main signal, or 80 dB above the receiver noise floor, thus a total of 80 dB of **non-linear self-interference cancellation** is required.

- Unlike the other components of the self-interference signals, the transmitter noise is, by nature, non-deterministic, that is it cannot be inferred by digital algorithms. So, the only way to cancel the transmitter noise is by taking a copy of it from where it originated (in the analog domain), and then subtract it from the received signal. Since the transmitter noise is 60 dB below the transmitted signal and 50 dB above the receiver noise floor, then any in-band full-duplex system needs to contain some analog circuitry that can provide 50 dB of **analog noise cancellation.**

- To avoid saturating the receiver, it is necessary to have a first level of cancellation, preferably before the amplifiers, to reduce the power of the self-interference signals to a level below the maximum input power of the receiver, which is determined by the dynamic range of the analog-to-digital converter (ADC). Assuming a 10-bit converter, the dynamic range is typically 60 dB above the receiver noise floor, and hence the maximum input power would be -30 dBm (with a -90dBm receiver noise floor). Accordingly, to satisfy this condition, we need to make sure that the strongest component (the main signal) is sufficiently canceled below the maximum input power, therefore, at least 50 dB of self-interference cancellation are needed before entering the amplifiers.
- Another parameter that needs to be considered, to avoid saturating the analog-to-digital converter, is the peak-to-average power ratio (PAPR), which determines the acceptable power peak compared to the average power content of a certain signal or waveform. A 1 dB PAPR indicates that no peaks exist in the waveform (as in DC signals) and a higher level of PAPR indicates that peaks exist in the waveform (as in sinusoidal signals). If a considerably extreme peak is present in the waveform, then it might saturate the receiver, and, in the best cases, it might reduce the accuracy of the analog-to-digital conversion, which means that the low-level signals will be lost in the quantization process. Thus, it is vital to keep the PAPR as low as possible, but, typically, a 10 dB PAPR is accepted, that is the peak power can be 10 times higher than the average power and still get an acceptable conversion quality. Hence, for any in-band full-duplex system, we need to have an extra 10 dB of margin below the maximum input power before entering the analog-to-digital converter, and consequently, we need to have at least 60 dB of analog cancellation before going to the digital domain.

In summary, any in-band full-duplex system need to provide at least 110 dB of linear self-interference cancellation, 80 dB of non-linear cancellation, 50 dB of analog noise cancellation, and, in general, at least 60 dB need to be achieved before reaching the digital domain. Also, the self-interference signals will be canceled at every stage of the receiver (antenna, analog, and digital), except for the transmitter noise which can only be canceled in the antenna and analog domains.

1.3 In-Band Full-Duplex Systems Overview

Figure 1.5 depicts a general block diagram of an in-band full-duplex heterodyne transceiver, only the important components are depicted in the figure to show the places at which self-interference cancellation takes place; the same concept can be extended to homodynes, super-heterodynes, and other radio architectures. Usually, self-interference cancellation takes place at three stages or levels: at the antenna level, at the analog level, and at the digital level. At the antenna level a single (or multiple) shared antenna(s) might be used simultaneously for transmission and reception, or multiple unshared antennas can be placed together, typically two, where one or more antennas are used for transmission while one or more antennas are used for reception. For shared antenna systems, the antenna(s) is (are) usually connected to a duplexing device, such as a circulator or a hybrid transformer which isolates the transmitted signal from the received signal.

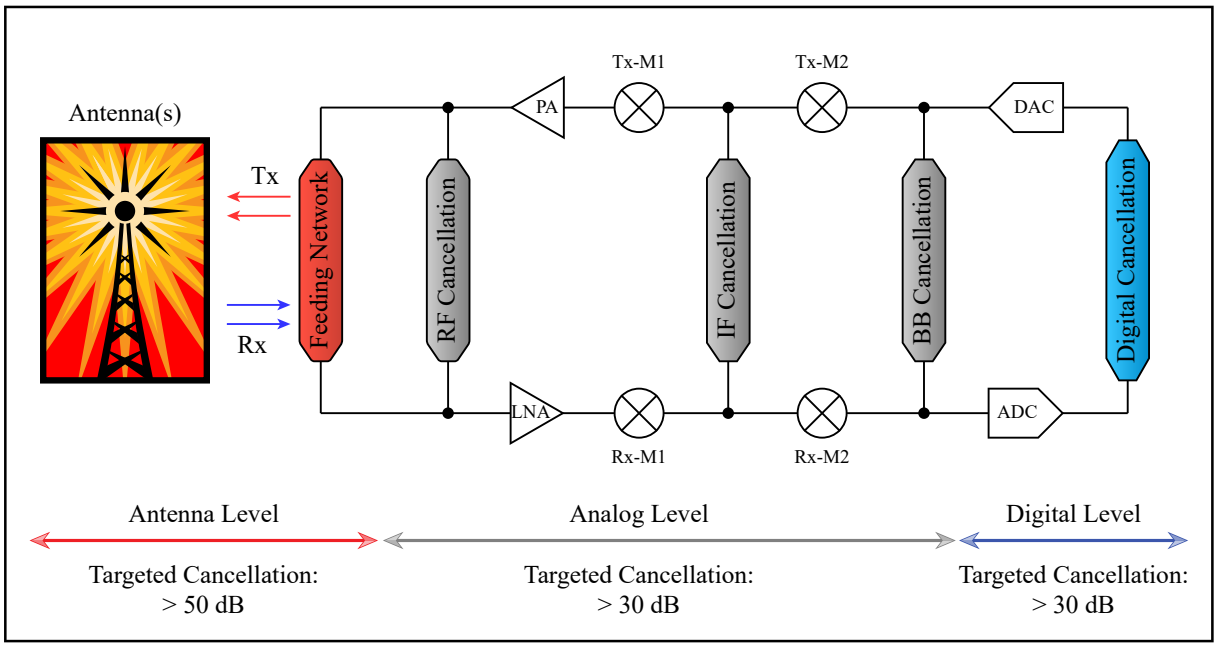

Figure 1.5: General block diagram of an in-band full-duplex heterodyne transceiver.

In the case of multiple unshared antenna systems, the main sources of self-interference are the direct path coupling between the transmit and receive antennas, and the multipath coupling resulting from wave reflections by objects from the surrounding environment. Direct path and multipath couplings are also present in the shared antenna(s) case, however, the direct path coupling mechanism is rather different: due to the finite isolation provided by the duplexing devices, a portion of the transmitted power manages to leak to the receiver. Also, an additional source of self-interference is present, which is the power reflected from the antenna(s) due to the impedance mismatch with the duplexing devices. The direct path coupling and antenna mismatch reflections are considered the strongest sources of self-interference and can be majorly predicted and measured, so they are usually the main focus of many works at the antenna and analog levels, while, on the other hand, multipath coupling is considered a minor source of self-interference and it varies greatly with the surrounding environment, so usually they are dealt with at the digital level along with the residual part of the direct path coupling.

Both the analog and digital levels benefit from the fact that the transmit and receive antennas are co-located on the same board or platform, and therefore, the receiver section has knowledge of the originally transmitted signal and of the characteristics of the direct path coupling, which can be predicted and measured. At the analog level, self-interference cancellation circuits can be deployed at three different stages: at the RF stage before the first pair of mixers, commonly before the low noise amplifier and the power amplifier, then at the intermediate frequency (IF) stage between the two pairs of mixers, and finally, at the base band (BB) stage directly before the analog-to-digital converter (ADC) and the digital-to-analog converter (DAC). But, typically, only one analog stage is adopted. The basic idea of analog cancellation is to take a copy of the transmitted signal before feeding it to the antenna, then processing it in some analog circuitry to create a replica of the self-interference signals, that will couple from the transmit antenna to the receive antenna. The analog circuitry will try to emulate the amplitude and phase changes of the self-

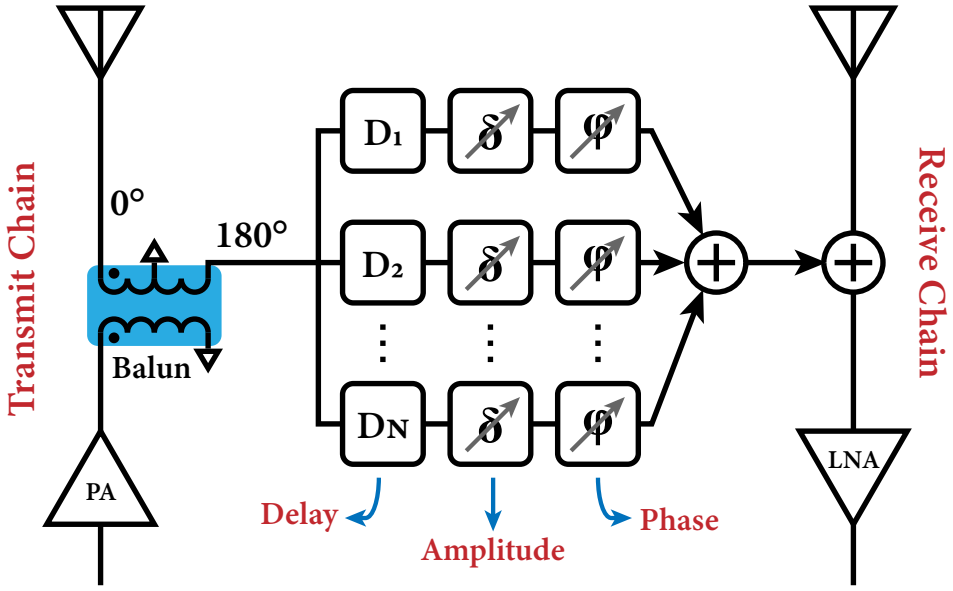

Figure 1.6: A basic block diagram of an analog self-interference cancellation scheme.

interference signals that propagate through air, and finally, the replica will be subtracted from the total received power.

Figure 1.6 depicts a basic block diagram of an analog cancellation scheme based on feedforward loops, which is implemented between the antennas and the power amplifiers. The first step to achieve self-interference cancellation using this scheme is to take a copy of the transmitted signal, before going to the antennas, and then feed it to the analog part. The copied signal needs to be inverted so that when it reaches the receiver it will be out-of-phase with respect to the received self-interference signals, and then they will cancel each other. This can be achieved by either using a 180° out-of-phase power divider (or a balun) to divide the transmitted signals into two out-of-phase signals, one will go to the antenna and the second one will go to the analog circuits, or by simply using an in-phase power divider to take a sample of the transmitted signal, and then a 180° phase shift can be generated inside the analog circuits using delay lines. After that, the sampled copy of the transmitted signal will be split into different branches known as taps. Each of these taps has a different time delay, denoted by D_N, and can independently adjust the signal's amplitude and phase before being combined into a single output. The time delay and the complex weighting of the taps allow the analog cancellation circuits to match the copied signal to both the direct path and the reflection path couplings, and to produce a signal that destructively combines with the self-interference signals at the receiver side. This type of circuit is known as an analog echo canceller.

At the digital level, the same self-interference cancellation procedure is implemented: a copy of the baseband digital signal is taken from the transmit chain and then fed to a digital signal processing (DSP) circuitry, which deploys various algorithms to create an inverse image of the digital self-interference signals, and then subtracts the replica from the received signals. The main purpose of the digital self-interference cancellation is to fully suppress any residual self-interference that remains after the different antenna and analog cancellation schemes. To achieve this, the digital processing unit needs to accurately model the different components of the self-interference signals. The benefit of

digital-domain cancellation is the increased flexibility in terms of modeling and parameter estimation, which facilitates the use of advanced self-interference signal models. This means that the significant analog impairments can be explicitly included in the modeling within the digital canceler, and consequently they do not pose a limit for the cancellation performance. Considering that in most cases the error vector magnitude (EVM) of the transceiver is dominated by the non-linear behavior of its power amplifier, incorporating a model of this non-linearity source into the digital processor can provide a significant improvement in the digital cancellation performance [8].

Finally, the total required level of self-interference cancellation can be accumulated at the antenna, analog, and digital stages consecutively, and achieving higher levels at a former stage can greatly relief the later stages in terms of requirements, complexity, and cost.

1.4 In-Band Full-Duplex Systems: Advantages and Disadvantages

By allowing simultaneous transmission and reception on the same frequency and the same time slot, in-band full-duplex not only doubles the spectral resources in a certain frequency band, but it can also provide many other advantages:

- Firstly, it enables the introduction of novel and efficient multiple access techniques [9]: full-duplex capable wireless devices can simultaneously listen to the radio channel while transmitting a signal to an access point in order to probe if other transmissions are occurring in the same radio channel, this would enable fast collision detection especially in packet-based multiple access techniques.
- Moreover, in-band full-duplex can be used in cognitive radios [10] to reduce the time needed to complete one cognitive period by half, that is, the two phases of the cognitive period (spectrum sensing and cognitive transmission), which occur serially, can now commence simultaneously by the aid of in-band full-duplex, thus halving the time of one cognitive period.
- Also, continuous wave radar systems, which traditionally used primitive self-interference cancellation techniques [11], can benefit from the advancements in in-band full-duplex to enhance their performance and reduce their size; these techniques will be discussed in a later section. Traditionally, radar systems needed to reduce their transmitted power to minimize the level of self-interference and to be able to receive properly, which limited continuous-wave radar systems to short-range applications, however, if enhanced self-interference techniques are used, the performance of radar systems can be extended to longer-range applications.
- Similarly, advances in self-interference cancellation can benefit antenna arrays, in particular multiple-input multiple-output (MIMO), which seek to increase the isolation between the individual elements of the array [12].
- Another advantage, which also relates to MIMO, is that transmitting at the same frequency and at the same time allows the transmitter and the receiver to have quite

the same Channel State Information (CSI), if the channel is quasi-reciprocal. This allows the transmitter to code the data tacking into account this accurately known CSI, which results in a better spectral efficiency of the transmission [13].

- Furthermore, implementing in-band full-duplex can reduce the air interface delay, this is achieved by simultaneously receiving feedback information (control channels, signaling related to error correction, etc.) while transmitting data, which minimizes the latency in data transmission [14].

- In addition to that, in-band full-duplex can form novel relay solutions [15] to enable almost instantaneous re-transmission. Also, it can allow a base transceiver station (BTS) to receive from one mobile user while transmitting to another at the same time and the same frequency. In both cases, only the relay or the base station need to operate in full-duplex mode while the source and destination nodes can operate in half-duplex mode.

- Finally, in-band full-duplex can add an extra level of security at the physical layer by adopting coordinated procedures between two nodes [16], whether solely or by the help of an intermediate relay, by injecting a jamming signal by the receiving node (or relay) while the transmitting node (or relay) is sending the data. The receiver node acquires a self-immunity to the jamming signal, with the aid of in-band full-duplex, and will be able to demodulate the data received from the transmitting node, while jamming the receiver of any eavesdropper in its range.

Despite this attractive list of advantages of in-band full-duplex systems, we should not dismiss their disadvantages which can be summarized as follows:

- Self-interference signals: perhaps the major challenge for in-band full-duplex systems is to totally eliminate the self-interference signals, which couple from the transmitter of the local node to its own receiver at a higher power level than the power received from a remote node, and failing to achieve that in a full scale might lead to dire consequences regarding the ability of the radio to receive properly, taking into consideration that any residual self-interference signals, although they might not saturate the receiver, but can act as noise and might degrade the receiver's sensitivity to low-power signals.

- Imperfect interference cancellation: in practice, we will not obtain the expected level of self-interference cancellation as in theory or simulation, and this can be referred to several reasons: fabrication imperfections in the realized circuits which might operate differently in practical measurements, the inaccurate estimation of self-interference signals especially those that might change with surrounding environment (reflected signals), and also the non-linearity of some components of the front-end itself and the self-interference cancellation circuitry, in particular at the analog level, which might grow out of control and manage to bypass the cancellation process.

- Higher power consumption and system complexity: as will be obvious later, to achieve self-interference cancellation in an in-band full-duplex system, additional components or parts need to be added to the radio front-end, which increases the

complexity of the system and increases its power consumption, and might, in some cases, degrade the efficiency of the system.

- Increased inter-user interference: this is especially critical to mobile communications in cellular networks and applications that require their users to transmit and receive in adjacent bands. In out-of-band full-duplex, one of the two communicating nodes can interfere with users on adjacent channels, mainly because the two nodes are always separated in frequency or time, however, for in-band full-duplex systems, both nodes transmit and receive on the same frequency and at the same time, and thus both nodes can now interfere with the adjacent users at the same time. Thus, we can say that the inter-user interference of in-band full-duplex, in theory, is twice that of out-of-band full-duplex.

1.5 Frame of Work

The field of in-band full-duplex is very recent, where the first works appeared in 2012, and it remains under development. The previously published works in this field were dedicated for narrowband applications, and the proposed self-interference cancellation techniques in those works could achieve high levels of cancellation over a very narrow bandwidth. However, considering their appealing advantages, it is highly desirable to implement full-duplex systems over wide bandwidths for civil, military, and space applications. A wideband full-duplex front-end can be considered as a general-purpose tool that can serve many applications and eliminates the necessity to design multiple front-ends for different standards; which can fit well the Software Defined Radio (SDR) approach. This type of wideband systems can be considered for diverse applications where capacity, low latency, and secrecy capabilities are required. That may concern, for example, in cellular telecommunication systems, backhaul microwave links between the core network and the radio access network, or wireless links between two remote base stations instead of using fiber optic. More broadly, the "sensing-as-transmitting" property, along with all other characteristics of in-band full-duplex, can be valuable for any wideband multi-standard communication operation, especially for cognitive radios and radar systems, which require continuously scanning a wide range of frequencies while transmitting.

Little work has been done on in-band full-duplex systems to extend their performances to cover wide bandwidths. Thus, the topic of wideband in-band full-duplex systems remains underdeveloped, vague, and not easy to implement, so more effort needs to be invested in that field. Some of the more recent publications on wideband full-duplex systems indicate that achieving high levels of self-interference cancellation over a relatively wide bandwidth is possible at the antenna level, but the analog and digital parts fall far behind with achieving wideband cancellation, mainly, due to circuitry bandwidth limitations, complexity, and cost. Although it might not be feasible or possible to implement a fully-developed wideband full-duplex front-end, with wideband analog and digital cancellation, but at least it is good to have a wideband full-duplex antenna system as a first step, which in turn can be used in multiple applications while the analog and digital parts can be tailored several times based on the application requirements. In the light of this, in this work, we mainly focus on implementing a wideband full-duplex antenna system that can provide a high level of self-interference cancellation, good gain,

and relatively compact size. Also, some self-interference cancellation techniques might require separating the beams of the transmitter and the receiver to achieve a higher level of isolation between them, and in this case the implemented system has to transmit in one direction and receive from a different direction, but in this work, we would like to have a system that can transmit and receive in the same direction.

Based on the above, a group of self-interference cancellation techniques will be presented in the next section, and after, we will determine the best suitable self-interference cancellation technique that we can use to build our system, taking into account the above-mentioned specifications.

1.6 Antenna Level Self-Interference Cancellation Techniques

The term *self-interference cancellation* became well known and widely used in the context of in-band full-duplex, however the concept appeared in different literatures many years ago, namely in fixed telephony, continuous-wave radar systems, multiple-input multiple-output (MIMO) antenna arrays, and radio-frequency identification (RFID). Terms like *Transmitter-Receiver Isolation*, *Transmit Leakage Cancellation*, and *Carrier Suppression* were used in those literatures to describe the same process or concept. Accordingly, some of the techniques presented in this section are invoked from these literatures and built upon toward in-band full-duplex. But, although the concept was investigated long time ago, yet it was not widely researched, mainly, because, in those literatures, the cancellation level needed was not so high and demanding. However, with the emergence of in-band full-duplex and the recent works [7, 17–26] in that field, self-interference cancellation gained more attention and investment by the scientific community, where some researchers managed to achieve notable breakthroughs and were able to achieve levels higher than 90 dB of self-interference cancellation.

When it comes to classifying self-interference cancellation techniques it turns out that there is no one way to do this, mainly because there are some techniques that can be collectively grouped in one or more families of techniques, and there are individual unique techniques that cannot be incorporated in any of those families. So, in this section, we organize the different techniques in a way that gives a broad view of the available techniques while focusing on the most relevant ones for our targeted wideband in-band full-duplex system. So, as previously mentioned, to accumulate the required levels of self-interference cancellation, several techniques can be applied successively at the antenna, analog, and digital domains. But in this work, we only focus on the antenna level where the self-interference cancellation techniques can be divided into two main categories: monostatic and bistatic.

The term *monostatic* was used in the literature of radar systems to describe a radar that simultaneously transmits and receives using a single shared antenna or multiple collocated antennas, and the term *bistatic* was used in the same literature to describe a radar system that uses separate antennas for transmission and reception at sufficiently different locations that their angles or ranges to the target are significantly different [27]. However, in the context of in-band full-duplex, the definitions of these two terms have

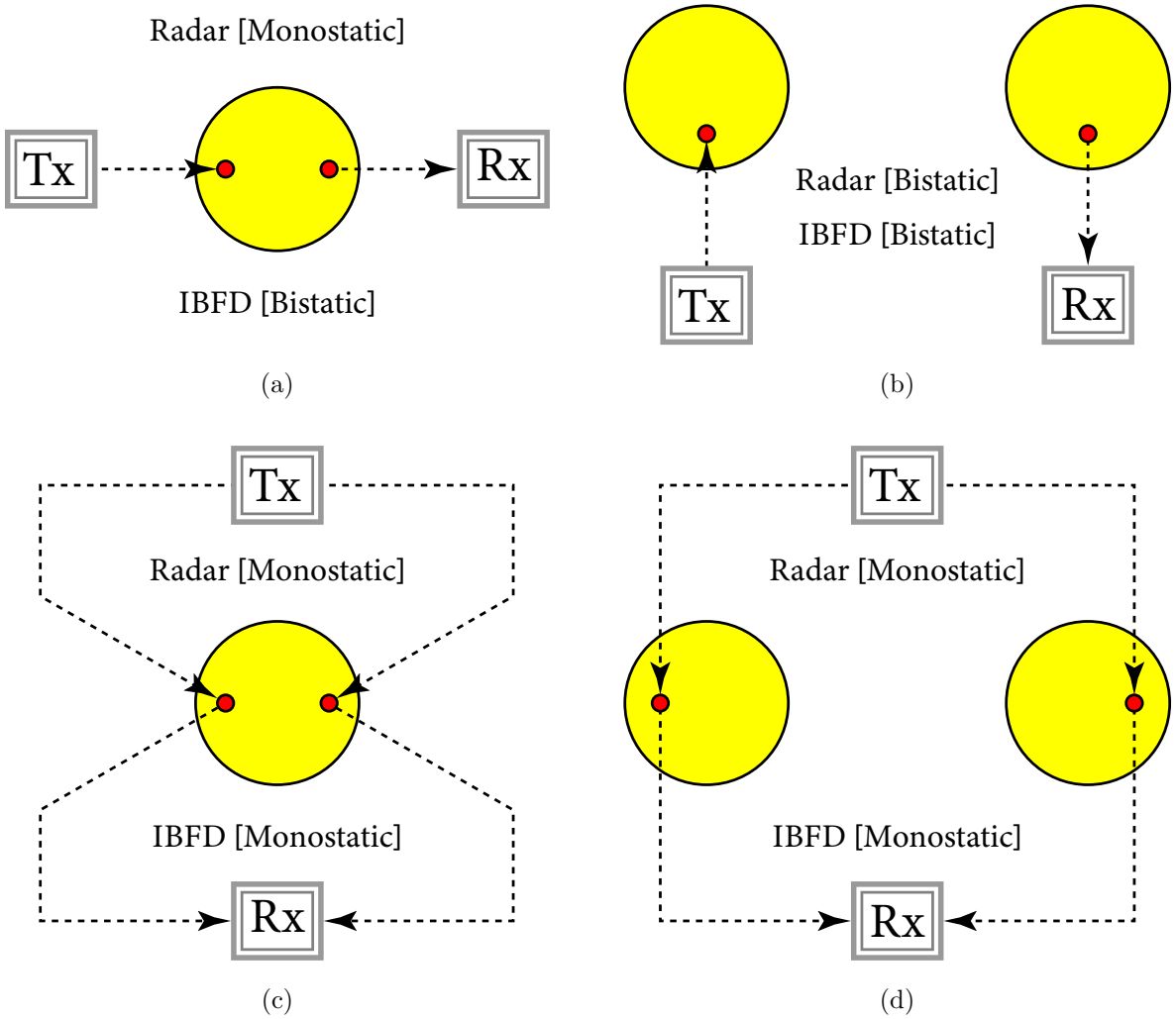

Figure 1.7: Different antenna configurations and their classification into monostatic and bistatic from the radar literature point of view and in-band full-duplex point of view (a) a dual fed circular patch antenna with one port connected only to the transmitter and the second port connected to the receiver, (b) two circular patch antennas with one feeding port: one connected to the transmitter and the second one connected to the receiver, (c) a dual fed circular patch antenna with the two ports simultaneously connected to the transmitter and the receiver, and (d) two circular patch antennas with one feeding port simultaneously connected to the transmitter and the receiver.

to be modified to better describe what is already published in the literature, because in some publications a single antenna with multiple ports can have a bistatic behavior and multiple antennas with single ports can provide a monostatic performance. So, in this context, both monostatic and bistatic systems can use single or multiple antennas, which can be collocated or not. But what distinguishes them from each other is that in a monostatic system, all ports of each individual antenna have to be physically connected to both the transmit and the receive feeding networks at the same time. Whereas in a bistatic system, one or more ports of each antenna should be only connected to the transmit feeding network, while the rest of the ports must be only connected to the receive feeding network. Figure 1.7 illustrates different antenna configurations and how

	Monostatic	**Bistatic**
Passive	• **Circulators:** ⋆ Loop Circulation • **Hybrid Transformers:** ⋆ Single 180°-Hybrid ⋆ Balun-Power Divider Combination ⋆ Single Quadrature-Hybrid ⋆ Two Circulators With Two Quadrature-Hybrids ⋆ Two Circulators With Balun-Power Divider Combination	• Antenna Separation • Beam Separation • Cross Polarization • Near-Field Nulling ⋆ Half-Wavelength Separation ⋆ Antiphase Feeding ⋆ Near-Field Cancellation ⋆ Circularly-Phased Arrays • Beam Diversity • Surface Current Suppression
Active	• Reflection-Leakage Collision	• Decoupling Networks • Co-Polarized Reflections

Table 1.1: Self-interference cancellation techniques at the antenna level.

they are classified into monostatic and bistatic from the radar literature point of view and in-band full-duplex point of view.

After that, for each of the aforementioned categories, self-interference cancellation techniques can be further divided into two subcategories: passive and active. The terms *passive* and *active* might also be slightly misleading in this context, and it does not mean necessarily that passive self-interference cancellation techniques use only passive devices or that active techniques use only active devices, but, on the contrary, both types of techniques can use active and/or passive devices. In fact, in this context, an active technique is a technique that requires a prior knowledge of the characteristics of the system components, surrounding environment, or transmitted signal to actively operate based on the available information; in such techniques, usually, the whole system needs to be tuned or redesigned if a single component is changed. On the other hand, passive techniques are agnostic to the system characteristics, surrounding environment, and the transmitted signal, and can operate independently without any prior knowledge of the system's parameters. Moreover, for passive techniques, changing a component in the

system does not usually require redesigning the whole system. Thus, based on the above definitions, analog and digital self-interference cancellation techniques are considered active as their operation depends mainly on a prior knowledge of the transmitted signal and the surrounding environment of the system. Table 1.1 organizes some of the published techniques under their categories, however, note that the names of these techniques in the diagram might be slightly different from the names given to them by the different authors, but for the sake of generality and consistency we try to give them expressive names that suit the coherence of this narrative, and more clarity of these names will appear when we explain them later in this section. Finally, for monostatic systems, the antennas need to be connected to a duplexing device, mainly a circulator or a hybrid transformer, hence in the monostatic category the techniques are subcategorized into circulator-based techniques and hybrid transformer-based techniques.

1.6.1 Monostatic Systems

1.6.1.1 Circulators

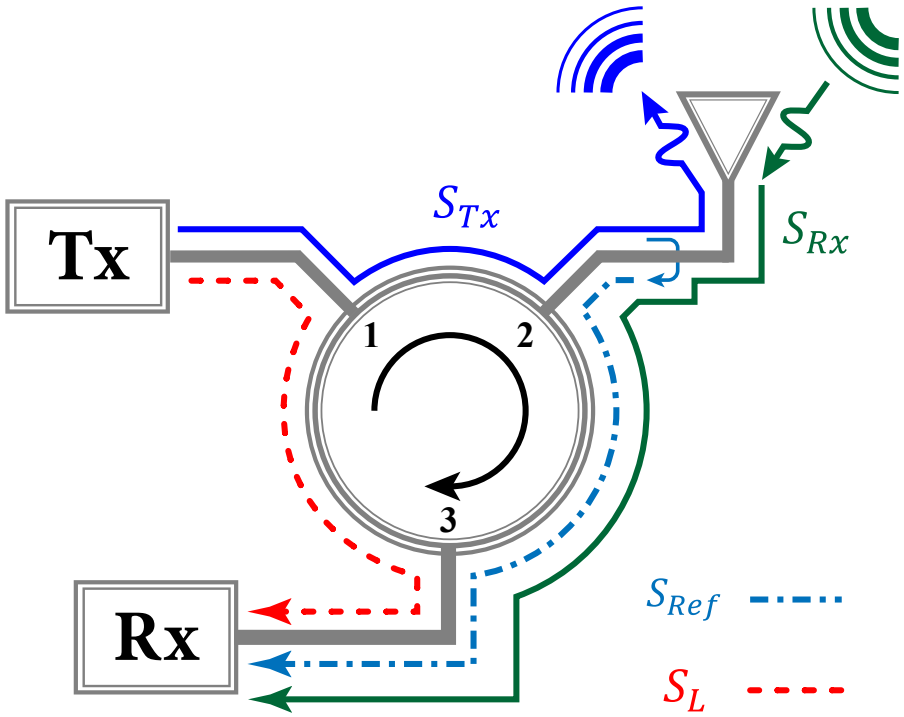

Figure 1.8: An illustrative drawing of a single antenna connected to a circulator that shows the port numbering of the circulator, direction of circulation, and the flow of signals between its ports.

Figure 1.8 depicts a circulator which is a three-port microwave device that can be lossless and matched at all ports but nonreciprocal, that is, power can flow from port 1 to port 2, port 2 to port 3, and port 3 to port 1, but not in the reverse directions [28]. Circulators were traditionally built using ferrite (or magnetic) materials, but,

more recently, they have also been designed using periodically switched devices, such as capacitors or transistors. Since the power entering the circulator is forced to circulate in a single direction but not in the opposite, its ports possess an inherent isolation from signals coming from the opposite direction, however, in practice, this isolation is finite and limited to more or less than 20 dB over a narrow bandwidth, or more or less than 10 dB over a slightly wider bandwidth. Although the inherent isolation of the circulator is limited and does not provide the targeted level of self-interference cancellation at the antenna level (50 dB), yet it constitutes a first step toward accumulating that level, especially if it is paired with additional self-interference cancellation techniques. However, the main drawback of all circulator-based self-interference cancellation techniques is the circulator's bandwidth constraint, which restrains such techniques from extending to wideband operation. Moreover, circulators are relatively bulky and, in some cases, are not easy to integrate on some boards or circuits.

Usually, the transmitted signal is fed to Port 1, and the antenna is connected to port 2, while the receiver is connected to port 3. Due to the finite and low level of isolation between its ports, a portion of the transmitted signal (S_{Tx}) is leaked to the receiver. In addition to that, in practice, there will be a mismatch between the antenna and the circulator, this means that also a portion of the transmitted signal will be reflected back to the circulator and will go directly to the receiver. So, in total, the receiver will receive three signals: the received signal (S_{Rx}), the leaked signal (S_L), and the reflected signal (S_{Ref}). The received signal is the only wanted signal while the leaked and reflected signals are considered as self-interference signals and need to be eliminated. Mainly, most circulator-based self-interference cancellation techniques manage to greatly reduce the leaked signal, however, some of them does not deal with the reflected signal, maybe because the reflected signal is not as much significant as the leaked signal. In what follows, we present some of these techniques that can also be subcategorized as passive or active:

I. Loop Circulation:

This technique [29, 30] uses three circulators instead of one arranged as shown in Figure 1.9, such that the transmitted, the received, the reflected, and the leaked signals have always to pass through at least two of the three circulators. Since the leaked signal moves against the direction of circulation, it gets weaker each time it passes through a circulator till it reaches the receiver. So, in this configuration the leaked signal is only weakened and is not totally eliminated. Also, in case there is a mismatch between the antenna and the circulator, the reflected signal, due to the mismatch, will flow directly to the receiver. But, perhaps, if the distances between the circulators are manipulated, then it is possible to alter the characteristics of both the leaked and reflected signals such that they combine 180° out-of-phase at the receiver. Anyhow, the obtained isolation between the transmitter and receiver is not significant and is not worthy, especially that it introduces some drawbacks. For instance, the size of one circulator is considered relatively bulky, so the size of three circulators can drastically increase the size of the system, also it increases the complexity of integrating all circulators on the same board and the cost of the system.

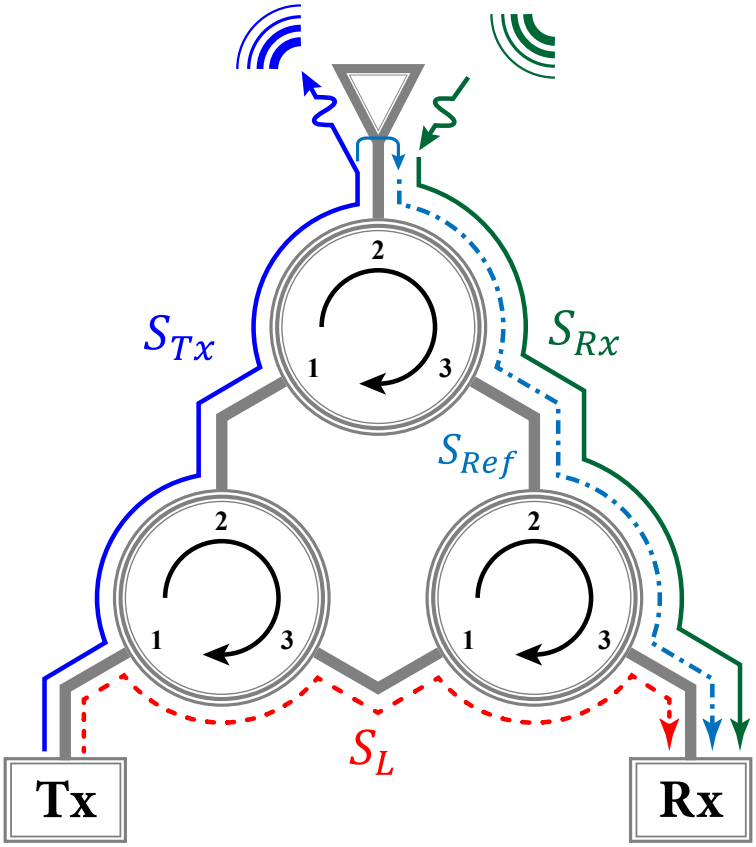

Figure 1.9: Loop circulation technique.

II. Reflection-Leakage Collision:

In [31, 32] the reflected signal (S_{Ref}) from the antenna to the circulator and the leaked signal (S_L) from the Tx port to the Rx port are forced to combine destructively at the Rx port by adding a tunable impedance mismatched terminal (IMT) between the antenna and circulator, the role of the terminal is to modify the phase and amplitude of the reflected signal such that the reflected signal and the leaked signal will have equal amplitudes and will be 180° out-of-phase such that the two signals will combine out-of-phase at the output (Rx) port and will eliminate each other, which drastically increases the level of self-interference cancellation. This technique requires a prior knowledge of the circulator's characteristics to be able to predict the characteristics of the leaked signal, and also requires a prior knowledge of the antenna's impedance mismatch with the circulator to predict the characteristics of the reflected signal. If a different antenna or a different circulator are to be used, a new terminal has to be designed to adapt to the new characteristics of the newly added components. Moreover, the terminal contains tunable components (variable capacitors or transistors) which induces non-linear effects in the system, and, in addition to that, the effect of the terminal on the antenna's effective gain was not demonstrated by the author's, but it is expected to decrease due to the power lost in the terminal components.

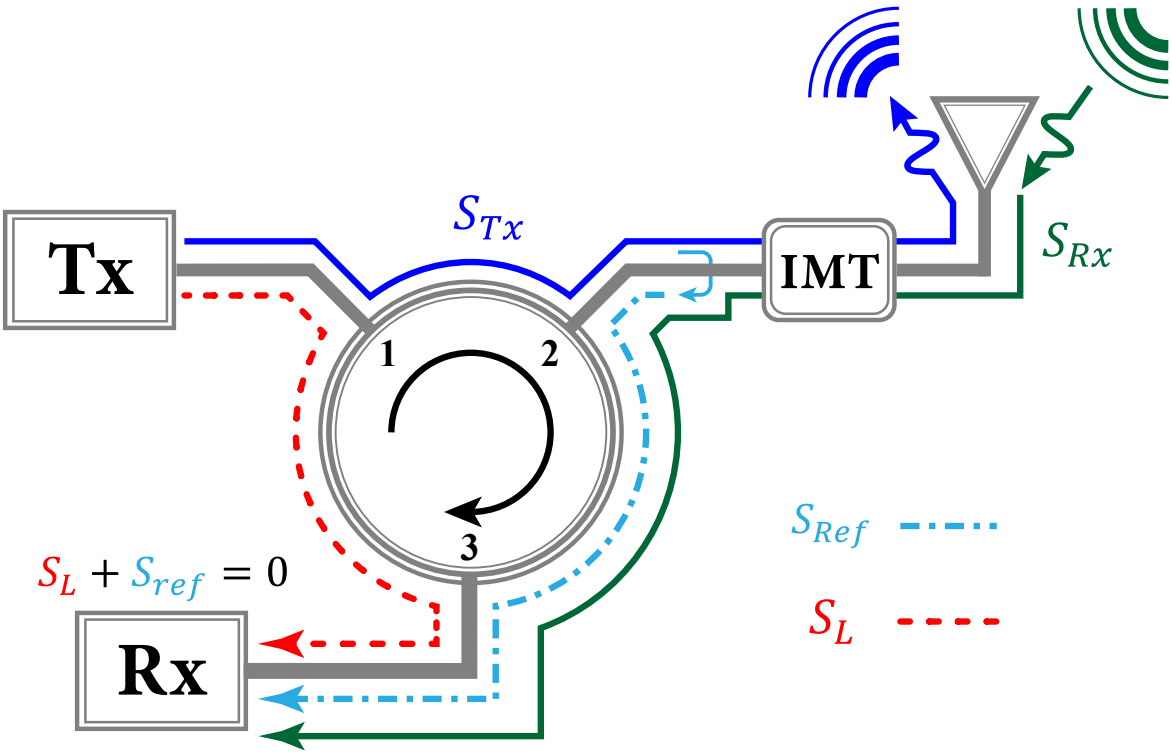

Figure 1.10: Circulator reflection-leakage collision with the aid of an impedance mismatched terminal.

1.6.1.2 Hybrid Transformers

I. Theoretical Background:

Hybrid transformers, also known as Electrical balanced transformers and balanced duplexers, belong to a class of networks called *maximum output networks* [33], that were first introduced in fixed telephony to deliver the maximum transmitted power from one fixed telephone apparatus to another, and to receive the maximum power from the second apparatus at the same time, while trying to isolate the two signals from each other. In simpler words, they were used to isolate the receive port of the telephone from its own transmit port, that is, to achieve self-interference cancellation in fixed telephony. After the birth of wireless communications, especially after the invention of continuous-wave radar systems, techniques based on hybrid transformer networks were exploited to cancel the power leaked from the transmit path of a wireless device to its own receive path, and after the emergence of in-band full-duplex, similar techniques were re-invoked to aid in the cancellation of self-interference. But before presenting these techniques, a description of the main characteristics and the behavior of hybrid transformers is presented next.

The hybrid transformer is a four-port network where each pair of opposite ports are conjugate (or isolated) depending on the matching at each port, that is, if the transmit and receive ports and a third port are matched, then the degree of conjugacy (or isolation) is directly related to the mismatch between the third and fourth port [34]. Hybrid

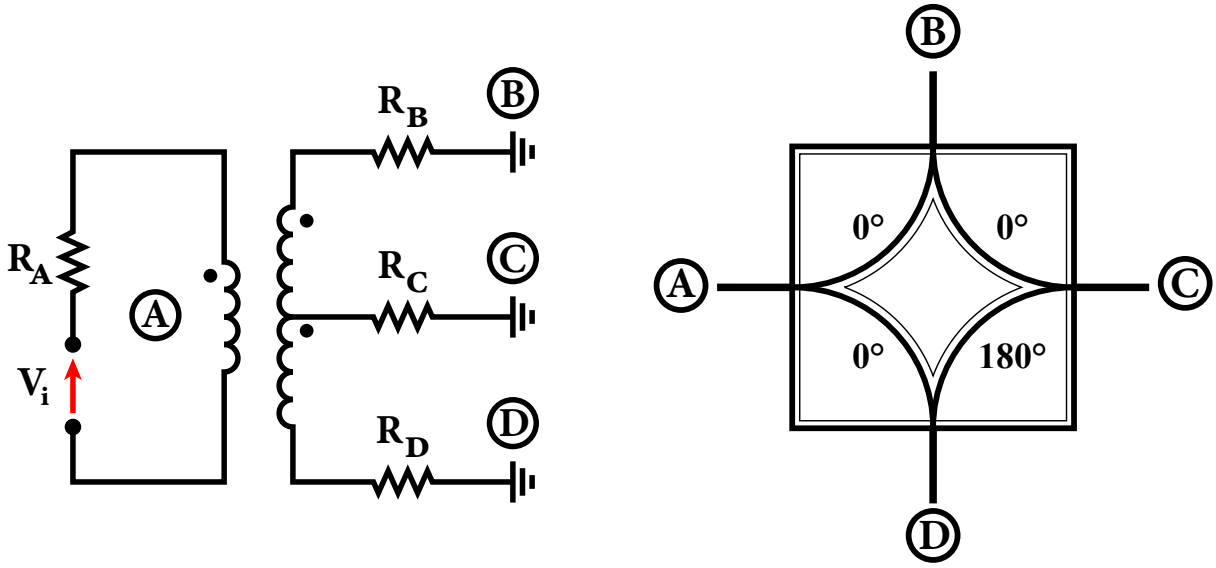

(a) (b)

Figure 1.11: (a) conventional symbol of the hybrid transformer in fixed telephony and (b) a more recent symbol used in microwaves theory.

transformers were conventionally built from windings, however, for RF applications they can be implemented using a combination of 90°- or 180°- hybrid couplers, in-phase or 180° out-of-phase power dividers, and also can contain circulators, which will be described in details later. Figure 1.11(a) shows a schematic of the conventional symbol used for hybrid transformers in old publications, also Figure 1.11(b) shows a more recent symbol used in microwaves theory. To demonstrate the conventional theory of hybrid transformers, the old symbol will be used, while the new symbol will be used after to explain its principle of operation in in-band full-duplex.

A network is called a hybrid transformer if it possesses the following four properties, by referring to Figure 1.11(a) and assuming ideal transformer: if the impedances at Ports B and D are equal ($R_B = R_D$), then no signal arrives from Port A to Port C; thus, Ports A and C are called conjugate ports. And, similarly, if the impedances at Ports A and C are equal ($R_A = R_C$), then Ports B and D are also conjugate. Hence, the usual hybrid transformer networks are biconjugate systems. The second property states that if the network is biconjugate and an impedance match exists at one port, then all the other ports of the network will be matched. And conversely, if all the ports are matched then the network will be biconjugate.

Under ideal conditions, there are no power losses inside the network and if the network is biconjugate, then the power from Port A can only reach Ports B and D. So, if we designate the power entering Port A as P_A and the powers received at Ports B and D as P_B and P_D respectively, then $P_A = P_B + P_D$. Based on this, the hybrid transformer can be designed to obtain any desired ratio between the powers P_B and P_D by manipulating the impedances between each two ports while preserving the matching at all ports and the biconjugacy conditions. If we designate this ratio as $r = P_B/P_D$, then we have:

$$\frac{P_B}{P_A} = \frac{r}{r+1} \qquad \frac{P_D}{P_A} = \frac{1}{r+1} \tag{1.1}$$

The same power ratios P_B/P_A and P_D/P_A can be also expressed in dB as follows:

$$R_{BA} = 10\ log_{10}\left(\frac{r}{r+1}\right) dB \qquad R_{DA} = 10\ log_{10}\left(\frac{1}{r+1}\right) dB \tag{1.2}$$

Usually, in most publications $r = 1$, that is the power entering Port A will be divided equally to Ports B and D, because it is much easier and simpler to have equal power division than unequal power division, but the latter is also possible to implement. Now, the third property of hybrid transformers states that the power transmitted from Port A to Port B must be equal to the power transmitted from Port B to Port A, and a similar condition holds for Ports A and D. In addition to that, if the used components in the network are lossy, then the power loss from Port A to Port B should be identical to the loss from Port D to Port C, and, similarly, the power loss from Port A to Port D must be identical to the loss from Port B to Port C. And, finally, the fourth property of hybrid transformers deals with the phases of the signals passing throw the four paths: A to B, B to C, C to D, and D to A, and it states that the phases of any three signals in any of the three paths should be zero, while the phase of the signal in the fourth path should be 180°.

II. Full-Duplex Operation:

For in-band full-duplex applications any two conjugate ports of the hybrid transformer can be chosen as transmit and receive ports, then an antenna will be connected to the third port and its equivalent impedance will be connected to the fourth port, as shown in Figure 1.12. If the transformer is designed to have equal power splitting (i.e., $r = 1$), then the power fed to the transmit port (Port A) will be divided equally, and, after that, half of the divided power will be delivered to the antenna (at Port B) while the other half will be delivered to the equivalent impedance (at Port D) where it will be absorbed. Similarly, the signal received by the antenna will be divided equally at Port B, then half the power will be delivered to the receiver at Port C and the other half will be delivered to the transmitter at Port A, however, in this case, the performance of the transmitter would not be affected because the transmitted signal is much stronger than the received signal. Nonetheless, half the transmitted and received powers will be lost in the transformer, which is the price we pay to implement a duplexing device without using magnetic materials. But these losses can be reduced by doing the following:

- To mitigate the power losses in the reception path, the power split ratio at Ports B and D can be increased or decreased to force more received power to go toward the receiver port and less power to go toward the transmit port. But it should be noted that if not the same splitting ratio is present at all four ports, then the third property is violated, and the network can no more be called a hybrid transformer.
- On the other hand, to reduce the power losses in the transmit path, the equivalent impedance at Port D can be removed and a second antenna, which is identical to the first one, is connected to the port. Or, alternatively, both the equivalent impedance and the antenna can be removed from the circuit, and a dual-fed antenna with two feeding ports can be connected to Ports B and D, respectively.

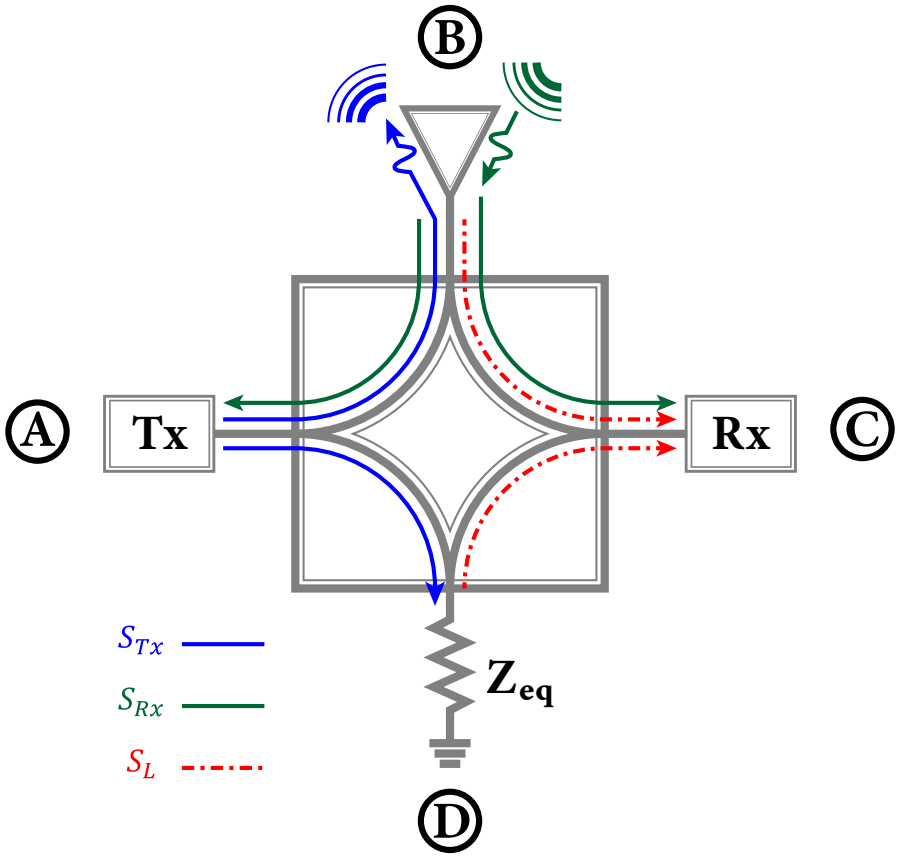

Figure 1.12: Basic in-band full-duplex system based on hybrid transformers.

The reader might wonder now why not a second antenna was connected at Port D in the first place, knowing that this solution can eliminate power losses in the transmission path. This is not the only advantage of this solution, but, additionally, it has two other important advantages: firstly, by using two identical antennas we eliminate the necessity to design the equivalent impedance, which might be cumbersome is some cases, and, secondly, if the two used antennas are wideband, then the performance of the full-duplex system can be potentially extended to wideband operation if there exists a wideband hybrid transformer. Nevertheless, although these advantages may seem alluring, but they come at a great cost in the far-field behavior of the antennas if they operate with single linear polarizations, because no matter what kind of antennas is used or the way the antennas are placed, oriented, and fed with respect to one another, there will always be a far-field null in either the transmit or the receive paths of the system, mainly in the broadside lobe of the radiation pattern, which means that the system will not be able to transmit or receive in a certain direction; this will be demonstrated later. However, this issue is not a big problem for dual-polarized or circularly-polarized antennas.

In practice, there will always be some power leakage from the transmitter to the receiver depending on the devices used to implement the hybrid transformer and on the mismatch between the transformer and the antenna on one side, and the mismatch between the equivalent impedance and the transformer on the other side, and, also, depending on whether both mismatches have equal values or not. Nonetheless, if there is a 180° phase shift in one of the paths between Ports A and C, then the two leaked signals

and the two reflected signals will combine, ideally, out-of-phase at the receiver port. But, although the leaked and reflected signals will be canceled at the receiver, it is always better to have less leakage in the transformer and better matching with the antennas to allow more energy to get radiated by the antenna(s) and less power to get destroyed inside the transformer, which enhances the power efficiency of the full-duplex system.

It is obvious that for in-band full-duplex operation, only the transmit and receive ports need to be conjugate (Ports A and C), and that conjugacy is not necessary for the other two ports (Ports B and D), thus the biconjugacy condition of the hybrid transformers is not necessary for in-band full-duplex operation, and it is sufficient just to have one pair of conjugate ports. Thus, this allows us to violate the biconjugacy condition for hybrid transformer without affecting the performance of the in-band full-duplex system, and the resultant transformer will have a quasi-hybrid behavior. By violating the biconjugacy condition we get more degrees of freedom for designing the transformer with a diverse variety of components. In addition to that, for in-band full-duplex applications, it is not necessary for the conjugate ports to be facing each other, and any two ports can be conjugate whether they are adjacent or on opposite sides, which also gives more freedom in the circuit design.

Based on the above, self-interference cancellation techniques using hybrid transformers are firstly subcategorized into passive and active techniques. Passive techniques describe the various methods to implement a hybrid transformer focusing mainly on the components inside the network, while active techniques focus mainly on manipulating the characteristics of the components connected to the transformer, namely the antenna and the equivalent impedance. Finally, for passive techniques, depending on whether the transformer network respects or violates the biconjugacy condition, the presented networks will be classified into "True-Hybrid Transformer Networks" and "Quasi-Hybrid Transformer Networks". Also, in the case of passive techniques, it is always assumed that the two antenna ports of the transformer (Ports B and D), unless otherwise mentioned, are always connected to a single dual-fed antenna and that there is no equivalent impedance at any port.

III. True-Hybrid Transformer Networks:

A. Single 180°-Hybrid:

180°-Hybrids can be actually considered as hybrid transformers as they satisfy all the properties of hybrid transformers. Classically, there are two devices that can be used as 180°-Hybrids: the rat-race couplers and the tapered coupled line coupler. For instance, let us consider the rat-race hybrid that is depicted in Figure 1.13, it has four ports with a characteristic impedance Z_0, each placed at a quarter-wavelength away from each other around the top half of a ring. The ring has an impedance equal to the characteristic impedance of the ports multiplied by the square root of two ($Z_0\sqrt{2}$), and the bottom half of the ring is three quarters of the wavelength. Its operation can be described as follows:

- If all ports are matched and a power is injected at Port A, then it will be split equally between Ports B and D while Port C remains isolated, but the signal at Port D will be phase-shifted by 180° with respect to the signal at Port B. Similarly,

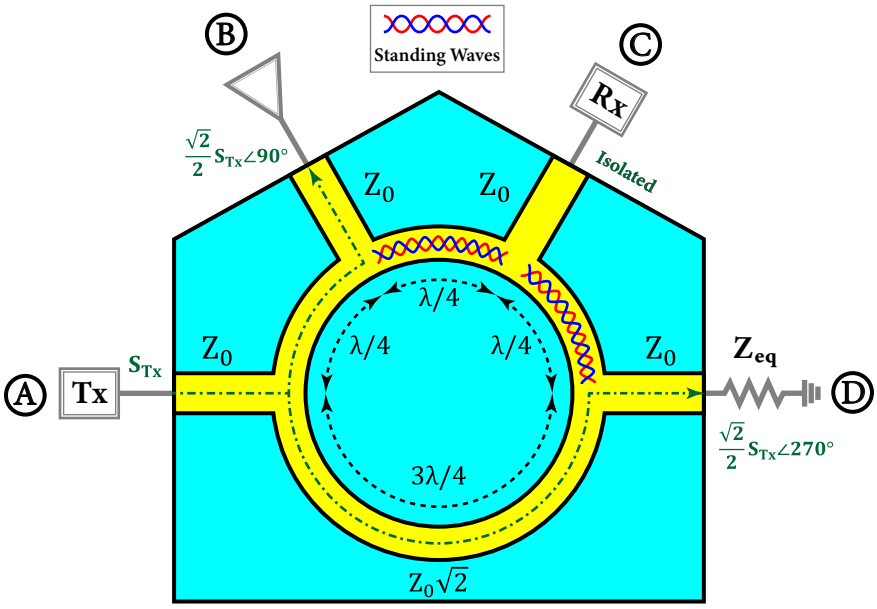

Figure 1.13: The rat-race coupler.

if the power injected at Port D then it will be split equally between Ports A and C while Port B remains isolated, such that the signal at Port A is also shifted by 180° with respect to the signal at Port C.

- Moreover, if the power is injected at Port B, then it will be split equally and in-phase at Ports A and C while Port D remains isolated. Similarly, if the power is injected at Port C, then it will be split equally and in-phase at Ports B and D while Port A remains isolated. So, it can be said that Ports A and C are isolated, and Ports B and D are also isolated, which means that the biconjugacy property is satisfied.

- In addition to that, the power that flows from one port to a second port is exactly equal to the power that flows from the second port to the first one, whatever two ports are selected.

- And, finally, only one path in the circuit generates 180° phase shift, which is the bottom half of the ring, while all other paths are in-phase. Hence, the rat-race coupler satisfies all properties of a hybrid transformer.

The isolation between any two conjugate ports of the rat-race hybrid is caused by the standing waves that originate during its transient state operation, mainly, due to the half-wavelength difference between the two paths that the signal takes to travel form the input port to its conjugate. For example, in the transient state, if the input signal is injected at Port A, as in Figure 1.13, then the power will travel to Port C following two paths: the first path passes by Port B and is half-wavelength long, while the second path passes by Port D and is one wavelength long. Obviously, there is a half-wavelength difference between the two paths, which causes standing waves to occupy the transmission lines between Ports B and C and also between Ports D and C. The standing waves will block those transmission lines and will prevent any signal from passing through them in the steady state, and that is how the isolation between the conjugate ports originates. However, the

isolation provided by the rat-race hybrid is finite and can reach 80 dB in simulation, but in practice it drops sometimes below 20 dB depending on the fabrication tolerances. Only, one publication on self-interference cancellation using a single conventional 180°-hybrids was found in [35]. Also, a novel 180°-hybrid based on microstrip-to-slotline transitions was demonstrated in [36] for dual-polarized in-band full-duplex arrays.

B. Balun-Power Divider Combination:

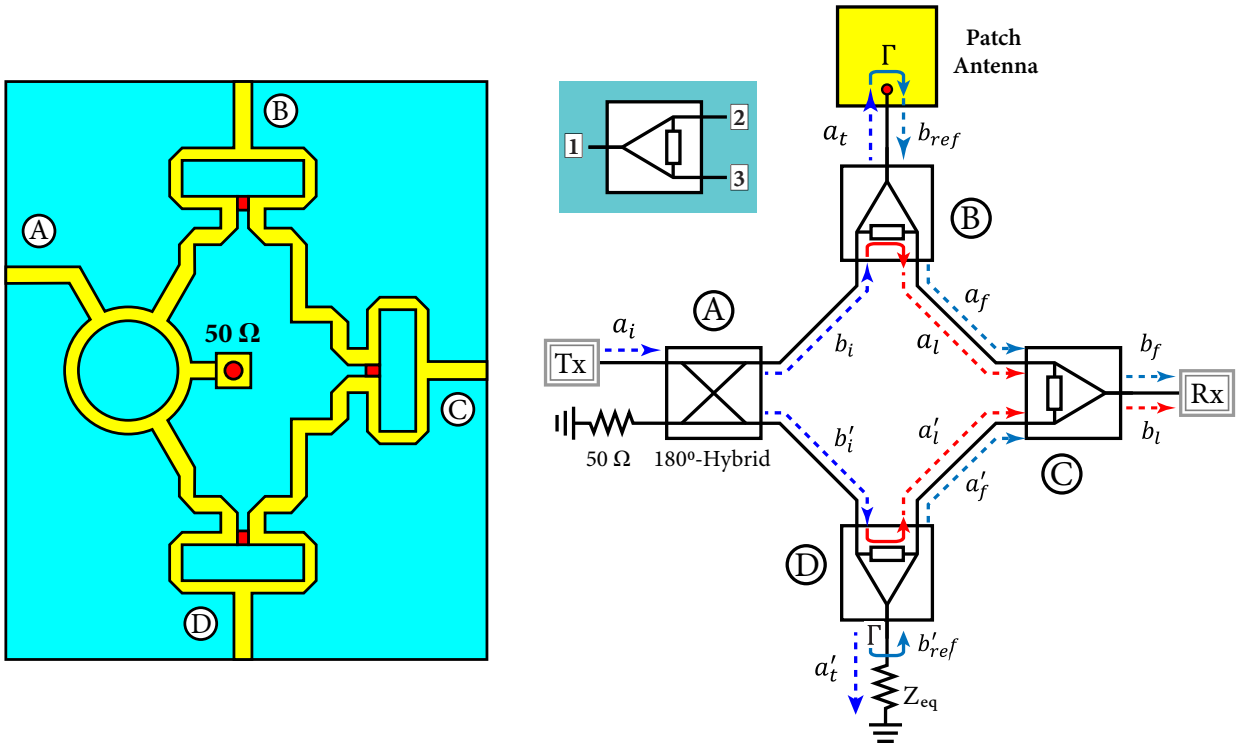

(a) (b)

Figure 1.14: (a) A hybrid transformer network implemented using a rat-race coupler and three Wilkinson power dividers/combiners and (b) an equivalent schematic showing its operation as an in-band full-duplex system.

For this technique, the proposed network is depicted in Figure 1.14 and it consists of a rat-race hybrid and three Wilkinson power dividers/combiners. The rat-race hybrid, in this case, operates as a 180° out-of-phase power divider/combiner (also known as balun) by connecting the input's conjugate port to a 50 Ω matching load; the load is represented in the figure by a red circle inside a metallic square; so, alternatively, the rat-race hybrid can be replaced with any three-port 180° out-of-phase power divider (or balun). Also, the Wilkinson power divider at Port C can be substituted by another rat-race hybrid that operates as an in-phase power combiner. Nonetheless, it is important to note that the demonstrated network with the rat-race hybrid cannot be actually considered as a true hybrid transformer, because the powers that flow from Port A to Ports B and D are not equal to the powers that flow from Ports B and D to Port A, since the power entering Port A will be divided in half between ports B and D, while only quarter the powers entering Ports B and D will reach Port A. Thus, the powers flowing from Port A to Ports

B and D are twice the powers flowing from Ports B and D to Port A, which violates the third property of hybrid transformers. However, if the rat-race hybrid is replaced with a three-port 180° out-of-phase power divider, then the third property will be respected again and the network can be considered as a true hybrid transformer, but, in either cases, the network operates similar to what is expected.

Also, it is good to know that the mechanism of isolating the conjugate ports in this network is different than the mechanism of isolation in the rat-race hybrid:

- The power entering the rat-race hybrid from Port A for example does not flow, ideally, to Port C, and instead it only flows toward Ports B and D, this happens because there will be standing waves between Ports B and C and between Ports D and C, which prevents the incoming power from flowing to Port C and, consequently, no power reaches Port C. But, as mentioned previously, the isolation of the rat-race hybrid is finite in practice and some power manages to leak to the receiver.
- On the other hand, for the proposed network, there are two layers of isolation: the first stage of isolation takes place inside the Wilkinson power dividers which try to force all the power coming from Port A to go directly to Port B or Port D, and try to prevent any power from leaking to Port C. But, similarly, the isolation of the Wilkinson power dividers is finite in practice, typically 20 dB, and some power will manage to flow to Port C through Ports B and D.
- However, the flowing powers in different branches of the network will arrive, ideally, equal in magnitude and 180° out-of-phase with respect to one another, and will cancel each other inside the power divider at Port C, which means that no power, ideally, reaches Port C from Port A. But in practice the second layer of isolation is sensitive to phase imbalances inside the network, and these imbalances will be present in the network due to fabrication tolerances which degrades the isolation.
- Thus, the difference between the rat-race hybrid and this network is that the power is preserved in the rat-race, while it is destroyed in the proposed network, which affects the power efficiency of the system.

To describe mathematically how the transmitted, leaked, and reflected signals are behaving in the system, and how their amplitudes and phases are changing at each stage, it is easier and more expressive to use some equations to describe the signals' behavior. For these equations, we think it is most suitable to work with power waves because they are compatible with S-parameters, where a_n denotes the power wave incident at the port n, and b_n denotes the power wave reflected or coming out from that port. Consequently, the incident and reflected powers carried by each wave are given as $|a_n|^2$ and $|b_n|^2$ respectively. The flow of power waves is depicted in Figure 1.14(b), and based on it, it can be shown that the power wave leaked from the transmitter to the receiver b_l is equal to zero (red dotted path in Figure 1.14(b)):

$$a_l = \frac{\sqrt{2}}{2} S_{32} a_i \qquad\qquad a'_l = \frac{\sqrt{2}}{2} S_{32} a_i e^{j\pi} \tag{1.3}$$

$$b_l = a_l + a'_l = \frac{\sqrt{2}}{2} S_{32} a_i \left[1 + e^{j\pi}\right] = 0 \tag{1.4}$$

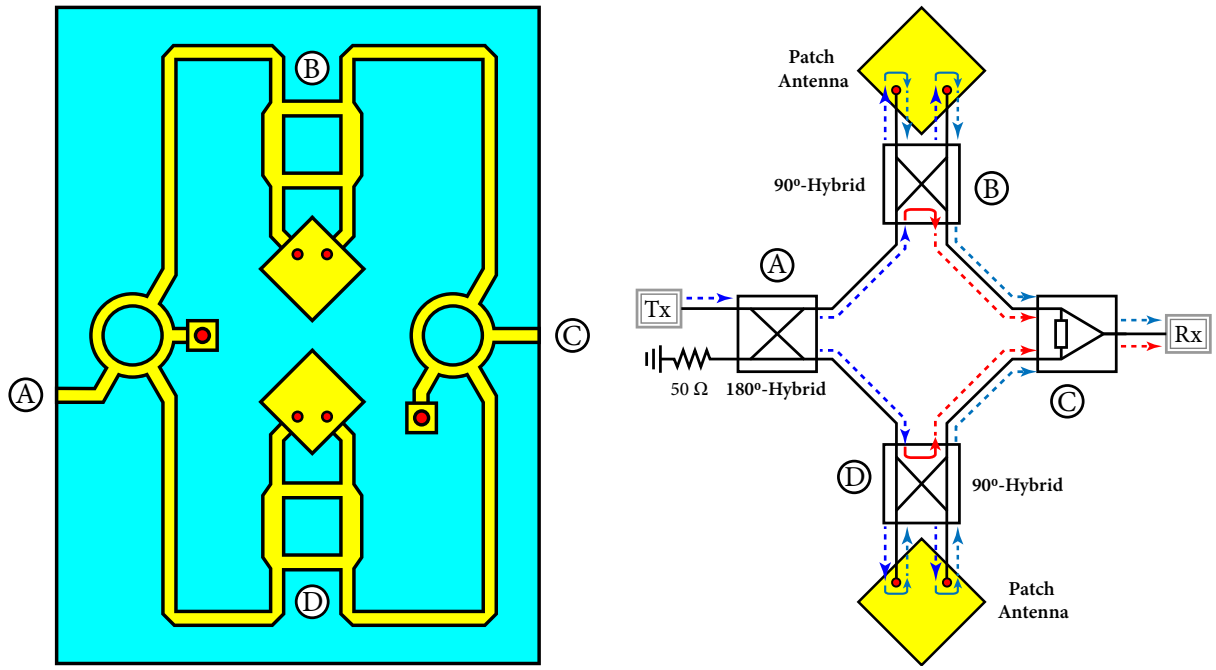

(a) (b)

Figure 1.15: (a) An in-band full-duplex system based on a hybrid transformer network implemented using one rat-race coupler operating as a 180° out-of-phase power divider, a second rat-race coupler acting as an in-phase power combiner, and two quadrature hybrids feeding two dual-fed patch antennas for circular polarization and (b) its equivalent schematic.

Similarly, it can also be shown that the two reflected signals from the antenna will combine 180° out-of-phase at the receiver (blue dotted path in Figure 1.14(b)):

$$a_f = \frac{\sqrt{2}}{2} S_{12} S_{31} \Gamma a_i \qquad a'_f = \frac{\sqrt{2}}{2} S_{12} S_{31} \Gamma a_i e^{j\pi} \tag{1.5}$$

$$b_f = a_f + a'_f = \frac{\sqrt{2}}{2} S_{12} S_{31} \Gamma a_i \left[1 + e^{j\pi}\right] = 0 \tag{1.6}$$

This topology was implemented in [37] using one rat-race hybrid and three Wilkinson power dividers and in [38] using one 180° out-of-phase and three in-phase power dividers. Also, there are some other variations of this technique that can be found in the literature:

- In [39, 40] the Wilkinson power divider at Port C was replaced by another rat-race hybrid working as in-phase power combiner, and the lateral Wilkinson power dividers were replaced by quadrature hybrids, as shown in Figure 1.15, however, the quadrature hybrids, in this case, are used to feed circularly-polarized patch antennas and the 90° phase shift generated between the output ports of the quadrature-hybrids does not interfere with the operation of the network, that is, at any time, the phase difference between the two signals propagating in the two branches of the network will always be 0° or 180° but never 90° or 270°.
- Similarly, in [41] the lateral Wilkinson power dividers in Figure 1.14 were replaced with two 180°-hybrids, which also do not affect the performance of the network but were used to differentially feed a dual-polarized spiral antenna array.

- Finally, in [42–44] the lateral Wilkinson power dividers were also replaced by Lange couplers, and the rat-race hybrid was removed from the network and was replaced by an integrated differential voltage-controlled oscillator (VCO) that internally generates two 180° out-of-phase output signals.

IV. Quasi-Hybrid Transformer Networks:

Quasi-hybrid transformer networks may contain circulators or quadrature hybrids: if two quadrature hybrids are placed at any two conjugate ports of the transformer such that 90°-output arms of both quadrature hybrids are in the same branch of the network, then for one path, between the two conjugate ports, the total phase shift is 180°. However, in this case, the phase shift between any two consecutive ports is always 0° or 90° but never 180°, hence the fourth property of hybrid transformers will be violated, and the implemented network will be a quasi-hybrid transformer. Moreover, for circulators, if at least one circulator is used in the network, let us assume at the antenna port, then the power going from Port A to Port B will not be equal to the power flowing from Port B to Port A, which also violates the third property of hybrid-transformers. Finally, note that circulator-less quasi-hybrid transformer networks as well as true-hybrid transformer networks can be potentially extended to wideband operation as they are not constrained in bandwidth as the circulator-based networks. In what follows, we present some of the quasi-hybrid transformer networks.

A. Single Quadrature-Hybrid:

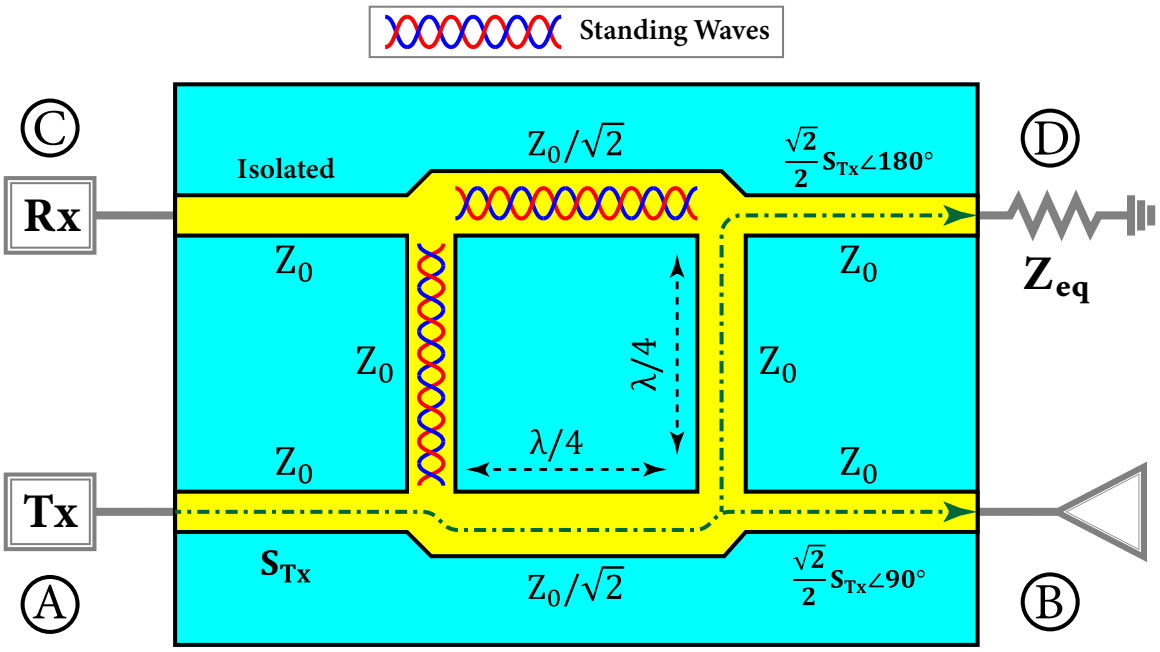

Figure 1.16: An in-band full-duplex system implemented using the branchline coupler.

Quadrature-hybrids are four-port devices that split the input power at one port into two signals that are equal in magnitude but are 90° out-of-phase, the two split signals are

delivered to two other ports while no power reaches the fourth port, just like the rat-race hybrid. Mainly, there are three devices that can be considered as quadrature hybrids: the branchline coupler, the coupled line coupler, and the Lange coupler. Let us take for example the branchline coupler which is depicted in Figure 1.16, it consists of two pairs of quarter-wavelength transmission lines: the vertical pair have their impedances equal to the characteristic impedance of the input ports (Z_0), while the horizontal pair have their impedances equal to the characteristic impedance divided by the square root of two ($Z_0/\sqrt{2}$). If a signal is injected at Port A while all other ports are terminated with matched impedances, then the signal will be split equally between Ports B and D while Port C remains isolated. The signal flowing from Port A to Port B will accumulate 90° of phase as it passes through the bottom quarter-wavelength transmission line, and the signal coupled from Port A to Port D will accumulate 180° of phase as it needs to pass throw two quarter-wavelength transmission lines, thus the phase difference between the two output signals is 90°.

Similar to a rat-race coupler, the isolation in the branchline coupler is a result of the standing waves which occupy the transmission lines leading to the isolated port. However, the isolation provided by the branchline coupler is also finite, about 30 dB of isolation in simulations and might be less than that in practice, depending on the fabrication tolerances. But, although its isolation is limited and does not provide the targeted level of self-interference cancellation at the antenna level (50 dB), yet it constitutes a first step toward accumulating that level, especially if it is paired with additional self-interference cancellation techniques. The branchline coupler can provide isolation over a narrow bandwidth, due to its wavelength dependence, but its bandwidth can be extended by cascading multiple transmission line sections together. Also, another drawback of quadrature hybrids for in-band full-duplex applications arises when there are impedance mismatches between the hybrid and the antenna, in this case, a portion of the transmitted signals will be reflected back to the hybrid, and the reflected signals will flow back to the transmit and receive ports at the same time. Now, assuming that the mismatches at both ports are identical, then the two reflected signals will combine out-of-phase at the transmit port and in-phase at the receive port, which might be good for systems that are sensitive to power reflections at the input, but it is not good for in-band full-duplex applications because the level of self-interference cancellation is reduced. This technique was discussed in [45] and implemented using single patch antenna [46, 47] and two orthogonal slot antennas [48–50].

B. Two Circulators with Two Quadrature-Hybrids

The proposed network in this section is depicted Figure 1.17 and it can be described as follows:

- The network is implemented using two hybrid couplers at the transmit and receive ports and two circulators at the antenna ports.
- The arms of both hybrids that produce the 90° phase shift should be in the same branch of the circuit, to make sure that the signals that manage to leak from the transmitter to the receiver will be 180° out-of-phase, and thus they will combine destructively. Otherwise, they will combine in-phase and reduce the level of isolation between the transmitter and receiver.

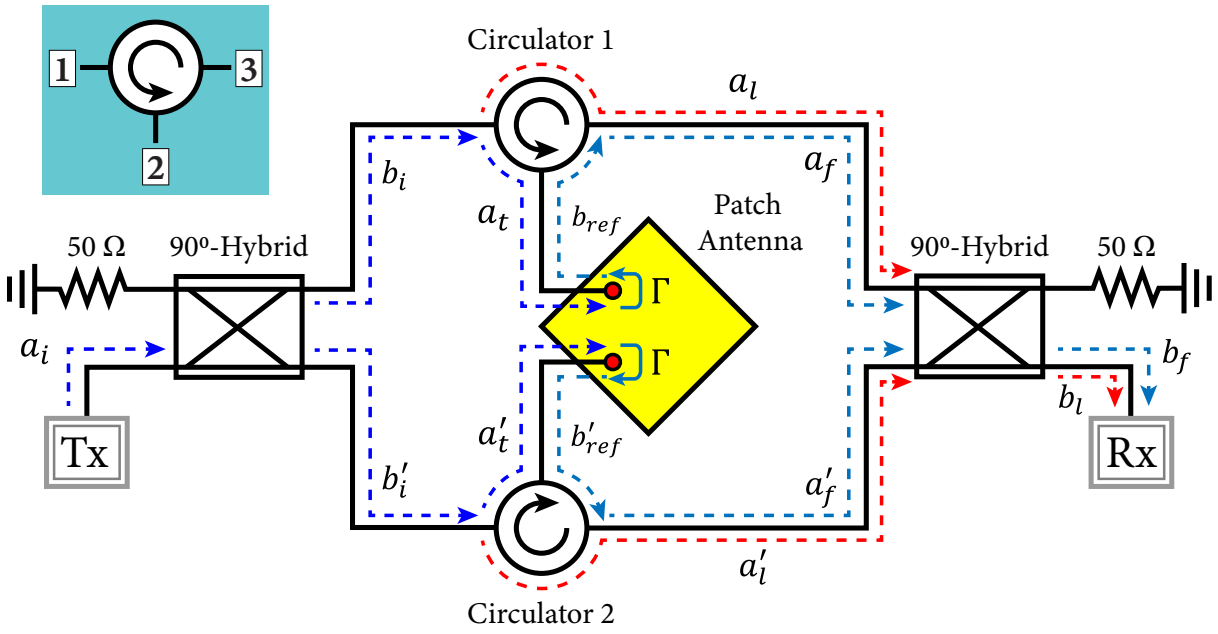

Figure 1.17: In-band full-duplex system based on quasi-hybrid transformer network using two quadrature hybrids and two circulators with a circularly-polarized patch antenna.

- Also, the circulators, in this case, are not the only source of isolation in the network, but rather the network as a whole is responsible for achieving the desired isolation.
- The other role of the circulators in the circuit is to direct the maximum power generated by the transmitter to the antenna, and also to direct the maximum power received by the antenna to the receiver. So, the circulators preserve the power efficiency of the system.
- Also, another advantage for this network is that the transmitter and the receiver are co-polarized, that is, the transmitter can transmit left-handed circularly-polarized waves and the receiver can only receive the same type of polarization.

By referring to Figure 1.17, it can be shown that the power wave leaked from the transmitter to the receiver b_l is equal to zero (red dotted path in Figure 1.17):

$$a_l = \frac{\sqrt{2}}{2} S_{31} a_i e^{j\frac{\pi}{2}} \qquad a'_l = \frac{\sqrt{2}}{2} S_{31} a_i \tag{1.7}$$

$$b_l = a_l e^{j\frac{\pi}{2}} + a'_l = \frac{\sqrt{2}}{2} S_{31} a_i \left[e^{j\pi} + 1\right] = 0 \tag{1.8}$$

Similarly, it can also be shown that the two reflected signals from the antenna will combine 180° out-of-phase at the receiver (blue dotted path in Figure 1.17):

$$a_f = \frac{\sqrt{2}}{2} S_{32} S_{21} \Gamma a_i e^{j\frac{\pi}{2}} \qquad a'_f = \frac{\sqrt{2}}{2} S_{32} S_{21} \Gamma a_i \tag{1.9}$$

$$b_f = a_f e^{j\frac{\pi}{2}} + a'_f = \frac{\sqrt{2}}{2} S_{32} S_{21} \Gamma a_i \left[e^{j\pi} + 1\right] = 0 \tag{1.10}$$

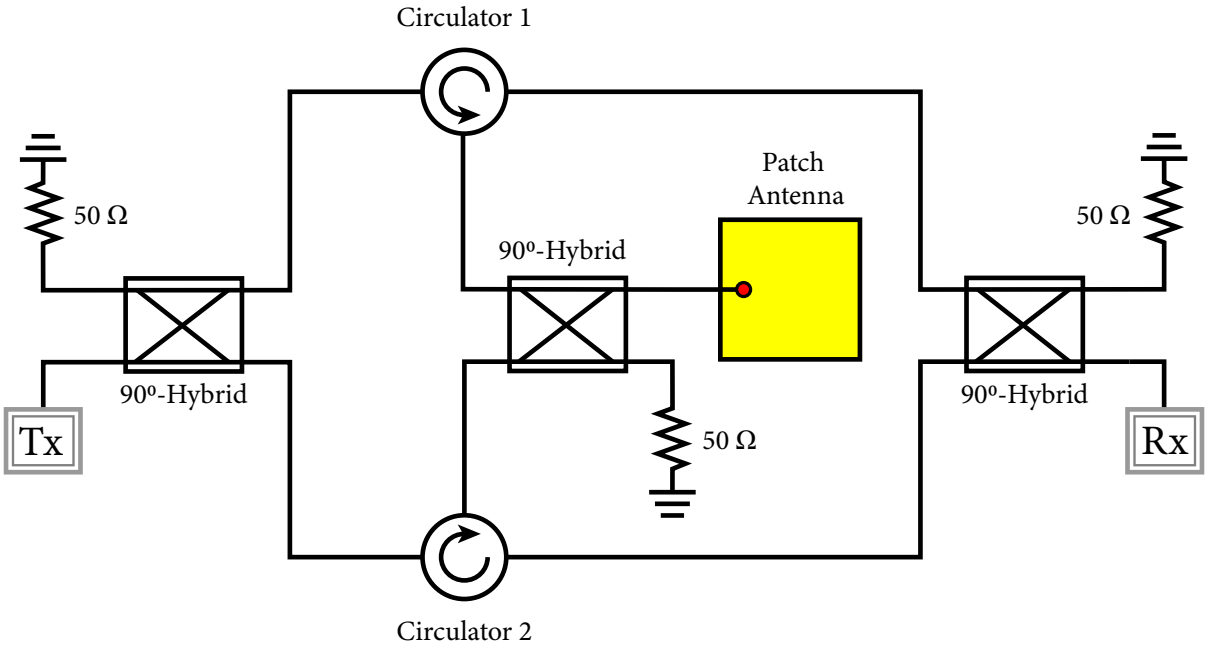

Figure 1.18: Linearly-polarized in-band full-duplex system based on quasi-hybrid transformer network using three quadrature hybrids and two circulators with a single-fed patch antenna.

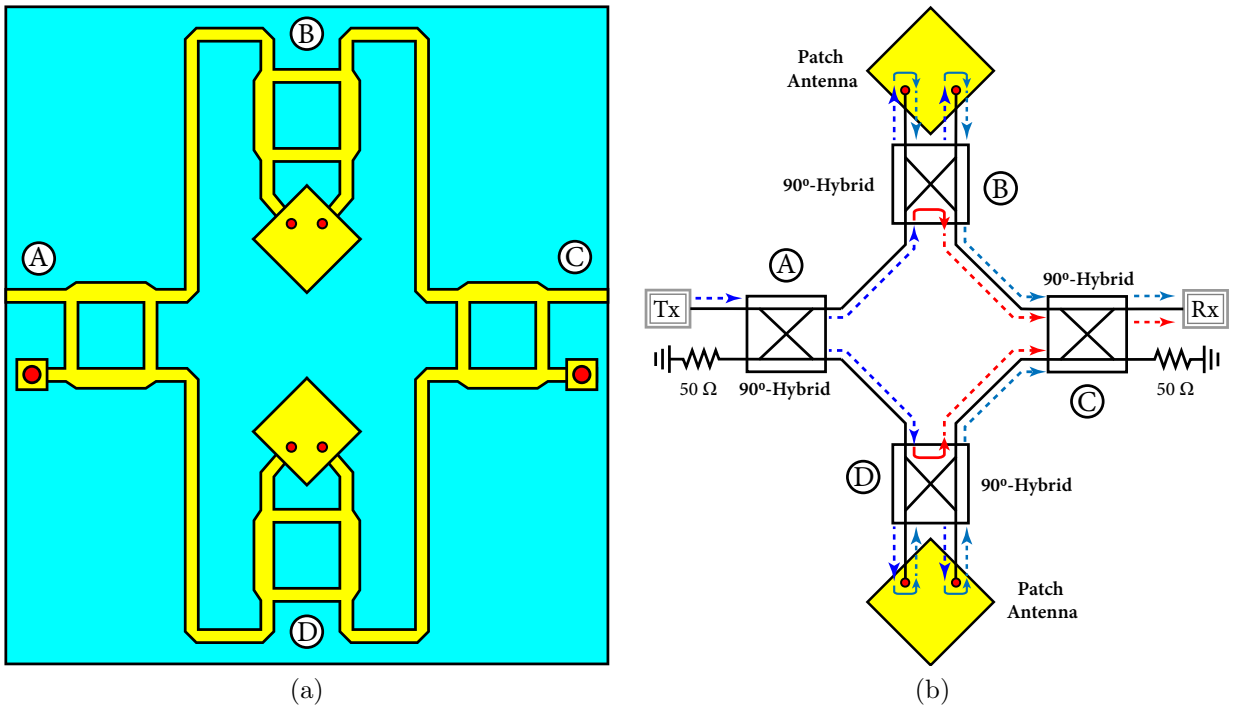

(a) (b)

Figure 1.19: (a) An in-band full-duplex system based on quasi-hybrid transformer network using four quadrature hybrids and two dual-fed patch antennas for dual circular polarization and (b) its equivalent schematic.

Thus from Equations (1.8) and (1.10) it can be inferred that this topology can achieve, theoretically, infinite isolation between the transmit and receive ports by eliminating the signals leaked from the circulators and the signals reflected from the antennas, only if

it is assumed that similar components in the system have identical performances or S-parameters, and if both mismatches between the antenna and the two circulators are also identical. This technique was presented in [51–55] using a single patch antenna, in [56–58] using reflector antennas, and in [59] using a four-arm spiral antenna. Also, the same system was studied in [30, 60] without any antennas. In addition to that, some other variations of this technique also exist in the literature:

- In [61], the quadrature hybrids at the transmit and receive ports were replaced with Wilkinson power dividers connected to a quarter-wavelength transmission lines at one of their outputs to create the 90° phase shift.
- Moreover, the basic configuration can be slightly modified to generate linear polarization by incorporating a third quadrature hybrid between the circulators and a single-fed patch antenna as shown in Figure 1.18. This has been demonstrated in [62], and also in [63, 64] but the circulators were substituted with transistors that provide a quasi-circulator behavior.
- In [65] the same network as in Figure 1.17 was used to generate single linear polarization by connecting one circulator to a patch antenna array while connecting the second circulator to an equivalent impedance.
- Finally, the circulators in the above network can be replaced with another two quadrature hybrids as shown in Figure 1.19, and the new quadrature hybrids will be used to feed two circularly polarized antennas. As compared to the circulators, the added hybrids can be considered more compact and can provide better isolation over a wider bandwidths. This has been implemented in [66–71].

C. Two Circulators with Balun-Power Divider Combination:

The proposed network in this section is depicted in Figure 1.20 and it is composed of an in-phase power divider, a 180° out-of-phase power divider (or balun), and two circulators connected to a dual-fed patch antenna to generate dual-linearly-polarized waves. This network operates in a manner similar to the "balun-power divider combination" network that was previously demonstrated. However, the only difference that the circulators introduce to the network is that they direct the maximum transmitted power to the antenna and the maximum received power to the receiver, but over a narrow bandwidth.

It can be shown that the power wave leaked from the transmitter to the receiver b_l (red dotted path in Figure 1.20) is equal to zero:

$$a_l = \frac{\sqrt{2}}{2} S_{31} a_i e^{j\pi} \qquad\qquad a'_l = \frac{\sqrt{2}}{2} S_{31} a_i \tag{1.11}$$

$$b_l = a_l + a'_l = \frac{\sqrt{2}}{2} S_{31} a_i \left[e^{j\pi} + 1 \right] = 0 \tag{1.12}$$

Similarly, it can also be shown that the two reflected signals from the antenna, a_f and a'_f, will combine 180° out-of-phase at the receiver (blue dotted path in Figure 1.20):

$$a_f = \frac{\sqrt{2}}{2} S_{32} S_{21} \Gamma a_i e^{j\pi} \qquad\qquad a'_f = \frac{\sqrt{2}}{2} S_{32} S_{21} \Gamma a_i \tag{1.13}$$

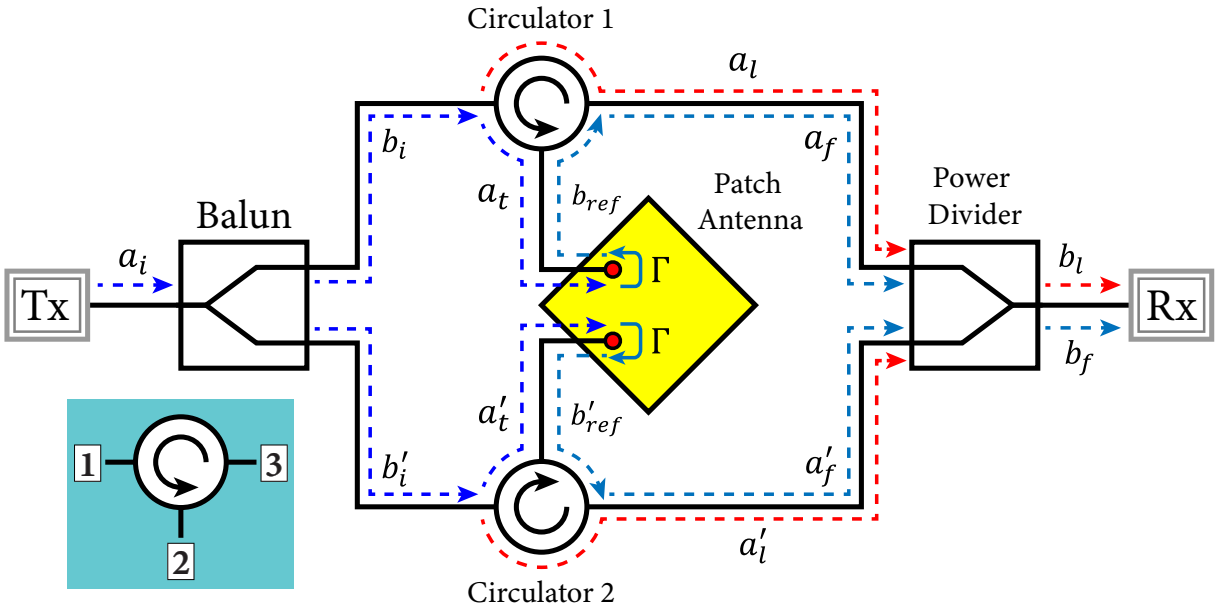

Figure 1.20: In-band full-duplex system based on quasi-hybrid transformer network using an in-phase power divider, a 180° out-of-phase power divider (or balun), and two circulators connected to a dual-polarized patch antenna.

$$b_f = a_f + a'_f = \frac{\sqrt{2}}{2} S_{32} S_{21} \Gamma a_i \left[e^{j\pi} + 1 \right] = 0 \tag{1.14}$$

Thus, from Equations (1.12) and (1.14) it can be said that this topology can also achieve, theoretically, infinite isolation between the transmit and receive ports by eliminating the signals leaked from the circulators and the signals reflected from the antennas, only if it is assumed that the circulators have identical performances or S-parameters, and if both mismatches between the antenna and the two circulators are also identical. This technique was presented in [72–74].

V. Reflection-Leakage Collision:

The basic full-duplex operation of hybrid transformers where the antenna is placed at one port (Port B) and its equivalent impedance at a second port (Port D), as in Figure 1.12, is considered active, because it requires the prior knowledge of the antenna's impedance to mimic it. As an alternative to the basic approach, the technique presented here achieves self-interference cancellation by replacing the equivalent impedance with a mismatched load at Port D, as depicted in Figure 1.21. The load can consist of lumped components, delay lines, or transmission line stubs, and is specifically designed to reflect the signal coming from the transmitter (S_{Tx}) to the receiver, such that the reflected and leaked signals from the antenna port (S_A) and the reflected signal from the mismatched load (S_{ref}) will combine 180° out-of-phase at the receiver [75–78]. However, in this case, the isolation is only obtained at an extremely narrow bandwidth, so in order to obtain isolation over a slightly wider bandwidth, the same approach was implemented in [79–81] by adding tunable components in the mismatched load to tune its impedance and obtain the maximum possible isolation. In [82] a modified branchline coupler with mismatched circuit placed at the equivalent impedance port is presented. The impedances and lengths

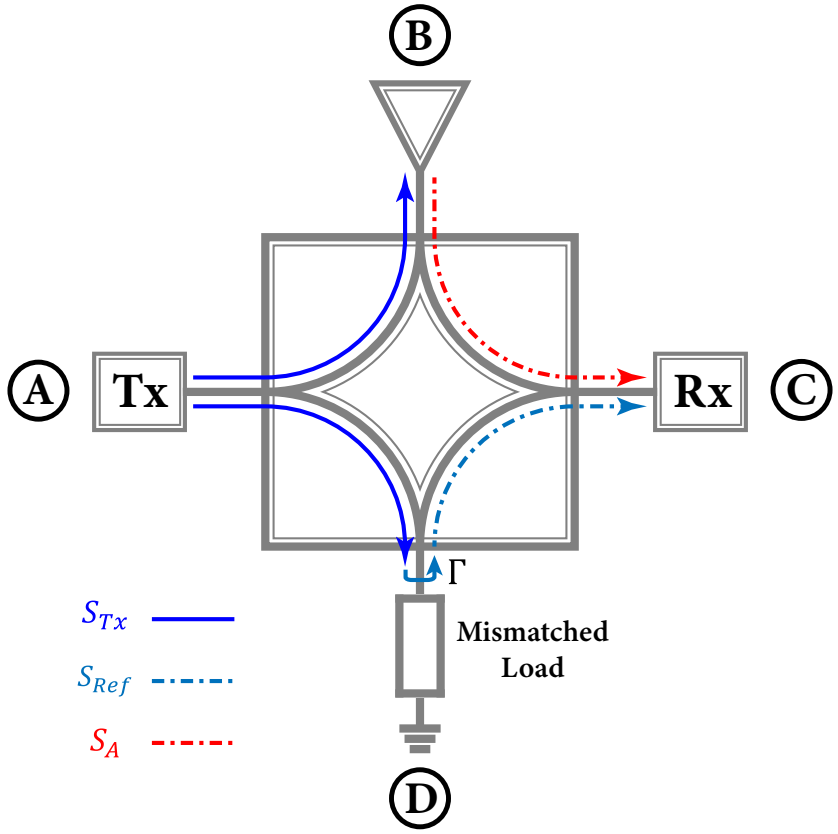

Figure 1.21: A hybrid transformer loaded with a mismatched load.

of the transmission lines of the branchline coupler were modified to force more power to flow from the transmitter to the antenna and from the antenna to the receiver, and to force less power to flow toward the equivalent impedance port, and, finally, the mismatched impedance was designed to counter the impedance and phase imbalances of the modified coupler and make sure that the reflected signal from the mismatched impedance and the power leaked from the transmitter will combine 180° out-of-phase.

1.6.2 Bistatic Systems

1.6.2.1 Passive Techniques:

I. Antenna Separation:

Any wave that propagates in the air suffers from free space path loss (FSPL) [83] which attenuates its radiated power flux density with the square of the distance traveled by the wave. Thus, by increasing the distance between the transmit and receive antennas [84, 85] (Figure 1.22(a)), the level of self-interference is expected to drop, however, at the expense of a larger system size. Figure 1.22(c) shows the simulated self-interference cancellation level as a function of the separation distance between two inset-fed circular patch antennas designed at 10 GHz, the distance was increased from λ up to 10λ then the levels of self-interference cancellation were recorded. It can be seen that the increase in

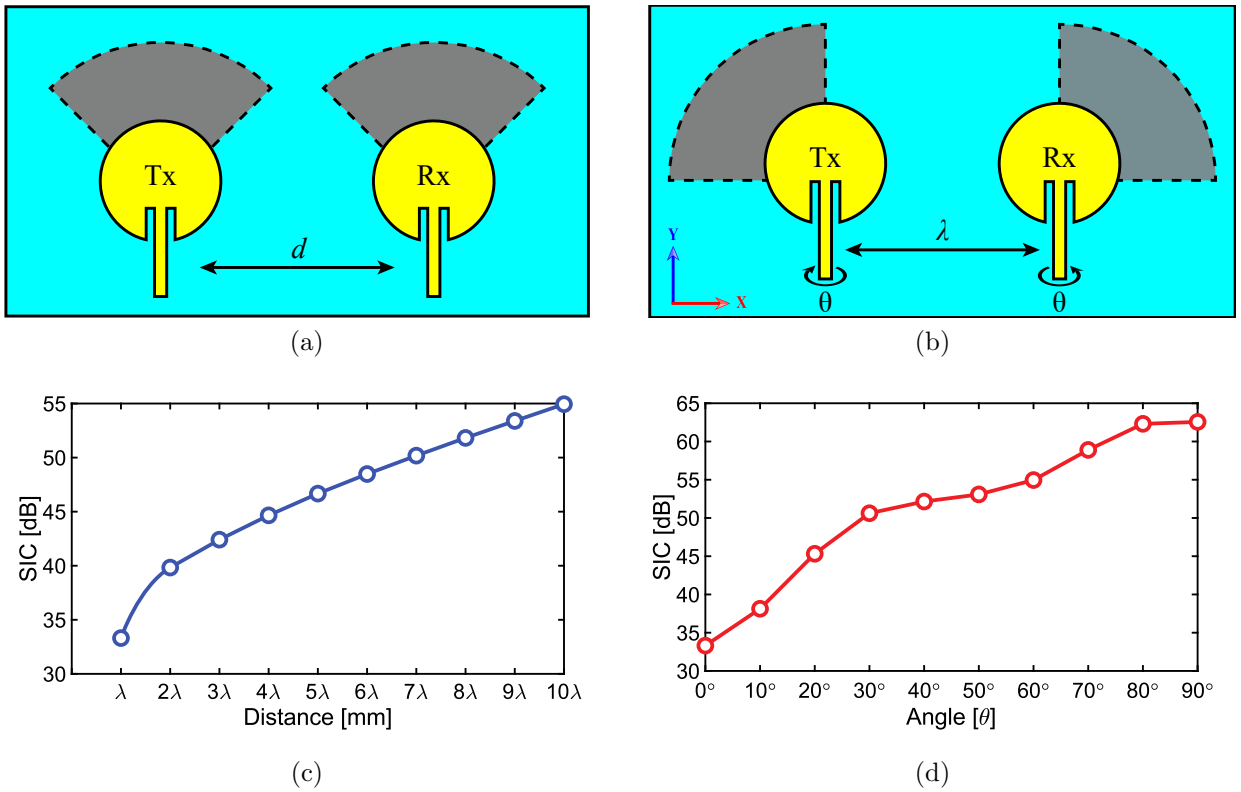

Figure 1.22: (a) Antenna separation technique, (c) and (d) are the simulated self-interference levels between two patch antennas at 10 GHz as a function of the separation distance *'d'* and beam rotation angle *'θ'* respectively.

the level of self-interference cancellation becomes much less significant as the separation distance increases where the most rapid increase in the cancellation is observed between λ and 2λ.

II. Beam Separation:

Instead of increasing the physical separation between antennas, the main beams radiated by the antennas can be separated instead [84, 86], this is achieved by rotating the patch antennas in Figure 1.22(b) along the y-axis in opposite directions, the transmit antenna can be rotated in a clockwise direction while the receive antenna can be rotated in a counter-clockwise direction. As the antennas rotate away from their initial positions, the overlap between the transmit and receive beams decreases, which in turn decreases the level of self-interference between the transmit and receive antennas. Nonetheless, this means that the system transmits in one direction and receives from another directions, and not all applications can tolerate to transmit and receive in different directions. Moreover, this technique is only applicable to directive antennas and is useless in omnidirectional antenna applications. Figure 1.22(d) plots the simulated level of self-interference cancellation as a function of the angle of rotation, which was increased from 0° up to 90°, while setting the distance between antennas to one wavelength at 10 GHz. It can be observed that even at the maximum angle of rotation (90°) the obtained level of self-interference cancellation is unsatisfying with respect to the disadvantages

introduced by the technique.

III. Cross Polarization:

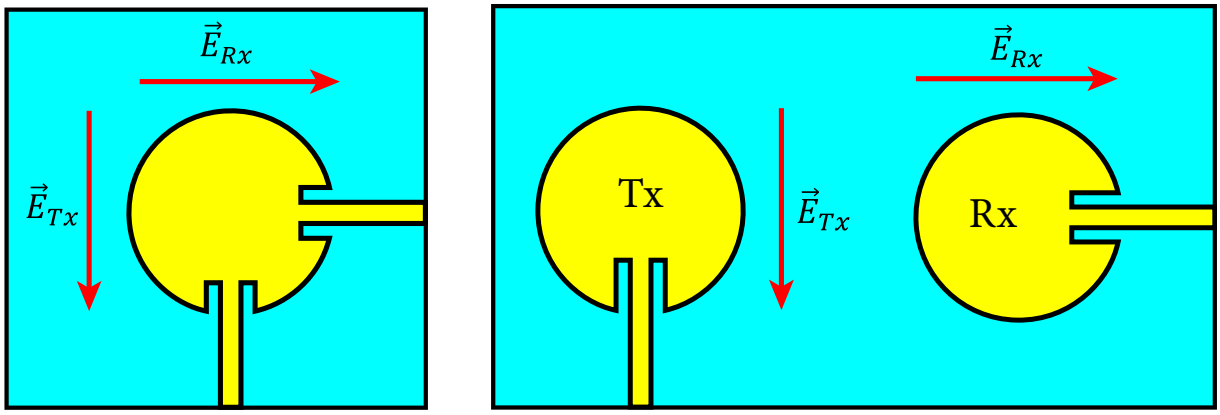

(a) (b)

Figure 1.23: (a) dual-fed patch antenna with two cross-polarized ports and (b) two single-fed cross-polarized patch antennas.

If two antennas radiate orthogonal electric fields then it can be said that they are cross-polarized. For instance, if the transmit antenna radiates an electric field that is vertically polarized, then the receive antenna can be placed in such a way it radiates horizontally polarized fields, this is demonstrated in Figure 1.23. Similarly, if the transmit antenna is right-hand circularly polarized (RHCP) then the receive antenna should be left-hand circularly polarized (LHCP). The transmit and receive antennas can be selected to operate on orthogonal polarizations which provides an inherent isolation between them because cross-polarizations do not couple to one another. In practice, the achievable level of self-interference cancellation is limited by the manufacturing imperfections of the antennas, especially, imperfections in antennas' placement and orientation. Also, if two systems were built with orthogonal polarizations, then it is required to have the transmit antennas of one system to be aligned with the receive antennas of the second system. Finally, cross-polarization can be considered a complementary source of cancellation and is usually implemented with some other primary techniques, and it cannot be always implemented depending on the targeted application. This concept has been implemented using linear polarization for monopole antennas [87], dipole antennas [88], a single patch antenna [89–100], two patch antennas [101–104], three patch antennas [105, 106], and four patch antennas [107, 108], as well as substrate integrated waveguide (SIW) antennas [109]. In addition to that, this technique was demonstrated with right- and left-hand circular polarizations using three patches [110], four patches [111–118], and spiral antennas [119, 120].

IV. Near-Field Nulling:

Near-field nulling is a family of techniques that uses at least two transmit antennas

or two receive antennas or both, then they introduce fixed phase differences between antenna elements to create near-field nulls in the transmit or receive radiation pattern, or both, then the receive antennas can be placed at the position of the transmit null, which can increase the level of self-interference cancellation. It was noticed by simulation that the level of self-interference cancellation of these techniques is highly sensitive to phase changes in the feeding signals and is less sensitive to amplitude changes, however, the contribution of amplitude changes is not negligible. The amplitude and phase changes come from various sources, mainly the phase and amplitude imbalances of the feeding device and the precision of the antenna fabrication and placement. There are four techniques that utilize this concept:

A. Half-Wavelength Separation:

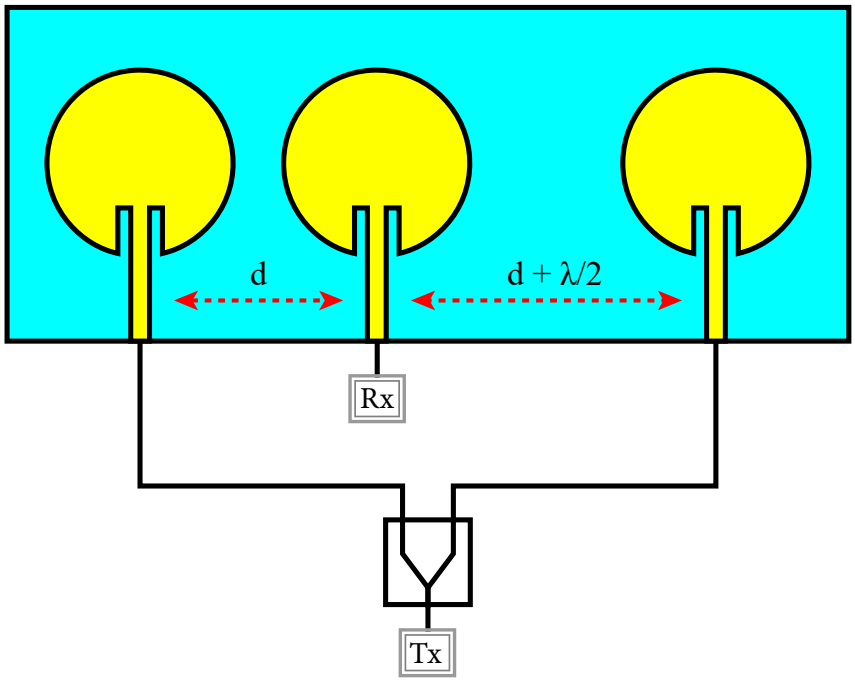

Figure 1.24: Half-wavelength separation technique.

This technique [18] uses two transmit antennas and one receive antenna (Figure 1.24): one transmit antenna is placed at a distance d to one side of the receive antenna, while the second transmit antenna is placed at a distance $d+\lambda/2$ on the other side of the receive antenna. Due to the half-wavelength difference between the two paths, both transmitted signals will arrive at the receive antenna with 180° phase difference, and hence both signals will combine destructively and will create a near-field null at the receive antenna's interface. This should yield, theoretically, a high level of self-interference cancellation. Note that since the distances between the receive antenna and the two transmit antennas are not equal, then the power received from the near antenna is higher than the power received from the far antenna, which means that although the two received signals are 180° out-of-phase, yet they are not of equal amplitudes, thus the signals will not cancel each other perfectly at the receiver's interface. So, in order to achieve better signal cancellation, the amplitudes of both signals need to be equalized, this is achieved by attenuating the

stronger signal by using an attenuator or by feeding the far antenna more power than the near antenna by using an unequal split power divider. In addition to that, this technique suffers from several drawbacks:

- The main drawback of this technique is that once the system is built and configured, then any further changes require redesigning the whole system especially the attenuation ratio or the power split ratio of the fed signals.
- Another major drawback of this technique is the wavelength (or frequency) dependence of the antennas' separation distance, which means that self-interference cancellation only takes place at the frequency of design and becomes weaker as we move away from this frequency, which renders the antenna placement technique useless for wideband applications.
- Also, we can observe multiple drawbacks of this technique concerning the far-field radiation patterns of the transmit and receive antennas, some of these drawbacks might also apply to other techniques that use multiple antennas to transmit or receive: firstly, since two antennas are used to transmit and one antenna is used to receive, the gain of the transmit link is higher than the gain of the receive link ($G_t = G_r + 3\ dB$), also the shapes of the far-field radiation patterns might differ for both links depending on the type of the used antennas, as it was observed that the main beam of the transmit link seems be more directive than the main beam of the receive link.
- Secondly, the two transmitted signals combine constructively in the far-field region at the center of the system, which is considered an advantage compared to other techniques presented in this section because no null regions are present in the far-field radiation pattern. However, the problem is that the receive radiation pattern is located at the position of the receive antenna and not at the center of the system, which means that there is a slight shift or skew between the transmit and receive radiation patterns.
- And, finally, if the separation distance between the two transmit antennas is higher than a half-wavelength at the frequency of design, two significant grating lobes will be observed in the far-field radiation pattern of the transmit link, yet the minimum separation distance is constrained by various factors in particular the size of the used antennas.

B. Antiphase Feeding:

In this technique an antenna configuration similar to that in the antenna placement technique is adopted but with some modifications (Figure 1.25(a)). The two transmit antennas are now placed at the same distance d away from the receive antenna, then both antennas are fed signals that are equal in amplitude but 180° out-of-phase, this is achieved by using a 180° power divider (or balun). Similar to the half-wavelength separation technique, the two transmitted signals will combine destructively at the receive antenna's interface and achieve, theoretically, infinite amount of self-interference cancellation. Also, the same level of self-interference cancellation and system performance can be, theoretically, obtained if the central antenna is used as transmitter and the lateral

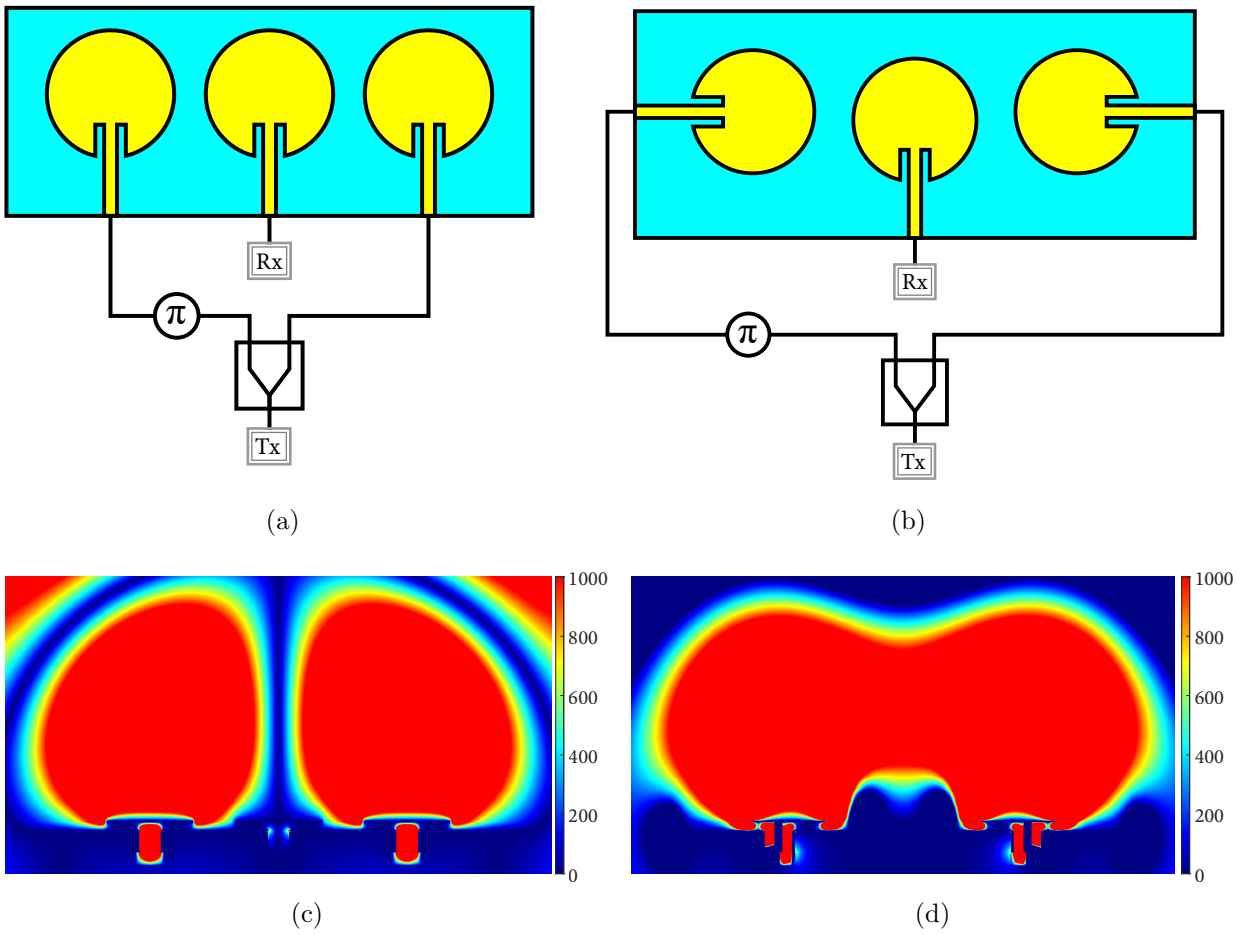

Figure 1.25: Antiphase Feeding technique (a) with Tx antennas oriented in the same direction and (b) with Tx antennas oriented in opposite directions and symmetric with respect to the center of the system. (c) and (d) are their corresponding transmit electric field distributions, respectively.

antennas are used as receivers. This technique solves several drawbacks that the half-wavelength separation technique suffers from:

- Since the two transmit antennas are placed at the same distance away from the receive antenna, no power attenuation or unequal power split is needed to feed the antennas, which simplifies the system design and reconfiguration.

- Also, since the distances between the transmit antennas and the receive antenna are independent of wavelength or frequency, then this technique can be used for wideband applications. But the only constraint on its bandwidth is the bandwidth of the antennas and the feeding balun, especially its ability to provide a relatively constant 180° phase difference between the two transmitted signals over the desired bandwidth.

- In addition to that, the radiation patterns of the transmit and receive links are now aligned at the center of the system, which means that the system can transmit and receive in the same direction or location.

Although this technique overcomes many drawbacks of the half-wavelength separation technique, yet it inherits two drawbacks from half-wavelength separation and introduces a third drawback:

- Firstly, since this technique uses two transmit antennas and one receive antenna then the transmit and receive links will have different gains and radiation patterns.
- Secondly, if the separation distance between the two transmit antennas is higher than a half-wavelength at the frequency of design, two grating lobes will be observed in the far-field radiation pattern.
- Thirdly, the near-field null, which is located at the center of the system, extends to the far-field region, and creates a null zone where no other device can receive the transmitted signals, this is depicted in Figure 1.25(c).

This technique was demonstrated for monopole antennas [121–125], dipole antennas [126], and patch antennas [90, 91, 95, 127, 128]. To eliminate the far-field null, the two lateral antennas should be placed and oriented oppositely or symmetrically with respect to the center of the system as depicted in Figure 1.25(b). Although the transmit and receive antennas are cross polarized in Figure 1.25(b) yet they can be co-polarized, however, cross-polarization is better because it increases the level of self-interference cancellation. The electric field distribution of this configuration is shown in Figure 1.25(d) where it can be observed that far-field null does not exist anymore while the near-field null is preserved. This concept was also implemented using single patch [93, 96–98], two patches [100, 102], three patches [105, 110, 129, 130], spiral antennas [131], and monopole antennas [87].

C. Near-Field Cancellation:

The near-field cancellation technique was proposed in [132, 133] and it follows a 2-step approach: in the first step, an antenna configuration similar to that in Figure 1.25(b) is adopted, where two transmit antennas are symmetrically placed at a distance d away from the center of the system and fed by a balun. After that, in the second step, two receive antennas are symmetrically placed along the perpendicular bisector of the transmit antennas at the same distance d away from the center, such that the transmit antennas also lie along the perpendicular bisector of the receive antennas, and then the two receive antennas are fed by another balun as shown in Figure 1.26. By using two antennas in the transmit and receive links, each fed by a balun, we obtain near-identical radiation patterns for both links with identical gains, which overcomes one drawback of the antiphase feeding technique while inheriting all its advantages. In addition to that, in theory, it is sufficient to connect just the transmit antennas to a balun or just the receive antennas to obtain infinite self-interference cancellation, however, in practice, a finite amount of self-interference cancellation is obtained due to imperfections in antennas' fabrication and placement, and also due to phase and amplitude imbalances of the used balun, thus having two baluns in the system can, in practice, increase the obtained level of self-interference cancellation.

Moreover, the distance from the center to the transmit antennas and the distance to the receive antennas can have equal or different values, and in both cases the same system performance is obtained in terms of self-interference cancellation and antenna

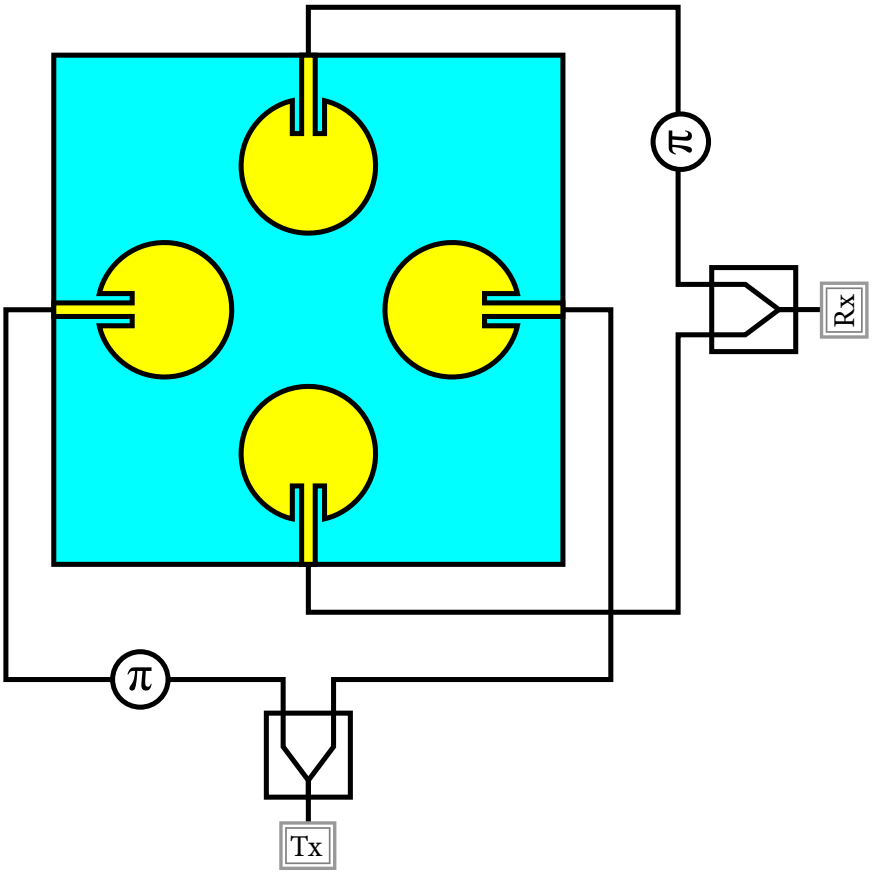

Figure 1.26: Near-field cancellation technique.

gains, however, if the distances are not equal then differences between the transmit and receive far-field radiation patterns will emerge, thus it is preferable to keep the distances equal and maintain high system symmetry to obtain similar radiation patterns. Above all its appealing advantages, near-field cancellation is the most suitable technique for in-band full-duplex multiple-input multiple-output (MIMO) applications and systems that implement this technique are the most compact as compared to all other techniques. This technique was implemented using one patch antenna [101], two patch antennas [103], four patch antennas [107, 108, 111–117, 134, 135], and an 8×8 patch array [136]. As well as single spiral antenna [137–144], four spiral antennas [41], and quad-ridged horn antennas (QRHA) [111].

D. Circularly Phased Arrays:

The concept of circularly phased arrays can be considered as an extension to the near-field cancellation concept explained previously. Usually, an even number of antenna elements are placed on a circle of a fixed radius and uniformly separated from one another, then the antenna elements are fed with a linear progressive phase shift, usually with the aid of a butler matrix, and each couple of opposite elements can be used for transmission or reception. As a result of the progressive phase shift and the opposite feeding of the antenna elements, a near-field null and a quasi-omnidirectional far-field radiation pattern are created. Figure 1.27 shows two different configurations of circular arrays: in the first

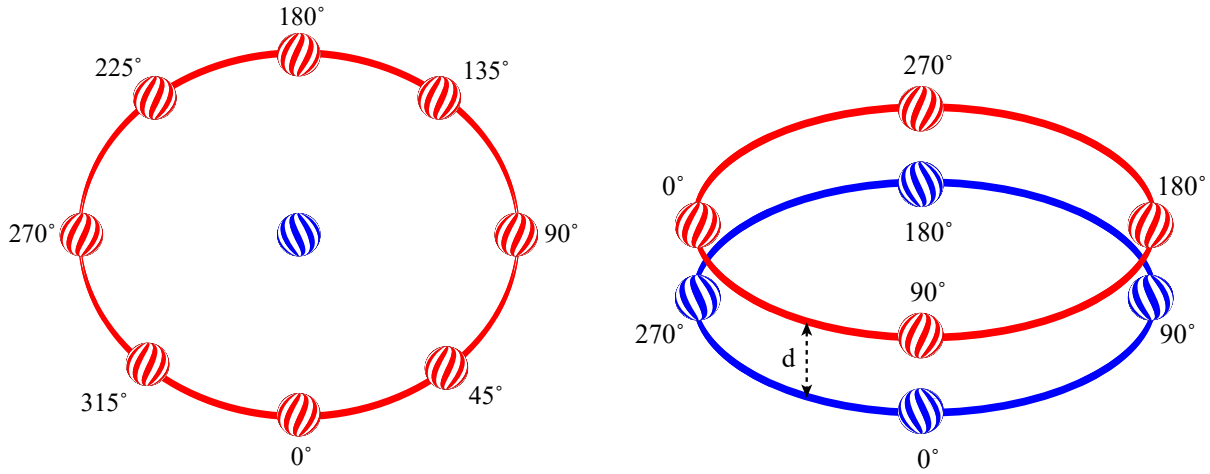

Figure 1.27: Circularly phased arrays (a) single layer fed "mode 1" with 45° phase step and (b) double layer configuration fed "mode 1" with 90° phase step.

configuration all the antennas are placed on a single layer and in the second configuration the transmit and receive antennas are placed on separate layers, this separation aids in reducing the level of self-interference. In the single layer case, four non-consecutive antennas can be used to transmit and the other four to receive, but in some publications the whole array can be used to transmit or receive, and an additional antenna can be placed at the center of the array to receive or transmit, by doing this the system exploits the beam diversity technique, which will be explained in the next section and which has its own disadvantages. In general, any number of antenna elements can be used in the array to increase its gain and directivity, however, at the expense of a greater system size and a more complex feeding network. This technique was implemented using monopole antennas [145–147], monocone antennas [148–150], loop antennas [151, 152], dipole antennas [153, 154], monopoles-dipoles combination [155], patch antennas [118, 156], horn antennas [157, 158], reflector antenna [159], spiral antennas [160, 161], conical sinuous antennas [162], planar inverted-F antennas (PIFA) [163], and quadruple inverted-F antennas (QIFA) [164].

V. Beam Diversity:

This technique is mainly applicable in antenna arrays where the beams of the transmit and receive antennas can be chosen differently by manipulating the transmit and receive beam-forming networks. In fact, by referring to Figure 1.28, manipulating the phase of the signals fed to each individual antenna in the array, can generate different beams that can be directed in several directions. To increase the isolation between the transmit and receive arrays, their beams can be steered away from one another to decrease the overlap between them, or at least two different beams can be selected even though they are overlapped. Similar to polarization diversity, different beams do not couple well as identical beams, which increases the level of self-interference cancellation, although the obtained isolation might not be significant in some cases. The main disadvantage of this

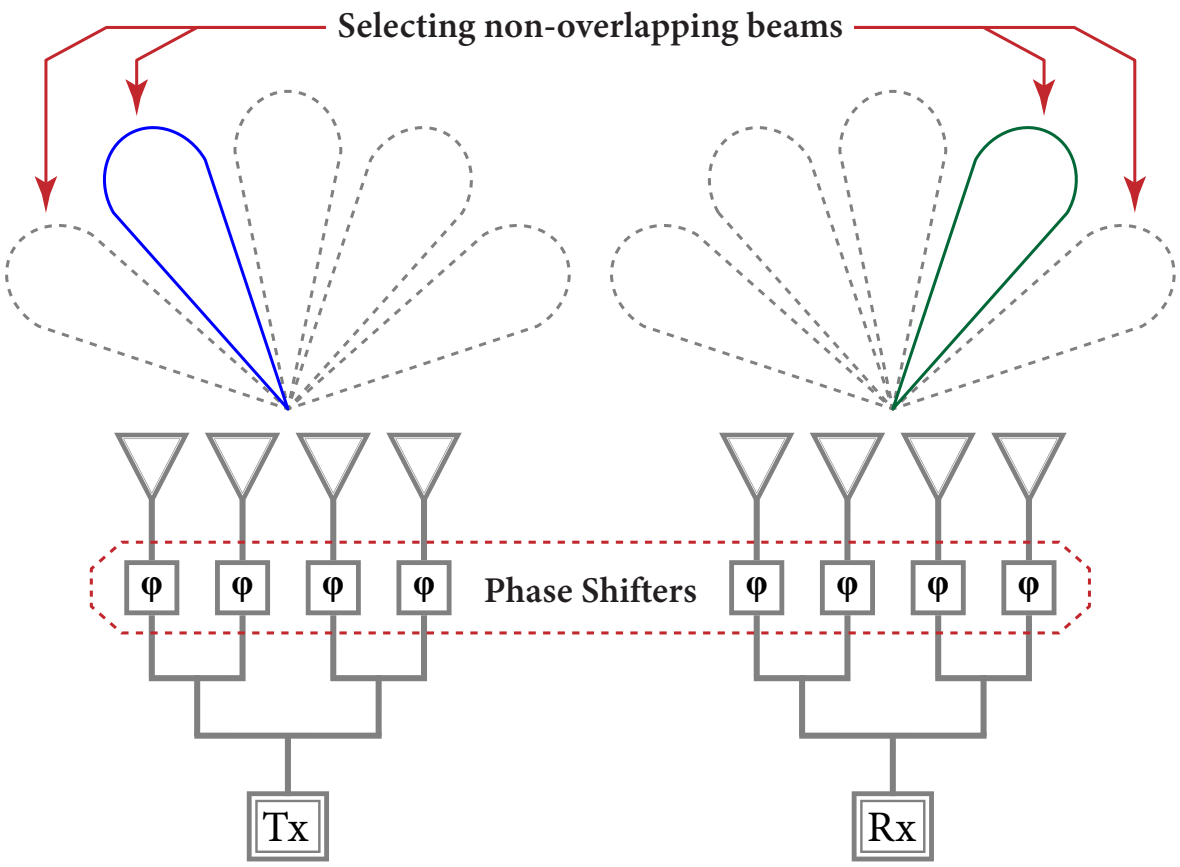

Figure 1.28: Two phased antenna arrays that can generate beams oriented in several directions while selecting the least overlapping beams to increase the isolation between them.

technique is that the implemented system will have to transmit and receive in different directions, that is, if two in-band full-duplex systems were each built with diverse beams, then the transmit beam of one system needs to be identical to the receive beam of the second system, otherwise the quality of communication between both systems will be degraded. This technique was used in [149–152, 155, 157]. Finally, beam diversity can be considered for monostatic arrays, however it cannot be easily implemented, mainly, because the transmit and receive beamforming networks in monostatic arrays are shared and restricted in the choice of devices, while in bistatic arrays the feeding networks are separate which gives more freedom of implementation using different devices.

VI. Surface Current Suppression:

Surface suppression techniques typically relate to directional antennas and involve the suppression of surface currents flowing between the transmit and receive antennas by using a specifically designed material, especially if the antennas are integrated on the same platform or share a common ground plane. Mainly, three types of materials or surfaces are used: absorbing surfaces, reflective surfaces, and high-impedance surfaces (HIS). Absorbing surfaces are comprised of dielectric materials with high loss tangents, and they are used to attenuate the self-interference signal that passes through them in

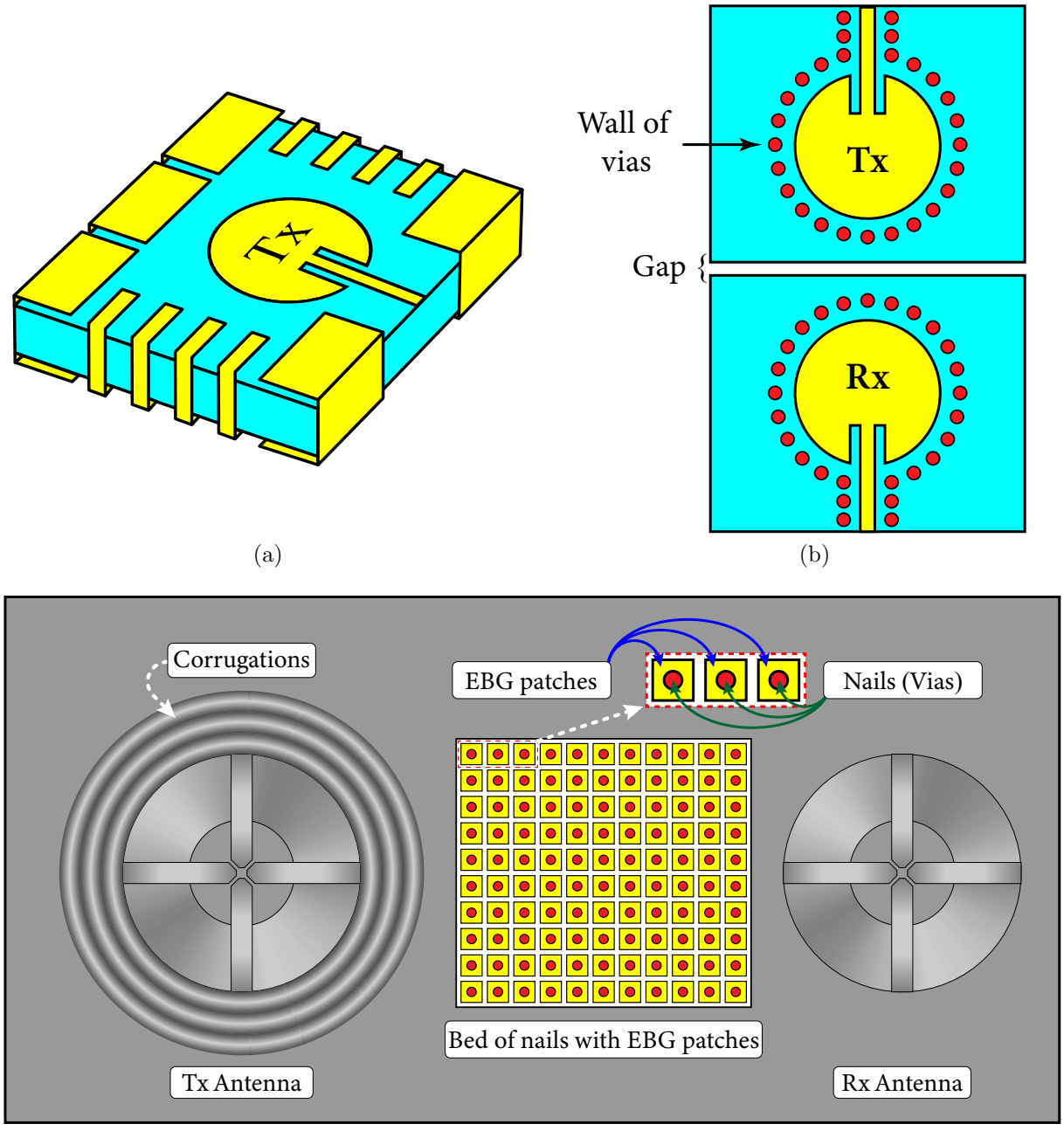

Figure 1.29: (a) an in-band full-duplex relay system with two patch antennas (the receive antenna is on the bottom layer) isolated by wavetraps, (b) two patch antennas surrounded with walls of vias on the same substrate with a defected ground plane, and (c) top view of two quad-ridged horn antennas integrated on a shared metallic platform with an electromagnetic bandgap bed of nails between them and corrugations around the transmit antenna.

a resistive manner [84, 165]. On the other hand, reflective surfaces aim to shield the receive antenna from the transmitted signal by introducing metallic parts between them [163, 166–175]. And, finally, high-impedance surfaces operate in a resistive manner similar to absorptive materials, however, they additionally incorporate reactive elements that modify the phase of self-interference signal to aid in its cancellation. Such surfaces can

be implemented in different configurations:

- For instance, wavetraps which are a series of planar quarter-wavelength transmission lines or parasitic patches that are short-circuited at one end to the ground plane [176–179], as depicted in Figure 1.29(a).
- Also, feed corrugations, which are quarter-wavelength rings or sections inscribed into the ground plane around the transmit antenna, as in Figure 1.29(c), can create a high negative reactance which forces the surface currents to radiate rather than propagate along the surface of the ground plane [180] thereby improving the self-interference cancellation. This concept was demonstrated with horn antennas [181].
- In addition to that, another type of high-impedance surfaces are the periodic surfaces such as the capacitive bed-of-nails, Figure 1.29(c), which consists of a grid of metallic pins (or Vias) structured in a periodic manner, and has also been demonstrated for horn antennas [182, 183].
- Moreover, in [183] the tops of the pins were loaded with metallic patches, known as metasurfaces or electromagnetic bandgap (EBG) materials, as in Figure 1.29(c), to enhance the bandwidth of the bed-of-nails. Electromagnetic bandgap materials were also implemented solely between patch antennas [171, 184–189], triple-ring antennas [190], and spiral antennas [120].
- In addition to the above, defected ground structures were used in [191–193], as in Figure 1.29(b), to filter the surface currents between the transmit and receive antennas in the bandwidth of design.
- Finally, in [194, 195] walls of vias were placed around the collocated transmit and receive antennas to prevent surface currents from coupling from one antenna to the other, as illustrated in Figure 1.29(b).

1.6.2.2 Active Techniques:

I. Decoupling Networks:

Any two closely co-located antennas can be represented in the form of an admittance π-network as depicted in Figure 1.30, where $-Y_{21}$ represents the admittance of the direct path coupling between the two antennas. Thus, to eliminate the direct path coupling another network with admittance Y_D can be connected between the two antennas such that $Y_D - Y_{21} = 0$. In fact, what happens is that the direct path signal and the signal passing from the transmit antenna to the receive antenna through the decoupling network will be of equal amplitudes and 180° out-of-phase, and thus they will eliminate each other. Once the decoupling network is introduced between the two antennas, the matching at the input ports will be probably lost, thus it is necessary to add matching networks at each antenna port to restore the matching to the system. Hence, it can be said that this technique adopts a 3-step approach: (step 1) design the antennas and measure the direct path admittance, (step 2) design a decoupling network to counter that admittance, and (step 3) design a matching network at the inputs of the antennas to fix the mismatch caused

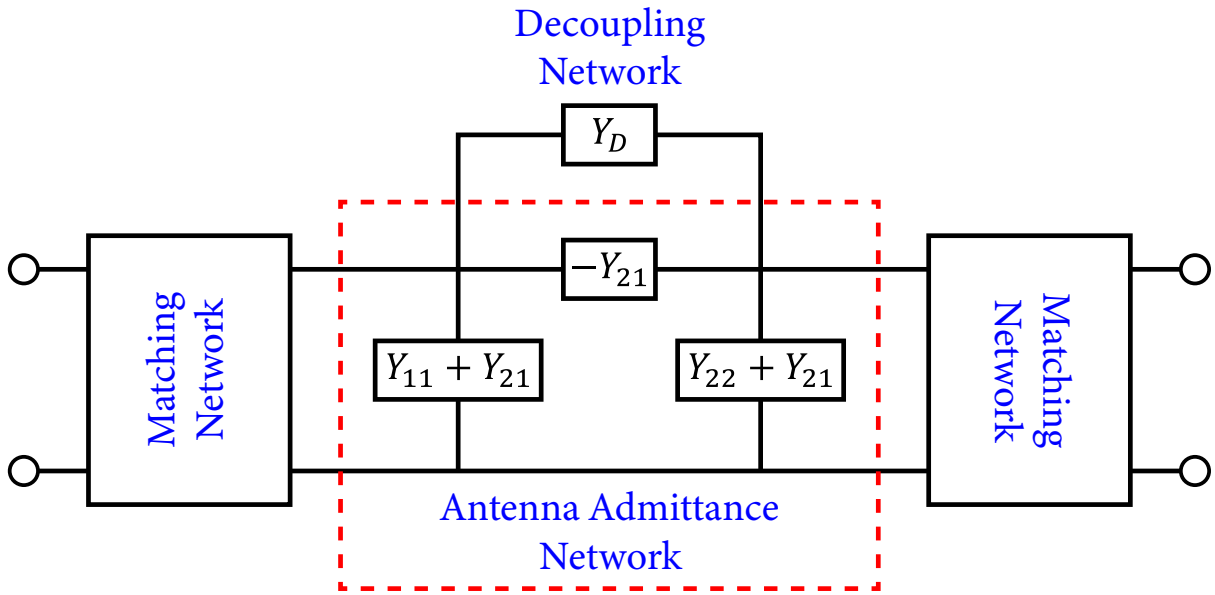

Figure 1.30: An admittance π-network of two closely spaced antennas with a decoupling network between them and two matching networks at the input of each antenna.

by the decoupling network. Decoupling networks are usually implemented with lumped components such as resistors, capacitors, or inductors, or sometimes using transmission lines, but also can be implemented using transistors or tunable components.

The main drawback of this technique is its bandwidth limitation due to the change in the value of the admittance with frequency, which requires designing multiple decoupling networks for different frequencies, and that in turn increases the size and complexity of the system. Alternatively, tunable components could be used to adaptively reconfigure the decoupling network, but this causes many problems in the system, mainly, because changing a single parameter in any of the components can drastically change the matching of the system, and even if the matching networks are also tunable there is no way to predict the impact of the change in the decoupling network on the performance of the system, and thus it will not be possible to counter this change by naively tuning the matching network. Another drawback is concerned with the power efficiency of the system, where the added matching and decoupling networks will absorb some of the transmitted or received powers, and also the power that passes through the decoupling network to the receive antenna will be destroyed at the receiver, which means that more power is being lost in the system. This technique was implemented using two monopole antennas [196–208], two patches [209–213], three patches [214], and four patches [135].

II. Co-Polarized Reflections:

Figure 1.31 shows the diagram of the proposed antenna configuration for this technique which consists of two collocated antennas with orthogonal polarizations to increase the initial isolation between the transmit and receive ports (Ports 1 and 3). Then, a co-polarized auxiliary port with the transmitter is introduced at the receiving antenna (Port 2) and is terminated with a variable reflective load. The impedance of the variable load is

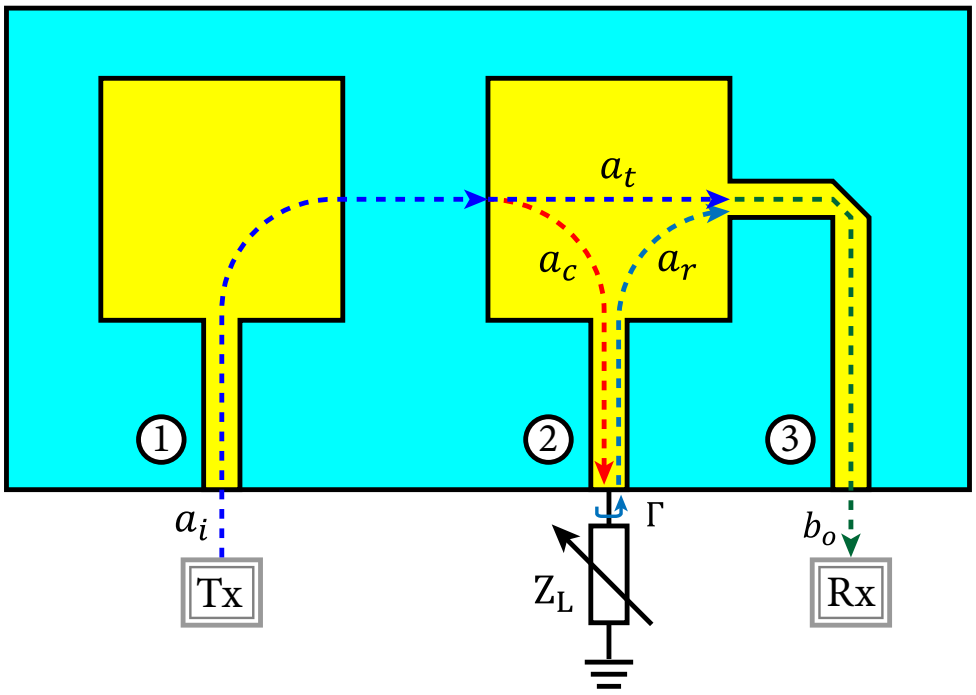

Figure 1.31: Two cross-polarized patch antennas with a co-polarized auxiliary port at the receive antenna terminated with a variable load.

intentionally mismatched with the auxiliary port to force the co-polarized power to reflect back to the cross-polarized port (Port 3). The power wave reaching the receiver (b_o) is a sum of the direct-path cross-polarized power wave (a_t) and the reflected co-polarized power wave (a_r), and it can be expressed in terms of the input power wave (a_i) at Port 1 as follows:

$$b_o = (S_{31} + S_{32}S_{21}\Gamma)\, a_i \tag{1.15}$$

It can be seen from equation (1.15) that if the variable load's impedance was designed such that $S_{32}S_{21}\Gamma = -S_{31}$, then the power coupling from the transmit antenna to the receive antenna will be zero, and, consequently, the isolation between them will be infinite. This technique was proposed in [104, 215].

1.7 Wideband Full-Duplex Systems

In this section we point to the self-interference cancellation techniques that were used to implement wideband in-band full-duplex systems, and to the techniques that have the potential to provide a wideband performance, however, before we commence, we need to reach a consensus on a common definition of a wide bandwidth and a wideband system. For this reason, if we assume that a full-duplex system operates over a certain bandwidth with an upper frequency f_u and a lower frequency f_l, then the fractional bandwidth can be defined as follows:

$$\text{FBW} = \frac{f_u - f_l}{f_u + f_l} \qquad\qquad \frac{f_u}{f_l} = \frac{1 + \text{FBW}}{1 - \text{FBW}} \tag{1.16}$$

Technique	**Advantages**	**Disadvantages**
Circulator	• Uses single antenna • Simple implementation • Conserves power efficiency • Transmits and receives in the same direction	• Bulky size • Narrowband • Low isolation
Hybrid Transformers	• Wideband potential • Uses single antenna • Can provide high isolation • Transmits and receives in the same direction	• Complex implementation • Reduced power efficiency • Sensitive to phase and amplitude imbalances
Antenna Separation	• Frequency-independent • Simple implementation	• Increased system size • Skew between Tx and Rx radiation patterns
Beam Separation	• Frequency-independent • Simple implementation	• Transmits and receives in different directions
Near-Field Cancellation	• Wideband potential • Can provide high isolation • Transmits and receives in the same direction	• Requires two baluns • Uses four antennas • Sensitive to phase and amplitude imbalances • Sensitive to antenna placement
Circularly-Phased Arrays	• Wideband potential • Can provide high isolation • Can transmit and receive in the same direction • Omnidirectional	• Complex implementation • Big number of antennas • Complex feeding networks

Table 1.2: Summary of some self-interference cancellation techniques at the antenna level.

According to [216] if a certain system has at least 20% of fractional bandwidth or at least 500 MHz of bandwidth (regardless of the fractional bandwidth), that is if $f_u = 1.5 f_l$ or $f_u = f_l + 500\text{MHz}$, then the system can be considered as wideband. However, the important question that arises is: according to what criteria we choose the upper and

lower frequencies? Apparently, there are no specific criteria to choose from and it really depends on the field of application and its specifications.

Firstly, there is the matching bandwidth of the antenna system, which corresponds to a voltage standing-wave ratio (VSWR) less than 2:1, or a reflection coefficient less than -10 dB. However, the matching bandwidth does not always mean that the performance of the system is good, because, in many cases, the antenna can be well matched, but its gain can be very low, which means that the power is being lost in the system, hence it is important to consider a gain bandwidth that corresponds to a gain level higher than a certain value. Similarly, if the system has a high gain then it does not mean necessarily that the system is well matched, so it is vital for the application to consider both the matching bandwidth and the gain bandwidth. Also, for some applications, it is essential to have a constant beam shape over a certain bandwidth, especially for circularly-polarized antenna systems that need to maintain the axial ratio below 3 dB, thus the bandwidth is determined by those metrics. For in-band full-duplex applications a new parameter needs to be considered when specifying the bandwidth, which is the level of self-interference cancellation that needs to be kept higher than a certain value over the chosen bandwidth. Consequently, in this work, the bandwidth of the presented self-interference cancellation techniques will be ruled by all the aforementioned parameters.

Based on the previous definition of wideband systems, some circulator-based techniques can be considered as wideband if a circulator with a 500 MHz of bandwidth is used [217], thus wideband circulator-based quasi-hybrid transformer networks can be found in [56–59]. However, no matter how much wideband the circulators are in their band of operation, yet they remain band limited and cannot be scaled to other frequency bands. On the other hand, circulator-less quasi-hybrid transformers and true-hybrid transformer networks have the potential to operate in wideband, mainly because their operation depends on transmission-line power dividers, baluns, or quadrature hybrids that can be easily modified and scaled to any frequency range and any percentage of fractional bandwidth. Wideband circulator-less quasi-hybrid transformer networks were not reported in the literature, but wideband true-hybrid transformer networks are reported in [37, 41].

The majority of the wideband systems found in the literature are bistatic, basically because their operation does not depend on duplexing devices, which in most cases are narrowband. Techniques like antenna separation, beam separation, polarization diversity, and beam diversity are frequency-independent, and thus they can be classified as wideband, although the amount of self-interference cancellation can vary with frequency. Moreover, those techniques are not usually used as primary techniques for self-interference cancellation, rather, they are used as a complementary source of cancellation with other techniques. On the other hand, near-field nulling techniques, except for half-wavelength separation, have proven to be the most adequate techniques to implement wideband full-duplex systems, in particular, near-field cancellation and circularly-phased arrays. Those techniques can provide 50 dB of self-interference cancellation and a good far-field behavior with a relatively compact size. The main requirements to implement those techniques is the availability of wideband baluns and wideband antennas. Table 1.3 summarizes some wideband full-duplex systems implemented in previous publications and it indicates the used self-interference cancellation technique, the bandwidth, the level of the self-

† Simulated Value

Ref.	Technique(s)	Frequency Range [GHz]	SIC [dB]	Gain [dBi]	Notes
[37]	Balun-Power Divider Combination	8.65 – 11.85	> 30	–	Reduced power efficiency
[58]	Quasi-Hybrid Transformer Network	4 – 8	> 25	> 20	Big system size & bandwidth limitation
[85]	Antenna Separation	15 – 40	> 60	> 20 †	Big system size & skew between Tx and Rx radiation patterns
[86]	Beam Separation	18 – 45 †	> 55 †	> 16 †	Big system size & skew between Tx and Rx radiation patterns
[131]	Antiphase Feeding	1.2 – 2 †	> 55 †	> 2 †	Low gain & different Tx and Rx beams
[143]	Near-Field Cancellation	0.5 – 3.5	> 37	> 4	–
[150]	Circular Arrays & Beam Diversity	0.8 – 1.7	> 28	> 4	Big system size & complex feeding network
[183]	Surface Current Suppression & Antenna Separation	6 – 19	> 60	> 7	Big system size & skew between Tx and Rx radiation patterns

Table 1.3: Summary of some wideband full-duplex systems.

interference cancellation, the gain, and the main disadvantages of the system.

1.8 Conclusion

In this chapter we have presented the context of in-band full-duplex technology and its ability to mitigate the spectrum congestion and spectral resources scarcity problems. Also, we have pointed to the main problem that stands in the way of implementing this technology, which is the high level of self-interference coupling between the transmitter and receiver of the same node that needs to be reduced. Then we have presented a general view of in-band full-duplex systems and indicated the different stages at which self-interference cancellation occurs and the targeted level of cancellation at each stage. After that, we

listed the potential advantages of in-band full-duplex in different applications and stressed on the importance of implementing wideband full-duplex systems as general-purpose tools for multi-standard or high data rate applications. Following that, we have demonstrated a number of the already published self-interference cancellation techniques at the antenna level, explained their principle of operation, and pointed to their strengths and weaknesses. Finally, we have specified which techniques were already used to implement wideband full-duplex systems and which ones have the potential to operate in wideband.

Chapter 2

Wideband Passive Devices and Antennas

Contents

2.1 Introduction

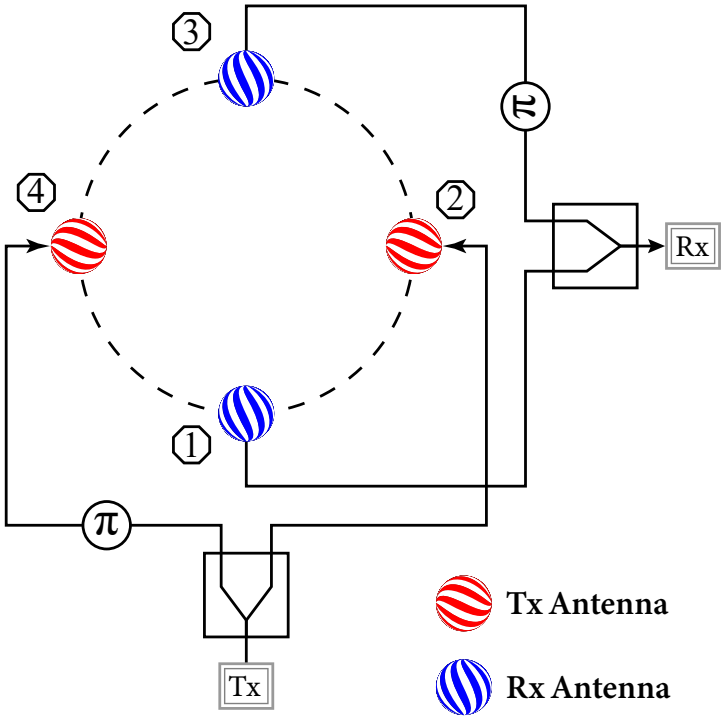

Figure 2.1: A schematic of the near-field cancellation technique.

Our preliminary study in the previous chapter has led us to the conclusion that the best self-interference cancellation techniques to implement a wideband in-band full-duplex system are near-field cancellation and circularly phased arrays. However, the targeted application of this system is a wireless link between two distant base stations, which might be tens of kilometers far away from one another, and thus the system needs to be directive and to have a high gain. As a result, the circularly phased array technique will be discarded, as it provides a quasi-omnidirectional radiation pattern, and, instead, a system based on near-field cancellation will be designed. Recall that the near-field cancellation technique requires at least four antennas and two 180° out-of-phase power dividers as shown in Figure 2.1, thus, to implement a wideband full-duplex system based on near-field cancellation we must find a wideband directive antenna and a wideband 180° out-of-phase power divider.

This chapter is dedicated to the study and design the most suitable components to implement a wideband full-duplex antenna system with the following characteristics: high self-interference cancellation level, wideband matching, good radiation patterns and gain across the entire bandwidth. We will begin by discussing the different ways to implement wideband 180° out-of-phase power dividers. In fact, there are two main approaches to implement an out-of-phase power divider:

1. The first approach is based on using a four-port 180° hybrid junction, such as a rat-race coupler or a tapered coupled line coupler, which can inherently perform out-of-phase power division. Or, alternatively, two quadrature hybrids can be cascaded together to obtain the 180° phase difference between the two output signals.

2. The second approach is based on connecting a 180° phase shifter or a phase inverter at the outputs of an in-phase power divider. Phase shifters and phase inverters can be also incorporated inside hybrids to extend their bandwidths.

In the light of this, we need first to make a review of the available wideband in-phase power dividers, phase shifters, and phase inverters, then we can move to discuss the implementation of wideband 180° out-of-phase power dividers based on each approach and on the presented wideband passive devices. This state-of-the-art will help us with choosing and designing the best 180° out-of-phase power divider topology that suits our needs, where wideband performance, compactness, and ease of design and implementation using planar transmission lines are highly desirable. A step-by-step design and optimization process of the proposed out-of-phase power divider is detailed and the simulated results will be compared to measured ones.

Finally, in this chapter, wideband antennas will be discussed, and their performances will be compared prior to choosing the best antennas for our applications, i.e. the Vivaldi antennas. To ensure the wideband performance of the antennas, a wideband microstrip-to-slotline transition, which will be introduced and used, initially, for the wideband out-of-phase power divider, will be, then, slightly modified and re-used to feed the Vivaldi antennas. The single antenna will be described, simulated, and fabricated, and after, the measurements will be carefully compared to the expected simulated results.

2.2 Wideband In-phase Power Dividers

The most commonly used types of in-phase power dividers (Figure 2.2) are the T-junction power divider and the Wilkinson power divider [218]. The T-junction power divider, usually, consists of a 50 Ω input transmission line connected to two 100 Ω output lines, but a quarter-wavelength transformer can be placed at the output to bring the impedance down to 50 Ω. In both cases the outputs are not matched and not isolated, this is due to the fact that a 3-port device cannot be reciprocal, lossless, and simultaneously matched at all ports. On the other hand, the Wilkinson power divider is, in fact, a T-junction with quarter-wavelength transformers and a 100 Ω resistor placed between them. By adding the resistor to the circuit, it becomes lossy and, hence, it can be now matched at all ports at the same time. Also, the added resistor aids in isolating the output ports. Theoretically, the signals in both branches of the Wilkinson power divider are of equal amplitudes and phases, thus the resistor will behave as an open circuit and no power will flow from one output port to the other, and no power will be lost in the resistor.

Apparently, the T-junction has a simpler design but it lacks matching and isolation at the output ports, while, on the other hand, the Wilkinson power divider is more complex to implement but it possesses matching and isolation at the output ports. Now, the legitimate question is which power divider is better for in-band full-duplex applications? Typically, for bistatic systems, a power divider with isolation is not required, because these systems use separate feeding networks for the transmit and receive links, and, usually, it is not necessary to isolate the antennas of the same link. On the other side, for most monostatic systems the isolation between the power divider's output ports is required, because such systems utilize a shared feeding network for both the transmit and the

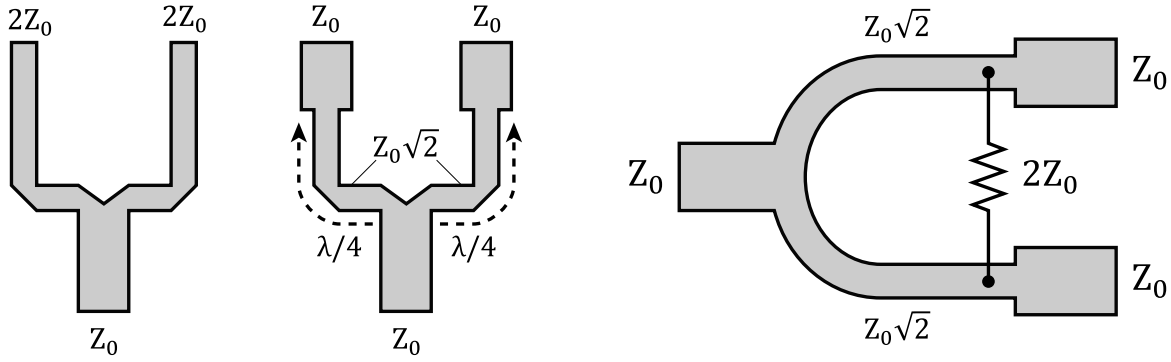

(a) (b)

Figure 2.2: (a) T-junction power divider and (b) Wilkinson power divider.

receive links, and, hence, it is necessary to isolate the transmit link from the receive link, otherwise, the level of self-interference cancellation can be degraded.

The T-junction power divider has no limit on its bandwidth, theoretically, if it does not contain any quarter-wavelength transformers, mainly, because the operation of the T-junction is based on persevering a 2:1 impedance ratio between the input transmission line and the two output transmission lines. Usually, the impedance of planar transmission lines remains relatively constant with frequency, which means that the 2:1 impedance ratio is frequency-invariant. On the other hand, the Wilkinson power divider contains quarter-wavelength transmission lines and thus it is a frequency-dependent device. Several approaches have been used to increase the bandwidth of the Wilkinson power divider: for example, by using three parallel coupled lines as the main power division mechanism [219–224], loading the outputs of the power divider with coupled lines [224–228], loading the input or output ports with short/open-circuit stubs [219, 221, 223–230], or loading the quarter-wavelength section with stubs [231, 232]. In addition to all the above, in [233, 234] a microstrip T-junction with an elliptical patch at the input is paired with a parallel slotline in the ground plane, then a resistor is placed inside the slotline to provide isolation between the output ports. Nevertheless, most of these techniques only deal with the matching bandwidth and do not address the isolation bandwidth.

One wideband technique that addresses both the matching and the isolation bandwidths was proposed by Cohn [235]. This technique proposes creating a multi-section Wilkinson power divider by cascading multiple pairs of quarter-wavelength transmission lines between the input and output ports, then terminating each pair of transmission lines by a shunt resistor. The impedances of the quarter-wavelength pairs decrease monotonically from 100 Ω near the input to 50 Ω at the output, which allows the propagating signals to smoothly flow from the input to the output without severe reflections, and thus provides a wideband matching. Also, the usage of multiple shunt resistors ensures a good isolation level over the matching bandwidth. This technique is the most used technique to implement wideband Wilkinson power dividers, mainly, because it can theoretically provide an infinite bandwidth with good isolation between output ports, depending on the number of the quarter-wavelength sections and the shunt resistors, and, also, because it can be scaled up or down, to operate at higher or

Ref.	Technique(s)	Frequency Range [GHz]	Matching Bandwidth	Isolation Level [dB]	Size [mm^2]
[221]	Three coupled lines with stub at input port	3.1 – 10.6	110%	$>$ 15	2.9×4.1
[227]	Loading outputs with coupled lines and stubs	3.1 – 10.6	110%	$>$ 10	–
[233]	T-junction with ground slotline	3.1 – 10.6	110%	$>$ 10	20×30
[237]	6-section Wilkinson power divider	8 – 67	157%	$>$ 20	5.5×1.2
[251]	7-section Wilkinson power divider	2 – 38	180%	$>$ 17	26×4

Table 2.1: Comparison of wideband in-phase power dividers.

lower frequencies, by just changing the length of the quarter-wavelength sections without affecting its performance. This technique was used to implement wideband Wilkinson power dividers using microstrip lines [236–256] and striplines [257–260], where most of these implementations can provide a multi-octave bandwidth, and some can provide more than a decade bandwidth. Finally, Table 2.1 summarizes some of the discussed in-phase power dividers, showing the technique used to implement them, the matching bandwidths, the level of isolation between output ports, and their sizes.

2.3 Wideband Phase Shifters

In general, phase shifters can be viewed as four-port networks consisting of two transmission lines: a reference line and a delay line, as the one in Figure 2.3. The delay line might be composed of one or more transmission lines with different characteristics, such that the total length of the delay line must be longer or shorter than the reference line. The length difference between the two lines induces a time delay between the signals passing through them, which translates into a phase shift between the two output signals. Usually, the length of the delay lines is set to a fraction of a wavelength at the desired frequency of operation, which makes them narrowband due to their frequency-dependence. The need for wideband phase shifters motivated many researchers to investigate alternative ways to obtain a relatively flat phase shift over a wide bandwidth. Several approaches have been reported in the literature, but, mainly, only two of them have managed to achieve

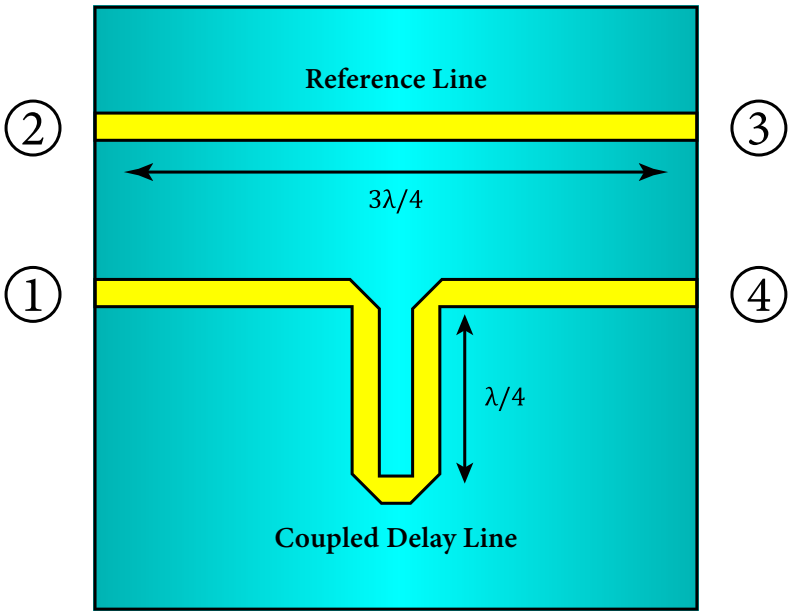

Figure 2.3: Schiffman phase shifter.

a relatively wide bandwidth using planar technologies: the first one is based on coupled transmission lines while the second is based on stub-loaded multi-section transmission lines having different characteristics. Before demonstrating these approaches, note that not all the cited phase shifters can provide 180° of phase shift, most of them can provide less than 120°, typically, 45° or 90°. In fact, it is much easier to obtain a lower value of phase shift over a relatively wide bandwidth, while it is more difficult to obtain higher phase shift values. Anyhow, several phase shifters with low phase shifting value can be cascaded together to obtain 180° of phase shift but the system's size increases. Also, the bandwidth of the phase shifter is determined according to the frequency range in which the phase shifter can maintain the targeted level of phase shift plus/minus a margin of error, this margin could be $\leq \pm 5°$ for lower phase shift values and might reach $\pm 10°$ for higher values.

One of the earliest attempts to implement a wideband phase shifter was carried out by Schiffman [261], who showed that the phase difference between a quarter-wavelength coupled transmission line, inter-connected at its ends, compared to a 3/4 wavelength reference line, would provide a nearly flat 90° phase difference over a wide bandwidth, as compared to conventional phase shifters. The bandwidth of the Schiffman phase shifter can be further increased by increasing the coupling factor between the coupled lines, this can be achieved by reducing the spacing between them. Unfortunately, this approach is limited by manufacturing constraints. Several modifications of the Schiffman phase shifter were adopted in different works [262–267] in an attempt to increase its bandwidth, nevertheless, all these approaches can hardly achieve 85% of fractional bandwidth in the best case. In addition to those, the theory of cascading multiple sections of coupled lines was demonstrated by Schiffman himself [268] and others [269–272], however, we could not find in the literature any implementation of these theories, probably due to fabrication difficulties and design complexity. Some other works, that utilize coupled transmission lines loaded with stubs, impedance transformers, and/or defected ground planes, were reported in [273–277]. The phase shifters reported in these works can achieve at least

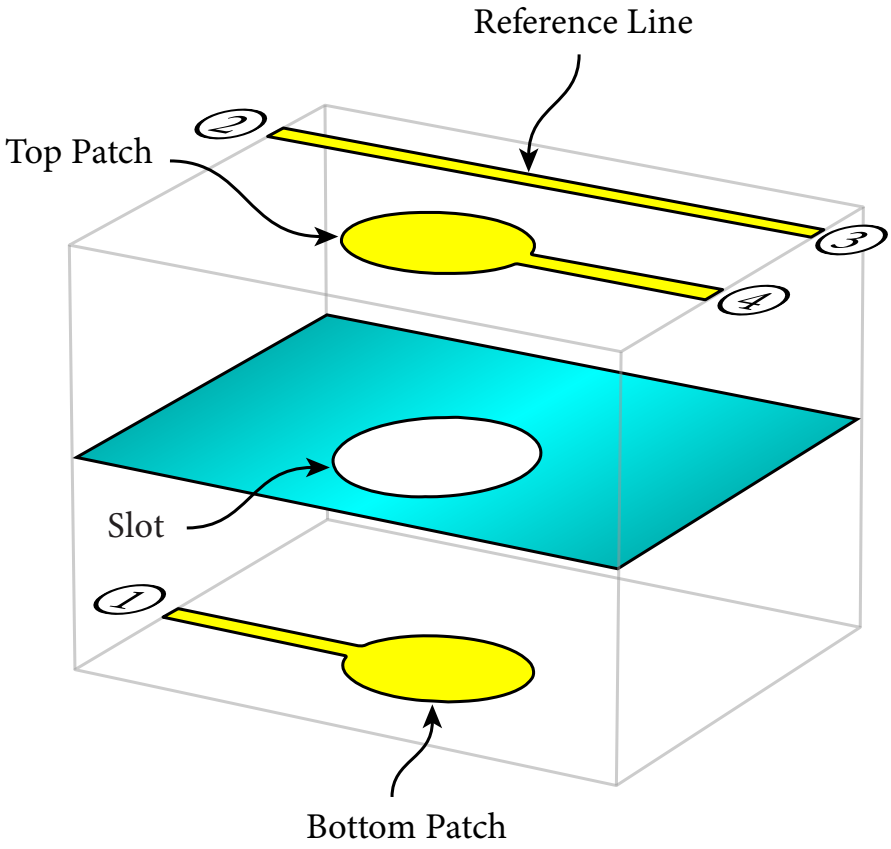

Figure 2.4: Wideband phase shifter based on broadside coupled patches.

100% of fractional bandwidth.

As an alternative solution, Abbosh [278, 279] introduced a tri-layered wideband phase shifter based on broadside coupled microstrip patches, which have shown a potential to operate over more than 120% of fractional bandwidth with a relatively constant phase. The phase shifter is depicted in Figure 2.4 where two elliptical microstrip fed patches are etched on the top and bottom layers respectively, such that they are aligned face-to-face. The patches couple power to one another through an elliptical slot which is etched in the middle layer between the two patches. This structure can maintain a constant coupling factor over a wide bandwidth, which translates into a constant phase shift over the bandwidth of operation. The dimensions of the microstrip patches and the elliptical slot dictate the obtainable phase shift. To increase the bandwidth of the proposed phase shifter, the microstrip patches were terminated by open-circuited stubs in [280], and exponentially tapered patches with a square slot were adopted in [281]. Also, to reduce the number of layers needed to realize this phase shifter, Abbosh introduced a bi-layer structure based on coplanar waveguide patches [282, 283]. The above-mentioned phase shifters were designed to provide 45° of phase shift, so, several works were carried out to build 90° [284–287] and 180° [288–290] phase shifters based on the same structure. Most of these works either manipulate the shapes of the patches, the slot, and the terminating stubs to obtain a higher phase shift, or cascade two phase shifters of a lower phase shifting level to obtain a higher phase shifting level.

Ref.	Technique(s)	Frequency Range [GHz]	Matching Bandwidth	Phase Value	Phase Error
[267]	Modified Schiffman phase shifter	1.47 – 3.52	85.4%	90°	±5°
[274]	Stub loaded coupled lines	3.1 – 11.1	113%	90°	±5°
[288]	Broadside coupled microstrip patches	1 – 10.2	164%	180°	±6°
[291]	Microstrip-to-slotline transitions	3.1 – 12	118%	180°	±8°
[294]	Transmission line resonators	1.16 – 4.76	122%	90°	±5.1°

Table 2.2: Summary of some wideband phase shifters.

In [291] a wideband phase shifter that utilizes microstrip-to-slotline transitions was reported. Although such transitions rely on a coupling mechanism to operate, however, in this case, the coupling is not the only factor that determines the value of the phase shift. From a different perspective, phase shifters based on coupled lines, although they provide a wideband performance, might be difficult to fabricate and might couple some unwanted power to other components in the system. Moreover, some of them have a multi-layered structure, which does not allow their integration with other components of the system on the same board. These drawbacks lead some researchers to investigate alternative methods for implementing wideband phase shifters without using coupled lines. Works in [292–299] reported phase shifters based on transmission line resonators, which usually consists of one or more sections of transmission lines, having different characteristics (impedance and length) and terminated with open- or short-circuited stubs of different shapes. Such phase shifters are built on a single layer and can achieve more than 100% of fractional bandwidth. Their bandwidth can be further extended by increasing the number of transmission line sections and/or stubs, which comes at the expense of bigger system size. Finally, Table 2.2 demonstrates some of the presented phase shifters, showing the technique to build them, their matching bandwidth, their phase shifting level, and the phase error in the bandwidth of operation.

All the reported wideband phase shifters operate at low frequencies; the highest reported frequency of operation is 12 GHz in [291]; and we could not find a publication

on wideband phase shifters operating at higher frequencies, at which transmission line parasitics become significant and have a great impact on the propagating signals and their phases. This indicates that phase shifters might not be the best choice for wideband high-frequency applications, rather, phase inverters might be better in this case, as their principle of operation is independent of frequency and of transmission line dimensions.

2.4 Wideband Phase Inverters

Phase inverters can be implemented using balanced-to-unbalanced (Balun) transformers, which are transitions that transform an unbalanced transmission line to a balanced transmission line. Transmission lines that have two conductors with equal impedances along their lengths with respect to a common ground plane are considered balanced, and otherwise they are considered as unbalanced. This means, any transmission line that uses two conductors of different sizes is necessarily unbalanced, while balanced transmission lines use symmetric conductors with equal sizes. Examples of unbalanced transmission lines are microstrip lines, striplines, and coplanar waveguides (CPW). While slotlines, coplanar striplines (CPS), and parallel striplines (PSL) are considered as balanced transmission lines. Those balanced transmission lines will be referred to, hereinafter, as two-conductor balanced transmission lines, and the currents flowing on the two conductors are of equal amplitudes and 180° out-of-phase, in this case, the line is said to be differentially balanced. Note that, two-conductor balanced transmission lines do not require the presence of a physical ground plane to operate. The ground plane is virtual in this case and there is only one signal that propagates between the two conductors, and it relies on the differential currents flowing in them.

Now, how does transitioning from a balanced transmission line to an unbalanced transmission line generates phase inversion? To illustrate this point, let us consider the double microstrip-to-coplanar stripline transition which is depicted in Figure 2.5. It consists of two transitions cascaded together. To transition from the microstrip line to the coplanar stripline, two strips with equal widths are placed on the top of the substrate, then the ground plane of the microstrip line is tapered until its width matches the width of the top strip. After that, the second strip is connected to the tapered ground plane using several vias. Finally, when the taper reaches the last via at position C, the metal below the strips is removed after that point, and no ground plane exists below the strips between C and E. Thus, the two strips of equal widths behave as a two-conductor balanced transmission line. The phase inversion of the input signal takes place after transitioning back from the balanced line to the unbalanced line, notice which strip of each transition is connected to the ground by vias in Figure 2.5(a). The opposite connection of strips results in inverting the electric fields at the output, this process is depicted in detail below the transition in Figure 2.5(a). On the other hand, if similar strips were connected to the ground plane, no phase inversion is induced in the transition, this is also shown in Figure 2.5(b). So, in summary, in order to obtain phase inversion, we need to transition from an unbalanced to a balanced transmission line first, then to transition back to another unbalanced transmission line, such that, the ground planes of the two unbalanced transmission lines need be connected to different conductors of the balanced transmission line.

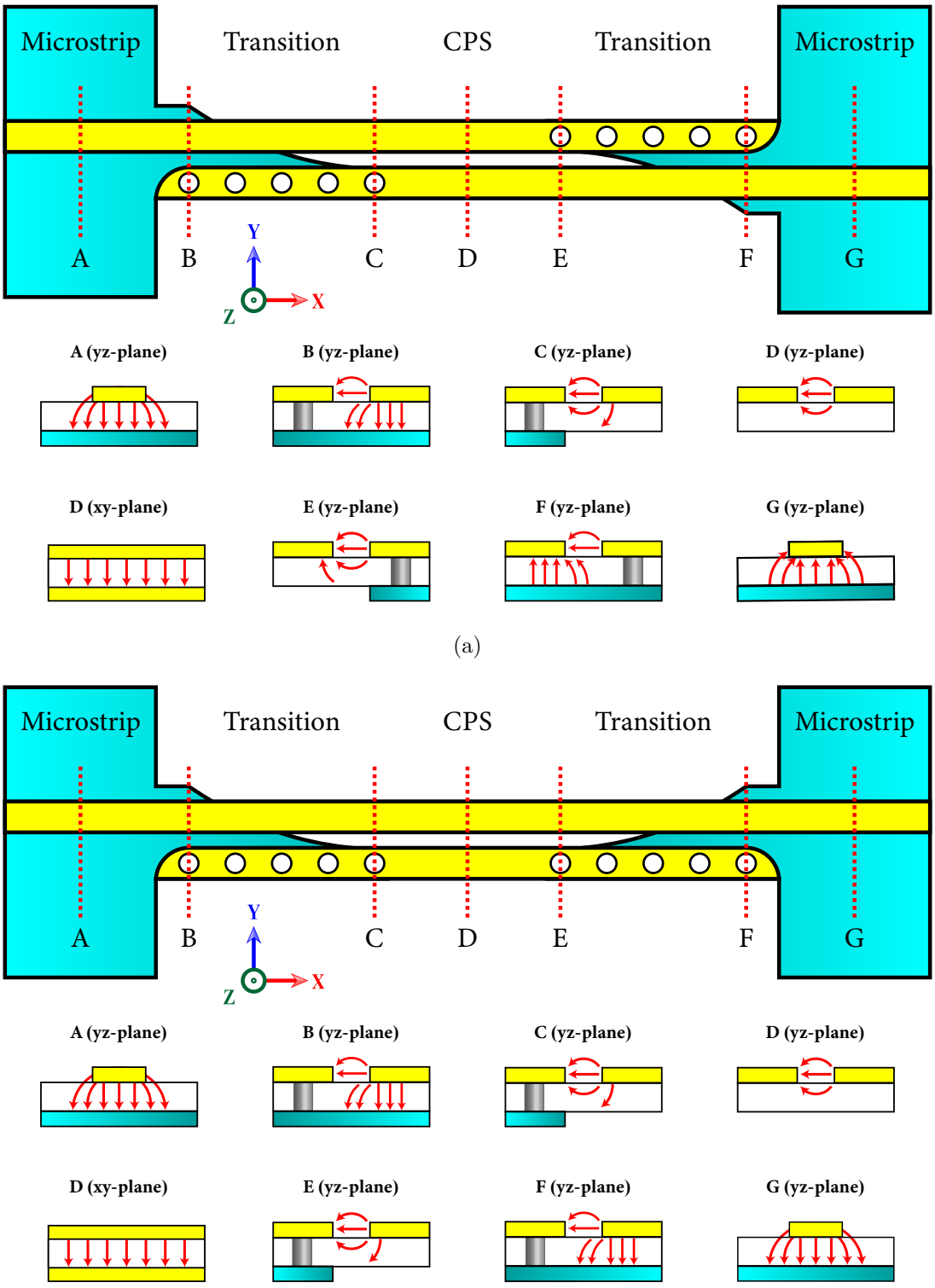

(a)

(b)

Figure 2.5: Double microstrip-to-coplanar stripline transition (a) with phase inversion and (b) without phase inversion.

For most transitions, the impedance of the balanced line will be much higher than the impedance of the unbalanced line, so, usually, a taper is used in the transitions to match their impedances, and hence the bandwidth and the size of the transition

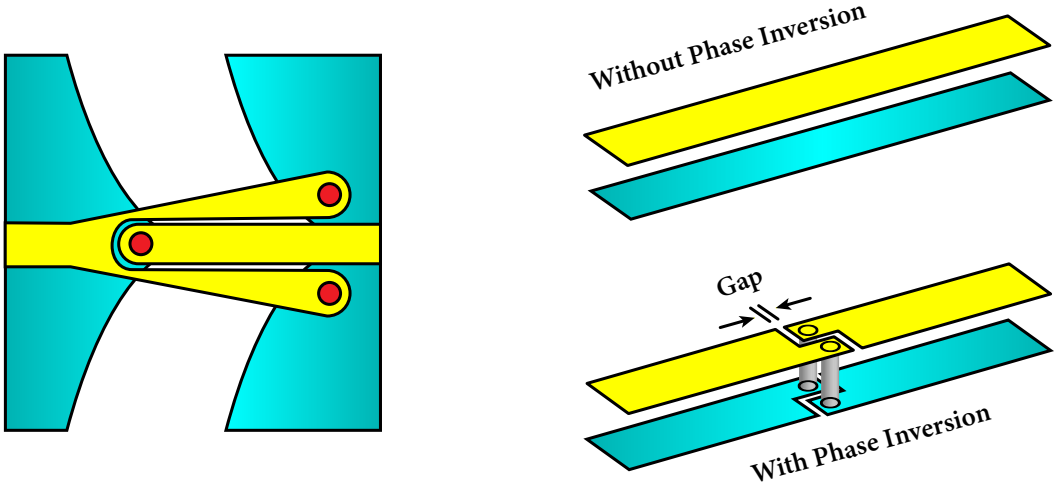

(a) (b)

Figure 2.6: Phase inverters based on (a) coplanar waveguide swap and (b) parallel stripline swap.

will be determined by the shape and length of the taper. This is why the ground plane of the microstrip-to-coplanar stripline transition is tapered. Fortunately, there are plenty of publications on extremely wideband transitions that can easily achieve a decade bandwidth, to mention a few: coplanar waveguide-to-coplanar stripline transitions [300–304], coplanar waveguide-to-parallel stripline transitions [305–308], microstrip-to-coplanar stripline transitions [309–315], microstrip-to-parallel stripline transitions [316–319], and microstrip-to-slotline transitions [320–322]. Also, a detailed and broad review of coplanar waveguide transitions can be found in [323]. In addition to that, substrate-integrated waveguide (SIW) transitions [324–326] have the ability to operate as phase inverters, yet they are more narrowband than other kinds of transitions.

Also, we found in the literature two phase inverters that do not employ a balanced-unbalanced (balun) transition, and they are depicted in Figure 2.6. The first one [327–329] is a coplanar waveguide inverter (Figure 2.6(a)) that starts and ends with 50 Ω microstrip lines in the upper layer. At the middle of the upper layer, the first microstrip line is divided gradually into two branches which surround the second microstrip line to compose a coplanar waveguide. The ends of both microstrip lines are semi-circular and the ground conductor below them is truncated in a semi-elliptical manner. After that, the ends of each microstrip line are connected to the ground conductor of the other microstrip line using via holes. This forces the currents flowing in the upper conductor of one microstrip line to go to the bottom conductor of the second line, and similarly, the opposite currents, which flow in the bottom conductor of the first line, will be forced to move to the upper conductor of the second line. The outcome of this process is an inverted electric field at the output port with respect to the input port. The second inverter (Figure 2.6(b)) employs a similar phase inversion mechanism using parallel striplines [330]. The top and bottom strips are separated into two parts by introducing a finite gap in each of them,

Ref.	Transition Type	Frequency Range [GHz]	Matching Bandwidth	Insertion Loss [dB]	Requirement
[302]	CPW-CPS	0 – 165	200%	$<$ 1.5	Vias
[305]	CPW-PSL	0.04 – 27	199%	$<$ 1.2	Vias
[312]	Microstrip-CPS	2 – 26.5	172%	$<$ 1.5	Vias
[317]	Microstrip-PSL	1 – 30	187%	$<$ 1.5	None
[321]	Microstrip-Slotline	1.02 – 13.9	173%	$<$ 1.5	None
[326]	Microstrip-SIW	17.5 – 30	53%	$<$ 1	Vias
[327]	CPW Swap	5.5 – 17.2	103%	$<$ 0.4	Vias

Table 2.3: Summary of some wideband transitions.

such that all the strip parts have the same area to preserve line balance, and the strip parts in each layer are symmetric to one another with respect to their centers, while the strip parts in the upper layer are symmetric to the strip parts in the bottom layer with respect to the plane parallel to the strips. Now, the top part of each stripline is connected, using a via, to the bottom part of the other stripline, which yields the signal inversion. Finally, Table 2.3 summarizes some of the most relevant articles that deal with wideband transitions.

2.5 Wideband 180° Out-of-Phase Power Dividers

Before we commence with presenting the approaches used to implement wideband 180° out-of-phase power dividers, we need to clarify one point. In the literature, the term *balun* is usually used to refer to a 180° out-of-phase power divider, that is, it is assumed that 180° out-of-phase power dividers can transform an unbalanced transmission line to a balanced transmission line. But how could it be? In fact, balanced transmission lines can be also created by combining two unbalanced transmission lines of the same type and of the same characteristics. For instance, by having two microstrip lines of equal widths on the same board with a shared ground conductor. The two strips together, in this case,

act as a balanced pair, because they have the same impedance with respect to the shared ground plane, although each individual strip with the ground conductor is unbalanced. This kind of balanced transmission lines will be referred to as three-conductor balanced transmission line, because it has three conductors: a pair of balanced conductors and a ground conductor.

Note that, unlike two-conductor balanced transmission lines, two signals flow in a three-conductor balanced transmission line, and they do not flow between the balanced pair directly, but, rather, between each balanced conductor and the ground plane. This implies that the currents flowing in the balanced conductors are not necessarily differential, that is, the two currents can be of equal amplitudes and phases. In fact, if two conductors carry differential currents that does not imply that they are balanced, and if they are balanced that does not also mean that they carry differential currents. This is due to the fact that balance is related to the line impedance and not to the properties of the propagating wave. So, we can have two differential lines with different impedances, and we can have balanced lines that are not differential. Based on the above explanations, power dividers can be considered as balanced-unbalanced (balun) transformers, because they transform a single unbalanced line into a three-conductor balanced line at the output. However, for some reason, the terms *balanced lines* and *differential lines* were used interchangeably in the literature to mean the same thing, although that is not always true, and based on this, the term *balun* was assigned to 180° out-of-phase power dividers and used by convention. Hence, in this manuscript, we will follow the same convention and use the term *balun* to refer to a 180° out-of-phase power divider.

2.5.1 Early Wideband Balun Designs

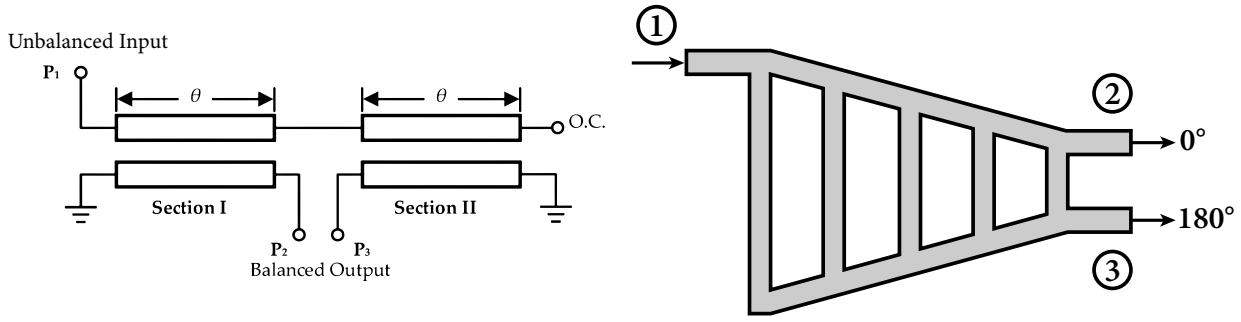

(a) (b)

Figure 2.7: Wideband 180° power dividers based on (a) Marchand balun, (b) log-periodic multi-section half-wavelength balun.

One of the earliest wideband baluns is the one proposed by Marchand [331], which was originally designed to transform an unbalanced coaxial line to a pair of balanced transmission lines carrying differential signals. The attractive performance of Marchand balun encouraged many researchers to implement it using planar transmission lines [332–339]. The balun is depicted in Figure 2.7(a) and it consists of two quarter-wavelength coupled transmission lines. The top parts of both lines are connected together at one end, and the other end of one part acts as the input port while the other end of the second part

is left open-circuited. The bottom parts of each coupled line are short-circuited at one end while the other ends act as output ports. Another wideband balun that consists of multiple sections of half-wavelength transmission lines separated by quarter-wavelength transmission lines was reported by Al Basraoui [340]. Al Basraoui also suggested that if the half-wavelength transmission lines were designed with lengths that vary according to a fixed geometric ratio, such that the geometry of the balun is log-periodic as depicted in Figure 2.7(b), then the balun can provide more bandwidth. This balun was also implemented in [341–343].

2.5.2 Wideband Hybrids

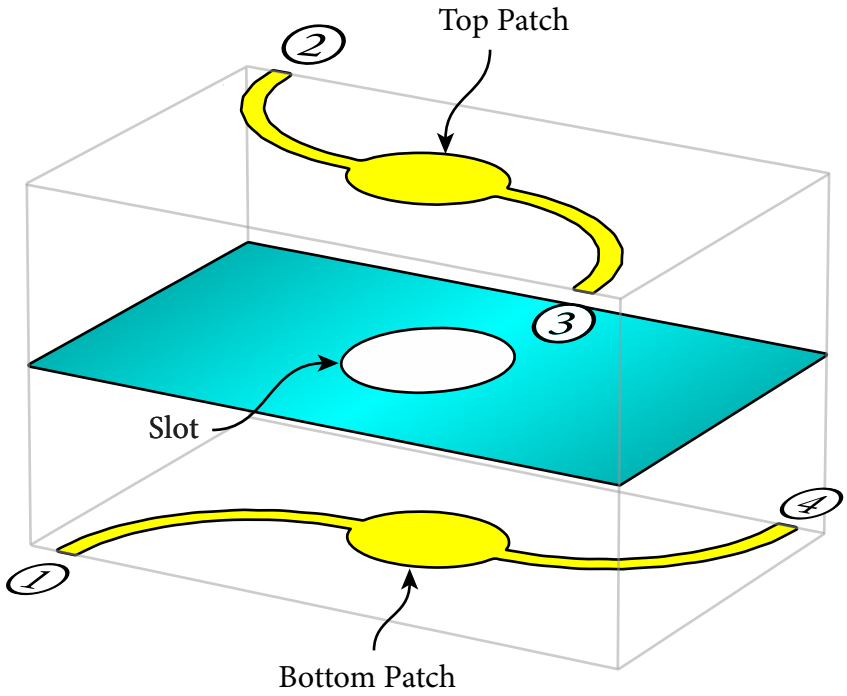

Figure 2.8: Wideband 90° hybrid based on broadside coupled patches.

As mentioned previously, wideband 180° out-of-phase power dividers can be, mainly, implemented by either using wideband four-port hybrids or cascading a wideband three-port in-phase power divider with a wideband phase shifter or phase inverter. In the case of hybrids either two wideband 90° hybrids can be cascaded together to yield the 180° phase difference, or a single 180° hybrid can be used instead. In the literature there are three approaches to implement wideband hybrids:

1. The first approach uses the classical theory of multi-section transmission lines to increase its bandwidth. This approach was used to implement wideband branchline couplers [344–346], 90° coupled line coupler [347, 348], and 180° coupled line couplers [347, 349–354].

2. The second approach is based on introducing a phase inverter in the hybrid such as a microstrip-to-slotline transition to build 90° hybrids [355] and 180° hybrids [356–362], or a coplanar waveguide-to-slotline transition to build 90° hybrids [363, 364]

Ref.	Hybrid Type	Technique	Frequency Range [GHz]	Matching Bandwidth	Isolation Level [dB]	Phase Imbalance
[348]	90°	Multi-section coupled line coupler	0.5 – 18	189%	–	±5°
[373]	90°	Broadside coupled patches	2.3 – 12.3	137%	> 23	±2.5°
[359]	180°	Microstrip-slotline transitions + CPW-microstrip transition	3 – 11	114%	> 20	±5°
[363]	180°	CPW-slotline transition	3.1 – 5.9	62%	> 18	±2.5°
[349]	180°	Tapered coupled line coupler	12 – 67	139%	> 19	±10°
[387]	180°	90° Broadside coupled coupler + broadside coupled phase shifter	2.5 – 8	105%	> 13	±11°
[369]	180°	CPW swap inverter	5.8 – 12.3	72%	> 30	±3°
[370]	180°	PSL swap inverter	0.8 – 3.2	120%	> 25	±5°

Table 2.4: Summary of some wideband hybrids.

and 180° hybrids [363–367]. Also, a 180° hybrid using microstrip-to-parallel stripline and microstrip-to-slotline transitions is demonstrated in [368], using the coplanar waveguide swap inverter in [369], and the parallel stripline swap inverter in [370].

3. The third approach is based on using a wideband phase shifter in the hybrid. For instance, the phase shifter using broadside coupled patches, which was described previously in Figure 2.4, can be modified to operate as a 90° hybrid [371–386], as illustrated in Figure 2.8. This broadside coupled 90° hybrid, in [387], was cascaded with a broadside coupled phase shifter to implement a 180° hybrid, and in [388] it was combined with microstrip-to-slotline and microstrip-to-parallel stripline transitions also to implement a 180° hybrid. And, finally, in [389], a 180° hybrid was implemented using four Wilkinson power dividers and two cascaded broadside coupled phase shifters.

Finally, Table 2.4 compares different implementations of wideband hybrids based on the above approaches.

2.5.3 Wideband Baluns using Phase Shifters/Inverters

Wideband 180° power dividers can also be formed by cascading a wideband in-phase power divider with any wideband phase shifter or phase inverter that were demonstrated

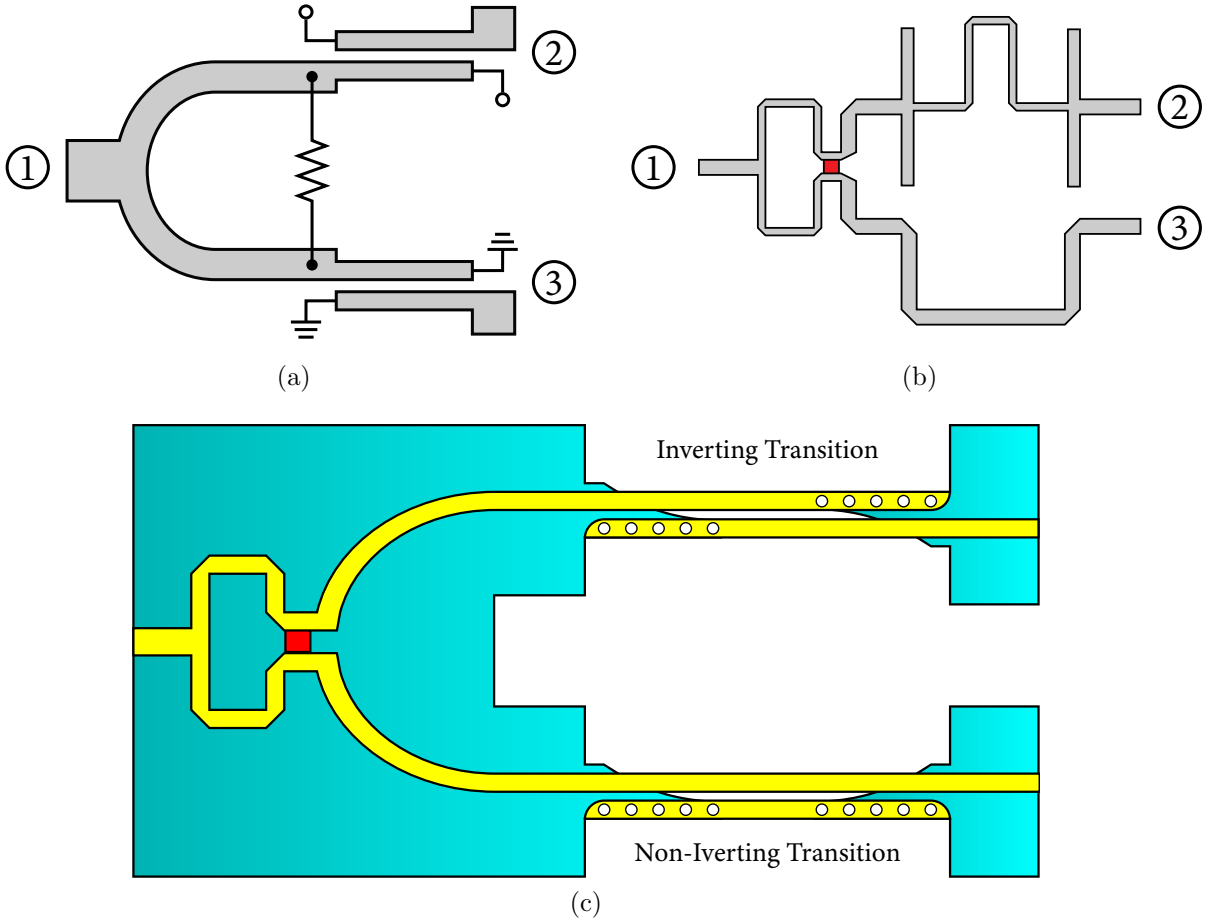

Figure 2.9: Wideband 180° power dividers implemented using (a) power divider plus coupled line phase shifter, (b) power divider plus delay line phase shifter, and (c) power divider plus two microstrip-to-coplanar stripline transitions.

previously. Note that, not all of the demonstrated phase shifters and inverters were used in the literature to implement wideband 180° power dividers, rather only few works were reported using some of them. In particular, in-phase power dividers with a coupled line phase shifter, as shown in Figure 2.9(a), were demonstrated in [390–394], and using delay line phase shifters, as shown in Figure 2.9(b), were demonstrated in [395, 396]. Similarly, power dividers with phase inversion were reported in [397, 398] using microstrip-to-coplanar stripline transitions, coplanar waveguide-to-microstrip transition [399–402], and the parallel stripline swap inverter [403–406]. An example of 180° power divider implemented using a Wilkinson power divider cascaded with inverting transitions, microstrip-to-coplanar stripline transitions (previously introduced in Figure 2.5), is depicted in Figure 2.9(c). Notice that two double transitions are needed in this case, one of transitions will perform phase inversion while the second will not. The input power will be divided equally and in-phase by the Wilkinson power divider, and one of the divided signals will get inverted while the second will not. This results in two output signals that are, ideally, equal in magnitude and 180° out-of-phase. The bandwidth of the transitions could be a decade or more, thus a power divider with a decade bandwidth will also be required, and the only way to do this is by increasing the number of sections in

the Wilkinson power divider. This can drastically increase the size of the circuit taking into consideration that the size of the transitions is also huge.

2.5.4 Wideband Compact Baluns

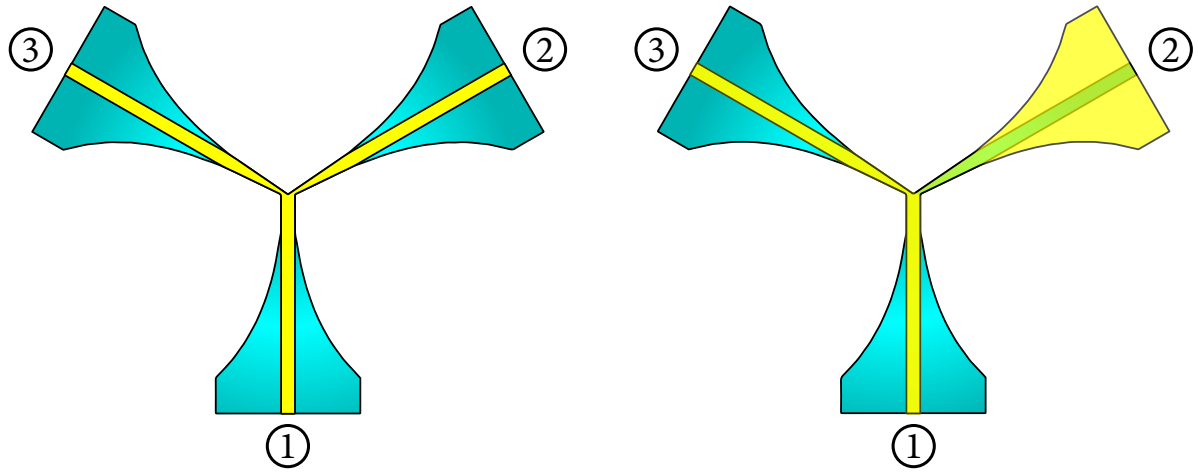

(a) (b)

Figure 2.10: A single 2-in-1 topology to implement (a) in-phase and (b) 180° out-of-phase power dividers based on microstrip-to-parallel stripline transitions.

The wideband performance of phase inverters is highly attractive and desirable in implementing 180° out-of-phase power dividers, nevertheless, the big size of the implemented circuit can be limiting for some applications. There are two points to consider for size reduction: the first point is the size of the multi-section Wilkinson power divider used to cover the desired bandwidth, which increases as the number of sections increases. The second point is the use of the double transitions, that is, we need to transition from microstrip line, or any unbalanced line, to any balanced line first, then we need to transition back from the balanced line to the unbalanced line again to perform phase inversion. The first point can be solved by replacing the Wilkinson power divider by a T-junction power divider, which has no theoretical bandwidth limit, and this can greatly reduce the size of the circuit at the expense of unmatched and unisolated output ports. The second point can be solved by implementing the T-junction in the balanced section rather than implementing it using the unbalanced lines. To better understand this point let's consider the power dividers in Figure 2.10, which consist of three microstrip-to-parallel stripline transitions connected in a T-junction configuration. To implement this kind of transitions, the ground plane of the microstrip line is continuously tapered until its width becomes equal to the width of the strip on the top layer. The first transition is responsible for transitioning from microstrip-to-parallel stripline, and then a T-junction is implemented in the parallel stripline section, which eliminates the need for a double transition at the output and we can directly transition back to microstrip from the junction. The beauty of this technique is not only limited to wideband performance and compactness, but also the fact that wideband in-phase and 180° out-of-phase power dividers can be generated using this technique by simply choosing whether to invert one

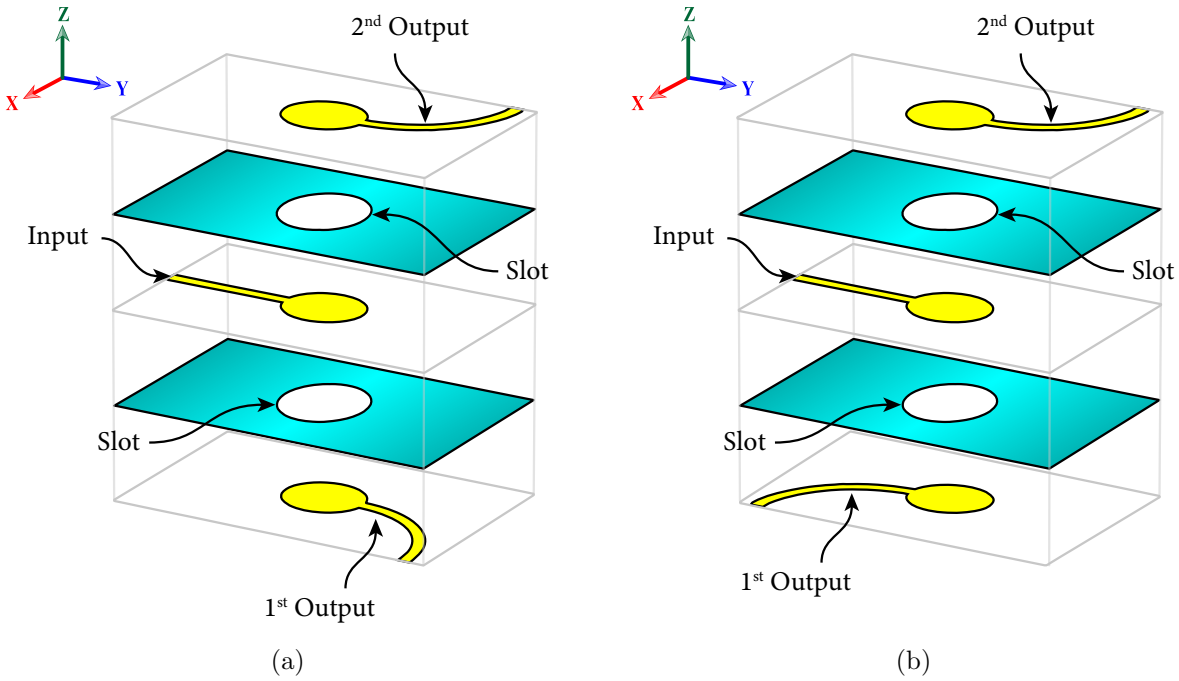

Figure 2.11: (a) In-phase and (b) 180° out-of-phase power dividers based on broadside coupled patches.

of the outputs or not. For example, if all the microstrip lines are placed on the top layer, as in Figure 2.10(a), then an in-phase power divider is generated. On the other hand, if one of the output microstrip lines is placed on the bottom layer while keeping the other microstrip lines on the top layer, as in Figure 2.10(b), then the two output lines will be inverted with respect to one another in this case, and a 180° out-of-phase power divider is generated. This technique was implemented using microstrip-to-parallel stripline transitions [318, 407–409], microstrip-to-slotline transitions [410–437], coplanar waveguide-to-coplanar stripline transitions [438, 439], and coplanar waveguide-to-slotline transitions [440–442].

Another 2-in-1 topology to implement both in-phase and 180° out-of-phase power dividers using broadside coupled patches was proposed in [443, 444]. The power dividers are depicted in Figure 2.11 and they consist of five metal layers and four dielectric layers. The input patch, which is placed in the middle layer, is a stripline fed patch sandwiched between two ground planes. Elliptical slots are etched in each ground plane to couple power from the input patch to the output patches, which are microstrip fed patches that are placed on the bottom and top layers. Notice that in Figure 2.11(a) the two output microstrip lines are oriented in the positive y-direction, which yields an in-phase power divider. On the other hand, if one of the output microstrip lines is oriented in the negative y-direction, while the second output is oriented in the positive y-direction, then a 180° out-of-phase power divider is obtained. Although, in the original work, the authors only presented the in-phase power divider, however, our simulations confirm that 180° phase difference between the output ports is obtained if one of the output microstrip lines is inverted with respect to the other. Also, we think that the number of layers can be reduced by eliminating one output patch and one ground plane, and the two output ports could

Ref.	Structure	Frequency Range [GHz]	Matching Bandwidth	Phase Imbalance	Amplitude Imbalance	Size [mm^2]
[335]	Modified Marchand balun	2 – 22	167%	±3°	±1 dB	–
[342]	Log-periodic balun	1.89 – 8.45	127%	±10°	±1 dB	120 × 40
[394]	Wilkinson power divider + coupled line phase shifter	6 – 20	108%	±7°	±0.6 dB	–
[395]	Wilkinson power divider + delay line phase shifter	3.2 – 9.8	102%	±15°	–	–
[397]	Wilkinson power divider + microstrip-CPS inverter	26.5 – 40	40%	±3.1°	±0.8 dB	–
[402]	Wilkinson power divider + CPW swap inverter	0.2 – 10	192%	±5°	±0.2 dB	65 × [∗]
[403]	Wilkinson power divider + PSL swap inverter	0.38 – 3.5	161%	±5°	±0.4 dB	20.7 × 20.8
[408]	Microstrip-PSL T-junction	3 – 11	114%	±0.5°	±0.3 dB	20 × 20
[429]	Microstrip-Slot T-junction	4 – 45	167%	±7°	±1 dB	3 × 8
[438]	CPW-CPS T-junction	16.5 – 40	83%	±8°	±1.1 dB	–
[441]	CPW-Slot T-junction	3 – 16	137%	±5°	±0.5 dB	≈ 17 × 10

Table 2.5: Summary of some wideband three-port 180° out-of-phase power dividers .

be derived from the same output patch. Moreover, the layers could be further reduced by incorporating coplanar waveguide patches.

2.5.5 Conclusion

Table 2.5 provides a summary of some wideband three-port 180° out-of-phase power dividers, while Table 2.4 provides a summary of some wideband hybrids. After a thorough study of each of the presented topologies, it turns out that devices implemented using multi-section transmission lines or using phase inverters, can provide extremely wide bandwidths, more than a decade, and their bandwidths can be easily extended to the high frequency range. In fact, each topology has its advantages and disadvantages.

For instance, the 180° tapered line coupler can occupy a very large size, but it can provide a good amount of isolation between its ports, and, also, it can be implemented using striplines, which gives it the advantage of being protected from unwanted coupling from other components in the system, and, at the same time, prevents it from coupling unwanted power to the other components. On the other hand, most of the phase inverters, especially those based on balanced-unbalanced transitions, cannot be implemented in a stripline-like configuration (up to our knowledge), thus they might couple power to other components in the system. Nevertheless, 180° out-of-phase power dividers employing phase inverters remain more compact than the tapered hybrid, even those that use a multi-section Wilkinson power divider. Moreover, 180° out-of-phase power dividers implemented using balanced-unbalanced T-junctions are much more compact than those implemented by cascading a multi-section Wilkinson power divider and a phase inverter, however, they lack isolation and matching at the output ports.

As mentioned before, for bistatic in-band full-duplex systems, it is usually not necessary to have isolation and matching at the outputs of the 180° out-of-phase power divider, thus we disregard the tapered line coupler and devices containing Wilkinson power dividers, and instead we work on a 180° out-of-phase power divider employing a balanced-unbalanced T-junction. In particular, we think that the microstrip-to-slotline power dividers, presented in [429], are the best candidates for our application. These power dividers can operate from 4 to 45 GHz with ±1 dB and ±7° of amplitude and phase imbalances, respectively, between the two output ports. Also, such power dividers are characterized by their extreme compactness if compared to other power dividers in the same category, and also by their ease of design and implementation. In fact, they do not require any vias or wire bonds, unlike other types of transitions, and they can easily be fabricated using the standard printed circuit board (PCB) technology. In the following section we give a detailed description of the chosen power dividers, but first, we present the theoretical background of microstrip-to-slotline transitions and their design procedure followed by a parametric analysis. After that, the designed and fabricated power dividers will be presented, and new power dividers with enhanced isolation will be proposed.

2.6 Microstrip-to-Slotline Devices

2.6.1 Microstrip-to-Slotline Transitions

A microstrip-to-slotline transition, which is depicted in Figure 2.12, consists of a slotline etched in the metallic layer at one side of the substrate, and a microstrip line perpendicular to it is etched on the other side of the substrate. After that, the microstrip line and the slotline are terminated with virtual short-circuited stubs that are quarter-wavelength at the frequency of design, although other shapes of stubs can be used as terminations. The different stubs shown in Figure 2.12 control the bandwidth and the total size of the transition, for instance, the quarter-wavelength stubs occupy more space and are more narrowband than the radial and the circular stubs. A detailed analysis of microstrip-to-slotline transitions can be found in [445], yet here we present a brief description for the reader to be consistent with the following sections.

The equivalent circuit of a microstrip-to-slotline transition terminated with microstrip

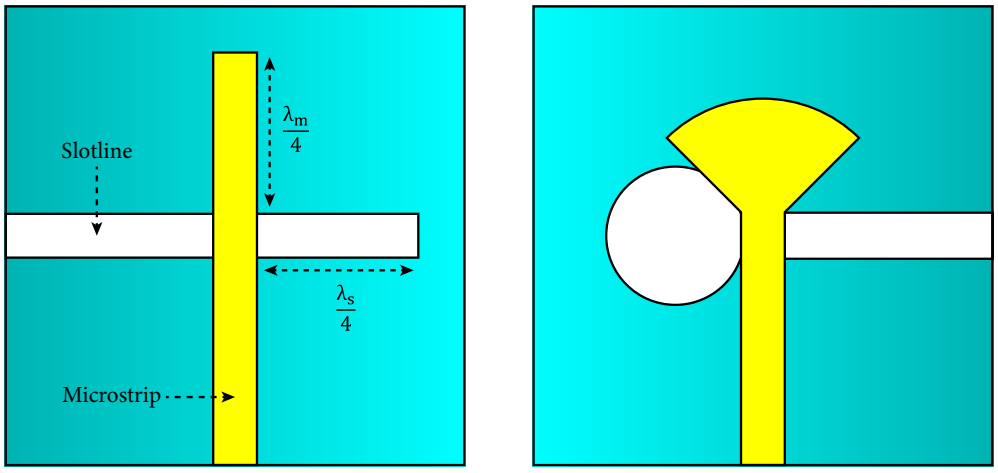

(a) (b)

Figure 2.12: Microstrip-to-slotline transitions terminated with (a) quarter-wavelength microstrip and slotline stubs, respectively, and (b) microstrip radial stub with slotline circular disk stub.

and slotline quarter-wavelength stubs is given by [446] and is demonstrated in Figure 2.13(a), where Z_m and Z_s denote the characteristic impedances of the microstrip line and the slotline, respectively. θ_m and θ_s are the electrical lengths of the microstrip and slot stubs, respectively. C_m denotes the equivalent capacitance of the microstrip stub, L_s denotes the equivalent inductance of the slotline stub, and n represents the magnitude of coupling between the microstrip line and the slotline. The equivalent circuit can be simplified as in Figure 2.13(b) by transforming the inductance and the capacitance of the microstrip and slotline stubs, respectively, to the position of the transition. Hence, we get:

$$jX_s = Z_s \frac{j\omega L_s + jZ_S \tan\theta_s}{Z_s - \omega L_s \tan\theta_s} \tag{2.1}$$

$$jX_m = Z_m \frac{1/j\omega C_m + jZ_m \tan\theta_m}{Z_m + 1/\omega C_m \tan\theta_m} \tag{2.2}$$

Z_s and jX_s are in parallel, thus their equivalent impedance can be written as:

$$\begin{aligned} Z_{eq} &= \frac{jX_s Z_s}{Z_s + jX_s} \times \frac{Z_s - jX_s}{Z_s - jX_s} \\ &= \frac{X_s^2 Z_s + jX_s Z_s^2}{Z_s^2 + X_s^2} \\ &= \frac{X_s^2 Z_s}{Z_s^2 + X_s^2} + \frac{jX_s Z_s^2}{Z_s^2 + X_s^2} \\ &= R_{eq} + jX_{eq} \end{aligned} \tag{2.3}$$

Where $R_{eq} = \mathrm{Re}\{Z_{eq}\}$ and $X_{eq} = \mathrm{Img}\{Z_{eq}\}$. Now, the input impedance Z_{in}, seen by the input port when looking at the transition, can be expressed as follows:

$$\begin{aligned} Z_{in} &= jX_m + n^2 Z_e q \\ &= n^2 R_{eq} + j\left(X_m + n^2 X_{eq}\right) \end{aligned} \tag{2.4}$$

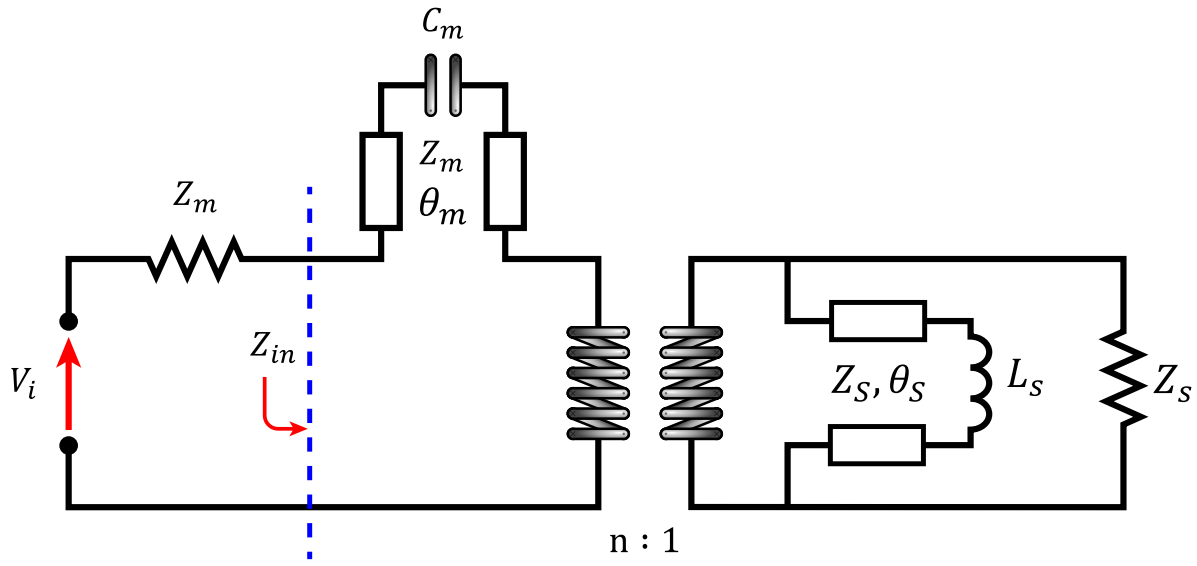

(a)

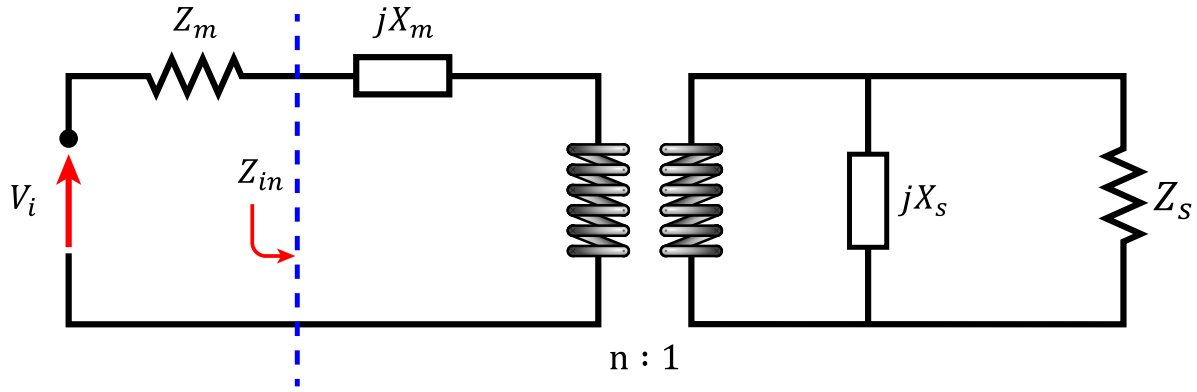

(b)

Figure 2.13: Equivalent circuit of a microstrip-to-slotline transition terminated by microstrip and slotline quarter-wavelength stubs.

For good matching between the microstrip line and the slotline the input impedance should be equal to the port impedance, that is, $Z_{in} = Z_m$, but since Z_m is purely real, then the imaginary part of Z_{in} needs to go to zero ($X_m + n^2 X_{eq} = 0$), which can only happen if the equivalent capacitance of the microstrip stub goes to zero and the equivalent inductance of the slotline stub goes to infinity. In practice, these conditions cannot be totally satisfied, however, the stubs can be optimized to reduce the value of the imaginary part of the input impedance to a minimum value. But for now, let's assume that the conditions are satisfied and that the imaginary part is equal to zero, this also means that X_m and X_s are equal to zero, consequently, we obtain:

$$Z_m = Z_{in} = n^2 R_{eq} = n^2 Z_s \tag{2.5}$$

Equation (2.5) implies that if the reactive behavior of the stubs is neglected, then the matching of the transition will be determined by the impedance of the microstrip line Z_m, the impedance of the slotline Z_s, and the coupling factor between them n. The coupling

factor can be obtained from the following equations:

$$n = \cos\left(2\pi\frac{h}{\lambda_0}u\right) - \cot(A)\sin\left(2\pi\frac{h}{\lambda_0}u\right) \tag{2.6}$$

$$A = 2\pi\frac{h}{\lambda_0}u + \arctan\left(\frac{u}{v}\right) \tag{2.7}$$

$$u = \sqrt{\varepsilon_r - \left(\frac{\lambda_0}{\lambda_s}\right)^2} \qquad\qquad v = \sqrt{\left(\frac{\lambda_0}{\lambda_s}\right)^2 - 1} \tag{2.8}$$

Where h and ε_r are the thickness and the relative permittivity of the substrate, respectively. λ_0 and λ_s are the free space wavelength and the guided wavelength in the slotline, respectively. To calculate the guided wavelength in the slotline, and also to calculate the microstrip line and slotline impedances, one can use the closed form equations which are included in Appendix A. Usually, we want the port impedance to be equal to 50 Ω, but if we assume that $n = 1$, then we need to have the slotline impedance also to be equal to 50 Ω. In practice, the minimum slotline width realizable by the classical technology for printed circuit boards (PCBs) is around 100 μm, for this slotline width we obtain a slotline impedance which is higher than 100 Ω (at least for $\varepsilon_r \leq 20$ and $h \leq 1.6\ mm$). The impedance of the slotline, unlike the impedance of microstrip lines, decreases only if the slotline width is decreased, however, since the minimum slotline width, provided by the available fabrication technology, yields an impedance higher than 100 Ω, thus there will always be a mismatch between the microstrip line and the slotline depending on the actual value of the coupling factor n, which limits the bandwidth of the transition.

To reduce the mismatch between the microstrip line and the slotline there are several approaches that can be adopted:

1. Firstly, the slotline impedance, corresponding to a fixed slotline width, can be further reduced by manipulating the characteristics of the substrate. For instance, the slotline impedance can be decreased by increasing the thickness or the relative permittivity of the substrate, or both, however, this requires a drastic increase in the thickness or the permittivity to obtain a minor reduction in the impedance value. Moreover, sandwiching the slotline by two dielectric layers can greatly help in reducing its impedance, but this increases the size of the transition. Nonetheless, we do not prefer to manipulate the characteristics of the substrate to reduce the slotline impedance, mainly, because the passive devices and the antennas presented in this chapter will be fabricated on the same substrate, and we give the priority in the substrate choice to the antennas, which require a low permittivity substrate with a relatively low thickness.

2. Alternatively, the low impedance of the microstrip line can be tapered to match the high impedance of the slotline by using any microstrip taper (linear, exponential, or Klopfenstein), which also increases the size of the transition depending on the length of the taper which is a function of the lowest frequency of operation.

3. Finally, the coupling factor n can be also manipulated to ensure a proper matching between the microstrip line and the slotline, this can be done by manipulating the thickness or the relative permittivity of the substrate, but, as we stated earlier, those parameters will be chosen in the favor of the antennas and cannot be manipulated after, so the value of n will be fixed.

2.6.2 Parametric Analysis

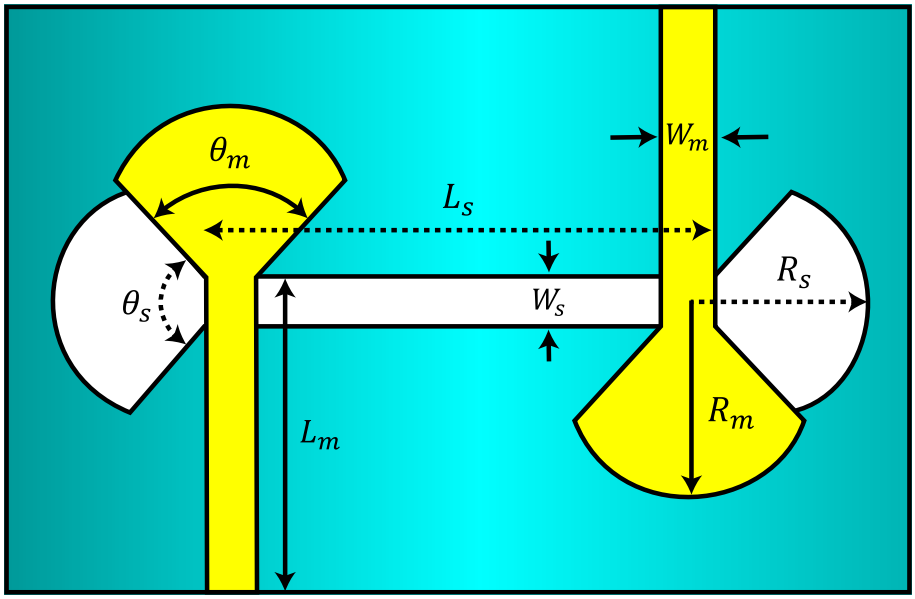

Figure 2.14: A microstrip-to-slotline transition terminated with radial stubs for both the microstrip line and the slotline. $\{W_m = 0.66\ mm,\ W_s = 0.156\ mm,\ L_m = 5\ mm,\ L_s = 5.25\ mm,\ R_m = 2.4\ mm,\ R_s = 2.6\ mm,\ \theta_m = 90°$, and $\theta_s = 90°\}$

To determine the bandwidth of matching between the microstrip line and the slotline, it is necessary to know the values of the equivalent capacitance C_m and the equivalent inductance L_s of the microstrip and slotline stubs, respectively. However, there are no theoretical studies that can provide closed form equations to describe the behavior of the stubs, especially the slotline stubs. Hence, an empirical approach is required to study the behavior of the stubs and their effect on the bandwidth of the transition. For this reason, in this section, we present a parametric analysis of the microstrip-to-slotline transition based on full-wave simulations performed in CST Microwave Studio, but, before, we need to decide the type or shape of the terminating stubs. For wideband operation, it was shown in [252] that more than a decade bandwidth can be obtained using radial stubs, and, moreover, radial stubs have two parameters that can be manipulated to optimize the bandwidth, namely their radius and angle, which gives us more degrees of freedom in the transition design as compared to other types of stubs.

A double microstrip-to-slotline transition terminated with radial stubs was demonstrated in [320], this transition is depicted in Figure 2.14. The double configuration facilitates the simulation of the transition, and is necessary to conduct measurements, because slotlines cannot be directly measured. The transition was built on a 0.635 mm thick RT/Duroid 6010 substrate with $\varepsilon_r = 10.2$. First, the microstrip line and the slotline

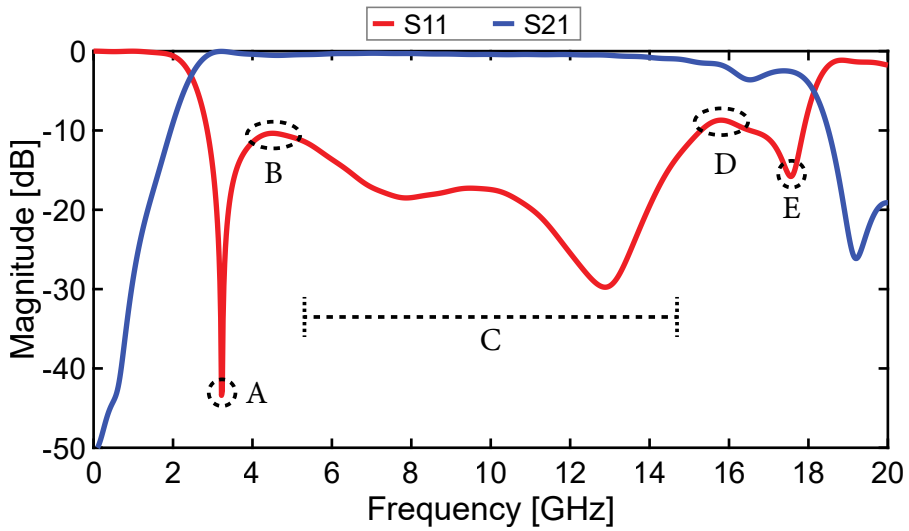

Figure 2.15: Simulated S-parameters of the microstrip-to-slotline transition of Figure 2.14.

	A	B	C	D	E
R_m	–	↓	–	↖	↖
R_s	←	↖	–	↓	–
θ_m	–	↓	–	↓	–
θ_s	–	↑	–	↙	↙
L_s	↖	↖	–	↑	–

Table 2.6: Results of the parametric analysis of the microstrip-to-slotline transition.

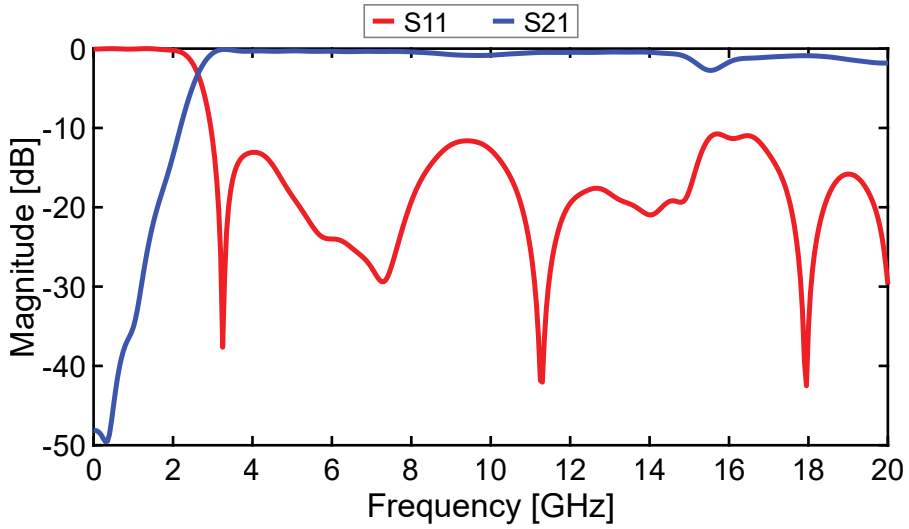

Figure 2.16: Optimized S-parameters of the microstrip-to-slotline transition of Figure 2.14. $\{W_m = 0.66\ mm,\ W_s = 0.156\ mm,\ L_m = 5\ mm,\ L_s = 8\ mm,\ R_m = 2\ mm,\ R_s = 2.4\ mm,\ \theta_m = 130°$, and $\theta_s = 90°\}$

impedances were calculated using the equations presented in the previous section and taking into account the fabrication limitations, then the radii of the stubs were set to one sixth of a wavelength at 10 GHz, and the angles of the stubs were set to 90° to prevent the stubs from overlapping, otherwise, the overlap might induce unwanted effects in the circuit. This transition was reproduced in CST and simulated with the initial parameters' values as in [320], which are also included in the captions of Figure 2.14.

The S-parameters of the simulated transition are demonstrated in Figure 2.15, where it can be noticed that the bandwidth is characterized by some specific points on the S_{11} curve: the position of the first local minimum (A), the level of the first local maximum (B), the level of the last local maximum (D), the position and the level of the last local minimum (E), and the level of the in-band section (C) that is situated between the two local maxima. Usually, the in-band section level is controlled by the levels of its bounding maxima, therefore, by keeping their values as low as possible we ensure that the level of (C) is also low. In order to obtain the widest bandwidth, the position of (A) should be shifted to the left of the frequency axis while decreasing the level of (B). In parallel, the position of (E) should be shifted to the right of the frequency axis, while maintaining its value and the value of (D) at a low level.

The parametric analysis will only study five parameters of the transition: the microstrip stub radius (R_m), the microstrip stub angle (θ_m), the slotline stub radius (R_s), the slotline stub angle (θ_s) and the slotline length (L_s). The microstrip line width (W_m) and the slotline width (W_s) were kept fixed as they correspond to fixed microstrip and slot impedances, respectively, and should not be altered. Also, the length of the microstrip line (L_m) has no effect on the behavior of the transition. The results of the parametric analysis are summarized in Table 2.6 that shows how different parts of the S_{11} plot are affected by increasing each parameter. The dashes in the table indicate that varying a specific parameter has no or negligible effect on a certain part of the bandwidth, while the arrow tells how and in which direction the curve will globally move if the parameter is increased. Also notice that different parts of the curve might be affected by multiple parameters simultaneously, and sometimes are affected oppositely, so a good balance and a good trade-off between the different parameters is needed to achieve the widest bandwidth possible. Finally, the optimized S-parameters are depicted in Figure 2.16, where the optimized values of the transition parameters are included in the captions of the figure. Initially, the transition operated in the 3–15 GHz frequency range, and after optimization it operated from 3 GHz and up to more than 20 GHz.

2.6.3 Ultra-Wideband Transitions

Although the optimized transition, from the previous section, can already operate over a wide bandwidth but we were looking for something that is more wideband. Also, the relative permittivity of the used substrate is very high and does not suit the antennas, because a high permittivity substrate absorbs and stores more energy and reduces the power radiated by the antenna. In addition to that, to reach higher frequencies we need to reduce the thickness of the substrate, otherwise, higher order modes will start to propagate in the substrate, and those modes can either remain trapped in the substrate as surface waves or might manage to reach the antenna and might get radiated, in this case, the radiation pattern of the antenna will be negatively affected as those modes will

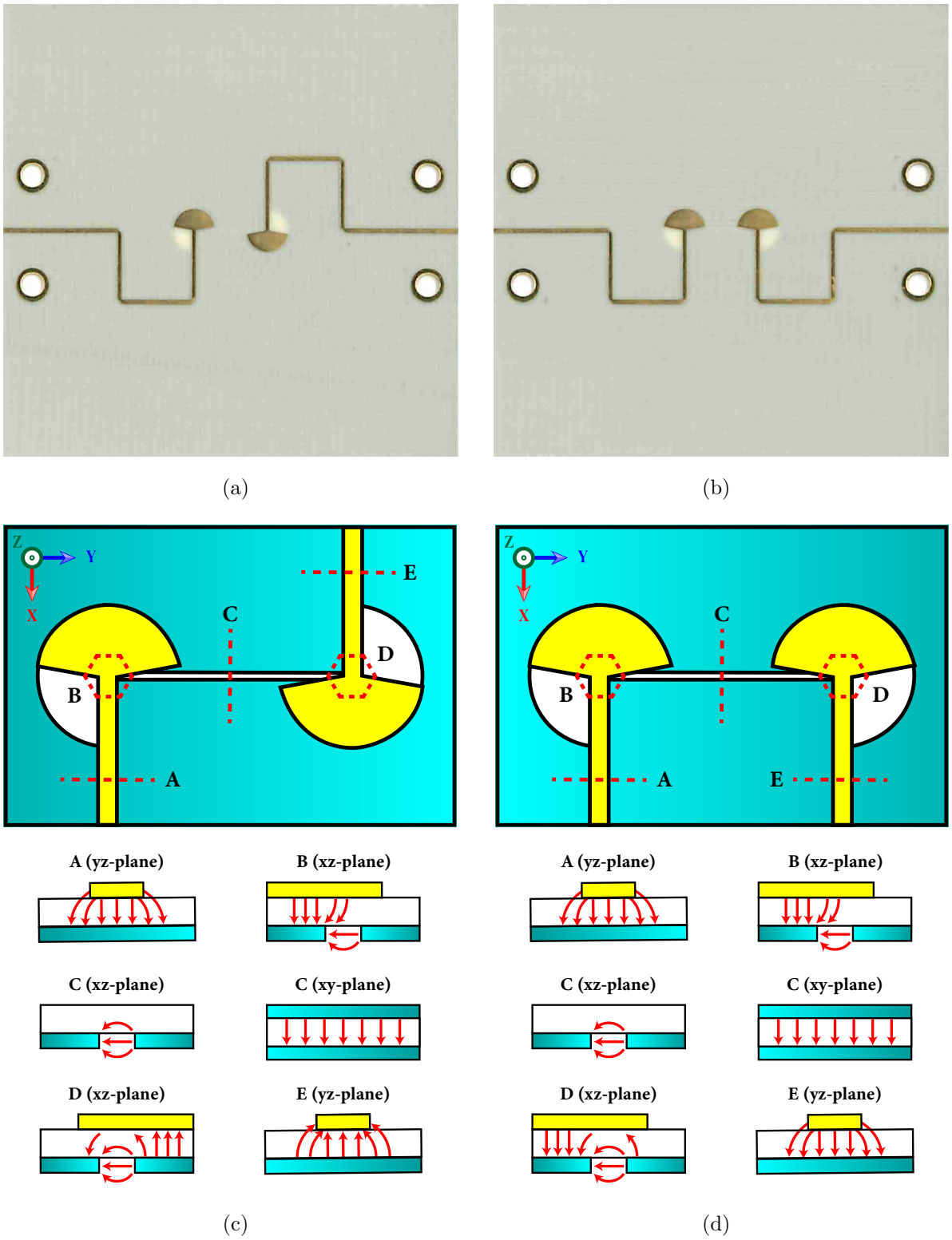

Figure 2.17: Pictures of (a) Type-1 and (b) Type-2 Transitions, (c) and (d) are zoom-in views of both types of transitions, respectively, showing the electric field distribution at different stages of each transition.

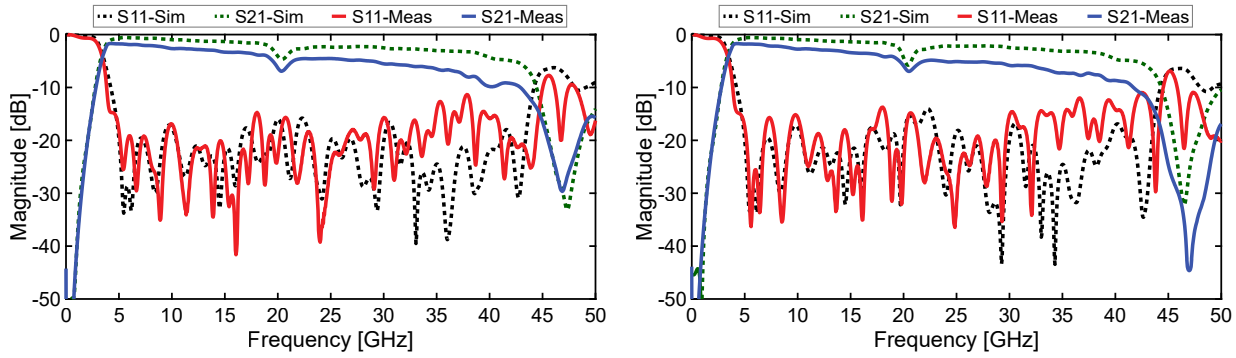

Figure 2.18: The simulated and measured S-parameters of (a) Type-1 transition and (b) Type-2 transition. $\{W_m = 0.4\ mm,\ W_s = 0.1\ mm,\ L_s = 8\ mm,\ R_m = 1.87\ mm,\ R_s = 1.85\ mm,\ \theta_m = 160°$, and $\theta_s = 170°\}$

appear mainly as side lobes. For all these reasons we have selected the RO4003C substrate ($\varepsilon_r = 3.55$) with a thickness of 203.2 μm to build our circuits on.

After selecting the substrate, we can now calculate the width of a 50 Ω microstrip line based on the equations in Appendix A, which turns to be equal, approximately, to 0.4 mm. Then by letting the width of the slotline to be 100 μm, we obtain the impedance of the slotline which is, approximately, 120 Ω at 20 GHz. The reason for specifying a frequency point for the slotline impedance is because the slotline impedance is frequency-dependent and can vary significantly with frequency, unlike microstrip lines which have a relatively constant impedance with frequency. Although the mismatch between the impedances of the microstrip line and the slotline is significant, we can still tune the parameters of the slotline stubs to reduce their reactances which in turn decreases the mismatch according to Equations (2.3) and (2.4). The parameters of the microstrip stubs can be tuned to reduce the imaginary part in Equation (2.4), which can further aid in the mismatch reduction.

So, based on the above analysis, a new transition was designed in CST using the selected substrate and the calculated microstrip line and slotline widths, while letting the values of the rest of the parameters, namely the radii and the angles of the stubs and the slotline length, be equal to the optimized values in the previous section. The new transition was simulated with the initial parameters and then manually optimized based on the observations of the parametric analysis explained previously. And, finally, after the manual tuning, the transition was further optimized using the native optimizer in CST. In fact, two types of transitions were designed and simulated, and they are depicted in Figure 2.17. The transition in Figure 2.17(a) will be named Type-1 transition and the transition in Figure 2.17(b) will be named Type-2 transition.

The output microstrip line (the right microstrip line) of Type-1 transition is oriented oppositely with respect to the input microstrip line, while the output of Type-2 transition is oriented in the same direction of its input. The purpose of designing the two transitions with different configurations can be explained by looking at the electric field distributions in each transition, which are demonstrated in Figure 2.17(c) and Figure 2.17(d), respectively. It can be observed form Figure 2.17(c) that the output electric fields of the output microstrip line of Type-1 transition are inverted with respect

to the input electric fields, while for Type-2 transition the output electric fields are not inverted with respect to the input electric fields. This means that the output electric fields of both transitions are inverted with respect to one another, consequently, the two output signals from both transitions will be 180° out-of-phase. And this will be our tool to create phase inversion.

Figure 2.18 shows the simulated and measured S-parameters of each transition and the values of the optimized parameters of these transitions. The actual size of the transitions is 12 $mm \times 4$ mm, however, they were built on a 40 $mm \times 40$ mm board for mechanical convenience. Three main observations can be extracted from the S-parameters plots: first, both transitions have good matching between 4 and 45 GHz, however, the measured S_{11} becomes worse at frequencies beyond 30 GHz as compared to the simulated results, this might be caused by the high frequency cables and connectors (Southwest 2.4 mm Connectors) used for measurements, these cables and connectors suffer from poorer matching at higher frequencies. The second observation is regarding the insertion loss which increases as the frequency increases, and this is mainly due to the dielectric losses and the slotline radiation losses. Radiation losses might become more significant than the dielectric losses at higher frequencies, where the radius of the slotline stub becomes comparable to the wavelengths at those frequencies. Also, the measured insertion loss is higher than the simulated one, and this can be caused by the change in the dielectric constant of the substrate during the fabrication process.

In fact, the dielectric constant of a lossy material is given by the following equation:

$$\varepsilon_r = \varepsilon_r' + j\varepsilon_r'' \tag{2.9}$$

where ε_r' and ε_r'' are the real and imaginary parts of the dielectric constant. The real part ε_r' represents the relative permittivity of the material that is usually found in the data sheet of the substrate (3.55 in our case), and it controls the phase that will be accumulated by the wave propagating inside the material, while the imaginary part ε_r'' is usually represented as a loss tangent ($\tan\delta$) in the datasheet, and it controls the rate of attenuation of the wave propagating inside the material. The higher insertion loss in the measured results indicates that the imaginary part has increased during circuit fabrication; and as we will see later, the real part has also changed.

The third observation is also regarding the insertion loss of the circuits, both simulated and measured. The insertion loss increases normally as frequency increases due to substrate dielectric losses and slotline radiation losses, but it is abnormal to sharply drop around 20.5 GHz. The reason behind this drop is the overlap between the microstrip stub and the slotline stubs. In fact, the microstrip stub acts like a small patch antenna that radiates energy and resonates around 45 GHz, which is outside the band of operation. However, when the microstrip stub is mated with a slotline stub below it, it will act as a small patch antenna with a defected ground plane, which results in decreasing the resonant frequency of the antenna down to 20.5 GHz. Although, in this case, the antenna is not perfectly matched at the resonant frequency, the stub still radiates a decent amount of energy causing the dip in the insertion loss. This problem can be solved by reducing the overlap between microstrip and slotline stubs, which was achieved by reducing the size of the microstrip stubs as shown in Figure 2.19. The simulated and measured S-parameters of the modified transitions, with reduced microstrip stubs, indicate that the insertion loss dip is eliminated, and a flatter curve is obtained, however, this comes at the expense of a

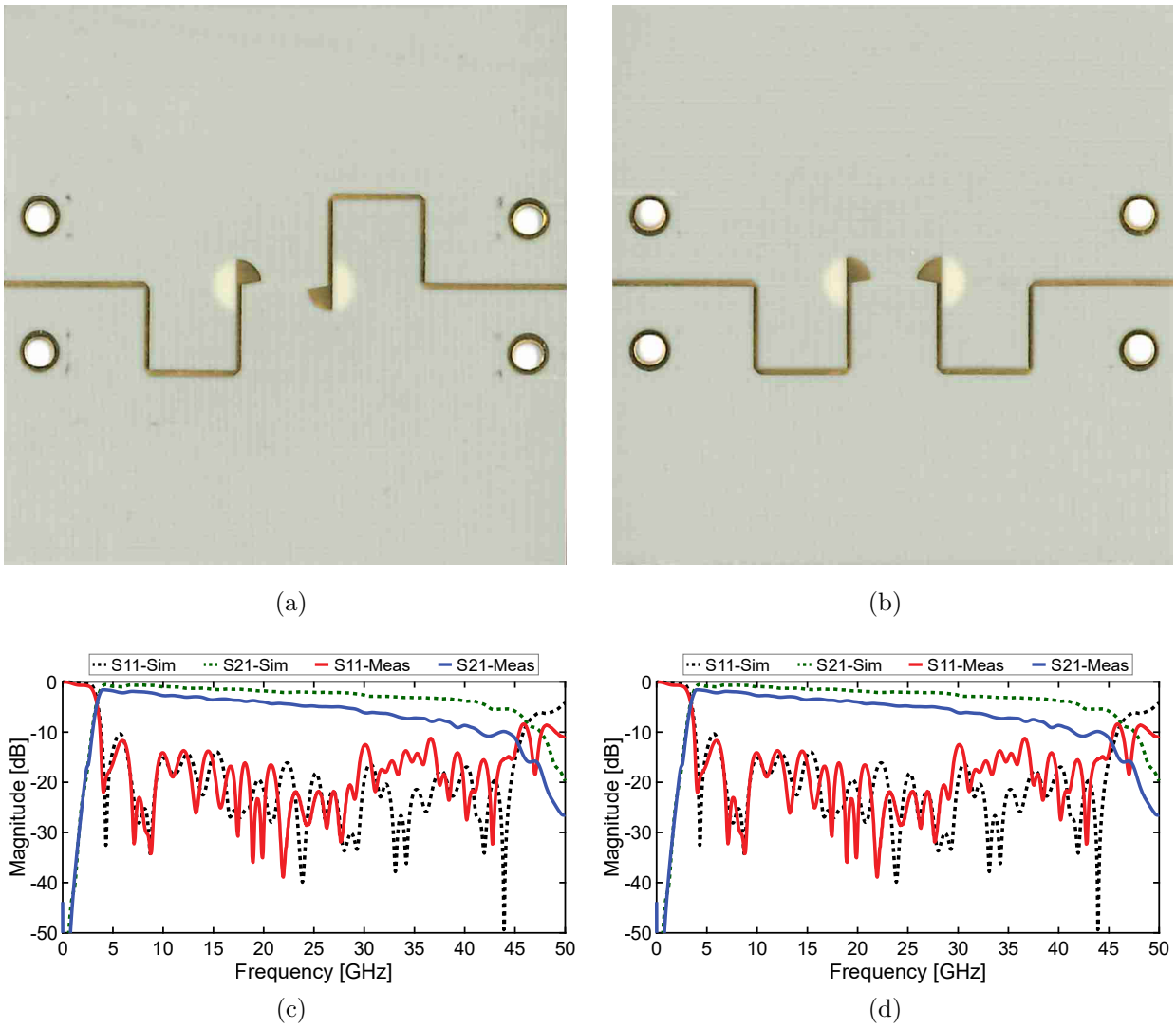

Figure 2.19: Modified (a) Type-1 and (b) Type-2 transitions with reduced microstrip stubs, and (c) and (d) are their corresponding S-parameters.

slightly worse matching at lower frequencies.

2.6.4 Ultra-Wideband In-Phase and 180° Out-of-Phase Power Dividers

Based on microstrip-to-slotline transitions, a novel topology to implement both in-phase and 180° out-of-phase power dividers with an ultra-wideband matching was demonstrated in [429]. Both types of power dividers are depicted in Figure 2.20 along with the electric fields distributions at different stages of each power divider. The power dividers have similar layouts with three microstrip-to-slotline transitions: the input power is injected in the middle transition, which is responsible for dividing the power equally between the right and left paths of the slotline, while the output powers are extracted from the two lateral transitions, which are responsible for phase inversion or non-inversion. Note that, full-size microstrip stubs were used in the original publication although the dip in the

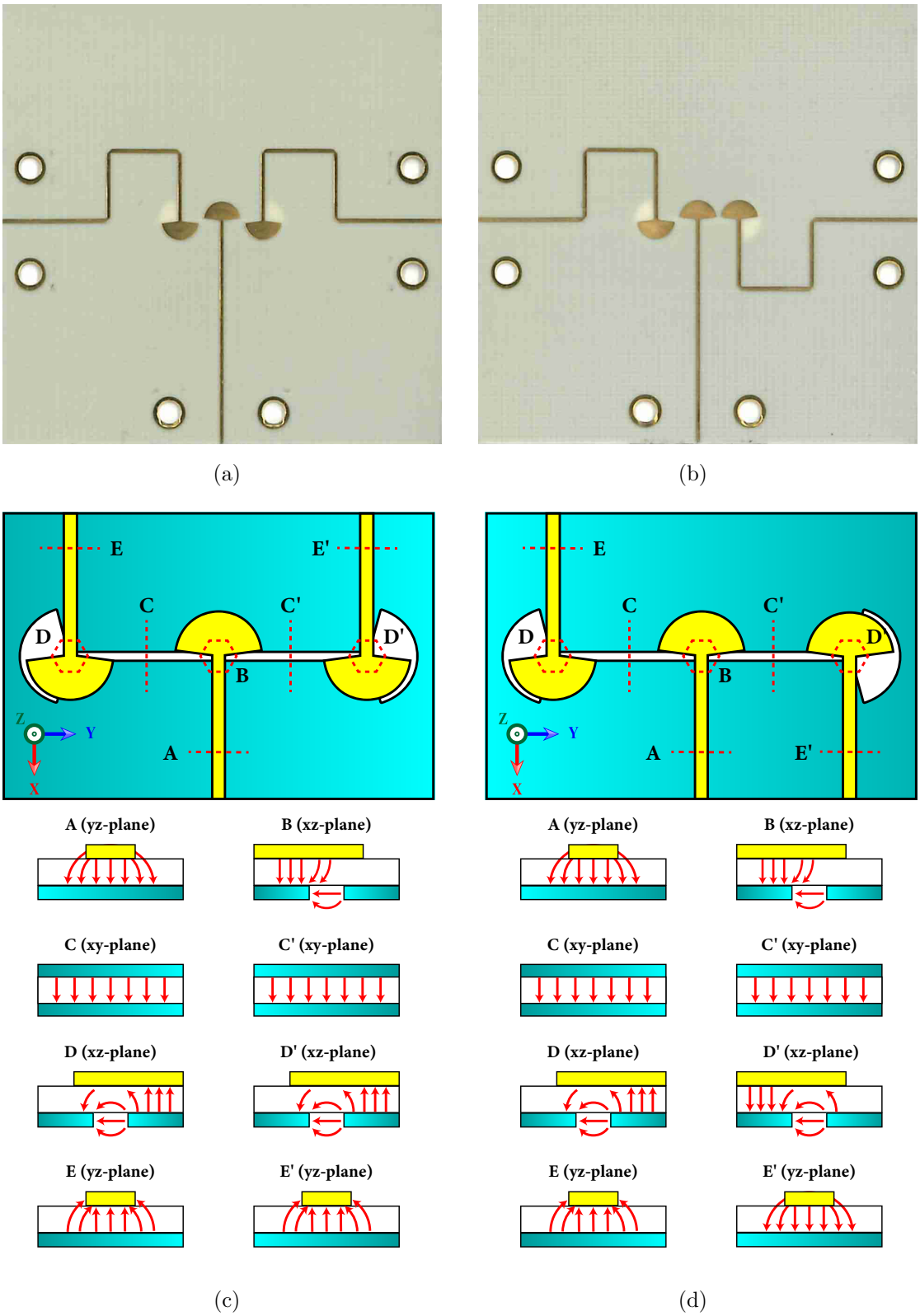

Figure 2.20: Ultra-wideband (a) in-phase and (b) 180° out-of-phase power dividers based on microstrip-to-slotline transitions, and (c) and (d) are exaggerated views of both power dividers showing the electric fields distribution at different stages of each power divider, respectively.

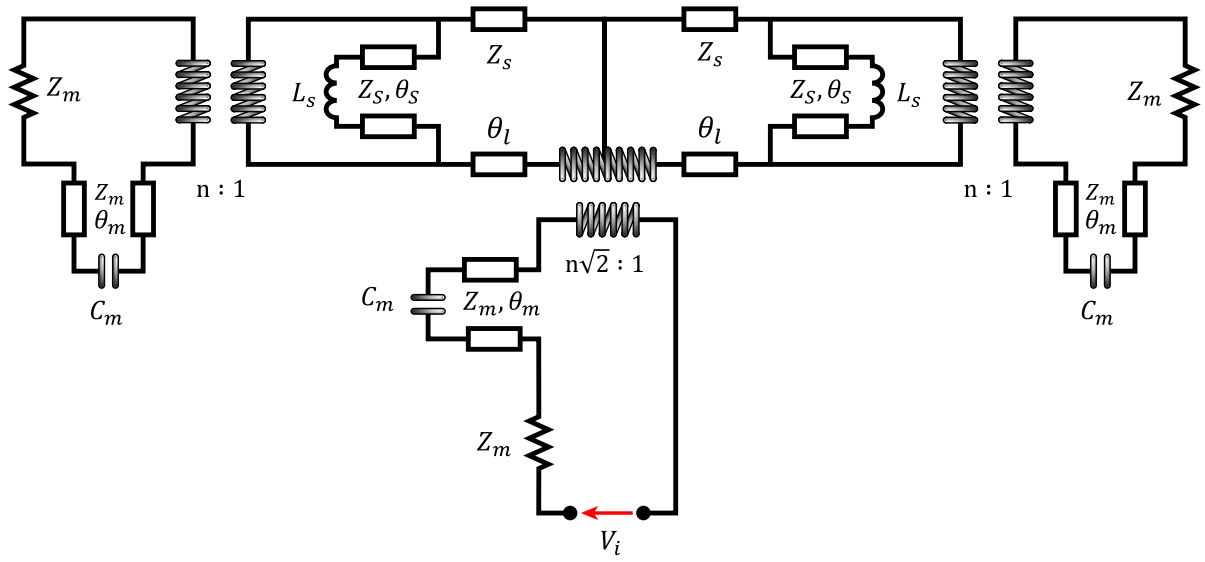

Figure 2.21: Equivalent circuit of the microstrip-to-slotline power dividers in Figure 2.20.

insertion loss was significant, however, here we continue to use full-size stubs because primary simulations did not show a significant insertion loss dip, in this case, and we did not think it was necessary to use half-size stubs.

To obtain in-phase power division, the output microstrip lines of the two lateral transitions should be oriented in the same direction with respect to one another, regardless of their orientation with respect to the input microstrip line. This can be verified by inspecting the electric fields distribution in Figure 2.20(c), where it can be seen that the two output electric fields oscillate in the same direction, although they are inverted with respect to the input electric field, but, anyhow, the two output signals will be in-phase. Also, to obtain 180° out-of-phase power division, the output microstrip line of one lateral transition should be oriented in the same direction of the input microstrip line, while the output microstrip line of the second lateral transition should be oriented in the opposite direction of the input microstrip line. Or, in simpler words, the two output microstrip lines need to be oriented in different directions with respect to one another. This can be verified by looking at the electric fields distribution in Figure 2.20(d), where it can be seen that the two output electric fields are inverted with respect to each other, and, consequently, the two output signals will be 180° out-of-phase.

Figure 2.21 illustrates the equivalent circuit of the proposed power dividers, where θ_l denotes the electrical length of half of the slotline. The input impedance of the equivalent circuit will not be developed here, as it does not provide any useful information about the choice of the slotline impedance, rather we will adopt an empirical approach to determine the slotline impedance based on the parametric analysis of the microstrip-to-slotline transition. However, before we initiate the manual tuning procedure, it would be helpful to use the following theoretical analogy in order to have an initial guess of the value of the impedance. In fact, the structure of the proposed power dividers is similar to a T-junction power divider, where the characteristic impedance of the two output ports should be twice the impedance of the input port ($Z_o = 2Z_i$), that is, if the impedance of the input port is 50 Ω then the impedance of the output ports needs to be 100 Ω. In this

case, we can let the impedance of the slotline and the output microstrip lines be equal to 100 Ω, however, this is not suitable for us because the power dividers will be connected to other circuits in the system that have a 50 Ω input port impedance. Alternatively, all port impedances of the T-junction can be set to 50 Ω and a quarter-wavelength transformer can be used to transform the output ports impedances to 100 Ω at the junction. Similarly, for the proposed power dividers, all the microstrip line impedances will be 50 Ω while the two halves of the slotline will be treated as quarter-wavelength transformers at the central frequency (20 GHz) and their impedances should be equal to $50\sqrt{2}$ Ω or 70.71 Ω. Nonetheless, this analogy does not take into consideration the effect of the radial stubs on the impedance of the power dividers and that the minimum realizable slotline width is 100 μm which yields a slotline impedance of 120 Ω at 20 GHz. In any case, the microstrip lines can be tapered starting from a high impedance at the intersection with the slotline to reach 50 Ω at the output port, which might increase the size of the circuit depending on the size of the taper.

Initially, we let all microstrip impedances to be 50 Ω without using any tapers, also we let $W_s = 100$ μm and $L_s \approx \lambda_s/2$ (or quarter-wavelength per half slotline length), and finally, we let the stubs' parameters be equal to the optimized values of the microstrip-to-slotline transition that are mentioned in Figure 2.18. The initial simulation results were satisfying and proved that the proposed power dividers can be matched over an extremely wide bandwidth, although the slotline and the output microstrip lines were not properly matched and no microstrip line tapers were implemented at the outputs. Note that, in the original publication [429] the authors used 75 Ω microstrip lines at the outputs to compensate for the mismatch between the slotline and the output ports impedances, however, in our work, we were able to implement the same topology with an ultra-wideband matching by using 50 Ω microstrip lines at all ports. Nonetheless, the obtained bandwidth was slightly less than the bandwidth obtained in the original work. After that, the power dividers were manually tuned and then were optimized in CST to obtain the maximum bandwidth possible.

The optimized parameters can be found in the captions of Figure 2.22 which shows the simulated and the measured S-parameters of both types of power dividers, respectively. The actual size of the transitions is also 12 $mm \times 4$ mm, however, they were built on a 40 $mm \times 40$ mm board for mechanical convenience. It can be observed that both types of power dividers are matched at the input port from 3.2 GHz up to 42.3 GHz and that the insertion loss starts with an approximate value of 3 dB at the lower band edge and reaches more than 8 dB at the upper band edge in simulation, and more than 10 dB in measurements, of which 3 dB are primarily caused by the power division. Also, both power dividers have poor matching and isolation between their output ports, which is normal due to the fact that a three-port device cannot be lossless, reciprocal, and simultaneously matched at all ports. And, finally, the measured amplitude and phase imbalances between the output ports are ±1 dB and ±7° respectively, at least up to 40 GHz. It can be noticed that the measured imbalances fluctuate more irregularly as compared to the simulated ones, especially the phase imbalances. This can be attributed to fabrication inaccuracies, in particular, the change in the value of the dielectric constant of the substrate (both the real part and the imaginary part), where this change does not seem uniform at different locations in the board.

The extremely wideband performance of those power dividers might be attractive

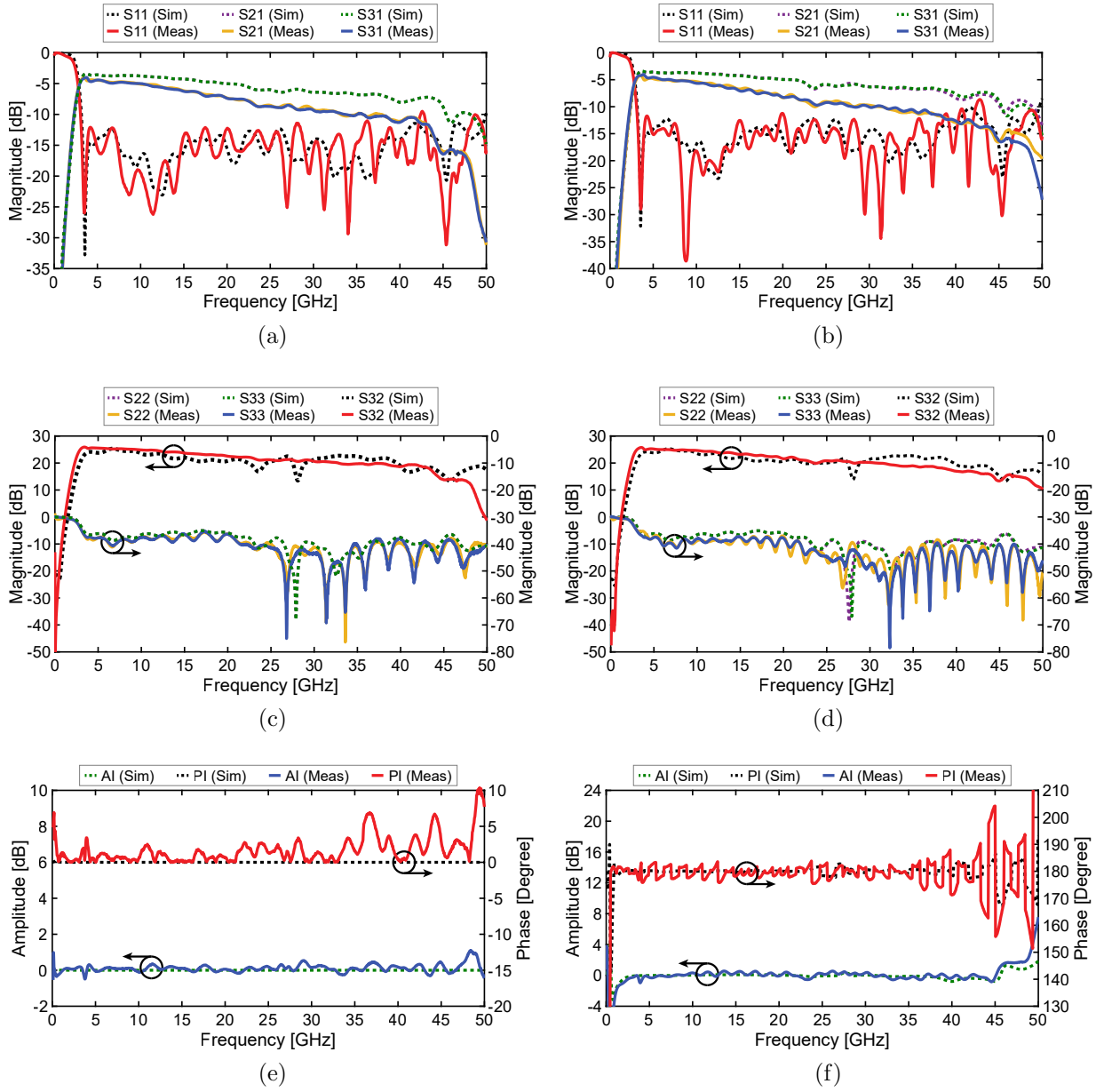

Figure 2.22: Simulated and measured S-parameters of the in-phase and 180° out-of-phase power dividers respectively: (a) and (b) are the input matching and insertion loss, (c) and (d) are the output matching and isolation, and (e) and (f) are the amplitude imbalances (AI) and phase imbalances (PI) between the output ports. $\{W_m = 0.4\ mm,\ W_s = 0.24\ mm,\ L_s = 8\ mm,\ R_m = 1.5\ mm,\ R_s = 1.7\ mm,\ \theta_m = 165°,$ and $\theta_s = 150°\}$

for many applications, and not just for in-band full-duplex systems. But some of these applications might require isolation and matching at the outputs of the power dividers, which is the case for monostatic in-band full-duplex systems. In the light of this, we present, in the next section, wideband power dividers with enhanced output isolation and matching.

2.6.5 Power Dividers with Enhanced Isolation

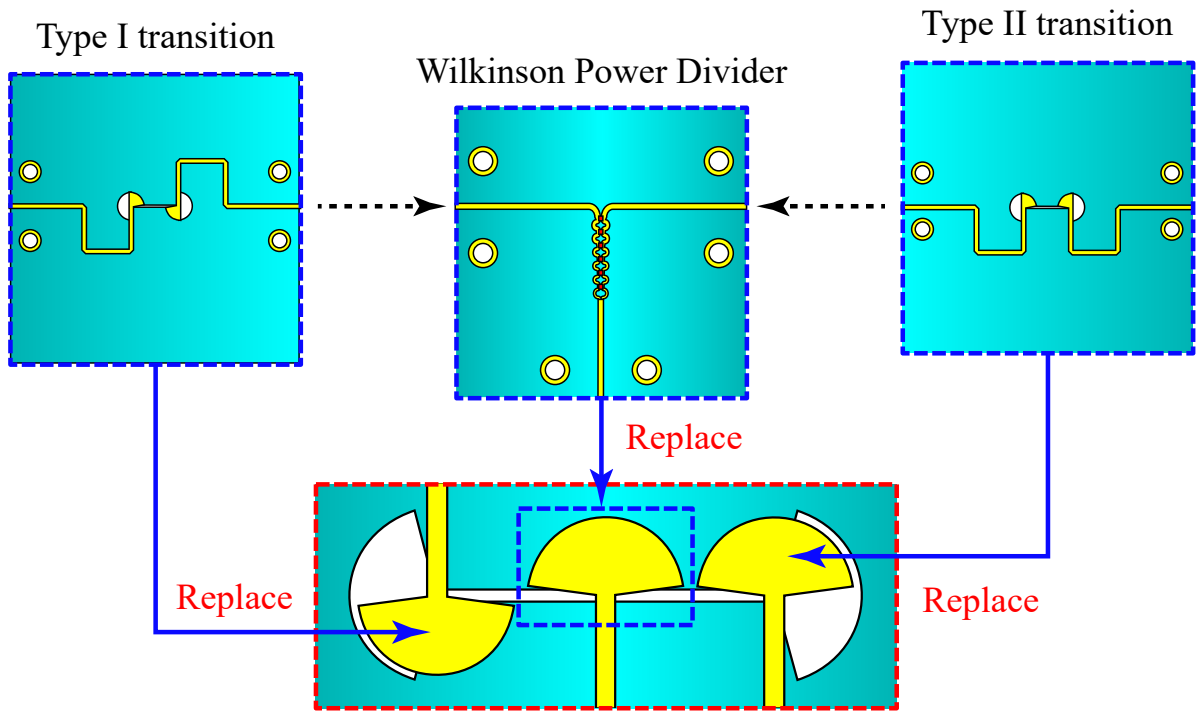

Figure 2.23: Evolution of the enhanced power dividers.

In order to have matching and isolation at the output ports of the previous power dividers, we need to make them lossy by introducing one or more resistive elements. So, if we compare them to a Wilkinson power divider, which has a resistor placed between the quarter-wavelength transmission lines, then we need to introduce a resistor between the two halves of the slotline, which is technically not feasible. Hence, we need a different approach to introduce the resistive elements. If we take a deeper look at the anatomy of the proposed power dividers, Figure 2.23, we can see that the middle transition is responsible for the wideband power division, while the lateral transitions are responsible for the wideband phase shifting. We need to introduce the resistive elements in the part that is responsible for the power division, but as mentioned earlier, it is not feasible. Thus, we can replace the middle transition with a Wilkinson power divider, which is characterized by the matching and isolation at its output ports. But the Wilkinson power divider, which is totally made of microstrip lines, cannot be directly connected to the slotlines of the lateral transitions. So, as a result, the lateral transitions can be replaced by two double transitions of Type-1 or Type-2, which are microstrip-compatible at all ports. Although Figure 2.23 only depicts the 180° out-of-phase power divider, however, the same approach can be applied also to the in-phase power divider. In fact, to obtain an in-phase power divider, two Type-1 or two Type-2 transitions need to be connected to the Wilkinson power divider, while, on the other hand, to implement a 180° out-of-phase power divider, one Type-1 and one Type-2 transitions need to be connected to the Wilkinson power divider. Both types of transitions were designed and optimized in a previous section, and they operate over an ultra-wide bandwidth. Now, all what we need to do is to implement an ultra-wideband Wilkinson power which can operate in the same frequency range of the transitions, and the best way to do this is to implement a

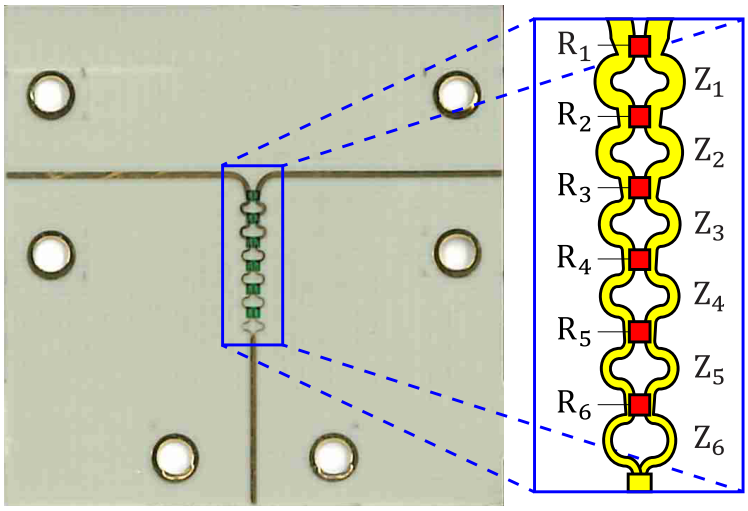

(a)

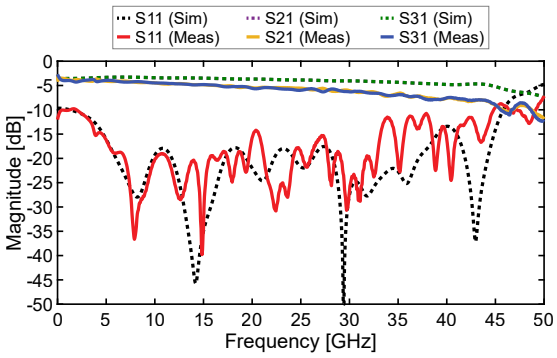

(b)

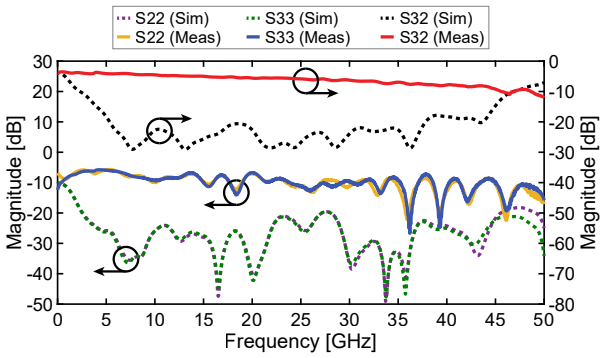

(c)

Figure 2.24: (a) picture of the fabricated 6-section Wilkinson power divider, and (b) and (c) are its simulated and measured S-parameters.{$Z_1 = 54\ \Omega$, $Z_2 = 59.1\ \Omega$, $Z_3 = 66.4\ \Omega$, $Z_4 = 75.3\ \Omega$, $Z_5 = 84.6\ \Omega$, $Z_6 = 92.6\ \Omega$, $R_1 = 675\ \Omega$, $R_2 = 500\ \Omega$, $R_3 = 315\ \Omega$, $R_4 = 200\ \Omega$, $R_5 = 120\ \Omega$, and $R_6 = 120\ \Omega$}

multi-section Wilkinson power divider.

A multi-section Wilkinson power divider (Figure 2.24) is composed of multiple couples of quarter-wavelength microstrip lines with gradually decreasing impedance steps from 100 Ω at the input microstrip line, and down to 50 Ω at the output microstrip lines. The gradual impedance steps ensure a smooth propagation of waves in the power divider over a wide bandwidth. Each couple of quarter-wavelength microstrip lines are then terminated with an isolation resistor with a specific value, the presence of the resistors in the circuit makes it lossy, and hence it can be matched and isolated at the output ports. Normally, no power should pass through the resistors as both microstrip lines carry the same voltage. So, theoretically, no power is actually lost in the resistors. Also, the bandwidth of the power divider is determined by the number of the quarter-wavelength sections, that is, if we want to increase the bandwidth of the power divider, we need to increase the number of sections, thus leading to an increase in the size of the power divider. Also, after a certain number of sections, the increase in the bandwidth becomes almost negligible, hence we need to wisely choose the minimum number of sections that can fit in our bandwidth.

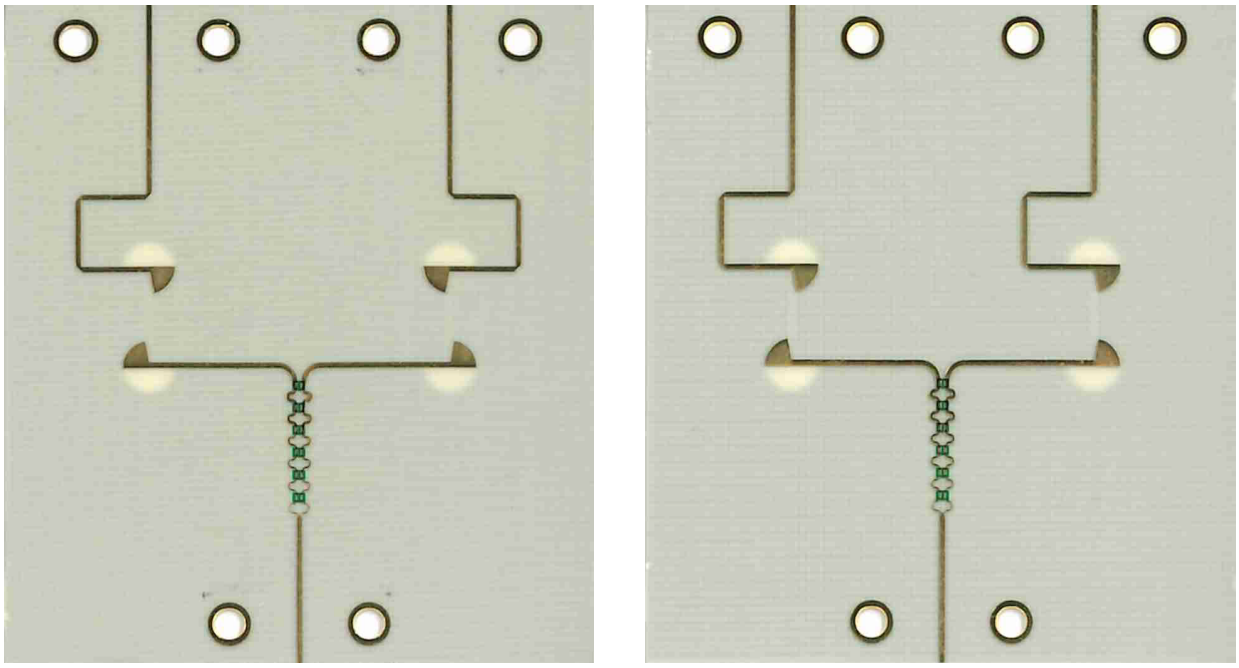

(a) (b)

Figure 2.25: Pictures of the fabricated (a) in-phase and (d) 180° out-of-phase power dividers, respectively.

Although, in our work, we are not constrained by any size specifications, and we prioritize bandwidth and isolation over size.

The design method of a multi-section Wilkinson power divider was studied by Cohn [235]. By following the guidelines laid in his paper, it turns out that at least a 6-section Wilkinson power divider is needed to cover the decade frequency range from 4 to 40 GHz. Based on this, we have calculated the impedance of each section and its corresponding resistor value; the calculated values can be found in the captions of Figure 2.24. As a first step, this calculated set of values is entered into an Advanced Design Systems (ADS) schematic to optimize and tune the structure, stressing mostly on the isolation between output ports. After that, a 3D simulation is performed in CST to confirm the results obtained in ADS, and then, full-wave optimization is performed to ensure maximum bandwidth and isolation. The actual size of the power divider is $8.6\ mm \times 1.8\ mm$ but it was built on a $30\ mm \times 30\ mm$ board for mechanical convenience. The measured S-parameters of the 6-section Wilkinson power divider indicate that the matching bandwidth, at the input port, is between 2 and 45 GHz, although we observe a worse matching compared to simulated results, especially at high frequencies where the mismatch comes, mainly, from the connectors and cables used in measurements. Also, we observe higher insertion loss in measurements due to the change in the imaginary part of the dielectric constant of the used substrate. Moreover, at the moment, there are no measurements available of the output ports matching and isolation due to technical issues and due to an extra delay in the delivery of the high-frequency resistors. However, simulated results indicate that good matching and at least 20 dB of isolation between the output ports can be obtained from 5 to 37 GHz, and at least 15 dB of isolation can be obtained between 4 and 44 GHz.

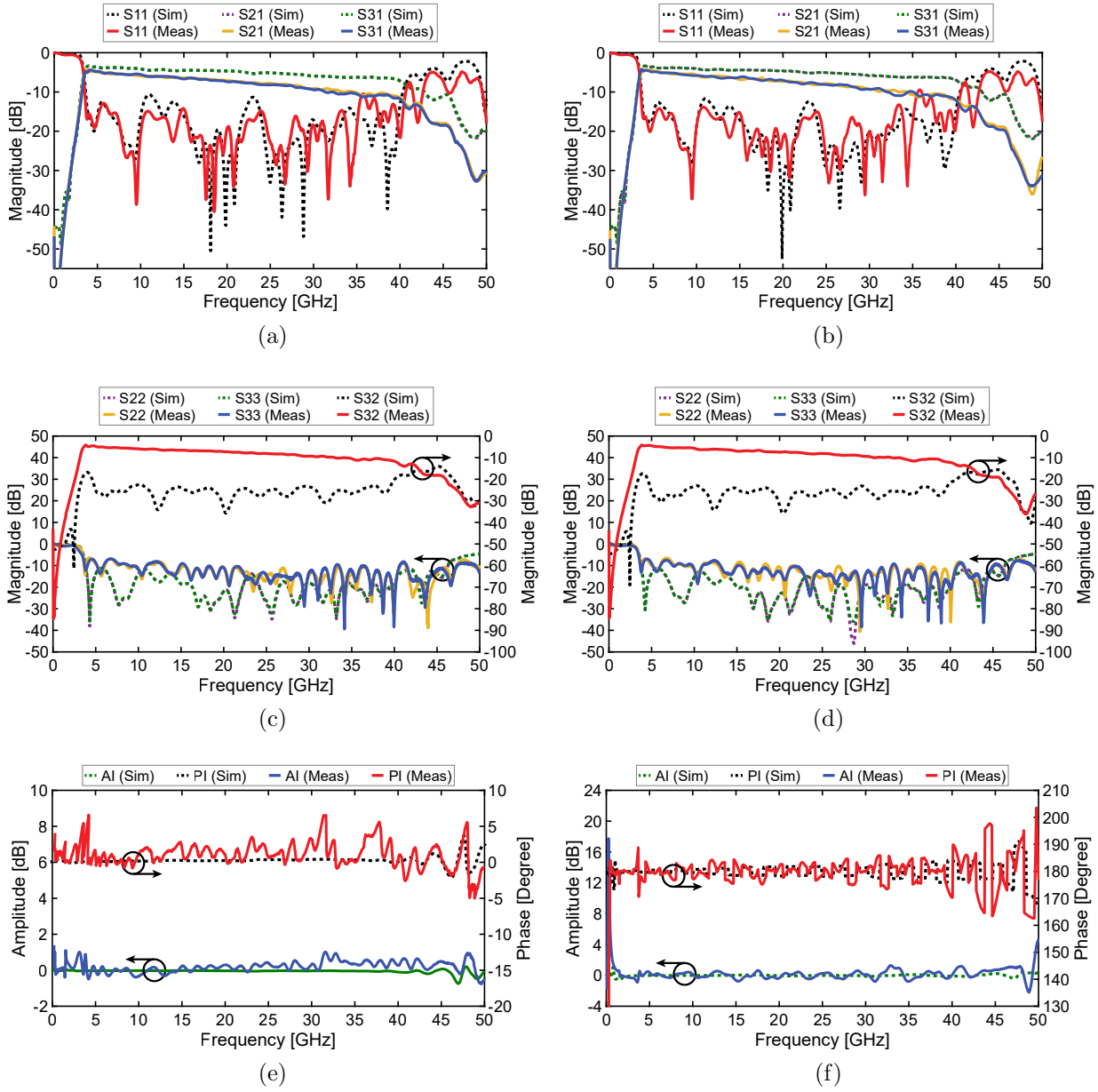

Figure 2.26: Simulated and measured S-parameters of the enhanced in-phase and 180° out-of-phase power dividers, respectively: (a) and (b) are the input matching and insertion losses, (c) and (d) are the output matching and isolation, and (e) and (f) are the amplitude imbalances (AI) and phase imbalances (PI) between the output ports.

As mentioned before, the enhanced in-phase power divider can be obtained by connecting the 6-section Wilkinson power divider to either two Type-1 or two Type-2 microstrip-to-slotline transitions, while the enhanced 180° out-of-phase power divider can be obtained by connecting the 6-section Wilkinson power divider to one Type-1 and one Type-2 transitions. Both types of power dividers are depicted in Figure 2.25. Transitions with reduced microstrip lines were used in this design to avoid any abnormal drop in the insertion loss of the circuits. Of course, there is no need to generate an in-phase power divider using this topology, instead, the 6-section Wilkinson power divider can be used directly as it exhibits lower losses and smaller size. However, if an application requires

using both in-phase and out-of-phase power dividers with similar performances, that is, if the application requires the same insertion loss in different branches of the system, then using the enhanced in-phase power divider with the enhanced balun may become vital.

The enhanced power dividers were also built on the same RO4003C substrate and they both occupy an area of 40 $mm \times 45$ mm. The simulated and measured S-parameters of both power dividers can be found in Figure 2.26. Both power dividers are well matched between 4 and 40 GHz, except for a small mismatch around 36 GHz for the out-of-phase power divider. Also, because of some technical issues, the output matching and isolation were not correctly measured, but in simulation, they exhibit the same isolation performance as the Wilkinson power divider over the targeted frequency band. Finally, the maximum amplitude difference between the two output ports is ± 1.2 dB and the maximum phase difference is $\pm 10°$. It seems that when the geometry of the power divider contains more bends in the microstrip lines, the phase and amplitude imbalances between the output ports become more severe.

2.7 Wideband Antennas

We define a wideband antenna as an antenna that has constant characteristics over a wide bandwidth; characteristics such as matching, gain, radiation pattern, beamwidth, and/or polarization. For our work, we are looking for a directive antenna with relatively high gain (> 5 dBi) and that is relatively compact, preferably planar, and that is easy to design and implement using the available technology. In general, antennas can be classified as traveling wave antennas and standing wave antennas. Traveling wave antennas, also called non-resonant antennas, use a traveling wave on a guiding structure as the main radiating mechanism, where the current that generates the radio waves travels through the antenna in one direction and the vast majority of the radiated power propagates also in that direction. This is in contrast to a standing wave (or resonant) antenna, such as monopoles or dipoles, in which the antenna acts as a resonator, with radio currents traveling in both directions, bouncing back and forth between the ends of the antenna, and thus forming a standing wave pattern along the antenna. The main advantage of traveling wave antennas is that since they are non-resonant, they often have a wider bandwidth than resonant antennas.

One family of traveling wave antennas is the frequency independent antennas described by Rumsey [447], which is a group of antennas that can maintain constant characteristics, theoretically, over an infinite bandwidth if their geometry is a function of angles, and if they are not constrained by size. This means that the characteristics of such antennas are invariant even if their sizes were scaled up or down. This family of antennas includes equiangular (or logarithmic) spiral antennas, log-periodic antennas, and sinuous antennas, which are balanced antennas that require a balanced feeding. The total size of the antenna determines the lowest frequency radiated by that antenna, and the minimum separation between the feed points determines the highest frequency. So, in practice, the actual realizable bandwidth depends on manufacturing constraints. Also, such antennas are characterized by their bidirectional radiation pattern, which might be suitable, mainly, for relaying applications, but for most applications, the back radiation needs to be suppressed by either adding an absorbent cavity or a reflective cavity at the back of the antenna,

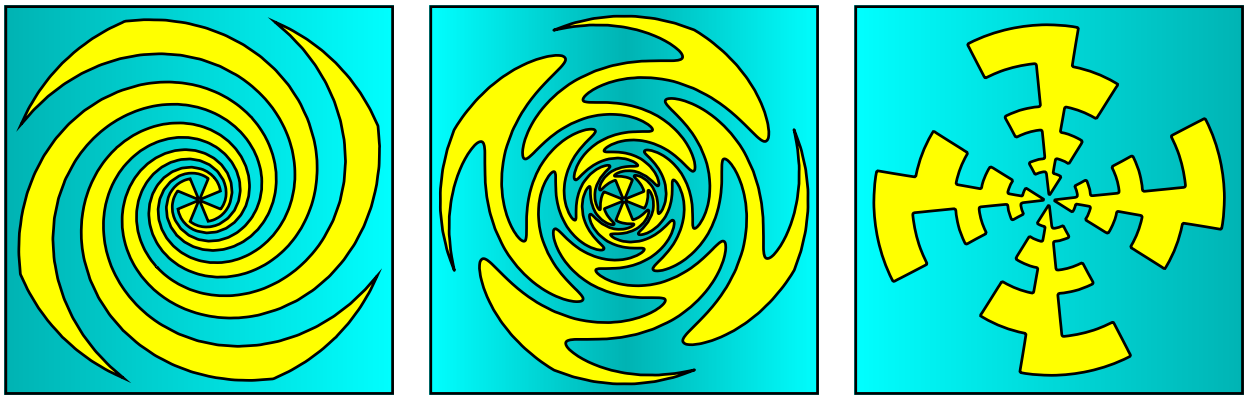

(a) (b) (c)

Figure 2.27: Four-arms (a) equiangular (logarithmic) spiral antenna, (b) sinuous antenna, and (c) log-periodic antenna.

which increases the size of the antenna and limits its bandwidth, and in some cases, it might also reduce the gain of the antenna.

In another work, Mushiake [448] argued that not only antennas defined by angles can be frequency independent, but also self-complementary antennas can have a frequency independent behavior regardless of the shape of the antenna, at least in terms of input impedance which is always equal to 60π Ω or approximately 188 Ω. Also, he argued and proved experimentally that the log-periodic structure is not frequency independent by nature, but it can be, if it was made self-complementary. Self-complementary antennas can be symmetric with respect to their centers or with respect to an axis. Center-symmetric antennas are necessarily balanced and have a bidirectional radiation pattern, while axially-symmetric antennas are not balanced, and they have a quasi-omnidirectional radiation pattern. In either case, a matching network is needed to match the antenna's high input impedance to a 50 Ω feed line.

More recently, several works showed that self-similar antennas can exhibit a frequency

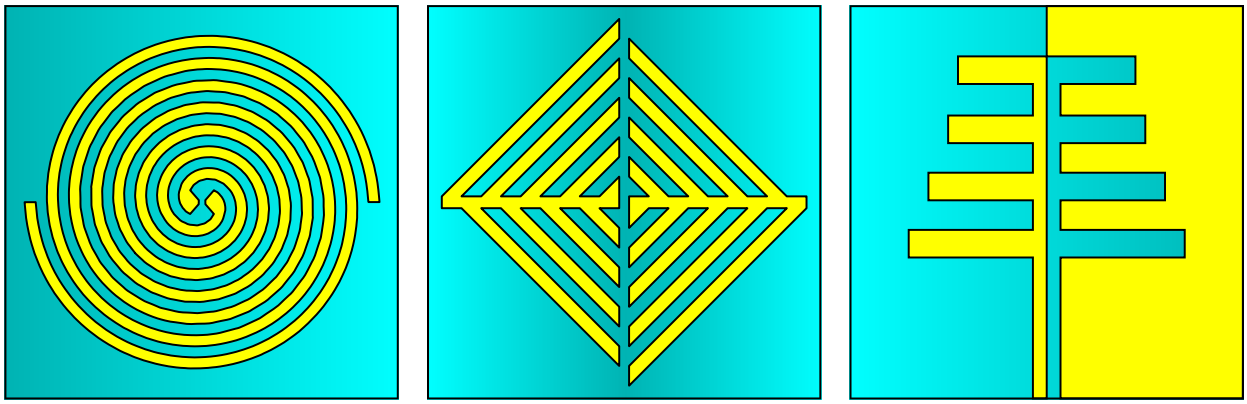

(a) (b) (c)

Figure 2.28: (a) self-complementary two arm Archimedean spiral antenna, (b) rectangular self-complementary antenna, and (c) axially symmetric self-complementary antenna.

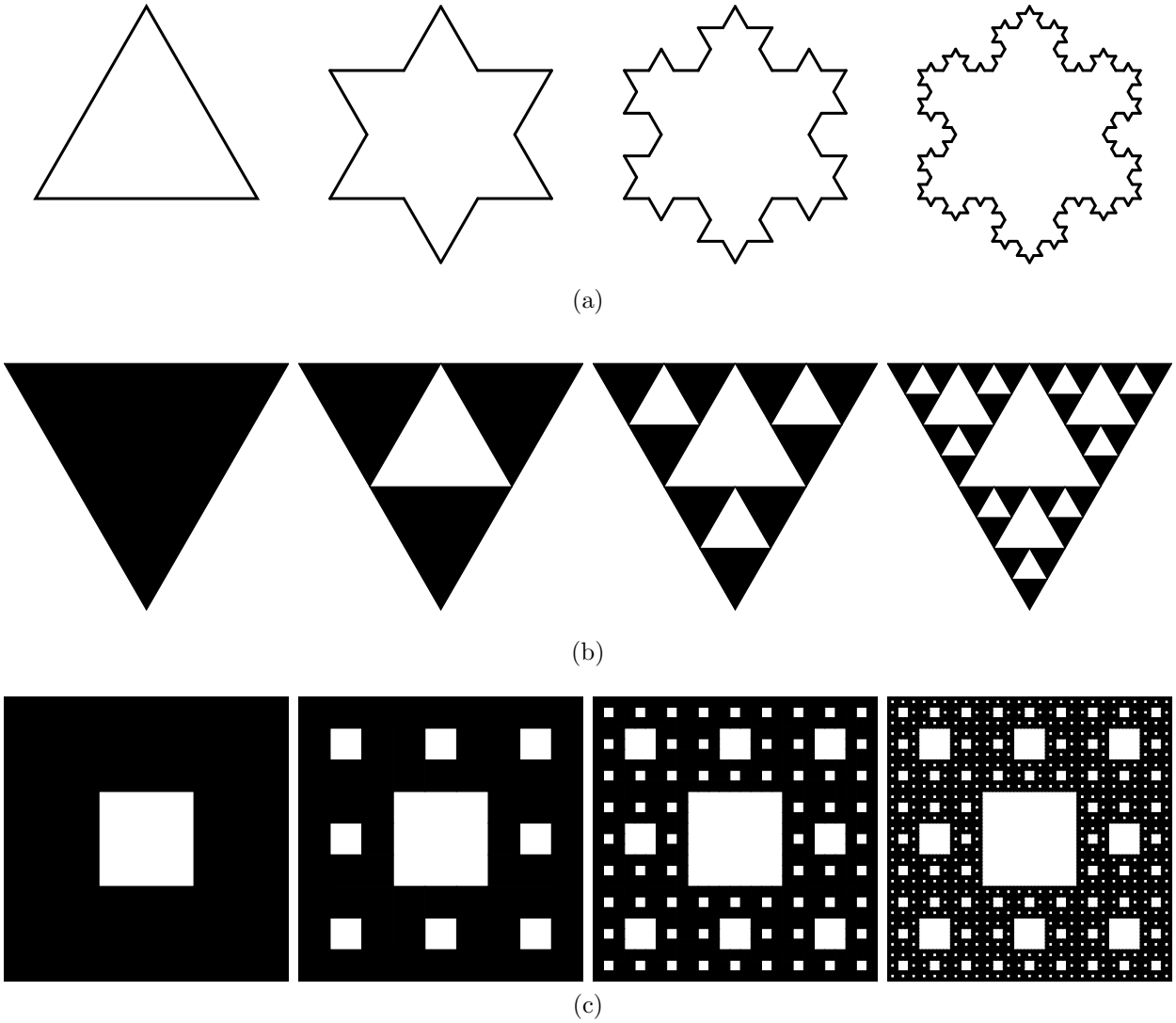

Figure 2.29: (a) Von Koch snowflake, (b) Sierpiński gasket, and (c) Sierpiński carpet.

independent behavior [449–451], mainly, because their geometry is invariant by size scaling. These antennas are designed using fractal geometries such as the Von Koch snowflake, the Sierpiński gasket, the Sierpiński carpet, the Minkowski island, etc. Such geometries are constructed by taking a conventional Euclidean shape and recursively repeating it in a certain pattern, and the shape of the final structure will look like as a part of itself; just like the Russian Matryoshka doll, in which the bigger doll contains a smaller replica. The other main advantage of fractal antennas is that their perimeter can be, theoretically, infinite by occupying a finite area, as opposed to Euclidean shapes that have their perimeters finite and directly proportional to the occupied area. This property permits antenna miniaturization. Fractal antennas can be constructed as monopoles suspended over a ground plane or monopoles with a defected ground plane, and, also, they can be constructed as balanced pairs similar to a bowtie antenna. In any case, their radiation pattern is omnidirectional.

In addition to the above, super wideband monopole antennas [452–454] (Figure 2.30) can provide an extremely wideband matching with a quasi-omnidirectional radiation

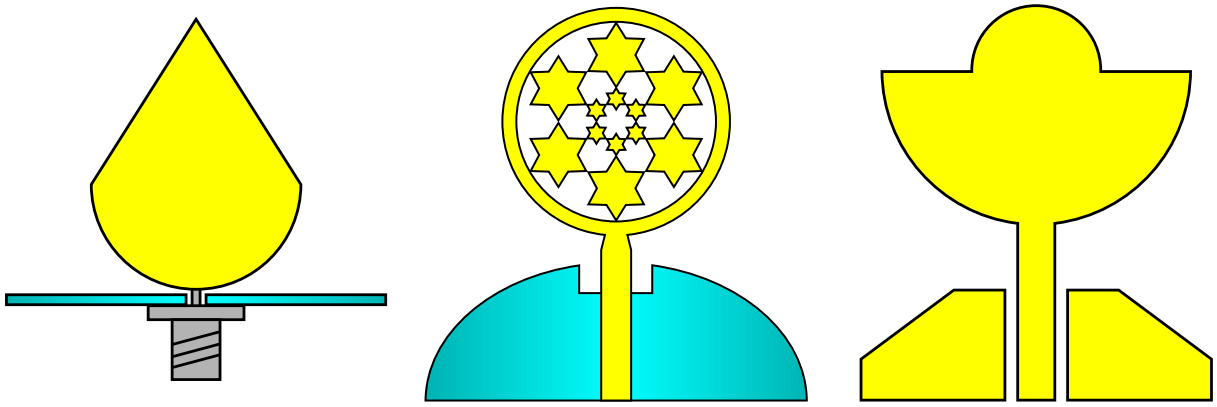

(a) (b) (c)

Figure 2.30: (a) suspended rain drop monopole antenna, (b) circumscribed fractal hexagrams monopole with semicircular ground plane, and (c) coplanar waveguide fed bowl-shaped monopole with a defected uniplanar ground plane.

pattern, although they do not follow any of the previously mentioned criteria of frequency independent antennas. They are usually implemented using two configurations: the monopole can be suspended above a ground plane, in this case the antenna will have a high profile and will need a mechanical support, or they can be implemented by taking a patch antenna and then reducing the size of its ground plane by a certain percentage. The monopole can be of any shape which can be manipulated for more bandwidth. Such antennas are mainly based on empirical approaches and, in most cases, there is no theoretical approach nor equations to support the obtained results or the design process.

(a) (b) (c) (d)

Figure 2.31: (a) Fermi-Dirac tapered slot antenna, (b) linearly tapered slot antenna, (c) constant width tapered slot antenna, and (d) exponentially tapered slot antenna or Vivaldi antenna.

Tapered slot antennas (Figure 2.31) are another family of traveling-wave antennas that does not follow any of the above-mentioned criteria, yet it can provide a frequency independent performance. Basically, these antennas are made of a slotline that is gradually tapered from a narrow width at the input to a wider width at the output, to match the wave impedance at the input to the air impedance at the output, this gives the antenna a directional end-fire radiation pattern with high gain. Several types of tapers can be used with different dimensions to obtain more gain, more bandwidth, smaller beamwidth, reduced side lobes, or more compactness. Conventionally, these antennas were fed by a coaxial cable, which affected the balance of currents on the edges of the slotline, which in turn affects the efficiency of the antenna. Later, microstrip-to-slotline transitions, coplanar waveguide-to-slotline transitions, and microstrip-coplanar stripline transitions were used to feed the antennas, this allows the direct fabrication and integration of the feed lines with the antennas in a coplanar or a uniplanar manner, which is a feature that is highly desirable for integrated antenna arrays.

Apparently, of all of the above-mentioned antennas, the best type of antennas that suits our specifications are the tapered slot antennas, mainly, because they are wideband, simple to design and implement, they are directive with a high gain, and also because these antennas can be fed by a microstrip-to-slotline transition, which we already have designed and optimized, and it operates over an ultra-wide bandwidth. We choose the exponentially tapered slot antenna, or the Vivaldi antenna, as the radiating element in our systems because, for a certain size, it can provide the widest bandwidth as compared to all other tapers, although it might have higher side lobes, wider beamwidth, or lower gain than the others. However, in this work, we are not concerned with implementing a super antenna with super characteristics, rather we only focus on showing that in-band full-duplex technology can be implemented over an ultra-wide bandwidth, regardless of the characteristics of the antenna. Later, the designer can work on enhancing specific characteristics of the system depending on his application requirements. In the light of this, in the next section we present a brief description of the design methodology of the Vivaldi antenna and its obtained performance.

2.7.1 The Vivaldi Antenna

The Vivaldi antenna is an exponentially tapered slot antenna that was proposed by Gibson [463], and it is characterized by its wideband matching, constant beamwidth, high gain, low side lobes, and a symmetric end-fire beam in the planes that are parallel and orthogonal to the antenna. The first prototype presented by Gibson achieved approximately 10 dBi gain and -20 dB side lobe level over an instantaneous frequency bandwidth extending from below 2 GHz to above 40 GHz. The Vivaldi antenna can theoretically achieve infinite bandwidth, but, in practice, the achievable bandwidth is limited by fabrication limitations and the availability of a wideband feeding structure. The Vivaldi antenna is depicted in Figure 2.32 and it consists of exponentially tapered slotline that is fed by microstrip-to-slotline transition, although it can be fed by other types of transitions. The dimensions of the slotline determines the bandwidth of operation of the antenna as well as the radiation characteristics. For instance, the minimum slotline width W_s determines the highest frequency that can be radiated by the antenna, while the maximum slotline width W_v, at the top of the antenna, and the length of the slotline

Ref.	Antenna	Frequency Range [GHz]	Matching Bandwidth	Radiation	Size [mm^3]
[455]	Equiangular spiral antenna	7.5 – 45	143%	Unidirectional broadside using back-reflector	$20 \times 20 \times 22$
[456]	Log-periodic dipole array	0.76 – 18	184%	Directional end-fire	$168 \times 132 \times 1.5$
[457]	Self-complementary spiral antenna	2 – 18	160%	Unidirectional broadside using back-reflector	$50 \times 50 \times 17.5$
[458]	Self-complementary quasi-elliptical monopole	1.25 – 50	190%	Omnidirectional	$31 \times 26 \times 1.6$
[459]	Von Koch fractal monopole with defected ground plane	3.1 – 12.7	122%	Omnidirectional	$31 \times 28 \times 1.6$
[460]	CPW-fed circle inscribed hexagonal fractal monopole	2.75 – 50	179%	Omnidirectional	$28 \times 27 \times 1.6$
[461]	Circumscribed hexagrams monopole with defected ground plane	4.6 – 50	166%	Omnidirectional	$19.7 \times 19 \times 1.6$
[462]	Leaf-shaped monopole suspended over substrate	1.3 – 29.7	183%	Omnidirectional	$80 \times 80 \times 68.34$
[463]	Vivaldi antenna	2 – 40	181%	Directional end-fire	–

Table 2.7: Examples of wideband Antennas.

determine the lowest frequency. Moreover, as the length of the slotline increases, the gain of the antenna increases, and the beam becomes narrower.

The two exponential tapers of the Vivaldi antenna can be expressed by the following equations:

$$y = Ae^{\alpha x} + B \qquad \textit{and} \qquad y = -Ae^{\alpha x} - B \tag{2.10}$$

where x is the position across the length of the antenna and y is the position across the width of the antenna. Also, we have:

$$A = \frac{y_2 - y_1}{e^{\alpha x_2} - e^{\alpha x_1}} \qquad \textit{and} \qquad B = \frac{y_1 e^{\alpha x_2} - y_2 e^{\alpha x_1}}{e^{\alpha x_2} - e^{\alpha x_1}} \tag{2.11}$$

with $x_1 = 0$, $x_2 = L_v$, $y_1 = W_s/2$, $y_2 = W_v/2$, and α is the exponential growth rate of the taper. The designer has the freedom to set the value of the growth rate, in [464] it is stated that a higher growth rate gives a higher matching bandwidth, however, our simulations contradict this statement. In fact, our simulations showed that the growth rate has an optimum value for which the obtained bandwidth is maximum, and any value above or below the optimum value reduces the bandwidth. The growth rate in Gibson's

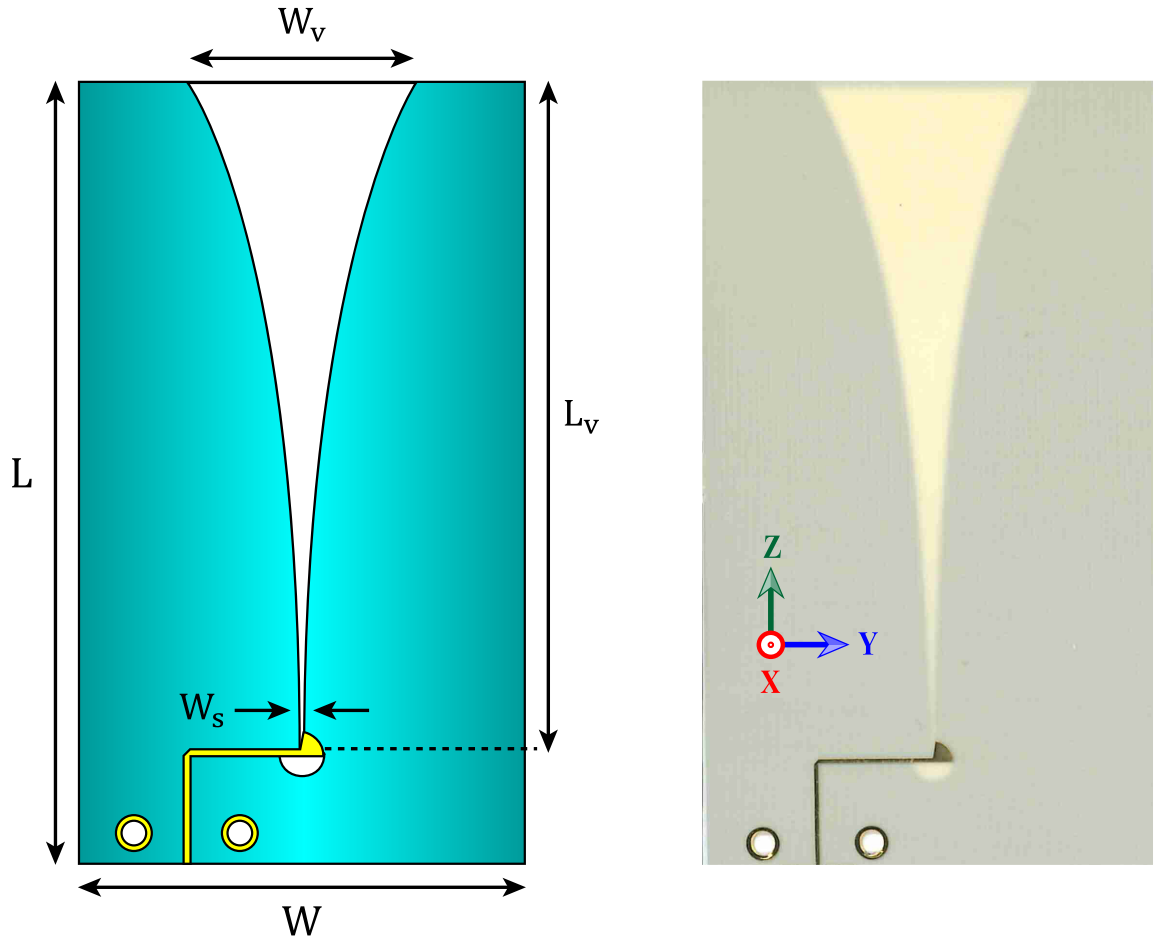

(a) (b)

Figure 2.32: (a) illustrative drawing of the designed Vivaldi antenna and (b) a picture of the fabricated antenna. $\{W = 40\ mm,\ L = 70\ mm,\ W_s = 0.1\ mm,\ W_v = 20\ mm,\ L_v = 60\ mm,$ and $\alpha = 0.05\}$

work was set to 0.052, and our simulations showed that this value is the optimum value for maximum bandwidth. Also note that the value of the growth rate affects the beamwidth.

Finally, the length of the slotline taper should be greater than a guided wavelength at the minimum operating frequency, and that the maximum slotline width should be greater or equal to the guided wavelength at the center frequency, and at the same time it should be less than or equal to half the guided wavelength at the lowest frequency. The dimensions of the fabricated antenna were chosen to fit in the bandwidth of the feeding microstrip-to-slotline transition, which operates from 4 GHz to 45 GHz. For this reason, the maximum slot width was set to a half wavelength at 4 GHz ($W_v \approx 20\ mm$), and the length of the slotline taper was set to one and half wavelength at 4 GHz ($L_v \approx 60\ mm$). Although it is sufficient to set the slotline length to one wavelength at the lowest frequency, here we used an extra half wavelength to get a better matching value at the lower frequencies, this also means that the radiated beamwidth will be narrower.

The simulated and measured return loss and gain of the fabricated Vivaldi antenna are depicted in Figure 2.33, as well as radiation pattern plots at 15 GHz. As expected,

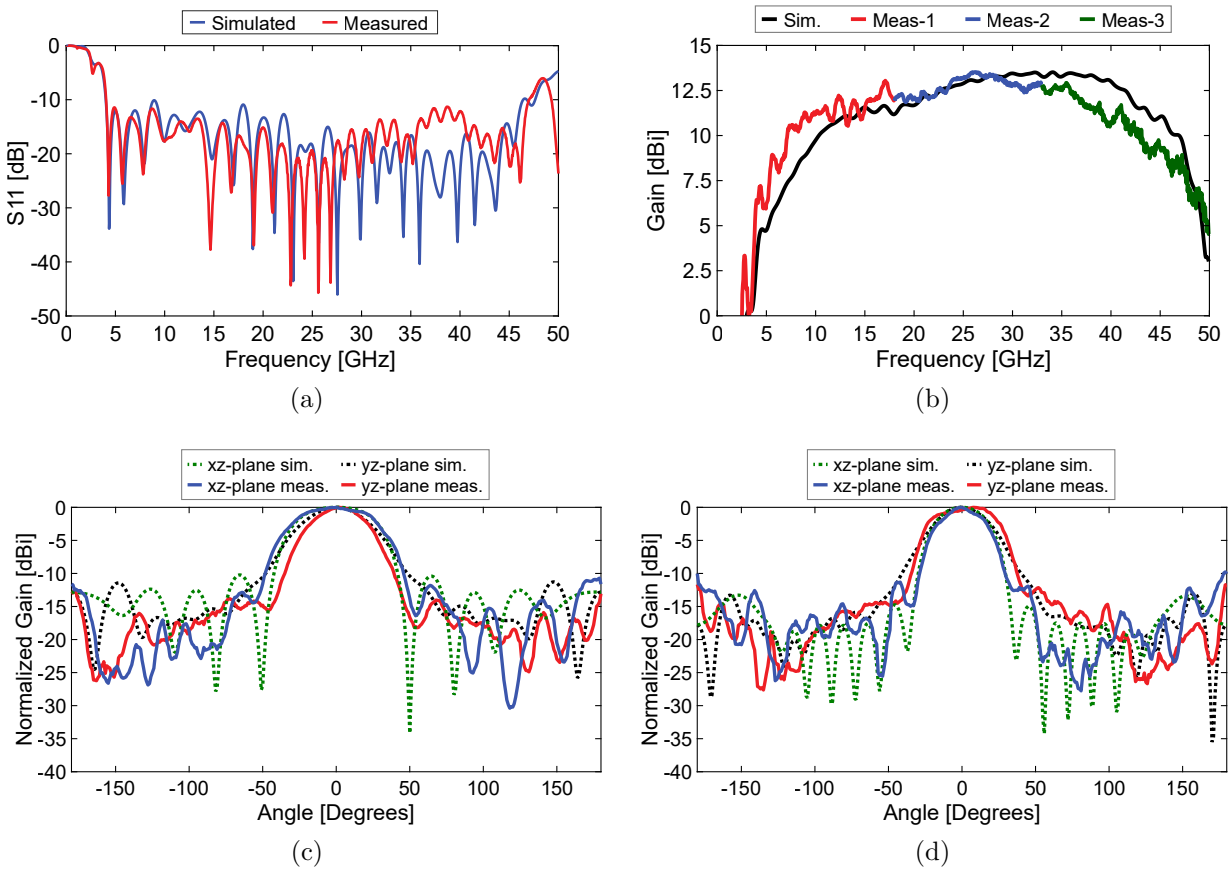

Figure 2.33: Simulated and measured (a) matching and (b) gain of the Vivaldi antenna. And radiation pattern plots at (c) 10 GHz and (d) 15 GHz, respectively.

the antenna has a matching bandwidth that is slightly wider than that of the microstrip-to-slotline transition (4 – 47 GHz), where the minimum gain in this bandwidth is 5 dBi and the average gain is about 11.15 dBi. Note that, in order to measure the gain of the antenna over this ultra-wide bandwidth we needed to use three reference antennas: the first covers the frequency range from 2 to 18 GHz, the second one from 18 to 33 GHz, and the third one from 33 to 50 GHz. The three measured gains using the three different reference antennas are plotted in different colors (red, blue, and green). There is a good agreement between the simulated and measured gains of the antenna, although we can notice a slightly higher gain in measurements at lower frequencies, and a slightly lower gain at higher frequencies. Also, the radiation pattern plots at 10 and 15 GHz show that the radiated beam is highly directive, and that the beamwidth in the xz-plane is less than 40° and less than 50° in the yz-plane. Moreover, the level of side lobes is -10 dB below the level of the main lobe.

2.8 Conclusion

At the end of chapter 1 and at the beginning of this chapter, we have stated that the best self-interference cancellation technique to implement a wideband in-band full-duplex system, with a directive radiation pattern, is the near-field cancellation technique, which

requires at least four wideband antennas and two wideband 180° out-of-phase power dividers. Following these requirements, we have shown that there are two main approaches to implement a wideband 180° out-of-phase power divider: either by cascading a wideband in-phase power divider with a wideband phase shifter or a wideband phase inverter, or by using wideband hybrids, which might, also, contain phase shifters or phase inverters. So, based on this, we have demonstrated a broad review of the reported wideband in-phase power dividers, phase shifters, and phase inverters. In fact, it turns out that the T-junction power divider and the multi-section Wilkinson power divider are the two best devices to implement a wideband in-phase power divider. The T-junction is more compact and simpler to design but lacks isolation and matching at the outputs, while the multi-section Wilkinson power divider can provide isolation and matching at the outputs, but it is more complex to implement and occupies a larger area. Also, it turns out that phase inverters can provide more bandwidth than phase shifters, and they are more suitable for high-frequency applications.

After that, we presented the different implementations of wideband 180° out-of-phase power dividers based on each approach, and it turns out that there are three devices that can operate as a 180° out-of-phase power divider over a decade of bandwidth. The first device is the 180° tapered-line coupler which occupies a relatively large area but can provide a good amount of isolation and can be implemented using striplines. The second device is formed by cascading a multi-section Wilkinson power divider with a double balanced-unbalanced transition, which can be more compact than the 180° hybrid and provide a good isolation level and matching at the output ports but can be more complex to design and implement. And the third device is the balanced-unbalanced T-junction, which is the simplest and the most compact device, but lacks isolation and matching at the outputs. Nonetheless, as bistatic full-duplex systems do not require isolation between the outputs of the out-of-phase power dividers, we decided to use a balanced-unbalanced T-junction for our application.

In particular, we chose the microstrip-to-slotline T-junction to implement our wideband 180° out-of-phase power divider, which has proved to operate over an extremely wide bandwidth with an extremely compact size, and it does not require any complex fabrication techniques such as vias or wire bonds. For this reason, we demonstrated the theoretical background of microstrip-to-slotline transitions followed by a parametric study, to show how each parameter of the transitions affects their performance. Next, we presented two types of double transitions, one can perform phase inversion while the second cannot. Both transitions were fabricated on RO4003C substrate and they occupy an area of $12 \times 4\ mm^2$. Their measured S-parameters show a good matching over the 4 – 45 GHz band, but we noticed an unusual insertion loss dip at the middle of the band, which was caused by the overlap between the microstrip stub and the slotline stub. To eliminate this dip, we proposed to use a microstrip stub with reduced size to reduce the overlap with the slotline stub.

We also demonstrated the wideband power dividers based on the microstrip-slotline T-junction, which use three microstrip-to-slotline transitions to perform wideband power division and wideband phase inversion. The power dividers were fabricated on the same RO4003C substrate and they also occupy an area of $12 \times 4\ mm^2$. Their measured S-parameters indicate that they can operate from 3.2 to 42.3 GHz with ±1 dB and ±7° of amplitude and phase imbalances, respectively. Of course, such power dividers lack

isolation and matching at the output ports, so we proposed better power dividers with enhanced output matching and isolation. The enhanced power dividers are composed of a multi-section Wilkinson power divider and two double microstrip-to-slotline transitions, and they occupy a total area of $40 \times 45\ mm^2$. Their measured S-parameters show that they have good matching between 4 and 40 GHz with ± 1.2 dB and $\pm 10^\circ$ of amplitude and phase imbalances, respectively, and simulations indicate that more than 15 dB of isolation can be obtained in the band of operation.

Finally, we presented a review of wideband antennas, and then we chose the Vivaldi antenna as the radiating element in our system due to its directive end-fire radiation pattern, wideband performance, high gain, simplicity of design and implementation, and due to the fact that it is fed by a microstrip-to-slotline transition, which we have already designed, optimized, and implemented. After that, we demonstrated the design methodology of the Vivaldi antenna and its parameters, and then, we showed the S-parameters of the fabricated antenna, which occupies an area of $70 \times 40\ mm^2$ and can operate with a 11.15 dBi average gain from 4 to 47 GHz.

Chapter 3

System Implementation

Contents

3.1 Introduction

After presenting the theoretical context of wideband full-duplex systems in Chapter 1 and designing and implementing some wideband devices in Chapter 2, we finally arrive at the stage where we will combine our knowledge and designs to implement the final full-duplex systems. Those systems will be based on the near-field cancellation technique which manages to achieve self-interference by canceling the transmitted electric fields in the near-field region, where the receive antennas are placed, while allowing the transmitted electric fields to recombine in the far-field region which preserves the radiation characteristics of the system. In fact, this chapter presents three different implementations of the ultra-wideband full-duplex antenna systems which are all based on the near-field cancellation technique but with slightly different configurations and characteristics:

1. The first system is a printed circuit board (PCB) system based on the antennas and baluns that were presented in the previous chapter. Also, for this system, a special 3D-printed support is specifically designed to hold and maintain the antennas together. This system is found to be mechanically fragile due to the low substrate thickness and suffers from a radiation problem where two grating lobes are noticed in its radiation pattern alongside the main lobe.

2. The second system configuration is similar to the first one but uses 3D-printed metalized Vivaldi antennas which operate over a narrower bandwidth but are more solid and more durable than the PCB antennas. The 3D-printed antennas are provided with coax-to-slot transitions as a way of feeding which replaces the microstrip-to-slotline transition in the planar antennas. And then the radiation of the system is improved by partially reducing the size of the antennas which helps in reducing the grating lobes level.

3. The third system is formed of a dual-polarized Vivaldi array that is made from Aluminium-machined antennas. The proposed antenna system can transmit and receive simultaneously two orthogonal polarizations while operating in full-duplex mode. The dual-polarized antennas are equipped with novel feeding networks: the first one is simpler and less demanding but causes some imbalances in the radiation pattern of the antenna, while the second feeding is more complex and have more requirements but can restore the balance to the radiation patterns. Both feedings will be presented and compared with one another and with the conventional feeding techniques.

In the following sections, we will explain how each system was designed, built, and measured, what the obtained results are, what the drawbacks of the presented systems are, and what solutions we proposed to overcome these problems. But before going into all of that, it is necessary to present, mathematically, a description of the principle of operation of the near-field cancellation technique.

3.2 Near-Field Cancellation: Principle of Operation

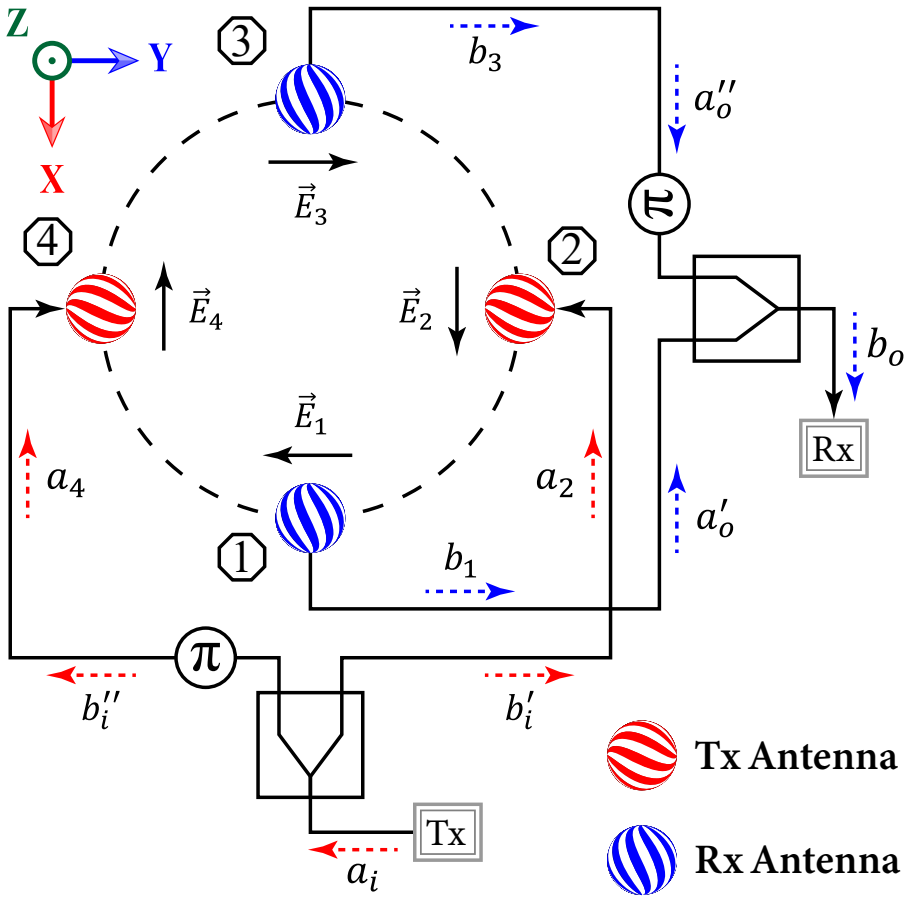

Figure 3.1: A schematic of the system showing antenna placement and numbering, flow of power waves, and the original electric fields radiated by each single antenna before connecting them to the baluns.

The electrical and physical behavior of the near-field cancellation technique were discussed, in detail, in Chapter 1, but in this section, we try to validate and describe its principle of operation by a mathematical approach. This approach applies to all the systems that are presented in this chapter. So we begin by recalling the basic system configuration required by the near-field cancellation technique, which is depicted again in Figure 3.1. The system is composed of four antennas which are placed on the perimeter of a circle of a fixed radius and are sequentially rotated by 90° from one another, thus forming two diametrically opposite pairs of antennas, where each pair is orthogonal to the other. One pair is used to transmit while the other is used to receive. Then each pair of antennas is fed signals of equal amplitudes and 180° out of phase by using baluns. Now, to explain the principle of operation of the proposed system, two approaches are adopted [112]: an inter-port approach that describes the very low power coupling between the input and output ports of the Tx and Rx baluns, and a field approach that presents the electric field behavior in the far-field region where the electric fields combine constructively.

Inter-Port Approach: in order to develop this approach, we find that it is most suitable to work with power waves, where a_n denotes the power wave incident at port n

and b_n denotes the power wave reflected from that port, and accordingly, the total powers carried by each wave are equal to $|a_n|^2$ and $|b_n|^2$ respectively. The flow of power waves in the system is depicted in Figure 3.1 assuming ideal conditions where no mismatch exists between the system components.

Now, the output power (P_o) at the output of the Rx balun can be expressed in terms of power waves coming from the receive antennas 1 and 3 as follows:

$$P_o = |b_o|^2 = |a'_o + a''_o e^{j\pi}|^2 = |b_1 + b_3 e^{j\pi}|^2 \tag{3.1}$$

Also b_1 and b_3 can be expressed in terms of the power waves incident on the transmit antennas 2 and 4 as follows:

$$b_1 = S_{12}a_2 + S_{14}a_4 \tag{3.2}$$

$$b_3 = S_{32}a_2 + S_{34}a_4 \tag{3.3}$$

Similarly, a_2 and a_4 can be written in terms of the power wave a_i incident at the input of the Tx balun:

$$a_2 = b'_i = \frac{\sqrt{2}}{2}a_i \tag{3.4}$$

$$a_4 = b''_i = \frac{\sqrt{2}}{2}a_i e^{j\pi} \tag{3.5}$$

By substituting (3.4) and (3.5) in (3.2) and (3.3) we obtain:

$$b_1 = \frac{\sqrt{2}}{2}S_{12}a_i + \frac{\sqrt{2}}{2}S_{14}a_i e^{j\pi} = \frac{\sqrt{2}}{2}a_i(S_{12} + S_{14}e^{j\pi}) \tag{3.6}$$

$$b_3 = \frac{\sqrt{2}}{2}S_{32}a_i + \frac{\sqrt{2}}{2}S_{34}a_i e^{j\pi} = \frac{\sqrt{2}}{2}a_i(S_{32} + S_{34}e^{j\pi}) \tag{3.7}$$

Finally, by substituting (3.6) and (3.7) in (3.1) we can obtain the output power (P_o) in terms of the input power (P_i):

$$\begin{aligned} P_o &= \left| \frac{\sqrt{2}}{2}a_i(S_{12} + S_{14}e^{j\pi}) + \frac{\sqrt{2}}{2}a_i(S_{32} + S_{34}e^{j\pi})e^{j\pi} \right|^2 \\ &= \frac{1}{2}|a_i|^2 \left| S_{12} + S_{14}e^{j\pi} + S_{32}e^{j\pi} + S_{34}e^{j2\pi} \right|^2 \\ &= \frac{1}{2}P_i \left| S_{12} - S_{14} - S_{32} + S_{34} \right|^2 \end{aligned} \tag{3.8}$$

Equation (3.8) implies that if $S_{12} = S_{14}$ and $S_{32} = S_{34}$, then the power coupled from the input port of the system to the output port will be equal to zero. This means that if the Rx antennas are placed along the perpendicular bisector of the Tx antennas, then infinite isolation is, theoretically, obtained between them. This conclusion holds only if the antennas are placed and aligned precisely and if the baluns operate ideally, that is if the two output signals of each balun are of equal amplitudes and 180° out-of-phase. Nonetheless, in practice, there will be slight misplacements of antennas and imbalances in the amplitude and phase of the baluns' output signals, thus the isolation between the input and the output ports of the system is expected to decrease.

Field Approach: Assuming that the antennas are not connected to the baluns and that the antennas are linearly polarized, then each individual antenna element radiates a

linearly polarized electric field of magnitude E_0. The orientation of the individual electric fields are also shown in Figure 3.1 and they can be expressed as follows:

$$\vec{E}_1 = E_0 e^{j\pi} \vec{y} \tag{3.9}$$

$$\vec{E}_2 = E_0 \vec{x} \tag{3.10}$$

$$\vec{E}_3 = E_0 \vec{y} \tag{3.11}$$

$$\vec{E}_4 = E_0 e^{j\pi} \vec{x} \tag{3.12}$$

Now, if the baluns are connected to the antennas, then the Tx and Rx electric fields can be described as follows:

$$\vec{E}_{Tx} = \vec{E}_2 + \vec{E}_4 e^{j\pi} = 2E_0 \vec{x} \tag{3.13}$$

$$\vec{E}_{Rx} = \vec{E}_1 + \vec{E}_3 e^{j\pi} = 2E_0 e^{j\pi} \vec{y} = -2E_0 \vec{y} \tag{3.14}$$

Equation (3.13) implies that the electric fields of the two transmit antennas will combine constructively in the far-field region and equation (3.14) implies the same observation for the receive antennas. However, this conclusion only holds if each two opposite antennas are symmetrically rotated with respect to the center of symmetry of the system, i.e. their feeding lines are oriented in opposite directions, and if the antennas are fed signals that are 180° out-of-phase. The antenna rotation (or feeding line opposite orientation) condition is especially critical, otherwise, electric fields will combine destructively in the far-field, which creates a far-field null, and thus the system will not be able to transmit or receive in the direction of this null.

Note that if the system is not symmetric, that is, if the number of transmit and receive antennas is not the same or if they are fed differently, differences between the transmit and receive far-field radiation patterns will emerge, thus it is extremely favorable to maintain high symmetry in the system. For this same reason, the transmit and receive antennas should be placed at the same distance away from the center of symmetry of the system, that is, they should be placed on a circle and not an ellipse. The antennas can be tangent or normal to the circle or could form any angle with the circle in general and can still achieve the same level of self-interference cancellation, however, this affects the total size of the system and the orientation of the radiation pattern. In addition to that, significant grating lobes can be observed in the far-field radiation pattern if the separation between the opposite antennas is greater than a half-wavelength at a certain frequency.

3.3 PCB System

The first wideband full-duplex system in this chapter uses of the printed antennas and baluns that were designed in Chapter 2. The system is depicted in Figure 3.2 where the substrates were omitted for better clarity. To implement near-field cancellation, four Vivaldi antennas are placed on the perimeter of a circle and sequentially rotated by 90° around its center, and then they are connected to the microstrip-to-slotline baluns using phase-paired cables. In this case, the antennas are tangent to the circle and thus they form a box-like shape, though they can be placed normal to the circle and form a cross-like shape as in Figure 3.5(a) and still obtain the same system performance. But for now we are going to stick with the box configuration because it is more compact. Moreover,

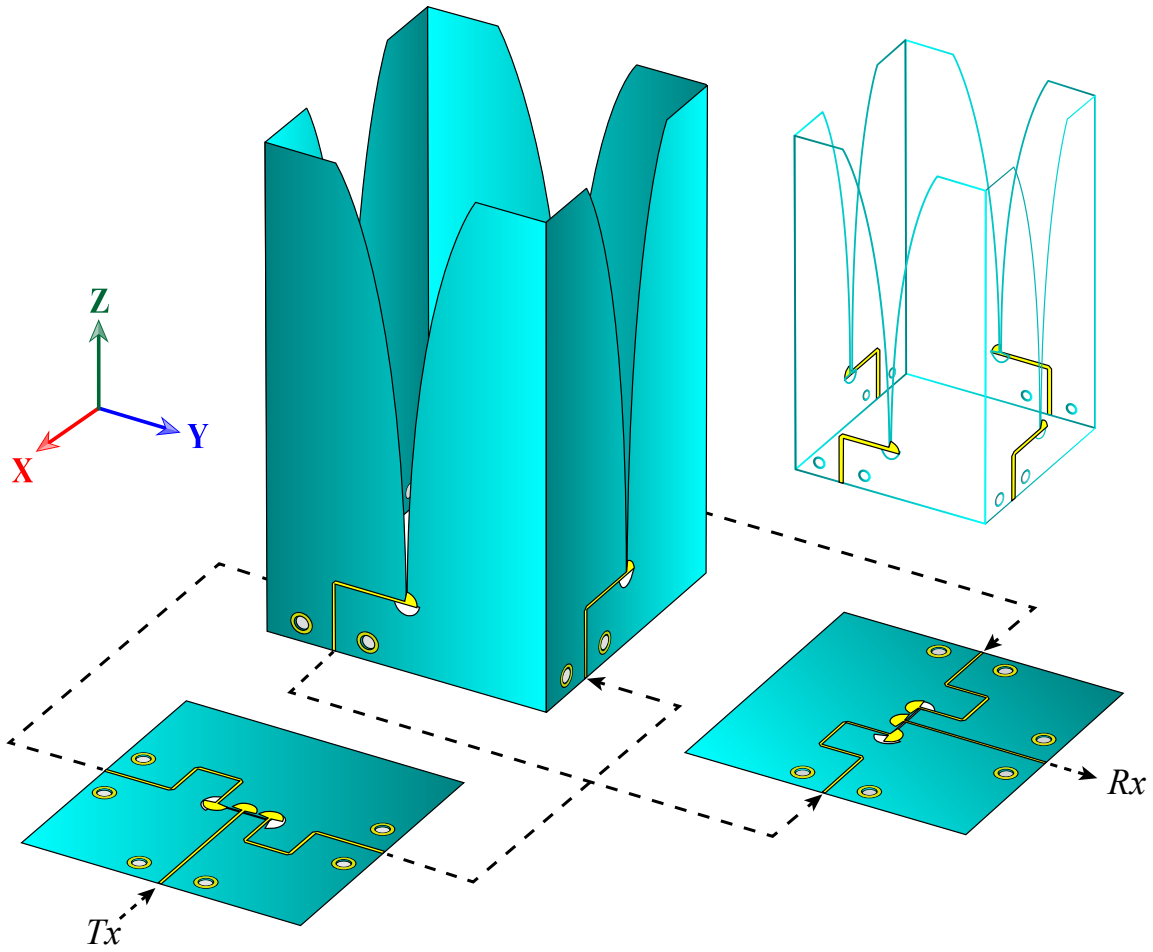

Figure 3.2: An illustration of the proposed wideband in-band full-duplex system with 4-element Vivaldi array and two microstrip-to-slotline baluns, and in the background a transparent view of the Vivaldi array showing the position and orientation of the microstrip feed lines.

recall that in order to avoid a null in the far-field region the feeding lines of the opposite antennas need to be oriented in opposite directions, otherwise the electric fields will fail to recombine in the far-field region. The orientation of the feeding microstrip lines of the Vivaldi antennas is shown in the background image in Figure 3.2, where the antennas were made translucent, also, for better clarity.

3.3.1 System Assembly

As mentioned before, in order to achieve self-interference cancellation and ensure proper system performance, it is of great importance to preserve a high symmetry when assembling the system, that is, the antennas should be placed exactly at the same distance away from the center of symmetry. While it is easy to place the antennas precisely and symmetrically in a simulation environment, yet, in practice it cannot be guaranteed. Moreover, it was noticed that the fabricated antennas tend to bend naturally due to the low thickness of the used substrate (203.2 μm), which also contributes to the asymmetry of the system. Also, the thickness of the substrate makes them very fragile and prone to fracturing, mainly, due to the tension exerted by the feeding cables and connectors. To

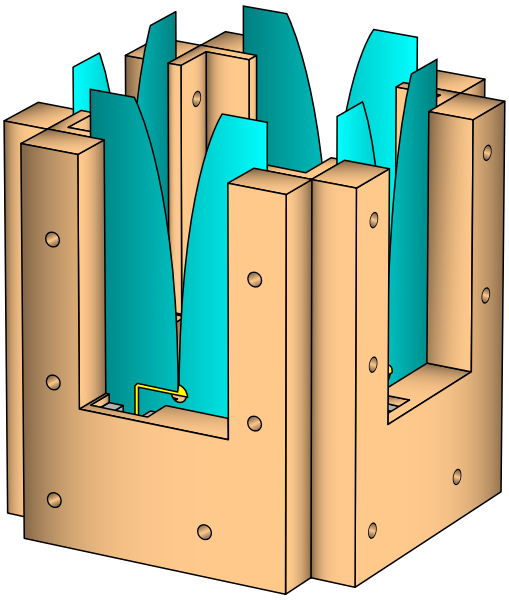

(a)

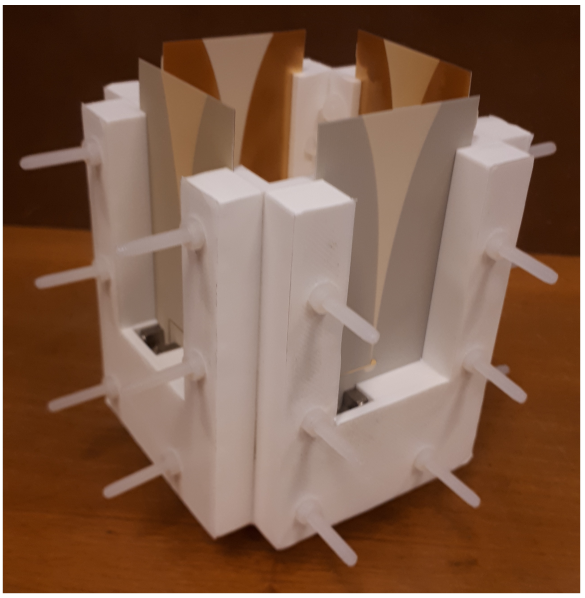

(b)

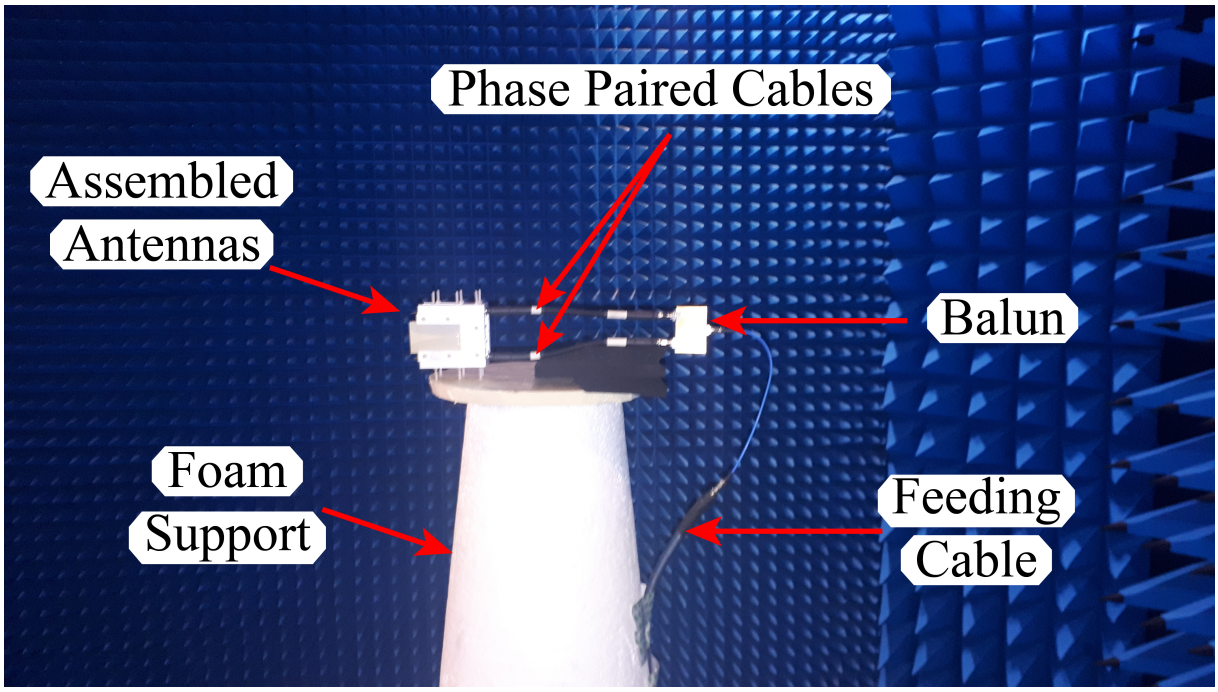

(c)

Figure 3.3: (a) An illustration and (b) a picture of the antenna assembly in the 3D-printed support and (c) system measurements in the anechoic chamber.

resolve those mechanical issues, a 3D-printed support is designed and fabricated to ensure precise antenna placement, to reduce antenna bending and to hold it fully erect, and to absorb mechanical tension from the feeding cables and connectors.

The 3D-printed support is shown in Figure 3.3 with the Vivaldi antennas installed in it. The support is made of the synthetic plastic polymer Polyvinyl-Chloride (PVC) with $\varepsilon_r \approx 3$, and Polytetrafluoroethylene (PTFE, $\varepsilon_r \approx 2.1$) screws are used to fix all the

printed parts together. The support is designed such that it only grasps the edges of the antennas and is kept sufficiently below the top of the antenna to ensure that it does not affect its matching or performance. Before installing the antennas inside the 3D-printed support, Southwest 2.92 mm connectors are mounted on all devices, and four Keysight N5448B phase-paired cables (± 5 *ps* skew) are used to connect the antennas to the baluns. Then, finally, the two-port measurements are made with Rhode&Schwarz ZVA67 vector network analyzer.

3.3.2 System Performance

The simulated and measured characteristics of the system are depicted in Figure 3.4. Note that simulations were done taking into account the PTFE screws and the 3D-printed support, which was modeled using a lossless dielectric material having $\varepsilon_r = 3$. Also, simulations take into account the extra separation distance between the antennas as per the fabricated design in Figure 3.3(b). Moreover, the simulated S-parameters of the system were obtained by combining, in a 2D-schematic, the simulated S-parameters of the baluns and the simulated S-parameters of the antennas with the 3D-printed support. This means that the signals entering the antennas are not ideal, that is they are not perfectly of equal amplitudes and 180° out-of-phase, but rather they are subject to the phase and amplitude imbalances of the baluns. This also means that the phase-paired cables and the 2.92 mm connectors were not considered in simulation.

Figure 3.4(a) shows that the assembled in-band full-duplex system has a return loss better than 10 dB over an ultra-wide frequency band (3.5-49.35 GHz), and Figure 3.4(b) shows that the measured self-interference cancellation level is higher than 50 dB starting from 4 GHz and up to 50 GHz. The measured matching seems to be better than the simulated one, this can be attributed to the higher insertion losses of the fabricated balun and also to the power losses resulting from the phase-paired cables and the 2.92 mm connectors, which were not considered in simulations. While these losses reflect positively on the system's matching, yet they reflect negatively on the measured gain of the system, which is depicted in Figure 3.4(e). Also, figures 3.4(c) and 3.4(d) depict sample radiation pattern cuts at 10 and 15 GHz respectively, where good agreement between simulated and measured results is observed. The far-field cuts reveal that highly directive main lobes are present, in the xz-plane, with two significant grating lobes that are 5 dB less than the peak of the main lobe, however, all other side lobes are at least 15 dB below the peak of the main lobe.

The grating lobes are present because the separation distance between the two opposite antennas is higher than a half-wavelength at 10 and 15 GHz, and their level continues to increase with frequency, as depicted in Figure 3.4(f). Similar results were observed in other publications on Vivaldi arrays [465]. This phenomenon can be considered as a major drawback of the system, though it cannot be avoided unless the separation distance between the antennas is reduced. However, for the presented Vivaldi array, this cannot be totally feasible because the separation distance is limited by the width of the single antenna element, which is usually equal or greater than a wavelength at the central frequency, or equal or smaller than a half-wavelength at the lowest frequency. This means, for such wideband system, whatever the antenna width is, there will always be a portion of the bandwidth (the higher frequency range) where the grating lobes are present.

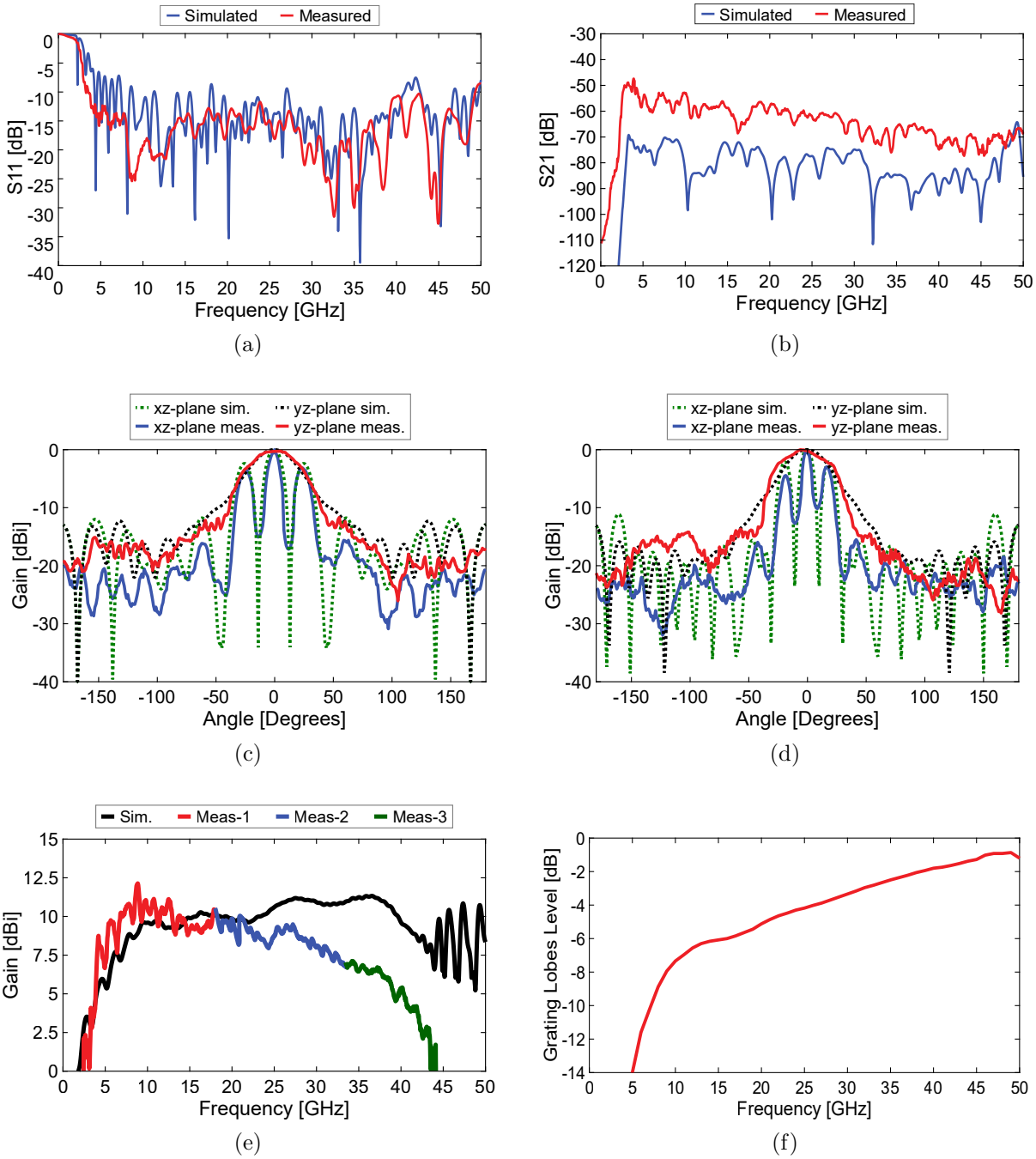

Figure 3.4: The proposed in-band full-duplex system's performance: (a) system matching, (b) self-interference cancellation level, (c) and (d) are the far-field radiation pattern cuts at 10 and 15 GHz respectively, (e) maximum realized gain of the system, and (f) the simulated grating lobes level below the main lobe level.

3.3.3 Alternative Configuration

In an alternative configuration, the four Vivaldi antennas can be placed as shown in Figure 3.5(a), where the antennas are still placed on the perimeter of a circle and sequentially rotated by 90° around the center of the array. However, the antennas are forming a cross-like shape and their edges are adjoined at the center of the array. This

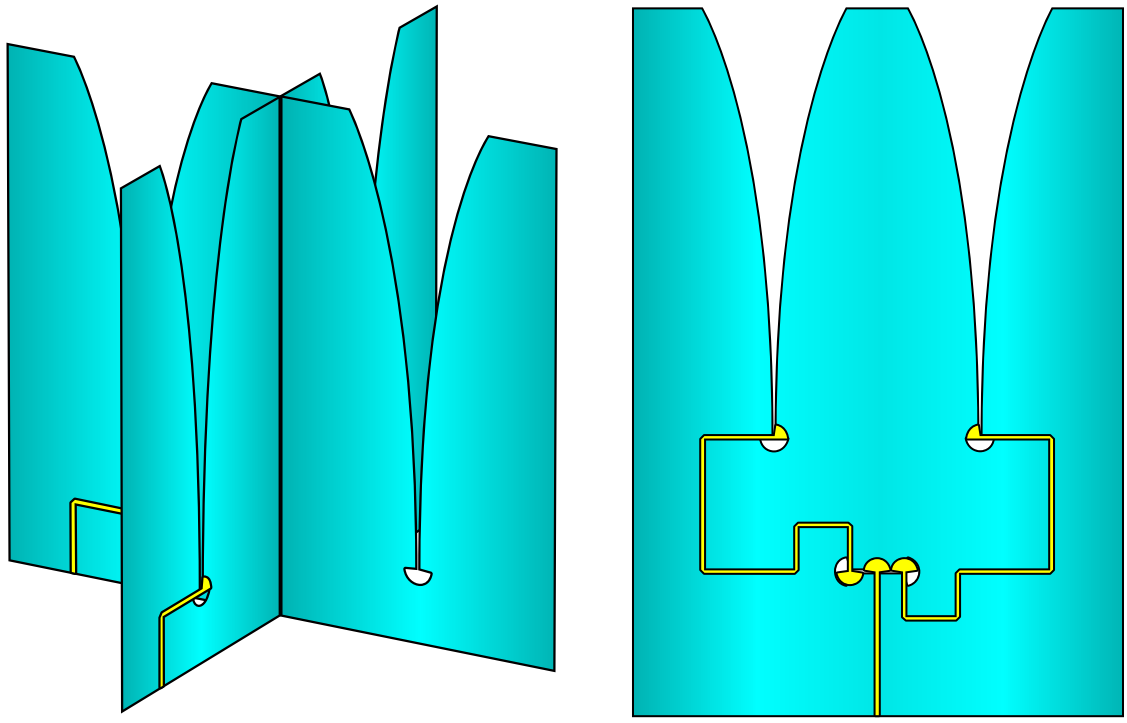

(a) (b)

Figure 3.5: (a) Vivaldi array of four antennas rotated sequentially by 90° around the center of the array and (b) two Vivaldi antennas integrated on the same board with their feeding balun.

cross-configuration has a near-identical performance to the array presented previously, but it has a bigger size compared to the previous array. The main advantage of this configuration is that it allows the integration of the feeding balun on the same board with the two opposite antennas as in Figure 3.5(b), which eliminates the need for phase-paired cables and connectors between the balun and the antennas. This in turn might reduce the phase and amplitude imbalances between the signals entering the antennas, hence we would expect the level of self-interference cancellation to increase, and also it reduces the losses from cables and connectors which might enhance the radiation efficiency of the system.

Two major challenges arise when trying to assemble all the antennas with their integrated baluns in one system: (1) there will be two boards, each with two antennas and one balun, and they need to be placed orthogonally to each other at their centers, thus we need to have some small cuts in each board to hold them together at the correct position. (2) the two integrated baluns will be at the center of the array and thus they will bisect each other, which will totally impair their matching. Having small cuts in the boards is tricky, because although it is possible to make those cuts by the available technology, but the fragility of the printed boards will be obstructive since the boards are extremely prone to fracturing and inducing those cuts will aggravate the problem more. Also, we have conducted several attempts to avoid the bisection of the baluns by moving them horizontally and vertically away from the center of the array and from one another, however, unfortunately, we could not restore matching to the system. Apparently, the baluns are sensitive to objects in their vicinity, and they must be sufficiently far away

from any other objects to be able to operate properly. Thus for these reasons we were not able to make this configuration work and we abandoned the idea, although it is highly advantageous and might deserve more investigation and development in a future work.

3.4 3D-Printed Vivaldi Antennas

The proposed PCB system has proved that in-band full-duplex technology can be implemented over an ultra-wide bandwidth with a decent amount of self-interference cancellation at the antenna level. However, the mechanical durability and the solidity of the system are a major drawback in practice, as the system might suffer a severe damage from a relatively light force -for example, the tension from the cables- and it requires much attention and care while working with the fabricated devices. The cause of this problem is the very low thickness of the substrate used to fabricate those devices, which is needed to operate in the high frequency range and provide the wideband performance. Thus, as a first solution, one can increase the thickness of the substrate while sacrificing a portion of the bandwidth. Nonetheless, the highest substrate thickness, that is commercially available, is approximately 1.6 mm, which can solidify the fabricated devices more and strengthen their resistance to external forces, but it does not totally solve the problem and more thickness is needed. Also, once the substrate thickness is changed, we need to redesign and re-optimize the microstrip-to-slotline transition, which is the basic building block in all the fabricated devices, and this will be time consuming. Moreover, even if we increase the thickness of the substrate, we still need the 3D-printed support to position and align the antennas, and we desire to get rid of it. Perhaps, the better solution is to abandon the printed-circuit boards and fabricate the Vivaldi antennas on thick metallic sheets, which are more solid, more rigid, and more resistant to pressure. And, moreover, all the antennas can be assembled together as one block without the need for an external support, maybe by screwing or soldering them together.

3.4.1 Single Antenna Design

In order to build the antennas on a metallic sheet, several manufacturing technologies could be considered: metal machining, metal molding, metal 3D-printing, or metallizing a 3D-printed dielectric. Before choosing any of these technologies, we need to consider their advantages and disadvantages, especially in terms of production cost, production time, and precision. For the initial prototype and lab trials, it is sufficient to use the standard 3D-printing technology to print the antennas as dielectric parts and then metallizing those parts, however, for commercial and mass production, metal machining or molding might be better. Whatever the technology is, a new way of feeding the antennas is needed, which has to take into consideration the effect of the thickness of the metal on the matching of the system, and it needs to incorporate a coax-to-slot transition, as in Figure 3.6.

In fact, the thickness of the metal in printed-circuit boards is usually neglected when calculating the impedance of the slotline, mainly, because the thickness is insignificant (typically $\leq 35\ \mu m$). However, this does not mean that the thickness of the metal has no effect on the slot impedance, especially when the thickness starts to increase significantly. Based on this, we denote here the slotline which is built on printed-circuit boards as thin

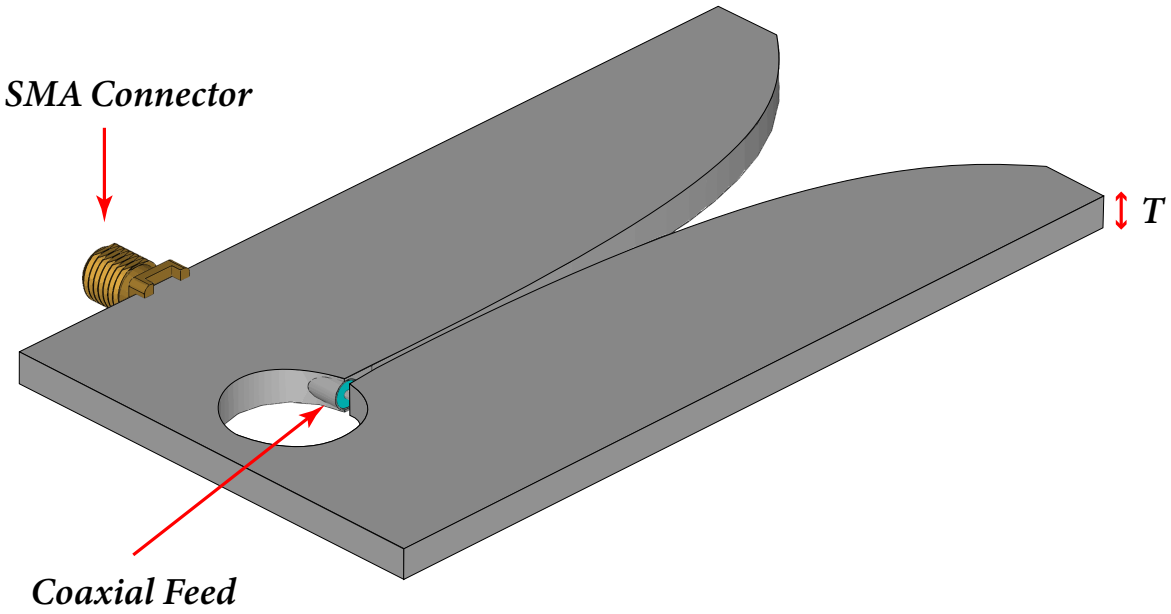

(a)

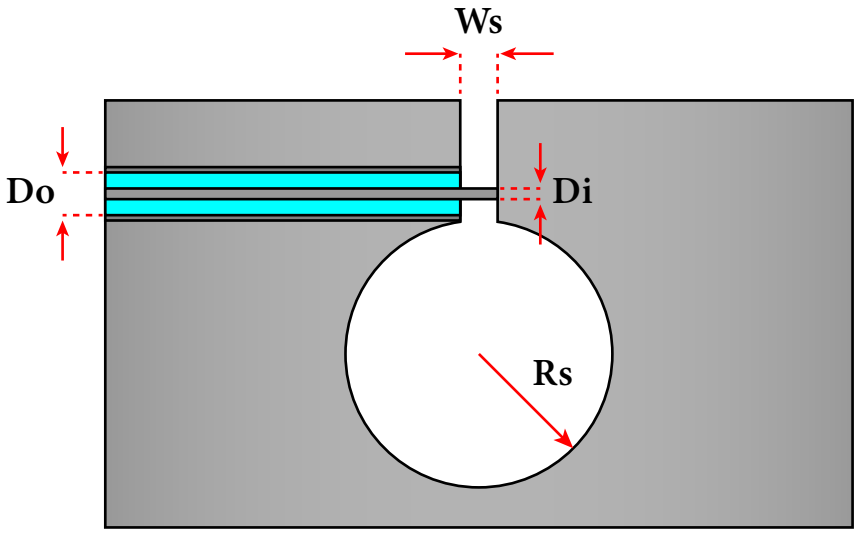

(b)

Figure 3.6: (a) Illustration of the 3D-Printed Vivaldi antenna and (b) a side view of its feeding.

slot, and the one built on thick metallic sheets as thick slot. Note that, for thin slot, there are three factors that determine its impedance: the slot width, the permittivity, and the thickness of the substrate. However, on the other side, the thick slot uses no substrate and is totally surrounded by air, and hence, the only two factors that determine its impedance are the slot width (W_s) and the metal thickness (T). Unfortunately, there are no closed-form equations, in the literature, that describes the variation of the thick slot impedance as a function of its width and thickness, thus we needed to obtain the impedance values empirically by full-wave simulations.

The results of the full-wave simulations indicate that the impedance of the thick slot

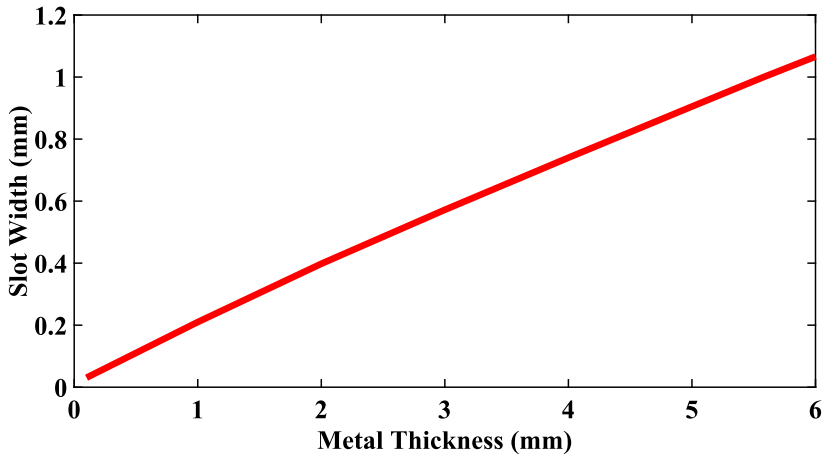

Figure 3.7: A curve corresponding to the values of the metal thickness and the slot width that yields a 50 Ω thick slot.

increases if the slot width (W_s) is increased or if the metal thickness (T) is decreased. However, the variation of the impedance is not linear with respect to the variation in the slot width or thickness and is rather exponential. Also, a slight change in the slot width has a major impact on its impedance and a great change in the metal thickness has a minor impact on the impedance. Multiple values of the slot width and thickness can yield the same impedance, thus before choosing the dimensions of the thick slot, which will determine its impedance, we need to take into consideration several factors:

- If a coaxial line with 50 Ω is to be used to feed the antenna, then the impedance of the slot needs to be designed to match the impedance of the coaxial feed.
- The antennas need to be thick enough to endure external pressure and to not break easily or bend. So, according to our experience with 3D-printed parts, a thickness of 5 mm can be sufficient.
- Also, the thickness of the antennas needs to be greater than the outer diameter of the coaxial feed ($T > D_o$), which will be embedded inside the body of the antenna.
- Manufacturing technology limitations and whether it can provide a narrow slot width (W_s) for a relatively thick metallic sheet. Keep in mind, that the minimum slot width determines the highest frequency that can be radiated by the antenna.

Based on the above specifications we have extracted, by simulation, the different slot widths, and metal thicknesses to obtain a 50 Ω thick slot, and their values are plotted in the graph of Figure 3.7. We chose the slot width (W_s) to be 1 mm in order to respect the 3D-printing limitations, and the corresponding metal thickness (T) was found to be 5.6 mm. The chosen slot width limits the highest frequency of operation to around 25 GHz, yet the obtained bandwidth is still very wide and can cover multi-standard applications.

After that, we needed to choose a coaxial feed line with an outer diameter that is sufficiently less than the thickness of the metal ($D_o < T$), and we found several coaxial cables that can satisfy this requirement. But there is another condition that also needs to be satisfied for optimum matching. In fact, our simulations revealed that, for better matching between the coax and the thick slot, the difference between the outer radius and

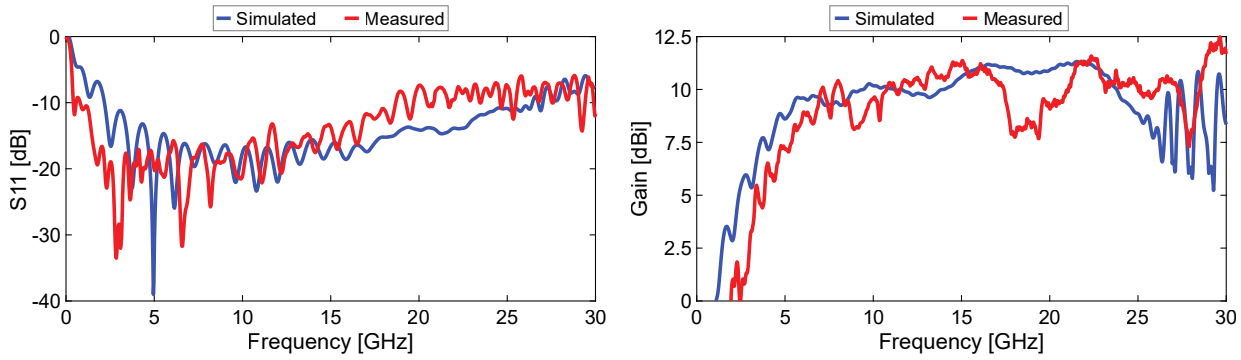

(a) (b)

Figure 3.8: Simulated and measured (a) return loss and (b) gain of the 3D-printed Vivaldi Antenna.

the inner radius of the coaxial line need to be exactly equal to the slot width ($(D_o - D_i)/2 = W_s$), otherwise the matching is degraded. Commercially available coaxial lines come in preset dimensions, and the ones that can almost satisfy our requirements are the 0.141-inch cables ($D_o = 3.58$ mm); though one can ask for customized coaxial parts with specific dimensions. Finally, after satisfying the impedance matching conditions between the coaxial line and the thick slot, a slot stub is needed to transition from coax to thick slot and to ensure proper matching; just like the microstrip-to-slotline transition, however, here we use a stub of a circular shape.

The radius of the slot stub (R_s) will determine the lowest frequency of matching, while the length of the exponential taper and the width of the aperture will determine the lowest frequency of radiation. The radius of the stub was initially set to 10 mm and it provides a matching bandwidth down to 2 GHz (according to our simulations). Ideally, we would like the antenna to radiate properly at 2 GHz, however, this demands to set the length of the exponential taper to at least one wavelength ($\lambda = 150\ mm$) and the width of the aperture to a half wavelength, which means that the size of the antenna will be relatively big. If fact, we are not limited by any size specifications, nonetheless, the 3D-printer has a limit on the size of the printed objects, such that big objects, which might exceed the size limit, need to be printed in several parts and then assembled after. For us, it was more important to print the antennas as one piece to ensure that they will be sufficiently robust and solid. Thus, to be consistent with the 3D-printer limitations, we decreased the length of the exponential taper to one wavelength at 3 GHz ($\lambda = 100\ mm$).

Figure 3.8 demonstrates the simulated and measured return loss and gain of the 3D-printed Vivaldi antenna. The simulated matching bandwidth starts from 2.25 GHz and goes up to 26.4 GHz, but, on the other hand, the measured bandwidth spans the frequency range from 0.8 to 18.6 GHz. The measured bandwidth is shifted to the left of the frequency axis with respect to the simulated bandwidth. Several retro-simulations were conducted in an attempt to find out the cause of the bandwidth shift, taking into consideration every possible imperfection that might generated during fabrication, but unfortunately, we could not reach a definitive conclusion about the cause of the bandwidth shift. In fact, multiple defects in the 3D-printed prototype might be present:

1. The 3D-printing process has its own tolerances, so it is not guaranteed that the

spacing between the flares of the antenna (the slotline width) have the same value of the simulated model.

2. After the 3D-printer finishes printing the antenna, it is immersed in a hot liquid metal bath, for a certain amount of time, to become metallized. The heat exposure from the metal bath manages to deform the antenna, and the misalignment between its flares become more significant.

3. Although the 3D-printed antenna is more solid and rigid than the PCB one, but, after all, if a sufficient force is applied to it, for example if the antenna is squeezed by hand, the antenna flares can bend or move closer to one another.

The change in the separation between the flares can cause the slot impedance to change, which means that we would expect some mismatches in measurements, but this does not explain the shift of the entire bandwidth.

Figure 3.8(b) shows that the simulated gain starts with 5 dBi at 2.25 GHz and continues to rise throughout the matching bandwidth, and it reaches a peak value of 11.3 dBi at 21.5 GHz, then it drops down to 6.65 dBi at 26.4 GHz. On the other hand, the measured gain follows a curve similar to the simulated one, however with some degradation throughout the bandwidth and a significant drop around 18 GHz. The general degradation in the gain can be attributed to the lossy nature of the metal used in the fabricated prototype. In fact, in simulation, the antenna was modeled as a perfect electric conductor (PEC) which has, ideally, infinite conductivity, no losses, and extreme surface smoothness, in contrary to the metal used in fabrication which has finite conductivity, more losses, and some surface roughness (we did not receive any information about these parameters from the manufacturer), which can explain the lower gain in measurements. Moreover, the gain drop around 18 GHz can be attributed to the frequency limitation of the anechoic chamber and the equipment used for measurements (the reference antenna, cables, connectors...), which can operate properly up to around 18 GHz but beyond that the obtained results are less reliable.

3.4.2 The Full-Duplex System

The full-duplex system proposed in this section has a similar principle of operation to the PCB system presented previously, and it consists of a four-element 3D-printed Vivaldi array and two Microstrip-to-slotline baluns. The four Vivaldi antennas were 3D-printed in one process in a box configuration as shown in Figure 3.9, and the two baluns were designed to operate in the frequency range from 2 to 20 GHz. At the bottom of the antenna array a small square metallic base is added to function as a support which holds the antennas together, and to act as a reflector to reflect the back radiated waves back to the direction of the main lobe. Finally, four Keysight N5448B phase-paired cables, which were used previously, are used here to connect the baluns to the antennas.

Figure 3.10 depicts the simulated and measured parameters of the proposed system where discrepancy between simulations and measurements can be observed. For instance, the simulated matching bandwidth starts at 3 GHz and ends at 19.5 GHz, and it seems that the matching level is not very good where some spikes in the curve almost reach -10 dB. On the other hand, the measured matching bandwidth spans the frequency range

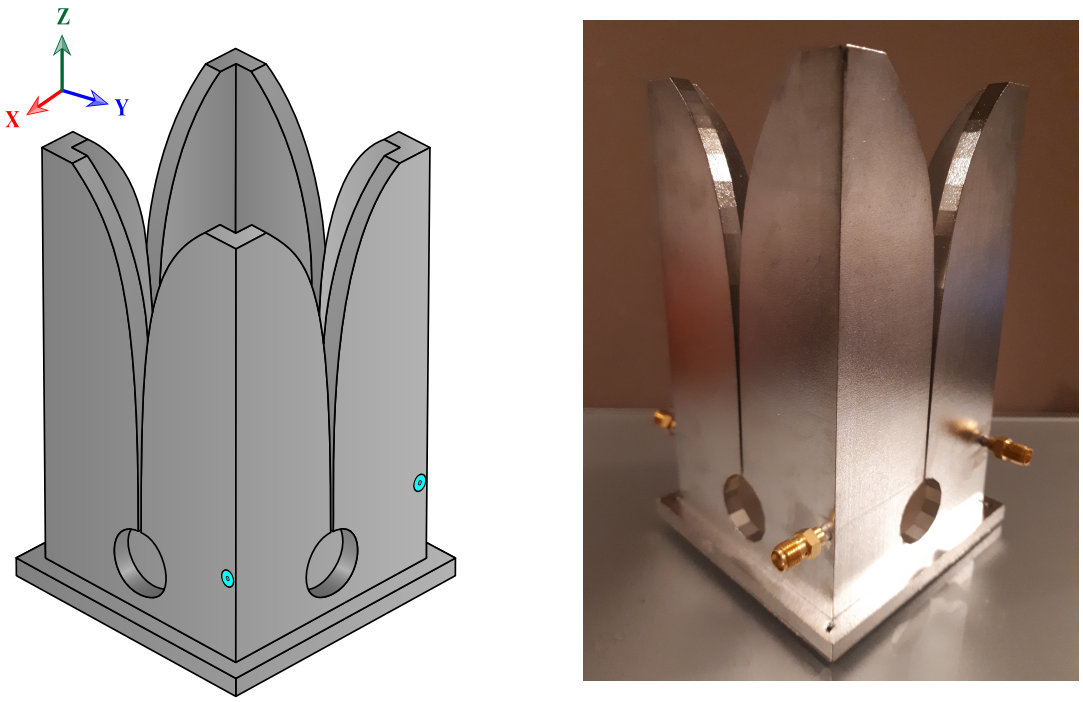

(a) (b)

Figure 3.9: The four-element 3D-printed Vivaldi array: (a) an illustrative drawing and (b) a picture of the fabricated prototype.

from 4.4 GHz to 28.65 GHz and the matching level seems better than simulation. Maybe the better matching in measurements can be a related to the losses of the used devices (baluns, cables, connectors...) which reflect positively on the measured return loss. In addition to that, Figure 3.10(b) reveals that the simulated self-interference cancellation level remains under -100 dB throughout the bandwidth, except for some spikes at some frequencies, while the measured cancellation remains below -40 dB at the low frequency side and above -80 dB at the high frequency side. Difference between the simulated and measured cancellation levels are expected because in simulation an ideal balun is used while in measurements the balun has phase and amplitude imbalances, and also due to the imperfections in the 3D-printing process, which were discussed previously and which lead to misalignment between the different elements of the antenna array.

The simulated system gain in Figure 3.10(c) gets higher than 10 dBi starting from 3 GHz and maintains an average value of 12.5 dBi, while the measured gain reaches 5 dBi at 3 GHz and maintains an average value of 9.783 dBi, then it starts dropping again around 18 GHz. This is perhaps caused by the frequency limitations of the equipment used in measurements which do not provide reliable results around and beyond 18 GHz. Of course, the gain in measurements was expected to be lower than the simulated one due to the high losses in the fabricated baluns. Finally, Figure 3.10(d) depicts sample radiation pattern cuts at 10 GHz, and it seems that there is a good agreement between simulation and measurement in the xz-plane, in general, where a main lobe and two grating lobes are observed, while all other side lobes at least 10 dB below the main lobe level. The presence of the grating lobes is related to the fact that the antenna separation is higher

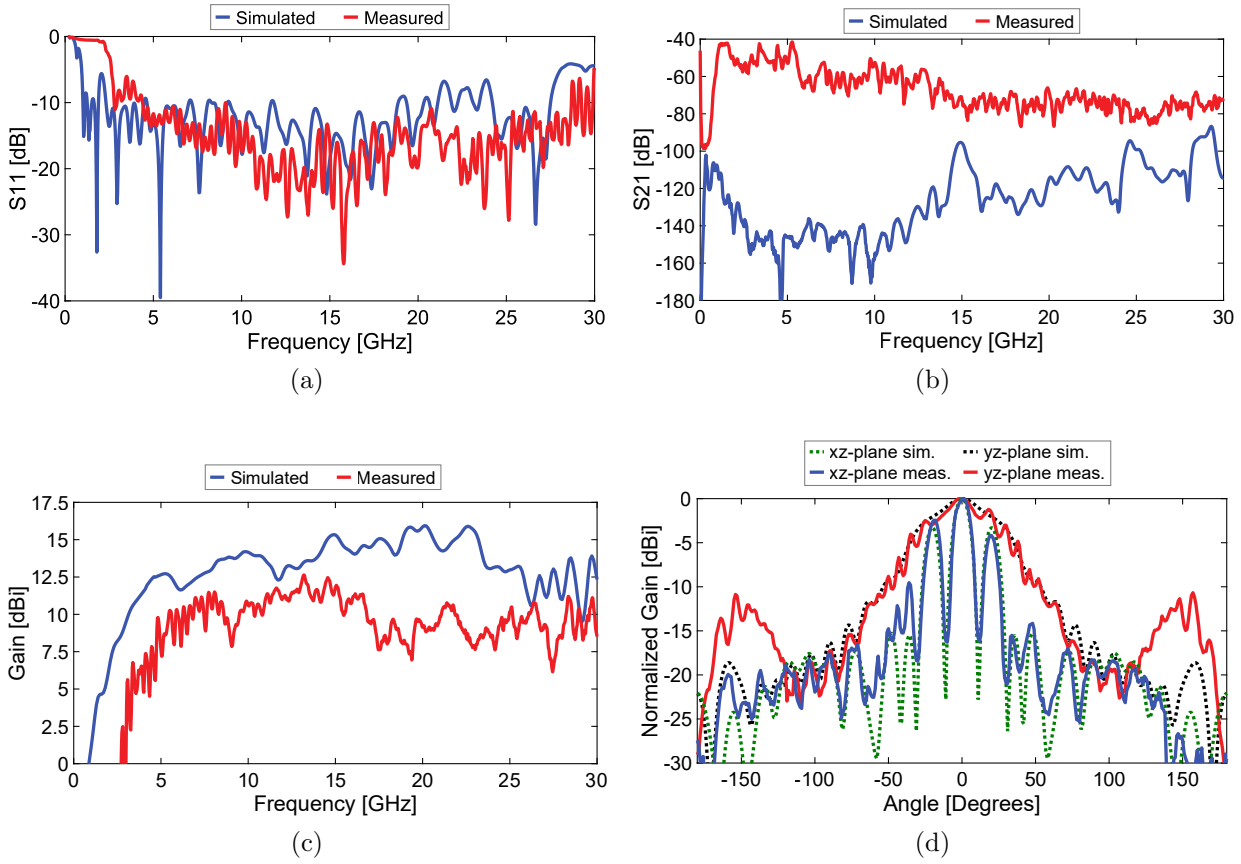

Figure 3.10: Simulated and measured metrics of the 3D-printed in-band full-duplex system: (a) system matching, (b) self-interference cancellation, (c) system gain, and (d) radiation pattern cuts at 10 GHz.

than a half wavelength at the measured frequency. On the other side, in the yz-plane, the simulated and measured main lobes are highly similar, but there is a difference in the side lobes level. It seems that the fabricated antenna has two significant back lobes, which are 10 dB below the main lobe level, but remain much higher than simulation. It is surprising to have back lobes in measurements especially that the antenna is equipped with a small square reflector at its base, which should, normally, force the energy to radiate to the front of the antenna. We assume that some of the currents flowing on the surface of the antenna manages to reach the reflector, and the reflector in turn radiates those currents from its edges.

3.4.3 Grating Lobes Reduction

The grating lobes are present in both the PCB and the 3D-printed systems and they result from the separation distance between the antenna elements which is higher than a half-wavelength beyond a specific frequency. The level of the grating lobes continues to increase with frequency, and it starts to approach the level of the main lobe at the higher frequencies. To eliminate or reduce the grating lobes the separation distance between the opposite antennas needs to be decreased, however, the separation distance is limited by the size of the antenna, and in particular the width of the antenna. Reducing the overall

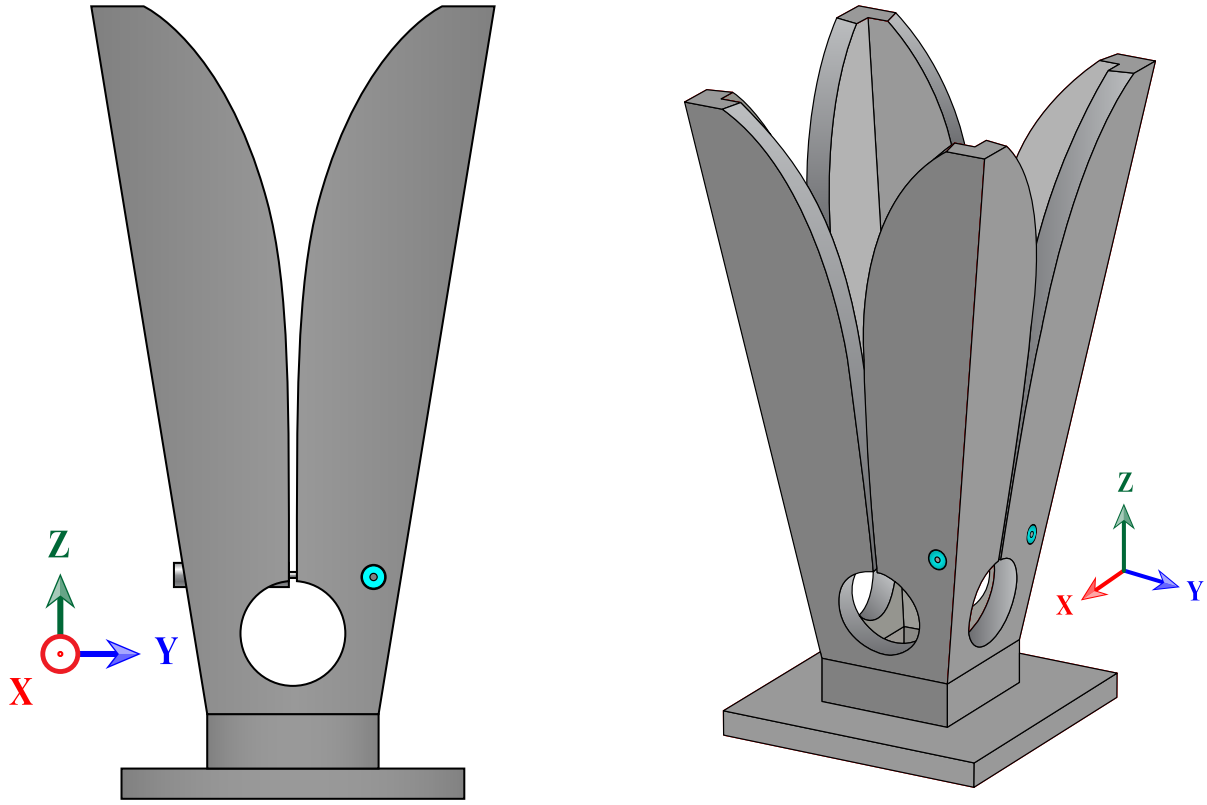

(a) (b)

Figure 3.11: The modified full-duplex array with reduced size and tilted 3D-printed Vivaldi antennas: (a) side view and (b) isometric view.

size of the antenna can degrade its matching and gain and can reduce its bandwidth. So, instead of reducing the size of the entire antenna we can reduce partially the size of some parts, and the partial size reduction is based on the following rationale: the high frequency radiation of the antenna is generated by the bottom part of the exponential slot taper, while the low frequency radiation is generated by the upper part of the exponential slot taper. Since the grating lobes are more significant at higher frequencies than at lower frequencies, then by reducing the separation distance between the bottom parts of the exponential slot tapers of the opposite antennas, while preserving the same distance between the upper parts of the exponential slot tapers, can help in reducing the level of the side lobes at higher frequencies without affecting the performance of the full-duplex system.

To better visualize this idea, let us take a look at Figure 3.11 which depicts how the size reduction of the single antenna element will be, and how the final full-duplex antenna array looks like. The width at the top of the antenna is kept the same while the width at the bottom is reduced, this allows to bring the antennas closer to each other at the bottom and reduce the separation distance at higher frequencies, while keeping the same separation at lower frequencies and maintaining the overall geometry of the antenna, which in turn preserves the matching and gain of the antenna. Bringing the antennas closer to each other at one end while keeping them fixed at the other end means that the antennas must be tilted slightly in the full-duplex array, which does not look like a box

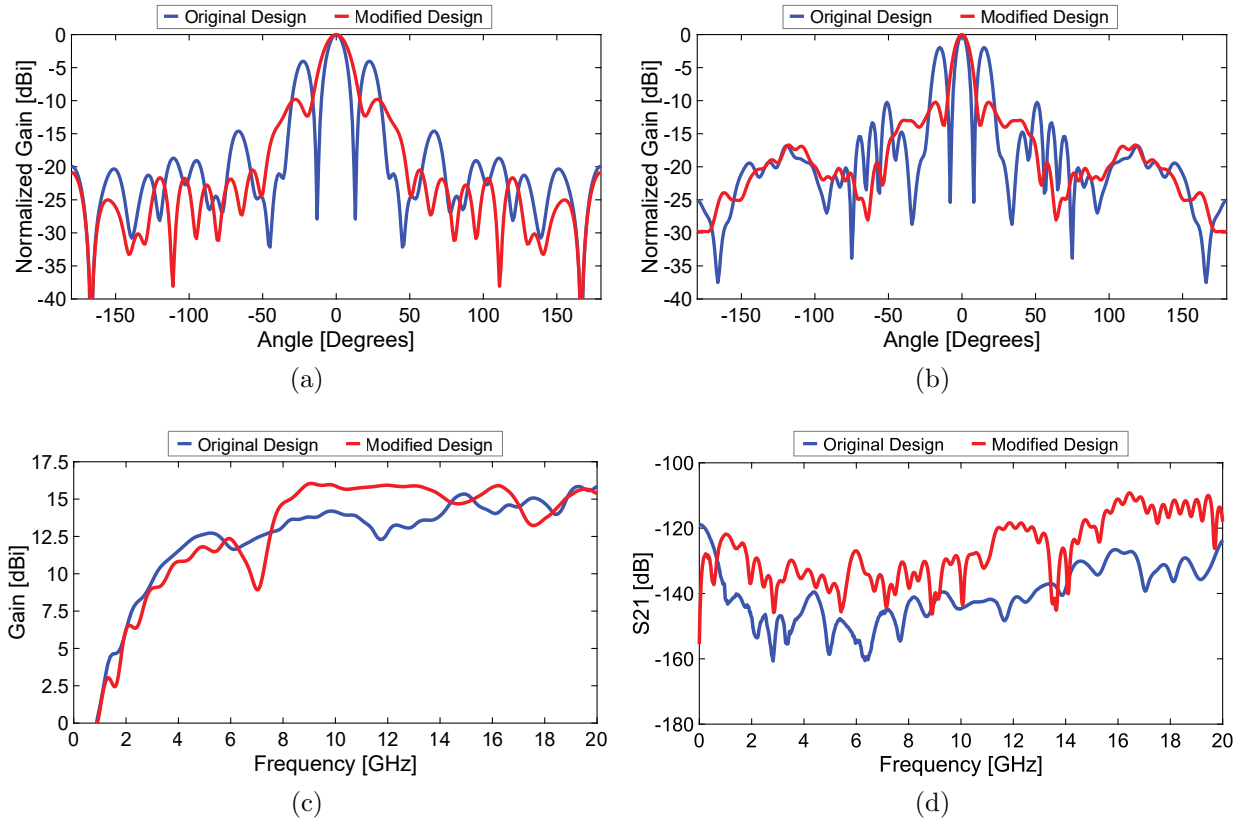

Figure 3.12: Radiation pattern cuts at (a) 10 GHz and (b) 15 GHz of both the original array design with the four antennas vertically straight and the modified array design with the tilted antennas.

anymore and it looks like an inverted pyramid, just like horn antennas. The tilt angle was found to be about 10°. Finally, note that, a fabricated prototype of the modified array is not available at the moment and is currently under construction, so we are only going to present the simulated results in Figure 3.12 assuming that the array is being fed with an ideal baluns, i.e. there are no losses and phase and amplitude imbalances between their output ports.

Now, the radiation pattern cuts in Figures 3.12(a) and 3.12(b) confirm the validity of the proposed approach, where it is observed that the grating lobes were reduced by 5 dB at 10 GHz and by 9 dB at 15 GHz, and in addition to that, side lobes in general were also reduced. The reduction in grating and side lobes means that more power will be radiated through the main lobe, which translates into a higher system gain. This is partially validated by Figure 3.12(c) where the gain of the modified system becomes higher than that of the original design starting form 8 GHz, although the modified system gain drops below the original system gain at some frequencies, in particular around 7 GHz, 14 GHz, and 18 GHz. This indicates that the approach is failing around those frequencies. After inspecting the radiation pattern plots at those frequencies, it was observed that although the grating lobes were reduced, yet some side lobes, at other angles, managed to grow bigger in size and consume some of the system's gain. This means that the proposed approach is a double-edged sword that can reduce the grating lobes on one hand, and at the same time, can cause other unwanted side lobes to grow bigger on the

other hand. But if we consider the frequency range from 8 to 13 GHz, we can say that the approach works perfectly. Finally, Figure 3.12(d) shows that the level of self-interference cancellation of the modified system is slightly degraded with respect to the original system especially as the frequency increases. In fact, this observation is normal, because the level of cancellation is also affected by the distance of separation between antennas, as this distance increases the level of cancellation increases and the distance decreases the level of cancellation also decreases. Since we partially brought the antennas closer to each other at the bottom side, where the high-frequency radiation takes place, the level of cancellation is expected to decrease as the frequency increases.

3.5 Dual-Polarized Full-Duplex Array

Our previously designed systems can operate with orthogonal linear polarizations (vertical and horizontal) for the transmit and receive antennas, however, one feature that some applications might require is simultaneously transmitting and receiving both types of polarizations, for example, in base transceiver stations that transmits both polarizations to make sure that the mobile user will receive a reliable signal regardless of his position and the alignment of the mobile antenna with respect to the base station. Hence, implementing a wideband dual-polarized full-duplex system might be interesting in this case, and to achieve that we need wideband dual-polarized antennas. We still want to use near-field cancellation as our wideband self-interference cancellation technique, so we need four dual-polarized antennas, and we want to make use of the Vivaldi antenna designs that we have already developed. Nevertheless, the Vivaldi antenna can only radiate a single linear polarization (vertical or horizontal) and it needs to be modified in order to radiate the orthogonal polarization simultaneously. In fact, a dual-polarized Vivaldi antenna can be obtained by placing two single elements orthogonal to one another as in Figure 3.13, and the two antenna elements are fed simultaneously by using a power divider. This conventional way of forming dual-polarized Vivaldi antennas has its own drawbacks, which are mainly related to its feeding. So, in the following section, we discuss the single dual-polarized antenna design and the drawbacks associated with it, then we present a novel way of feeding the antennas to overcome those drawbacks. And after, we present the full-duplex array that uses four single dual-polarized antennas.

3.5.1 Single Antenna Design

The conventional way of building a dual-polarized Vivaldi antenna is depicted in Figure 3.13 where two single Vivaldi elements are put together and orthogonally placed with respect to one another. This means that the coax-to-slotline transitions that are feeding each antenna must overlap, which results in several drawbacks:

1. In this configuration, four flares need to be grouped near the center of the system, but the orthogonal flares must not come into contact with each other otherwise the antenna will not work. Thus to prevent them from touching each other, the separation between the opposite flares (W_s) must be greater than the thickness of the flare (T). However, since the flare thickness is about 5 mm in our case, the

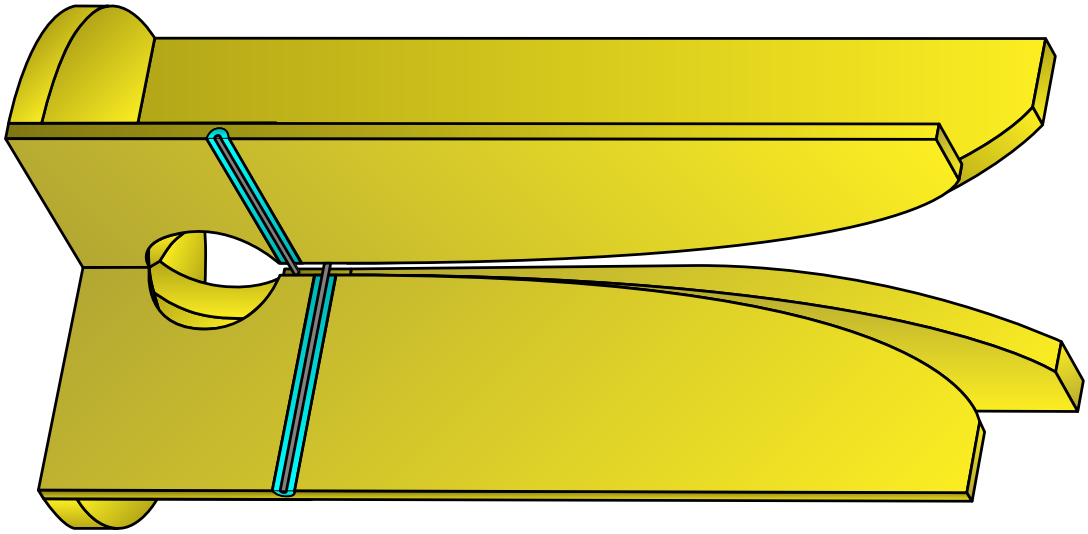

(a)

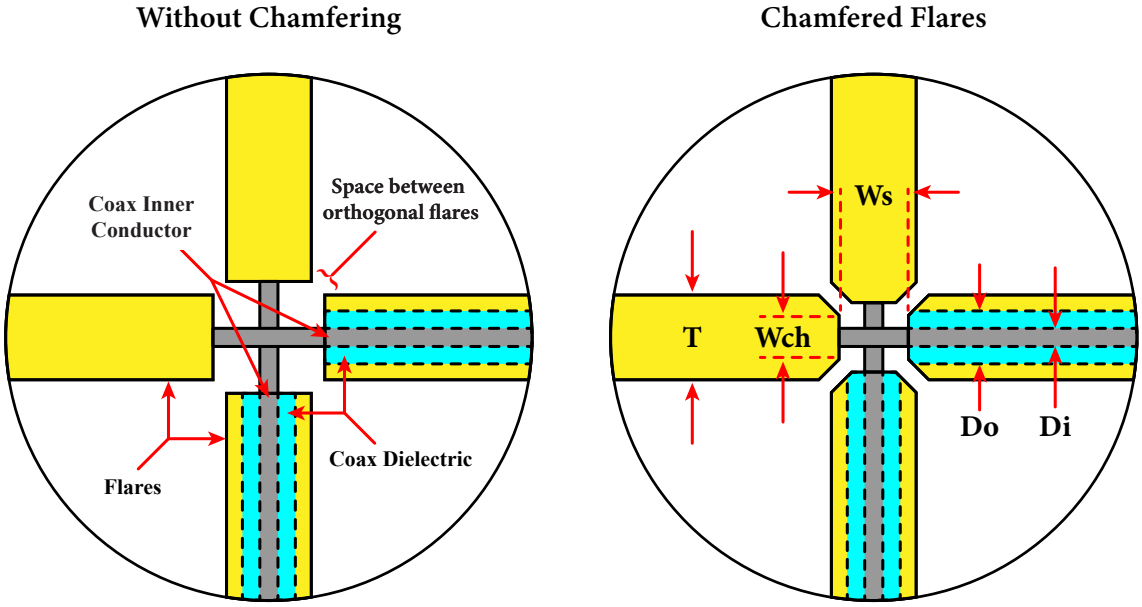

(b)

Figure 3.13: (a) A conventional dual-polarized Vivaldi antenna and (b) top view of the antenna feeding with and without chamfering the flares.

separation between the flares must be at least 6 mm for example (depending on fabrication tolerances). A 6 mm slot will have a very high impedance and will not be matched to the 50 Ω coaxial line, thus the separation between the flares cannot be increased randomly and without limit. Usually, as a compromise between the flare separation and the slot impedance, the flares near the center of the system are chamfered, which reduces their thickness and gives more space to bring them closer. Ideally, we would like to get the width of the chamfered (W_{ch}) edge as low

as possible, but this is limited by the ability of the fabrication process to provide a very low metal thickness and the mechanical fragility of the thin metal.

2. The impedance of the slot, in this case, is not only controlled by its width and thickness but also by two additional parameters that enters the equation. The first parameter is the number of the flares that surround the slot, where the slot now is confined between four flares instead of two, and the second parameter is the chamfering of the flares (W_{ch}), which might affect the slot impedance slightly but should not be neglected. So, the four parameters that control the slot impedance need to be selected carefully to meet the mechanical limitations, which increases the complexity of the antenna design.

3. To prevent the coaxial lines of the orthogonal antennas from intersecting near the center of the system, one of them needs to be alleviated above the other. The alleviated coax can obstruct the waves passing through the slot from the orthogonal antenna which affects its radiation performance. Moreover, the antennas are optimally matched if the feeding coax is closer to the matching stub, but since the alleviated coax is more distant from the stub, then the antenna with the alleviated coax will suffer from matching degradation. So, in summary, the conventional way of feeding the dual-polarized Vivaldi antenna generates differences in matching and radiation between the orthogonal antenna elements.

Based on the above, the first step to build the dual-polarized antenna is to decide the values for the chamfered edge thickness (W_{ch}) and the separation between the opposite flares (W_s), which were chosen to be 1 mm and 2.5 mm, respectively, taking into consideration the mechanical limitations of the fabrication technology. The calculated slot impedance for the chosen values was found to be around 100 Ω, which means that a significant mismatch between the slot and the coax will be present, and that will greatly narrow the bandwidth of operation of the antenna. But since our goal is to build a wideband dual-polarized antenna, we needed to find another way of feeding it that can have wideband matching and that can preferably eliminate the matching and radiation differences between the orthogonal antenna elements, which are consistent with the conventional way of feeding.

The principle of the new way of feeding, which is depicted in Figure 3.14, is to transfer the position of the feeding point from the center of the antenna to its sides, which is achieved by bending the bottom slot to one side of the antenna, such that the slot stub and the feeding coax are not any more at the center of the antenna. So, by doing this we eliminate the overlap between the feedings of the two antenna elements, which means that they will both have similar matching and radiation performances. But the most prevailing feature of this feeding technique is the additional freedom to choose the width of the side slot, which can be made to match the impedance of the coaxial line, and hence the antenna can now be matched over a wide bandwidth.

3.5.2 Single Antenna Implementation and Performance

The mechanical defects which are associated with the 3D-printing process, especially the misalignment between the antenna flares, motivated us to explore alternative ways to

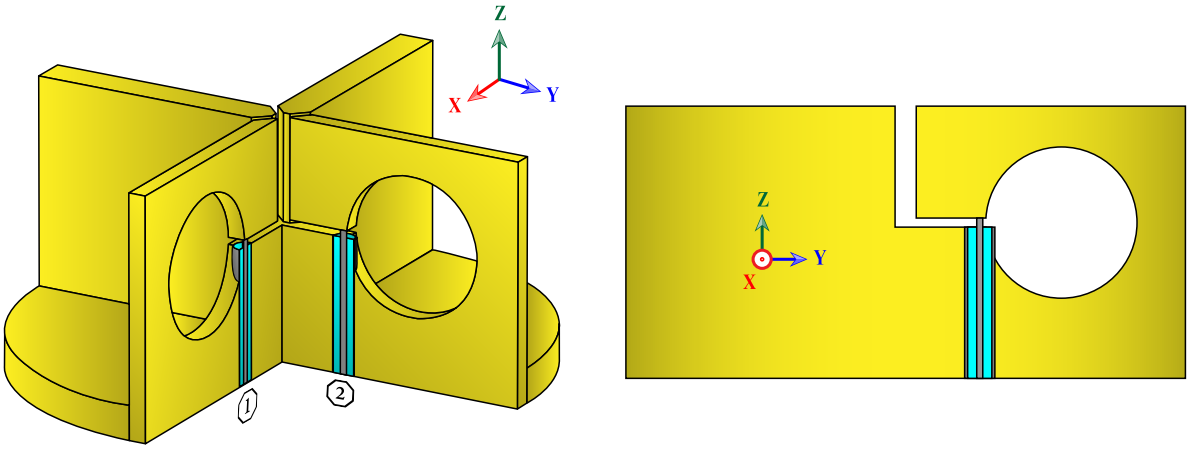

(a) (b)

Figure 3.14: The novel feeding technique for the dual-polarized Vivaldi antenna (a) isometric cut view and (b) side view of a single antenna element feed.

produce more mechanically reliable parts, while trying to preserve the electrical behavior of the antenna. After weighing the different possibilities, we concluded that building our antennas from a metallic material using computer numerically controlled (CNC) machining, which takes a block of metal and carves it into the wanted shape by performing a series of mechanical processes (cutting, milling, drilling...), is the best alternative for 3D-printing because we assume that metallic antennas will be more precise with the flares alignment and they will be more immune to deformation resulting from external mechanical pressure or force. But of course, the process has its own tolerances.

The fabrication of the dual-polarized Vivaldi antenna is not complete at the time of writing this manuscript, so only simulation results will be presented in this section. It is good to note that the antennas were modeled in the 3D-simulator as lossy Aluminum with finite conductivity and high surface smoothness, however, in practice, the surface of the antenna might be rough, which can slightly affect the surface current distribution on the antenna flares and consequently their radiation. It can be noticed from Figure 3.15 that the antenna is matched from 3.5 GHz to beyond 20 GHz with an average 10 dB level of cross-polarization between the orthogonal antennas and 8 dBi level of average gain for a single polarization. However, the radiation pattern plots point to a major drawback of this antenna where it can be noticed that the radiation patterns are not symmetric and more power is being radiated toward the right side of the antenna, in particular toward the feeding point. The asymmetry in the radiation patterns is less noticeable at lower frequencies and becomes more significant as we go higher in frequency. This asymmetry is attributed to the surface current imbalance caused, mainly, by the bend in the slotline, which means that the flare directly above the feeding point carries currents that are higher in amplitude and in phase than the currents flowing on the opposite flare. We are going to address the radiation pattern asymmetry of a single dual-polarized antenna in a later section, but in the next section we are going to present the full-duplex array using the current antenna design, but we expect for the array to have more symmetry in its radiation pattern because of the symmetric placement of the antennas in the array. This means that we are still expecting to see some anomalies in the array radiation patterns

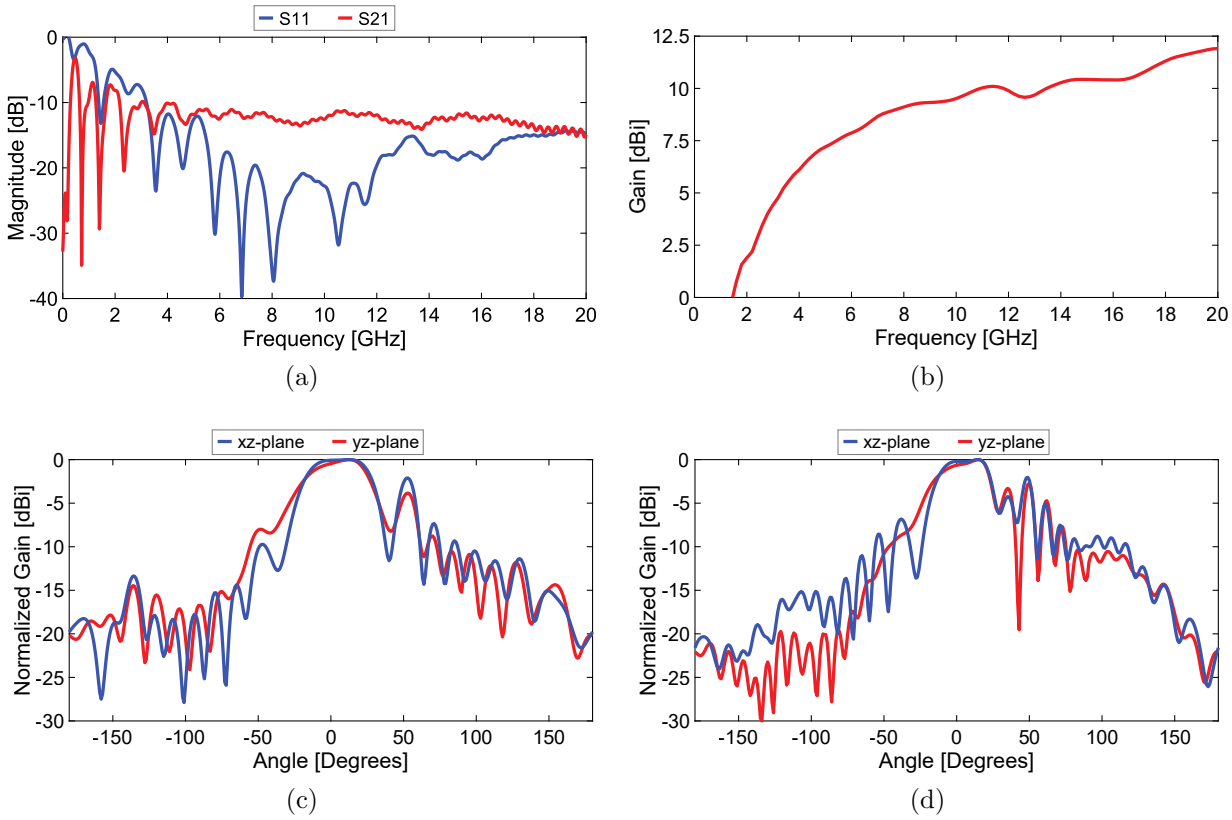

Figure 3.15: Simulated (a) S-parameters, (b) gain, (c) and (d) radiation pattern cuts at 10 and 15 GHz respectively of the dual-polarized Vivaldi antenna with the novel feeding technique.

but they will be less significant as compared to the single antenna.

3.5.3 The Full-Duplex Array

The dual-polarized full-duplex array is also based on the near-field cancellation technique, thus four dual-polarized Vivaldi antennas need to be placed and sequentially rotated by 90° with respect to one another around the center of the array as in Figure 3.16, and each two opposite antennas will be used to transmit or receive. Now, for the array to operate in full-duplex mode each couple of opposite antennas need to be fed signals of opposite phases by using a balun, also each single dual-polarized antenna has two ports that must be fed simultaneously using a power divider, thus, in total, the array needs at least two baluns and four power dividers to operate as a dual-polarized full-duplex system. A schematic of the array feeding network is depicted Figure 3.16(c) and it shows the signal phases at each port of the array. In fact, two types of feeding networks were considered in simulation: an ideal feeding network based on ideal power dividers and baluns (no losses and no phase and amplitude imbalances) to show the ideal performance of the array, and the second network was formed from S-parameter files of commercially available baluns and power dividers from Marki Microwaves (Balun Model: BAL-0026 [466] and Power Divider Model: PD-0126 [467]). The simulation with commercial devices can give an initial estimation of the expected matching and self-interference cancellation levels of the full-duplex array that will be fabricated.

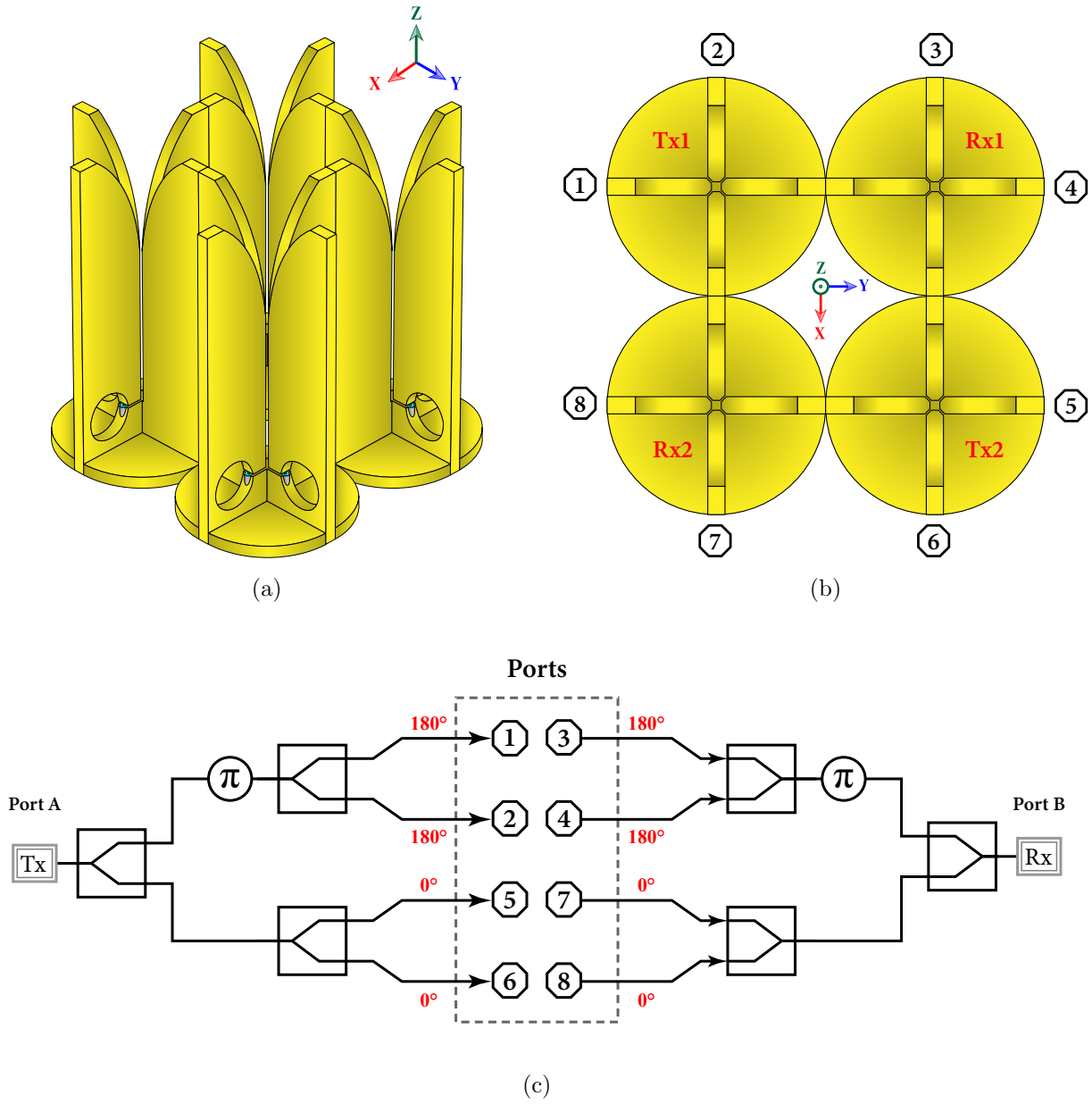

Figure 3.16: The dual-polarized full-duplex array (a) isometric view, (b) top view showing the port numbering, and (c) schematic of the array feeding network.

Figure 3.17(a) shows that the matching bandwidth of the array using ideal components is from 3 to 10.5 GHz, while the matching bandwidth using commercial devices starts around 2 GHz and goes beyond 20 GHz. The difference in matching between ideal and commercial devices can be attributed to the losses in the commercial devices which translates into more power dissipation and less power reflection to the input port, however this will impact the gain of the array. Moreover, Figure 3.17(b) indicates that the ideal level of self-interference cancellation can be around 120 dB, but the actual level of cancellation using commercial devices can be around 40 dB at the low frequency side and can reach 80 dB at the high frequency side. Moreover, the radiation pattern plots in figures 3.17(c) and 3.17(d) indicate that the radiation pattern of the array has become more symmetric, as expected before, but the number and level of grating lobes

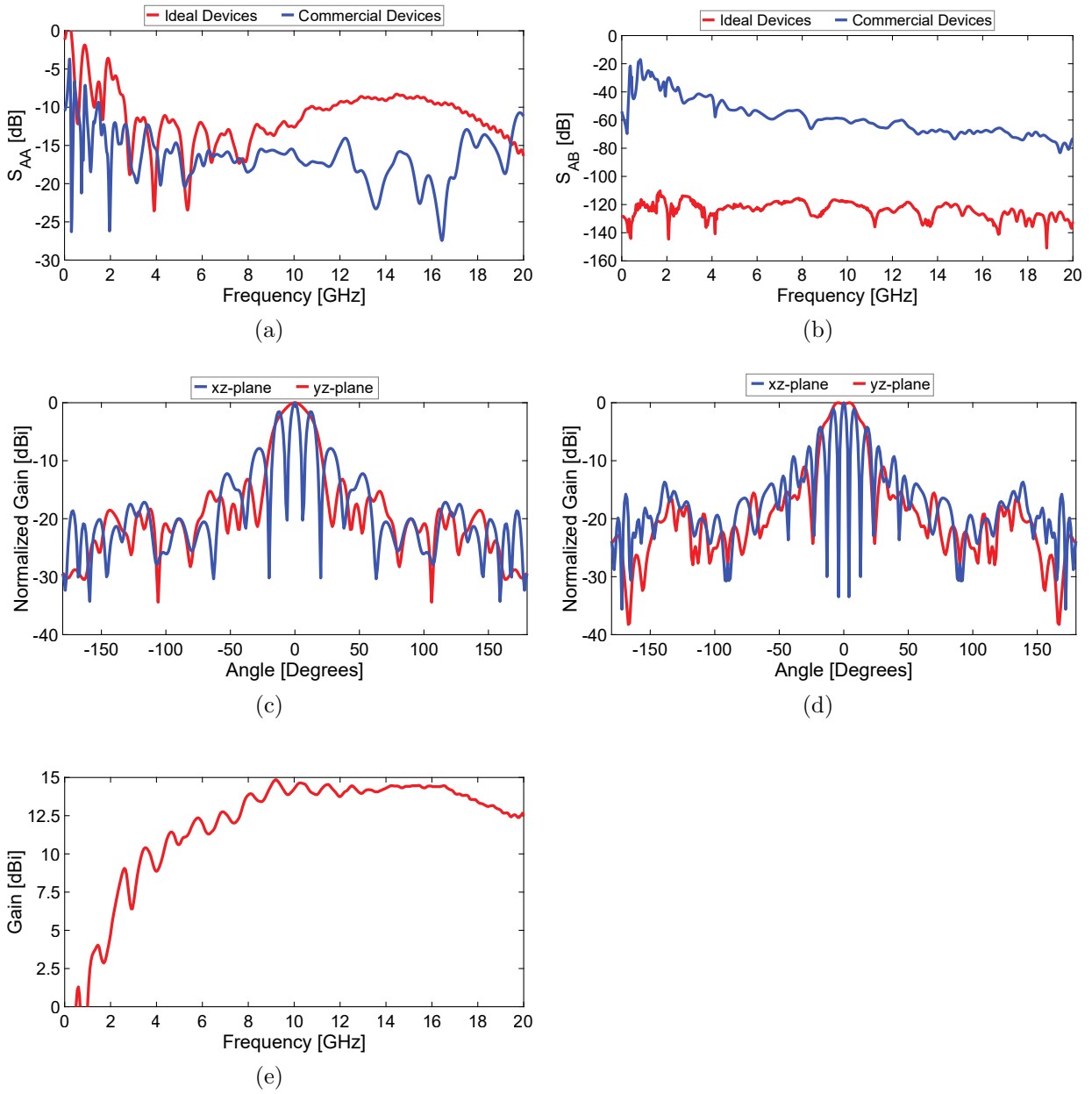

Figure 3.17: Simulated parameters of the dual-polarized full-duplex array (a) matching, (b) self-interference cancellation, (c) and (d) are its radiation pattern cuts at 10 GHz and 15 GHz, respectively, and (e) array gain.

are increasing with frequency. The presence of the grating lobes is expected and has been observed in all the other systems that we demonstrated previously, and they result from the separation distance between the opposite antennas if it is greater than a half-wavelength at a certain frequency. The level of the grating lobes increases as the separation distance increases, while the number of the grating lobes increases when the separation distance becomes greater than a multiple of half-wavelength. In fact, the size of a single antenna is $72.5 \times 72.5 \times 130$ mm^3 and that makes the minimum separation distance between the opposite antennas about 10 cm, which is equal to a wavelength at 3 GHz, and this means that the grating lobes are present at all frequencies in our band, and their

level and number will increase with frequency. Finally, the array shows a gain better than 10 dBi almost throughout the entire band.

3.5.4 Balanced Dual-Polarized Vivaldi Antenna

The dual-polarized Vivaldi antenna presented in the previous section presented good wideband performance but with asymmetric radiation patterns, which we think that it is caused by the current imbalances between the two antenna flares due to the slot bend, however this is not the only cause. In fact, the presented antenna has only one coaxial feed for each of the two antenna elements forming it, and the coax is by nature an unbalanced transmission line where the currents flowing on its inner conductor are not equal to the currents flowing on its outer conductor. But, since the outer conductor of the coax is connected to one flare of the antenna element and the inner conductor is connected to the opposite flare, the currents that will be flowing on the opposite flares will be out-of-balance which can affect the symmetry of the radiation pattern of the antenna.

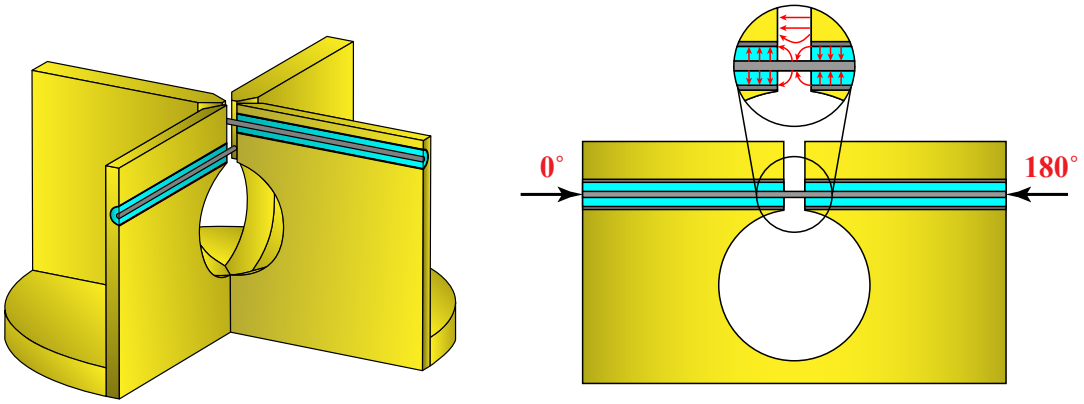

(a) (b)

Figure 3.18: The conventional balanced feeding of the dual-polarized Vivaldi antenna: (a) isometric cut view and (b) side view of single antenna element feed showing the electric field distribution near the center of the antenna.

In order to balance the currents on the opposite flares, two coaxial lines can be used for each antenna element (four in total for the whole antenna) as depicted in Figure 3.18, and each coax will pass through one of the opposite flares. The outer conductors of each coax will be touching the flares while their inner conductors will be joined at the center of the antenna, and after that the coaxs will be fed signals that are 180° out-of-phase by an external balun. If the balun is ideal, then the outer conductors of both coaxs should carry equal currents with opposite phases, and the same can be said about their inner conductors. The equal currents on the outer conductors will flow to the flares and will get radiated, which restores the symmetry of the radiation pattern, while the currents flowing on the inner conductor will cancel each other at the center of the antenna.

Balancing the Vivaldi antenna can not only make the radiation pattern more symmetric, but it can also increase the level of cross-polarization between the orthogonal antenna elements. This is a feature that many applications might desire and in particular

in-band full-duplex: instead of using both antenna elements to simultaneously transmit or receive for dual polarization, one antenna element can be used as a transmit antenna while the orthogonal element can be used as a receive antenna. The high cross-polarization level between the orthogonal antenna elements translates into high self-interference cancellation for in-band full-duplex. However, balancing the Vivaldi antenna using the conventional way of feeding, where the feeding point is at the center of the antenna and one coax is alleviated above the other, can increase the complexity and difficulty of the antenna design, in particular matching the slot impedance to the coax impedances. Also it can lead to differences in matching and radiation between the orthogonal antenna elements, as discussed before, and it can also restrict the bandwidth.

To eliminate those problems we propose a new way of balanced feeding based on the novel feeding technique presented in the previous section, which transfers the position of the feeding point from the center of the antenna to its sides. The new balanced feeding way is shown in Figure 3.19 where two side slots are horizontally connected to the center slot, and each side slot is terminated with a matching stub and is fed by a 50 Ω coaxial line. Of course, the side slot width is designed to match the slot impedance to the coax impedance. Finally, the coaxial lines will be then connected to an external balun to obtain the out-of-phase feeding. Thus in total two baluns are needed to feed each individual polarization. It is also good to mention that the balanced antenna can be used also to generate circular polarization instead of dual linear polarizations, but the feeding network must be modified such that the phases at the four ports of the antenna must be 0°, 90°, 180°, and 270° consecutively.

Simulations were also conducted using an ideal balun and a commercial balun (the same as before) to show the ideal performance of the antenna and to have an estimation of the performance of the antenna that will be fabricated. Figure 3.20(a) shows that the matching bandwidth of the balanced antenna using an ideal balun starts at around 4 GHz and extends to beyond 20 GHz, while the simulated bandwidth using the commercial balun starts around 3 GHz and goes up to 20 GHz, however, it is noticed that the matching level of the commercial balun is worse than that of the ideal balun around the center of the band. Moreover, Figure 3.20(b) shows that the ideal level of cross-polarization is more than 100 dB, while it is more than 20 dB for the commercial balun. This indicates that we have obtained at least 10 dB more of cross-polarization using the balanced feeding as compared to the unbalanced one. In addition to that, the radiation pattern plots in Figures 3.20(c) and 3.20(d) proves the validity of the balanced feeding technique where it can be clearly observed that the radiation pattern symmetry is restored. Finally, Figure 3.20(e) shows that the balanced antenna exhibits a gain better than 7.5 dBi per single polarization starting from 4 GHz, which is almost similar to the gain of the unbalanced antenna, but here we observe higher gain level near the center of the band starting around 6 GHz. The higher gain level can be attributed to the symmetry of the radiation pattern, as less power is being lost in the side lobes and more power is being forced to radiate in the direction of the main beam.

While the balanced antenna provides a superior performance as compared to the unbalanced antenna, yet its feeding network is more complex such that a single balun is needed to feed each polarization independently, and to activate the dual-polarization, the two baluns need to be fed simultaneously by a power divider which will be connected to Ports A and B in Figure 3.19(b). So, in total, the balanced antenna needs one power

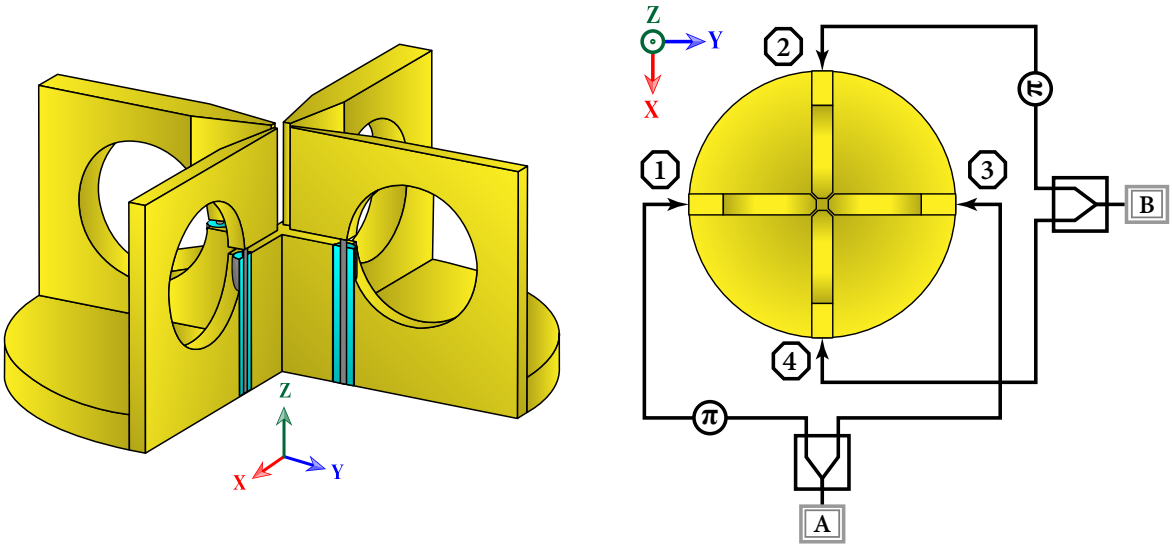

(a) (b)

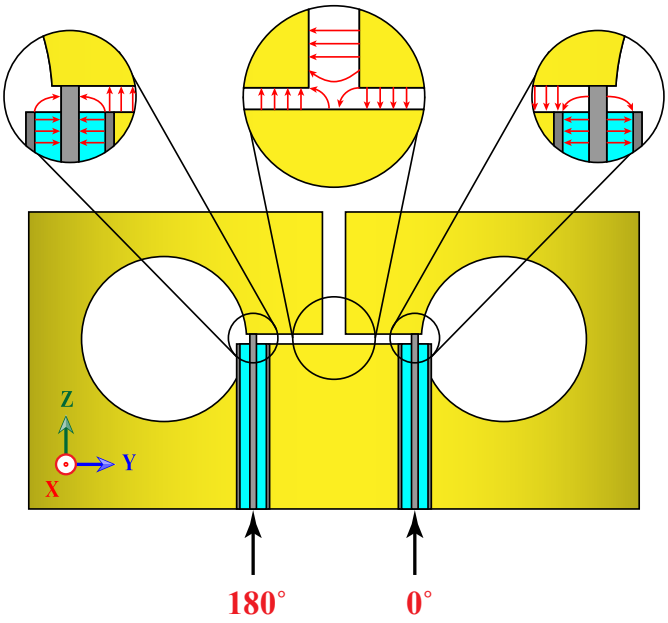

(c)

Figure 3.19: The novel balanced feeding of the dual-polarized Vivaldi antenna: (a) isometric cut view, (b) top view of the antenna showing port numbering and the feeding network, and (c) side view of single antenna element feed showing the electric field distribution at different positions.

divider and two baluns to operate in dual-polarization. Now to implement a dual-polarized full-duplex array we need four balanced antennas each with its own power divider and baluns, and this increases the complexity and cost of the system. This is why in the first place we used the unbalanced antenna instead of the balanced one to build the array, because the unbalanced antenna is less demanding and has a simpler feeding network.

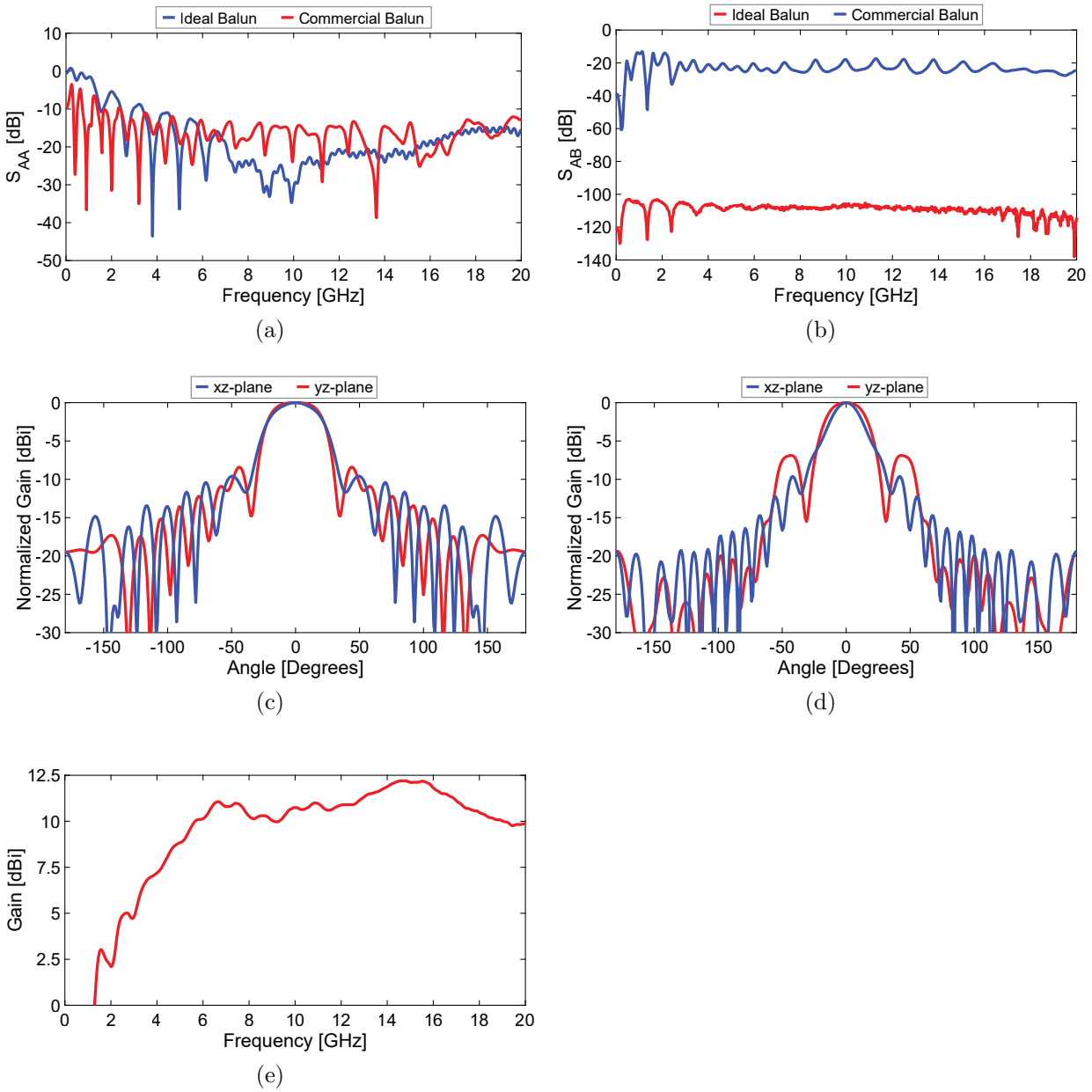

Figure 3.20: Simulated (a) matching, (b) cross-polarization level, (c) and (d) radiation pattern cuts at 10 and 15 GHz respectively, and (e) the gain of the balanced Vivaldi antenna fed by an ideal balun and a commercial balun.

3.6 Figure of Merit

To assess the merits of the proposed systems a new figure of merit, wideband full-duplex figure of merit (FoM_{WFD}), is introduced, and it accounts for the achieved self-interference cancellation level, the gain, the bandwidth, and the normalized size of the system. Firstly, both the values of the self-interference cancellation and the gain of the system should be linear and not in dB, however, note that the dB value of the self-interference cancellation should be positive before converting it to a linear scale. Secondly, concerning the size of the system, some systems have a two-dimensional geometry, such as systems fabricated

on printed-circuit boards (PCBs) where the thickness of the substrate is almost negligible, while other systems possess a three-dimensional geometry, which is the case for our system. Moreover, some systems have their feeding network directly integrated on the same board or platform while other systems have their feeding networks built on separate boards and connected with cables. These differences make it difficult to find a common and fair way to compare sizes of different systems. Thus, here, we propose a method which is based on three points: (a) we let the system be inscribed in a sphere of radius R, this radius will be used in the figure of merit to represent the size of the system, (b) if the feeding network is integrated with the antennas on the same board then it will be accounted for in the size calculation, and, otherwise, it will be disregarded, (c) after calculating the radius of the sphere it will be normalized by the wavelength at the center frequency. Based on all the above, the figure of merit is expressed as follows:

$$\mathrm{FoM}_{\mathrm{WFD}} = log_{10}\left(\frac{SIC \times Gain \times FBW}{R \ / \ \lambda_c}\right) \tag{3.15}$$

$$R = \frac{1}{2}\sqrt{l^2 + w^2 + h^2} \tag{3.16}$$

SIC: average self-interference cancellation level
$Gain$: average system gain
FBW: fractional bandwidth
f_u: upper frequency
f_l: lower frequency
f_c: central frequency
λ_c: wavelength at the central frequency
R: radius of the sphere circumscribing the full-duplex system
l: length of the full-duplex system
w: width of the full-duplex system
h: height of the full-duplex system

The proposed figure of merit is an initial attempt to combine different parameters of in-band full-duplex antenna configurations or topologies in an expressive way to evaluate the performances of the proposed systems and compare them to each other. However, depending on the targeted application, it might be modified to incorporate other metrics related to the field of application, such as the type of polarization, the number of polarizations (singular or dual), number of antennas used, antenna efficiency and level of side lobes, and the performance of the feeding network. Finally, Table 3.1 compares this work to other in-band full-duplex antenna topologies previously published in the literature, especially in terms of bandwidth, level of self-interference cancellation, system gain and size, and the newly introduced figure of merit where it can be noticed that our fabricated systems achieved the highest score.

[†]Some parameters' values were extracted from figures or graphs.

Reference	Frequency Range [GHz]	FBW	SIC [dB]	Gain [dBi]	$l \times w \times h$ $[cm \times cm \times cm]$	R [cm]	FoM_{WFD}
[181] †	6 - 19	1.04	60	12	$38 \times 13 \times 19$	22.215	4.651
[183] †	4 - 8	0.67	45	25	$40 \times 40 \times 25.3$	30.984	4.531
[151] †	0.5 - 2	1.2	45	5	$20 \times 20 \times 12.5$	15.462	4.77
[150] †	0.8 - 1.7	0.72	40	4	$60 \times 60 \times 30$	45	3.784
This work (PCB)	4 - 40	1.64	64	7.8	$8 \times 8 \times 9.4$	7.55	5.072
This work (3D-Printed)	4.45 - 28.65	1.4675	69.2	9.783	$8.42 \times 8.42 \times 13.56$	9	5.4193

Table 3.1: A table comparing the full-duplex antenna systems presented in this work to other works in the literature.

3.7 Conclusion

This chapter demonstrated the different implementations of wideband in-band full-duplex systems based on the near-field cancellation technique. The first system was built from the PCB devices in Chapter 2: four Vivaldi antennas and two microstrip-to-slotline baluns built on an RO4003C substrate ($\varepsilon_r = 3.55,\ h = 203.2\ \mu m$). The antennas were assembled in a box-like configuration by the help of a 3D-printed support which was designed to ensure the proper placement and alignment of the antennas, and also to absorb the external pressure exerted by measurement cables on the fragile antennas. The system was able to achieve an average self-interference cancellation level of 64 dB over the ultra-wide frequency range from 4 to 40 GHz while maintaining an average gain of 7.8 dBi. The main drawbacks of the presented system are the mechanical fragility resulting from the low thickness of the substrate used, and the emergence of grating lobes in the radiation pattern at some frequencies where the separation distance between the antennas is higher than a half-wavelength.

The mechanical fragility of the PCB system was found to be a limiting factor in practical cases as the antennas were prone to fracturing from a relatively light force, this led us to shift from PCB antennas to more rigid antennas built from thick metallic sheets while sacrificing a portion of the ultra-wide bandwidth. The new antennas were 3D-printed first and then externally metallized, and they were fed by a coax-to-slot transition which was described in detail. The 3D-printed full-duplex array was printed as one piece to achieve precise antenna placement and alignment, and it showed more resistance to external pressure in particular from cables. The array operates from 3 to beyond 20

GHz with more than 40 dB of self-interference cancellation and an average gain of 8.5 dBi throughout the bandwidth. The 3D-printed system also exhibits grating lobes in its radiation pattern, thus we proposed a way to reduce their level by partially reducing the size of the antenna at its bottom, which led to a significant grating lobe reduction at higher frequencies (9 dB reduction at 15 GHz for example).

After demonstrating the wideband potential of the near-field cancellation technique to implement wideband full-duplex antenna arrays with good performance, we moved to add some supplementary features to the arrays, which might interest some applications, in particular the ability to transmit and receive two polarizations simultaneously while operating in full-duplex mode. To achieve this, we needed some dual-polarized Vivaldi antennas that can operate over a wide bandwidth. However, the conventional way of implementing a dual-polarized Vivaldi antenna has many drawbacks and is not so wideband. Thus, we proposed a novel technique that moves the feeding point of the antenna from the center to its sides, which proved to generate wideband matching but leads to asymmetry in the radiation pattern. The full-duplex array was formed by placing and sequentially rotating four of the dual-polarized antennas and was fed by commercial baluns and power dividers. Simulations showed that the array can provide more than 40 dB of cancellation in a bandwidth spanning from 3 GHz to beyond 20 GHz with a gain better than 10 dBi. After that, we presented a balanced way to feed the antenna, with four feeding points where each two are connected to an external balun, that managed to restore the symmetry to the radiation pattern of the antenna. Measurement results for the novel antennas are not yet available and were not presented because the antennas are currently under construction.

Finally, the chapter was enclosed by proposing a new figure of merit dedicated to wideband full-duplex antenna system which takes into account the level of self-interference cancellation, the gain, the bandwidth, and the size of the system. It was found that our fabricated systems achieved the highest score for the newly proposed figure of merit compared to other works in the literature.

General Conclusion

In-band full-duplex is the technology that allows two radios to transmit and receive simultaneously at the same frequency by eliminating the self-interference signals which couple from the transmitter of the radio to its own receiver. Self-interference cancellation techniques could be implemented at all stages of the radio front-end: antenna, analog, and digital domains. State-of-the-art self-interference cancellation techniques were conventionally dedicated for narrowband applications and few works dealt with wideband full-duplex systems. Some of these works were identified to be potentially suitable for wideband self-interference cancellation at the antenna level but no technique can achieve such wideband operation at the analog and digital levels. Thus, in this work, we try to validate the possibility by implementing ultra-wideband full-duplex antenna systems that can be used for multi-standard applications.

Finding a technique that maintains an acceptable level of cancellation at the antenna level throughout the wide bandwidth, without affecting the antenna performance, was the main focus of Chapter 1, where a broad literature review was conducted in order to highlight the available techniques in the literature and to nominate the best candidates for wideband operation. In fact, for monostatic systems, there are few and limited self-interference cancellation techniques because the transmit and receive links share a common feeding network, while techniques for bistatic systems are more versatile, wideband potential, and have more degrees of freedom as the feeding networks for both links are separate. Thus, in this work, we adopted a bistatic technique called near-field cancellation which uses at least four antennas and two 180° out-of-phase power dividers (or baluns) to achieve cancellation. The technique creates a transmit near-field null at the positions of the receive antennas, which contributes to the cancellation procedure, while preserving the far-field behavior of the system without any nulls.

After choosing the desired cancellation technique, the next step was to design some wideband baluns and antennas that can be used in the full-duplex system to achieve the wideband cancellation, and this was the main goal of Chapter 2. So, a thorough literature review on the different ways to implement a wideband balun was conducted first, which led us to choose a wideband balun based on microstrip-to-slotline transitions that can be easily implemented using low-cost PCB technology. The balun consists of three transitions: one central transition that works as an in-phase power divider and two lateral transitions that operate as phase inverters. Based on an extensive parametric analysis that we conducted, we were able to design ultra-wideband microstrip-to-slotline transitions that can operate from around 4 GHz to beyond 40 GHz (a decade bandwidth). The optimized transitions

were used to obtain the wideband balun which operated in the same frequency range with ± 1 dB and ±7° of amplitude and phase imbalances, respectively. Also, the same transitions were used to feed the Vivaldi antennas that we chose as the radiating elements for our systems after presenting a brief review of the available wideband antennas in the literature. The designed antenna is matched over the same bandwidth with a 11.15 dBi average gain and highly directive radiation pattern.

The final step was to assemble and use the designed antennas and baluns to build the targeted full-duplex antenna system, this was discussed in detail in Chapter 3. The four antennas need to be placed such that they are orthogonal and rotated by 90° with respect to one another around the center of the system, taking a box-like shape, and then each two can be fed by a separate balun and used either to transmit or receive. This way of positioning the antennas means that the system transmits and receives in different polarizations. Antenna placement and alignment are critical for the proper operation of the system. Thus, to ensure a precise antenna placement and alignment, we designed and fabricated a 3D-printed support to hold the antennas at the exact position. The 3D-printed support was used to rectify two other problems that resulted from the fragility of the used substrate: the first problem was that the antennas tend to bend naturally as a result of the very thin substrate, so the support was designed to hold the antennas straight and fully erect; while the second problem comes from the tension caused by the relatively heavy cables and connectors used in measurements, which led to fracturing the fabricated devices, thus the 3D-printed support was used also to absorb any external forces that might damage the fabricated devices. The assembled system was matched starting from below 4 GHz to beyond 40 GHz with an average self-interference cancellation level of 64 dB and an average gain of 7.8 dBi. The degradation in gain was attributed to the high losses in the fabricated devices. Moreover, the radiation pattern plots showed another major drawback of the system which is the presence of two grating lobes beside the main lobe of radiation, those grating lobes are more significant at high frequencies and they exist when the separation between the opposite antenna elements is higher than a half-wavelength at a certain frequency.

To overcome the mechanical fragility of the previous system we decided to sacrifice a portion of the bandwidth and increase the thickness of the antennas. For this reason we abandoned the use of printed-circuit boards and decided to make some metallized 3D-printed antennas with sufficient thickness to endure external tension coming from cables. Designing the antennas from thick metallic sheets was first investigated by full-wave simulations and a coax-to-slot transition was specifically designed to feed those antennas, the details of the design process were outlined in Chapter 3. The fabricated system adopts a similar configuration of the PCB system where the four antennas were 3D-printed together in a box-like manner with a small square patch below them that works as a base support and a reflector. System matching was found to span the frequency range from 3 to 28.5 GHz (still close to a decade bandwidth) in measurements with around 62 dB of average self-interference cancellation and almost 8.5 dB of average system gain. Also, the radiation pattern plots of the 3D-printed system presented the same grating lobes behavior of the PCB system, so, in order to mitigate the grating lobe level we proposed a modified antenna configuration where the antenna size was reduced at the bottom of the antenna while it was kept the same at its top. This size reduction allows bringing together the four antennas at their bottom parts while keeping them at the same distance

at their top parts. Since the high frequency radiation of the Vivaldi antenna takes place at its bottom part while the low frequency radiation takes place at its top part, then by bringing the antennas closer to one another at their bottom parts we manage to reduce the high frequency separation distance, and thus we managed to reduce the grating lobe levels by a decent amount (5 dB at 10 GHz and 9 dB at 15 GHz) without affecting the low frequency and the overall performance of the system. The proposed approach of grating lobe reduction might be mechanically challenging, especially in terms of the maximum size reduction that we can perform before the bottom part of the antenna becomes relatively fragile. As a future perspective, alternative techniques can be investigated and developed to reduce the grating lobe level without jeopardizing the mechanical solidity of the system.

Adding some supplementary features to our wideband full-duplex systems such as simultaneously transmitting and receiving in the two orthogonal polarizations might be desired for some applications, so, for this reason, we worked on designing a dual-polarized Vivaldi antenna. To obtain the dual-polarization, usually, two single Vivaldi elements, each with its own feeding, are placed orthogonal to one another at the center of the system. This means that the feedings of the antenna elements will overlap at the center of the system and will affect and create differences in the matching and the radiation of the dual-polarized antenna. Thus, to eliminate the complexities and drawbacks of this overlap, we proposed a new way of feeding the antenna elements, which aims to transfer the feeding points from the center of the antenna to its sides by bending the central slot to the side of the antenna elements. The new way of feeding manages to achieve wideband matching and to overcome the drawbacks of the conventional way, however, it was noticed that it causes an imbalance between the currents flowing on the opposite flares of the antenna which in turn leads to asymmetry in its radiation pattern. The asymmetry in the single antenna radiation pattern is less significant in the dual-polarized full-duplex array, which was formed by placing four dual-polarized Vivaldi antennas and sequentially rotating them by 90° around the center of the array. The dual-polarized array can provide, in simulation, a level of cancellation better than 40 dB and gain higher than 7.5 dBi starting from 4 GHz to beyond 20 GHz. However, due to the relatively big size of the single antenna, about $72.5 \times 72.5 \times 130\ mm^3$, the distance between the centers of opposite antennas becomes big, about 10 cm, which leads to an increase in the level and number of the grating lobes. Thus, for future work, it is worth researching some techniques to reduce the size of the antenna without affecting its performance. At last, the asymmetry in the radiation pattern of the single antenna was solved by introducing a balanced way of feeding which uses four feeding points (one feeding point for each flare) and two external baluns. This way of feeding balances the currents flowing on the opposite flares of the antenna which restores the symmetry to the radiation pattern but at the expense of a more complex and costly feeding network.

Finally, to evaluate and compare our wideband full-duplex systems to some other works in the literature, we proposed a new figure of merit dedicated to wideband full-duplex antenna system ($\mathrm{FOM_{WFD}}$), which takes into account the system bandwidth, the achieved self-interference cancellation level, the gain, and the size of the system. Also, we presented a table that compares our work to other publications and the table showed that our PCB system obtained the highest score for the proposed figure of merit. The figure of merit can be further modified to include additional parameters that might interest other applications. Parameters such as the number of antennas used, complexity of the

system design, type, and number of polarizations, etc. However, in its current form, the proposed figure of merit is sufficient to give a general evaluation of any wideband antenna full-duplex system.

Detailed Contributions

The field of wideband full-duplex systems was not widely explored previously and remained underdeveloped, and our work can be considered as one exploratory journey in that field, which builds upon the findings of the previous works and paves the way for future journeys. The outcomes of our work were discussed, in detail, in the previous section, so, here, we try to list and summarize our achievements and contributions to that field of research:

- Our work manages to generate decade bandwidth full-duplex systems with a level of self-interference cancellation which is $\geq$ 50 dB at the antenna level using a combination of cross-polarization and opposite feeding for the Tx and Rx antennas. The obtained bandwidth, in particular for the PCB system, is remarkable as no other published worked managed to cover such bandwidth, and in those works, usually, multiple systems are implemented to cover a wide bandwidth.
- The presented systems can be used for applications other than in-band full-duplex. For instance, the system, as a whole, can be used to generate dual-polarized waves by feeding all the antennas simultaneously, and, in this case, the cross-coupling between the two polarizations will be reduced by at least 50 dB. In addition to that, the systems can be used to generate circularly-polarized waves by feeding the four ports of the system with signals that have the same amplitudes but their phase are 0°, 90°, 180°, and 270°, respectively.
- The near-field cancellation technique, which was used to build all our systems on, was traditionally implemented using planar antennas (such as patch antennas or spiral antennas) and was never implemented using non-planar antennas. Thus, our work can be considered as one of the first implementations of non-planar systems in that domain whether by using the PCB antennas or the 3D-antennas.
- The microstrip-to-slotline transition can be considered the foundation stone of the PCB system, as it was used to feed the antennas and to form the baluns. Microstrip-to-slotline transitions were sufficiently studied in the literature and indeed several wideband transitions were reported. However, our work is the first to demonstration of a decade bandwidth transition that can operate starting from the C-band at the lower frequency edge and up to the Ka-band at the higher frequency edge, whereas all other works did not manage to surpass the Ku-band.
- Vivaldi arrays, in particular 3D Vivaldi arrays, are usually dedicated for space applications where a very high directivity is required, but they are usually narrowband. Our work can be considered the first to introduce a 3D Vivaldi antenna that can be matched over a very wide-bandwidth. And moreover, we proposed two novel techniques to feed the dual-polarized Vivaldi antennas which helped in overcoming the drawbacks of traditional techniques of feeding.

Appendix A

Microstrip Line and Slotline Equations

The following definitions apply to all equations in this appendix:

h:	is the thickness of the substrate.
ε_r:	is the relative permettivity of the substrate.
ε_{reff}:	is the effective relative permettivity of the substrate.
W_m:	is the width of the microstrip line.
Z_m:	is the impedance of the microstrip line.
η:	is the impedance of free space and is equal to $120\pi\ \Omega$.
λ_0:	is the free space wavelength.
Z_S:	is the impedance of the slotline.
W_s:	is the width of the slotline.

A.1 Microstrip Line Impedance Equations

$$Z_m = \begin{cases} \dfrac{\eta}{2\pi\sqrt{\varepsilon_{reff}}} \ln\left(\dfrac{8h}{W_m} + 0.25\dfrac{W_m}{h}\right) & \text{if } \dfrac{W_m}{h} \leq 1 \\ \dfrac{\eta}{\sqrt{\varepsilon_{reff}}}\left[\dfrac{W_m}{h} + 1.393 + 0.667\ln\left(\dfrac{W_m}{h} + 1.444\right)\right]^{-1} & \text{if } \dfrac{W_m}{h} \geq 1 \end{cases} \tag{A.1}$$

$$\varepsilon_{reff} = \frac{\varepsilon_r + 1}{2} + \frac{\varepsilon - 1}{2}k \tag{A.2}$$

$$k = \begin{cases} \left(1 + 12\dfrac{h}{W_m}\right)^{-0.5} + 0.04\left(1 - \dfrac{W_m}{h}\right)^2 & \text{if } \dfrac{W_m}{h} \leq 1 \\ \left(1 + 12\dfrac{h}{W_m}\right)^{-0.5} & \text{if } \dfrac{W_m}{h} \geq 1 \end{cases} \tag{A.3}$$

A.2 Slotline Impedance and Guided Wavelength Equations

1. For $0.0015 \leq W_s/\lambda_0 \leq 0.075$ and $2.22 \leq \varepsilon_r \leq 3.8$

$$\frac{\lambda_s}{\lambda_0} = 1.045 - 0.365 \ln \varepsilon_r + \frac{6.3(W_s/h)\varepsilon_r^{0.945}}{238.64 + 100 W_s/h} - \left[0.148 - \frac{8.81(\varepsilon_r + 0.95)}{100\ \varepsilon_r}\right] \ln\left(\frac{h}{\lambda_0}\right) \tag{A.4}$$

$$\begin{aligned} Z_s = {} & 60 + 3.69 \sin\left[\frac{(\varepsilon_r - 2.22)\pi}{2.36}\right] + 133.5 \ln(10\ \varepsilon_r)\sqrt{\frac{W_s}{\lambda_0}} \\ & + 2.81\left[1 - 0.011\ \varepsilon_r(4.48 - \ln \varepsilon_r)\right] \frac{W_s}{h} \ln\left(\frac{100h}{\lambda_0}\right) \\ & + 131.1(1.028 - \ln \varepsilon_r)\sqrt{\frac{h}{\lambda_0}} \\ & + 12.48(1 + 0.18 \ln \varepsilon_r)\frac{Ws/h}{\sqrt{\varepsilon_r - 2.06 + 0.85(Ws/h)^2}} \end{aligned} \tag{A.5}$$

2. For $0.0015 \leq W_s/\lambda_0 \leq 0.075$ and $3.8 \leq \varepsilon_r \leq 9.8$

$$\frac{\lambda_s}{\lambda_0} = 0.9217 - 0.277 \ln \varepsilon_r + 0.0322(W_s/h)\sqrt{\frac{\varepsilon_r}{W_s/h + 0.435}} - 0.01 \ln\left(\frac{h}{\lambda_0}\right)\left[4.6 - \frac{3.65}{\varepsilon_r^2\sqrt{W_s/\lambda_0}(9.06 - 100 W_s/h)}\right] \tag{A.6}$$

$$\begin{aligned} Z_s = {} & 73.6 - 2.15\ \varepsilon_r + (638.9 - 31.37\ \varepsilon_r)\left(\frac{W_s}{\lambda_0}\right)^{0.6} \\ & + (36.23\sqrt{\varepsilon_r^2 + 41} - 225)\frac{W_s/h}{W_s/h + 0.876\ \varepsilon_r - 2} \\ & + 0.51(\varepsilon_r + 2.12)\frac{W_s}{h} \ln\left(\frac{100h}{\lambda_0}\right) - 0.753\ \varepsilon_r \frac{h/\lambda_0}{\sqrt{W_s/\lambda_0}} \end{aligned} \tag{A.7}$$

3. For $0.075 \leq W_s/\lambda_0 \leq 1$ and $2.22 \leq \epsilon_r \leq 3.8$

$$\frac{\lambda_s}{\lambda_0} = 1.194 - 0.24 \ln \varepsilon_r - \frac{0.621\ \varepsilon_r^{0.835}(W_s/\lambda_0)^{0.48}}{1.344 + W_s/h} - 0.0617\left[1.91 - \frac{\varepsilon_r + 2}{\varepsilon_r}\right] \ln\left(\frac{h}{\lambda_0}\right) \tag{A.8}$$

$$Z_s = 133 + 10.34(\varepsilon_r - 1.8)^2 + 2.87\left[2.96 + (\varepsilon_r - .1582)^2\right]$$

$$\times \left[\{W_s/h + 2.32\ \varepsilon_r - 0.56\}\{(32.5 - 6.67\ \varepsilon_r)\left(\frac{100h}{\lambda_0}\right)^2 - 1\} \right]^{1/2}$$
$$- \left(684.5\frac{h}{\lambda_0}\right)(\varepsilon_r + 1.35)^2 + 13.23\left[(\varepsilon_r - 1.722)\frac{W_s}{\lambda_0}\right]^2 \quad \text{(A.9)}$$

4. $0.075 \leq W_s/\lambda_0 \leq 1$ and $3.8 \leq \epsilon_r \leq 9.8$

$$\frac{\lambda_s}{\lambda_0} = 1.05 - 0.04\varepsilon_r + 1.411 \times 10^{-2}(\varepsilon_r - 1.421)$$
$$\times \ln\left[\frac{W_s}{h} - 2.012(1 - 0.146\varepsilon_r)\right]$$
$$+ 0.111(1 - 0.366\ \varepsilon_r)\sqrt{\frac{W_S}{\lambda_0}}$$
$$+ 0.139 + 0.52\ \varepsilon_r \ln(14.7 - \varepsilon_r)\left(\frac{h}{\lambda_0}\right)\ln\left(\frac{h}{\lambda_0}\right) \quad \text{(A.10)}$$

$$Z_s = 120.75 - 3.74\ \varepsilon_r + 50[\tan^{-1}(2\ \varepsilon_r) - 0.8]$$
$$\times \left(\frac{W_s}{h}\right)^{[1.11+0.132(\varepsilon_r - 27.7)/(5+100h/\lambda_0)]}$$
$$\times \ln\left[\frac{100h}{\lambda_0} + \sqrt{\left(\frac{100h}{\lambda_0}\right)^2 + 1}\right]$$
$$+ 14.21(1 - 0.458\varepsilon_r)\left(\frac{100h}{\lambda_0} + 5.1\ln\varepsilon_r - 13.1\right)$$
$$\times \left(\frac{W_s}{\lambda_0} + 0.33\right)^2 \quad \text{(A.11)}$$

Publications

National Conferences

- Hijazi, Hadi, Marc Le Roy, Raafat Lababidi, Denis Le Jeune, and Andre Pérennec. "Diviseur de Puissance Compact Ultra-Large-Bande 3-40 GHz." In 21èmes Journées Nationales Microondes, pp. 1-2. 2019.

International Conferences

- Hijazi, Hadi, Marc Le Roy, Raafat Lababidi, Denis Le Jeune, and Andre Pérennec. "4-40 GHz In-Phase/180° Out-of-Phase Power Dividers with Enhanced Isolation." In 2020 14th European Conference on Antennas and Propagation (EuCAP), pp. 1-5. IEEE, 2020.

Unpublished Papers

- "Ultra-Wideband Antenna System for In-Band Full-Duplex Applications" submitted to IET Microwaves, Antennas, and Propagation Journal. The paper discusses the PCB full-duplex system presented in Chapter 3.
- "Ultra-Wideband 3D-Printed Vivaldi Array for In-Band Full-Duplex Applications" submitted to IET Electronics Letters. The paper discusses the 3D-printed full-duplex system which was presented in Chapter 3.
- One or more other papers describing the dual-polarized antennas and full-duplex arrays, which were also discussed in Chapter 3, will be produced once the antenna fabrication and measurements are carried out.

Bibliography

[1] IT Union. IMT Traffic Estimates for the Years 2020 to 2030. *Report ITU*, 2015.

[2] Mohammed S Elbamby, Mehdi Bennis, Walid Saad, Mérouane Debbah, and Matti Latva-aho. Full-Duplex Non-Orthogonal Multiple Access Networks. In *Multiple Access Techniques for 5G Wireless Networks and Beyond*, pages 285–303. Springer, 2019.

[3] Ayaz Ahmad, Sadiq Ahmad, Mubashir Husain Rehmani, and Naveed Ul Hassan. A Survey on Radio Resource Allocation in Cognitive Radio Sensor Networks. *IEEE Communications Surveys & Tutorials*, 17(2):888–917, 2015.

[4] Lin Zhang, Ming Xiao, Gang Wu, Muhammad Alam, Ying-Chang Liang, and Shaoqian Li. A Survey of Advanced Techniques for Spectrum Sharing in 5G Networks. *IEEE Wireless Communications*, 24(5):44–51, 2017.

[5] Andrea Goldsmith. *Wireless Communications*. Cambridge university press, 2005.

[6] TS ETSI. 100 910 v8. 20.0 (2005-11). *Digital cellular telecommunications system (Phase 2+)—Radio Transmission and Reception—3GPP TS 05.05 version 8.20. 0 Release 1999*, 2005.

[7] Dinesh Bharadia, Emily McMilin, and Sachin Katti. Full Duplex Radios. In *Proceedings of the ACM SIGCOMM 2013 conference on SIGCOMM*, pages 375–386, 2013.

[8] Hirley Alves, Taneli Riihonen, and Himal A Suraweera. *Full-Duplex Communications for Future Wireless Networks*. Springer, 2020.

[9] Md Amin, Md Hossain, Mohammed Atiquzzaman, et al. In-Band Full Duplex Wireless LANs: Medium Access Control Protocols, Design Issues and Their Challenges. *Information*, 11(4):216, 2020.

[10] Khalid A Darabkh, Oswa M Amro, Haythem Bany Salameh, and Raed T Al-Zubi. A–Z Overview of the In-Band Full-Duplex Cognitive Radio Networks. *Computer Communications*, 145:66–95, 2019.

[11] Andrew G Stove. Linear FMCW Radar Techniques. In *IEE Proceedings F (Radar and Signal Processing)*, volume 139, pages 343–350. IET, 1992.

[12] Xu Du, John Tadrous, Chris Dick, and Ashutosh Sabharwal. MIMO Broadcast Channel with Continuous Feedback Using Full-Duplex Radios. In *2014 48th Asilomar Conference on Signals, Systems and Computers*, pages 1701–1705. IEEE, 2014.

[13] Jesús Arnau and Marios Kountouris. Timely csi acquisition exploiting full duplex. In *2017 IEEE Wireless Communications and Networking Conference (WCNC)*, pages 1–6. IEEE, 2017.

[14] B. Debaillie, B. van Liempd, B. Hershberg, J. Craninckx, K. Rikkinen, D. J. van den Broek, E. A. M. Klumperink, and B. Nauta. In-band full-duplex transceiver technology for 5g mobile networks. In *ESSCIRC Conference 2015 - 41st European Solid-State Circuits Conference (ESSCIRC)*, pages 84–87, 2015.

[15] Gang Liu, F Richard Yu, Hong Ji, Victor CM Leung, and Xi Li. In-Band Full-Duplex Relaying: A survey, Research Issues and Challenges. *IEEE Communications Surveys & Tutorials*, 17(2):500–524, 2015.

[16] Binh Van Nguyen, Hyoyoung Jung, and Kiseon Kim. Physical Layer Security Schemes for Full-Duplex Cooperative Systems: State of the Art and Beyond. *IEEE Communications Magazine*, 56(11):131–137, 2018.

[17] DW Bliss, PA Parker, and AR Margetts. Simultaneous Transmission and Reception for Improved Wireless Network Performance. In *2007 IEEE/SP 14th Workshop on Statistical Signal Processing*, pages 478–482. IEEE, 2007.

[18] Jung Il Choi, Mayank Jain, Kannan Srinivasan, Phil Levis, and Sachin Katti. Achieving Single Channel, Full Duplex Wireless Communication. In *Proceedings of the sixteenth annual international conference on Mobile computing and networking*, pages 1–12, 2010.

[19] Mayank Jain, Jung Il Choi, Taemin Kim, Dinesh Bharadia, Siddharth Seth, Kannan Srinivasan, Philip Levis, Sachin Katti, and Prasun Sinha. Practical, Real-Time, Full Duplex Wireless. In *Proceedings of the 17th annual international conference on Mobile computing and networking*, pages 301–312, 2011.

[20] Melissa Duarte and Ashutosh Sabharwal. Full-Duplex Wireless Communications Using Off-the-Shelf Radios: Feasibility and First Results. In *2010 Conference Record of the Forty Fourth Asilomar Conference on Signals, Systems and Computers*, pages 1558–1562. IEEE, 2010.

[21] Melissa Duarte, Chris Dick, and Ashutosh Sabharwal. Experiment-Driven Characterization of Full-Duplex Wireless Systems. *IEEE Transactions on Wireless Communications*, 11(12):4296–4307, 2012.

[22] Melissa Duarte and Ashutosh Sabharwal. Full-Duplex Wireless Communications Using Off-the-Shelf Radios: Feasibility and First Results. In *2010 Conference Record of the Forty Fourth Asilomar Conference on Signals, Systems and Computers*, pages 1558–1562. IEEE, 2010.

[23] Ashutosh Sabharwal, Philip Schniter, Dongning Guo, Daniel W Bliss, Sampath Rangarajan, and Risto Wichman. In-Band Full-Duplex Wireless: Challenges and Opportunities. *IEEE Journal on selected areas in communications*, 32(9):1637–1652, 2014.

[24] Dongkyu Kim, Haesoon Lee, and Daesik Hong. A Survey of In-Band Full-Duplex Transmission: From the Perspective of PHY and MAC Layers. *IEEE Communications Surveys & Tutorials*, 17(4):2017–2046, 2015.

[25] Kenneth E Kolodziej, Bradley T Perry, and Jeffrey S Herd. In-band Full-Duplex Technology: Techniques and Systems Survey. *IEEE Transactions on Microwave Theory and Techniques*, 67(7):3025–3041, 2019.

[26] Chinaemerem David Nwankwo, Lei Zhang, Atta Quddus, Muhammad Ali Imran, and Rahim Tafazolli. A Survey of Self-Interference Management Techniques for Single Frequency Full Duplex Systems. *IEEE Access*, 6:30242–30268, 2017.

[27] IEEE Standard for Radar Definitions. *IEEE Std 686-2017 (Revision of IEEE Std 686-2008)*, pages 1–54, 2017.

[28] David M Pozar. *Microwave Engineering*. John Wiley & Sons, 4th edition, 2012.

[29] Jae Ho Jung, Joon Hyung Kim, Sung Min Kim, and Kwang Chun Lee. New Circulator Structure With High Isolation for time Division Duplexing Radio Systems. In *VTC-2005-Fall. 2005 IEEE 62nd Vehicular Technology Conference, 2005.*, volume 4, pages 2766–2769. IEEE, 2005.

[30] Frederic Meyer, Philip Schmidt, Peter Kuhn, Gerd vom Boegel, Marcel Saxler, and Anton Grabmaier. A Comparison of Several Carrier Suppression Techniques. In *Smart SysTech 2016; European Conference on Smart Objects, Systems and Technologies*, pages 1–7. VDE, 2016.

[31] Seiran Khaledian, Frahad Farzami, Besma Smida, and Danilo Erricolo. Inherent Self-Interference Cancellation at 900 MHz for In-Band Full-Duplex Applications. In *2018 IEEE 19th Wireless and Microwave Technology Conference (WAMICON)*, pages 1–4. IEEE, 2018.

[32] Seiran Khaledian, Farhad Farzami, Besma Smida, and Danilo Erricolo. Inherent Self-Interference Cancellation for In-Band Full-Duplex Single-Antenna Systems. *IEEE Transactions on Microwave Theory and Techniques*, 66(6):2842–2850, 2018.

[33] George A Campbell and Ronald M Foster. Maximum Output Networks for Telephone Substation and Repeater Circuits. *Transactions of the American Institute of Electrical Engineers*, 39(1):231–290, 1920.

[34] Eugene Sartori. Hybrid Transformers. *IEEE Transactions on Parts, Materials and Packaging*, 4(3):59–66, 1968.

[35] Zhong Hu Ma and Jian Hong Yang. A High Isolation Rate Race Circuit Compose the Carrier Leakage Canceler for RFID. In *Applied Mechanics and Materials*, volume 236, pages 994–998. Trans Tech Publ, 2012.

[36] Yi-Ming Zhang, Shuai Zhang, Jia-Lin Li, and Gert Frølund Pedersen. A Dual-Polarized Linear Antenna Array with Improved Isolation Using a Slotline-Based 180° Hybrid for Full-Duplex Applications. *IEEE Antennas and Wireless Propagation Letters*, 18(2):348–352, 2019.

[37] Xuekun Du, Zhenhai Shao, and Chang Jiang You. Implementation of an X Band Leakage Cancellation Network for Bandwidth Improvement. In *2015 Asia-Pacific Microwave Conference (APMC)*, volume 2, pages 1–3. IEEE, 2015.

[38] Udara De Silva, Sravan Pulipati, Satheesh Bojja Venkatakrishnan, Shubhendu Bhardwaj, and Arjuna Madanayake. A Passive STAR Microwave Circuit for 1-3 GHz Self-Interference Cancellation. In *2020 IEEE 63rd International Midwest Symposium on Circuits and Systems (MWSCAS)*, pages 105–108. IEEE, 2020.

[39] Han-Lim Lee, Wang-Ik Son, and Jong-Won Yu. 24-GHz Transceiver Patch Array Front-End with a Balanced Tx Leakage Canceller. *Microwave and Optical Technology Letters*, 53(3):559–562, 2011.

[40] Han Lim Lee, Won-Gyu Lim, Kyoung-Sub Oh, and Jong-Won Yu. 24 GHz Balanced Doppler Radar Front-End with Tx Leakage Canceller for Antenna Impedance Variation and Mutual Coupling. *IEEE Transactions on Antennas and Propagation*, 59(12):4497–4504, 2011.

[41] Ehab A Etellisi, Mohamed A Elmansouri, and Dejan S Filipovic. Wideband Monostatic Spiral Array for Full-Duplex Applications. In *2017 IEEE International Symposium on Antennas and Propagation & USNC/URSI National Radio Science Meeting*, pages 1101–1102. IEEE, 2017.

[42] Jeong-Geun Kim, Sangsoo Ko, Sanghoon Jeon, Jae-Woo Park, and Songcheol Hong. Balanced Topology to Cancel Tx Leakage in CW Radar. *IEEE Microwave and wireless components letters*, 14(9):443–445, 2004.

[43] Choul-Young Kim, Jeong-Geun Kim, Donghyun Baek, and Songcheol Hong. A Circularly Polarized Balanced Radar Front-End with a Single Antenna for 24-GHz Radar Applications. *IEEE transactions on microwave theory and techniques*, 57(2): 293–297, 2008.

[44] Jeong-Geun Kim, Sangsoo Ko, Sanghoon Jeon, Jae-Woo Park, and Songcheol Hong. Balanced Topology to Cancel Tx Leakage in CW Radar. *IEEE Microwave and wireless components letters*, 14(9):443–445, 2004.

[45] Peng Bai, Yingzeng Yin, and Xi Yang. A Novel Rx-Tx Front-Ends for Passive RFID Reader with High Isolation. In *2007 International Symposium on Microwave, Antenna, Propagation and EMC Technologies for Wireless Communications*, pages 332–335. IEEE, 2007.

[46] Patrícia Bouça, João Nuno Matos, Sérgio Reis Cunha, and Nuno Borges Carvalho. Low-Profile Aperture-Coupled Patch Antenna Array for CubeSat Applications. *IEEE Access*, 8:20473–20479, 2020.

[47] Huy Hung Tran, Nghia Nguyen-Trong, and Hyun Chang Park. A Compact Dual Circularly Polarized Antenna with Wideband Operation and High Isolation. *IEEE Access*, 2020.

[48] Paul Le Bihan, Yelzhas Zhaksylyk, Pascual David Hilario Re, Symon K Podilchak, María García-Vigueras, and George Goussetis. Dual-Circularly Polarized Patch Antenna Using Simple Isolation Techniques and Its Array Application. 2018.

[49] Markus Berg, Rameez Ur Rahman Lighari, Tommi Tuovinen, and Erkki T Salonen. Circularly Polarized GPS Antenna for Simultaneous LHCP and RHCP Reception with High Isolation. In *2016 Loughborough Antennas & Propagation Conference (LAPC)*, pages 1–4. IEEE, 2016.

[50] Xiao-Zheng Lai, Ze-Ming Xie, Qi-Qiu Xie, and Xuan-Liang Cen. A Dual Circularly Polarized RFID Reader Antenna with Wideband Isolation. *IEEE Antennas and Wireless Propagation Letters*, 12:1630–1633, 2013.

[51] Michael E Knox. Single Antenna Full Duplex Communications Using a Common Carrier. In *WAMICON 2012 IEEE Wireless & Microwave Technology Conference*, pages 1–6. IEEE, 2012.

[52] Michael E Knox. Passive Interference Cancellation in a 2× 2 STAR MIMO Antenna Network. In *2019 International Workshop on Antenna Technology (iWAT)*, pages 221–224. IEEE, 2019.

[53] Changyoung An and Heung-Gyoon Ryu. Double Balanced Feed Network for the Self-Interference Cancellation in Full Duplex Communication System. *Wireless Personal Communications*, 92(4):1599–1610, 2017.

[54] Myunggi Kim, Changyoung An, and Heung-Gyoon Ryu. Effective Self-Interference Cancellation for IBFD (In-Band Full Duplex) Communication System. In *2019 Eleventh International Conference on Ubiquitous and Future Networks (ICUFN)*, pages 490–493. IEEE, 2019.

[55] Myunggi Kim and Heung-Gyoon Ryu. Bandwidth Expansion of the IBFD Communication System Using Balanced Feed Networks. In *2020 IEEE 91st Vehicular Technology Conference (VTC2020-Spring)*, pages 1–4. IEEE, 2020.

[56] Prathap Valale Prasannakumar and Mohamed A Elmansouri. Full-Duplex Antenna Subsystem for Microwave Radio Links.

[57] Prathap Valale Prasannakumar, Mohamed A Elmansouri, and Dejan S Filipovic. Broadband Monostatic Simultaneous Transmit and Receive Reflector Antenna System. In *2017 IEEE International Symposium on Antennas and Propagation & USNC/URSI National Radio Science Meeting*, pages 553–554. IEEE, 2017.

[58] Prathap Valale Prasannakumar, Mohamed A Elmansouri, and Dejan S Filipovic. Broadband Reflector Antenna with High Isolation Feed for Full-Duplex Applications. *IEEE Transactions on Antennas and Propagation*, 66(5):2281–2290, 2018.

[59] Ehab A Etellisi, Mohamed A Elmansouri, and Dejan S Filipović. Wideband Multimode Monostatic Spiral Antenna STAR Subsystem. *IEEE Transactions on Antennas and Propagation*, 65(4):1845–1854, 2017.

[60] Won-Gyu Lim and Jong-Won Yu. Balanced Circulator Structure with Enhanced Isolation Characteristics. *Microwave and Optical Technology Letters*, 50(9):2389–2391, 2008.

[61] Won-Gyu Lim, Seo-Young Park, Sang-Yun Lee, Moon-Que Lee, and Jong-Won Yu. Balanced Directional Coupler Structure with Insensitive Isolation for Load Impedance. In *2008 38th European Microwave Conference*, pages 1280–1283. IEEE, 2008.

[62] Siu K Cheung, William H Weedon, and Craig P Caldwell. High Isolation Lange-Ferrite Circulators with NF Suppression for Simultaneous Transmit and Receive. In *2010 IEEE MTT-S International Microwave Symposium*, pages 1352–1355. IEEE, 2010.

[63] S Cheung, T Halloran, W Weedon, and C Caldwell. Active Quasi-Circulators Using Quadrature Hybrids for Simultaneous Transmit and Receive. In *2009 IEEE MTT-S International Microwave Symposium Digest*, pages 381–384. IEEE, 2009.

[64] Siu K Cheung, Timothy P Halloran, William H Weedon, and Craig P Caldwell. MMIC-Based Quadrature Hybrid Quasi-Circulators for Simultaneous Transmit and Receive. *IEEE transactions on microwave theory and techniques*, 58(3):489–497, 2010.

[65] Vojislav Milosevic, Milos Radovanovic, Branka Jokanovic, Olga Boric-Lubecke, and Victor M Lubecke. Tx Leakage Cancellation Using Antenna Image Impedance for CW Radar Applications. In *2016 46th European Microwave Conference (EuMC)*, pages 425–428. IEEE, 2016.

[66] Won-Gyu Lim, Seo-Young Park, Wang-Ik Son, Moon-Que Lee, and Jong-Won Yu. RFID Reader Front-End Having Robust Tx Leakage Canceller for Load Variation. *IEEE Transactions on microwave theory and techniques*, 57(5):1348–1355, 2009.

[67] Hyeong-Seok Jang, Won-Gyu Lim, and Jong-Won Yu. UHF RFID Reader Front-End Having Wideband and Stable Tx/Rx Isolation Characteristic. *Microwave and Optical Technology Letters*, 52(11):2467–2473, 2010.

[68] Han-Lim Lee, Dong-Hoon Park, Hyun-Sung Tae, Moon-Que Lee, and Jong-Won Yu. Four-Port Balanced Antenna Feeding Network for Switchable Polarizations and Stable Tx/Rx Isolation Characteristics. *Microwave and Optical Technology Letters*, 56(1):17–23, 2014.

[69] Hyun-Seung Lee and Choul-Young Kim. An LTCC Multilayer Packaged 24-Ghz Short-Range Radar with an Embeded Tx Leakage Canceller. *Microwave and Optical Technology Letters*, 56(3):671–677, 2014.

[70] Choul-Young Kim, Jeong-Geun Kim, and Songcheol Hong. A Quadrature Radar Topology with Tx Leakage Canceller for 24-GHz Radar Applications. *IEEE transactions on microwave theory and techniques*, 55(7):1438–1444, 2007.

[71] Choul-Young Kim, Jeong Geun Kim, Joon Ho Oum, Jong Ryul Yang, Dong-Kyun Kim, Jung Han Choi, Sang-Wook Kwon, Sang-Hoon Jeon, Jae-Woo Park, and Songcheol Hong. Tx Leakage Cancellers for 24 GHz and 77 GHz Vehicular Radar Applications. In *2006 IEEE MTT-S International Microwave Symposium Digest*, pages 1402–1405. IEEE, 2006.

[72] Aimin Tang and Xudong Wang. Balanced RF-Circuit Based Self-Interference Cancellation for Full Duplex Communications. *Ad Hoc Networks*, 24:214–227, 2015.

[73] Mohammed Mahdi, Mohammad Darwish, Hossam Tork, and Ayman A Eltager. Balun Based Transmitter Leakage Cancellation for Wide-Band Applications. In *2020 12th International Conference on Electrical Engineering (ICEENG)*, pages 254–257. IEEE, 2020.

[74] Farnaz Foroughian and Aly E Fathy. Wideband Leakage Cancellation Network for Monostatic Continuous-Wave Radars. In *2019 United States National Committee of URSI National Radio Science Meeting (USNC-URSI NRSM)*, pages 1–2. IEEE, 2019.

[75] Wan-Kyu Kim, Moon-Que Lee, Jin-Hyun Kim, Hyung-Sun Lim, Jong-Won Yu, Byung-Jun Jang, and Jun-Seok Park. A Passive Circulator with High Isolation Using a Directional Coupler for RFID. In *2006 IEEE MTT-S International Microwave Symposium Digest*, pages 1177–1180. IEEE, 2006.

[76] Wan-Kyu Kim, Won Na, Jong-Won Yu, and Moon-Que Lee. A High Isolated Coupled-Line Passive Circulator for UHF RFID Reader. *Microwave and Optical Technology Letters*, 50(10):2597–2600, 2008.

[77] Hui Zhuang, Jintao Li, Weibiao Geng, Xiaoming Dai, Zhongshan Zhang, and Athanasios V Vasilakos. Duplexer Design and Implementation for Self-Interference Cancellation in Full-Duplex Communications. In *2016 24th European Signal Processing Conference (EUSIPCO)*, pages 125–129. IEEE, 2016.

[78] Feng Wei, XW Shi, QL Huang, DZ Chen, and XH Wang. A New Directional Coupler for UHF RFID Reader. *Microwave and Optical Technology Letters*, 50(7): 1973–1975, 2008.

[79] Sung-Chan Jung, Min-Su Kim, and Youngoo Yang. A Reconfigurable Carrier Leakage Canceler for UHF RFID Reader Front-Ends. *IEEE Transactions on Circuits and Systems I: Regular Papers*, 58(1):70–76, 2010.

[80] Moon-Que Lee. Lumped Directional Coupler with a Varactor Tuned Reflector for RFID Applications. *IEICE Electronics Express*, 6(2):129–134, 2009.

[81] Edward A Keehr. A Low-Cost, High-Speed, High-Resolution, Adaptively Tunable Microwave Network for an SDR UHF RFID Reader Reflected Power Canceller. In *2018 IEEE International Conference on RFID (RFID)*, pages 1–8. IEEE, 2018.

[82] Bo-Yoon Yoo, Jae-Hyun Park, and Jong-Ryul Yang. Quasi-Circulator Using an Asymmetric Coupler for Tx Leakage Cancellation. *Electronics*, 7(9):173, 2018.

[83] Harald T Friis. A Note on a Simple Transmission Formula. *Proceedings of the IRE*, 34(5):254–256, 1946.

[84] Evan Everett, Achaleshwar Sahai, and Ashutosh Sabharwal. Passive Self-Interference Suppression for Full-Duplex Infrastructure Nodes. *IEEE Transactions on Wireless Communications*, 13(2):680–694, 2014.

[85] Nathan Jastram and Dejan S Filipovic. Isolation of Millimeter Wave Antennas Over Cylindrical and Rectangular Ground Planes. In *2016 IEEE International Symposium on Antennas and Propagation (APSURSI)*, pages 2201–2202. IEEE, 2016.

[86] Prathap Valale Prasannakumar, Mohamed A Elmansouri, and Dejan S Filipovic. Wideband Bi-static Offset-Fed Reflector Simultaneous Transmit And Receive Antenna System. In *2018 IEEE Indian Conference on Antennas and Propogation (InCAP)*, pages 1–3. IEEE, 2018.

[87] Kahani Kumari, Rahul Kumar Jaiswal, and Kumar Vaibhav Srivastava. A dual band full-duplex monopole antenna for wlan application. In *2019 IEEE Indian Conference on Antennas and Propogation (InCAP)*, pages 1–4. IEEE, 2019.

[88] Jingni Zhong, Elias A Alwan, and John L Volakis. Ultra-Wideband Dual-Linear Polarized Phased Array With 60° Scanning for Simultaneous Transmit and Receive Systems. In *2017 International Workshop on Antenna Technology: Small Antennas, Innovative Structures, and Applications (iWAT)*, pages 140–141. IEEE, 2017.

[89] Haq Nawaz and Ibrahim Tekin. Three Dual Polarized 2.4 GHz Microstrip Patch Antennas for Active Antenna and In-Band Full Duplex Applications. In *2016 16th Mediterranean Microwave Symposium (MMS)*, pages 1–4. IEEE, 2016.

[90] Haq Nawaz and I Tekin. Three Ports Microstrip Patch Antenna With Dual Linear and Linear Co-polarisation Characteristics. *Electronics Letters*, 53(8):518–520, 2017.

[91] Haq Nawaz and Ibrahim Tekin. Compact Dual-Polarised Microstrip Patch Antenna With High Interport Isolation for 2.5 GHz In-Band Full-Duplex Wireless Applications. *IET Microwaves, Antennas & Propagation*, 11(7):976–981, 2017.

[92] Haq Nawaz, Özgür Gürbüz, and I Tekin. High Isolation Slot Coupled Antenna With Integrated Tunable Self-Interference Cancellation Circuitry. *Electronics Letters*, 54 (23):1311–1312, 2018.

[93] Haq Nawaz and Muhammad Abdul Basit. Single Layer, Dual Polarized, 2.4 GHz Patch Antenna With Very High RF Isolation Between DC isolated Tx-Rx ports for Full Duplex Radio. *Progress In Electromagnetics Research*, 85:65–72, 2019.

[94] Haq Nawaz, Özgür Gürbüz, and I Tekin. 2.4 GHz Dual Polarised Monostatic Antenna with Simple Two-Tap RF Self-Interference Cancellation (RF-SIC) Circuitry. *Electronics Letters*, 55(6):299–300, 2019.

[95] Haq Nawaz, Özgür Gürbüz, and Ibrahim Tekin. Co-polarized Monostatic Antenna With High Tx-Rx Isolation for 2.4 GHz Single Channel Full Duplex Applications. *Microwave and Optical Technology Letters*, 61(4):1065–1069, 2019.

[96] Haq Nawaz, Muhammad A Basit, and Furqan Shaukat. Dual Polarized, Slot Coupled Monostatic Antenna With High Isolation for 2.4 GHz Full Duplex Applications. *Microwave and Optical Technology Letters*, 62(3):1291–1298, 2020.

[97] Haq Nawaz and Ahmad U Niazi. A Compact Proximity-Fed 2.4 GHz Monostatic Antenna With Wide-Band SIC Characteristics for In-Band Full Duplex Applications. *International Journal of RF and Microwave Computer-Aided Engineering*, 30(3):e22087, 2020.

[98] Mikail Yilan, Hayrettin Ayar, Haq Nawaz, Ozgur Gurbuz, and Ibrahim Tekin. Monostatic Antenna In-Band Full Duplex Radio: Performance Limits and Characterization. *IEEE Transactions on Vehicular Technology*, 68(5):4786–4799, 2019.

[99] Muhammad Sohaib Amjad, Haq Nawaz, Kerem Özsoy, Özgür Gürbüz, and Ibrahim Tekin. A Low-Complexity Full-Duplex Radio Implementation With a Single Antenna. *IEEE Transactions on Vehicular Technology*, 67(3):2206–2218, 2017.

[100] Girdhari Chaudhary, Junhyung Jeong, Phanam Pech, Phirun Kim, and Yongchae Jeong. High Self-Interference Cancellation Antenna for In-Band Full Duplex Communication System. In *2019 49th European Microwave Conference (EuMC)*, pages 236–239. IEEE, 2019.

[101] Girdhari Chaudhary, Junhyung Jeong, and Yongchae Jeong. Differential Fed Antenna With High Self-Interference Cancellation for In-Band Full-Duplex Communication System. *IEEE Access*, 7:45340–45348, 2019.

[102] Girdhari Chaudhary, Junhyung Jeong, Yongchae Jeong, and Woonchul Ham. Microstrip antenna with high self-interference cancellation using phase reconfigurable feeding network for in-band full duplex communication. *Microwave and Optical Technology Letters*, 62(2):919–925, 2020.

[103] Haq Nawaz, Ahmad Umar Niazi, M Abdul Basit, Furqan Shaukat, and Muhammad Usman. Dual-Polarized, Monostatic Antenna Array With Improved Tx-Rx Isolation for 2.4 GHz In-Band Full Duplex Applications. *International Journal of Microwave and Wireless Technologies*, 12(5):398–408, 2020.

[104] Tolga Dinc, Anandaroop Chakrabarti, and Harish Krishnaswamy. A 60 GHz CMOS full-duplex transceiver and link with polarization-based antenna and RF cancellation. *IEEE journal of solid-state circuits*, 51(5):1125–1140, 2016.

[105] Seiran Khaledian, Farhad Farzami, Besma Smida, and Danilo Erricolo. Robust Self-Interference Cancellation for Microstrip Antennas by Means of Phase Reconfigurable Coupler. *IEEE Transactions on Antennas and Propagation*, 66(10):5574–5579, 2018.

[106] KueiJih Lu, Carlene Goodbody, Tutku Karacolak, and Nghi Tran. An Interior Parasitic Patch Antenna with Wide Isolation Bandwidth for Simultaneous Transmit

and Receive (STAR). In *2019 IEEE International Symposium on Antennas and Propagation and USNC-URSI Radio Science Meeting*, pages 1513–1514. IEEE, 2019.

[107] Juan M Laco, Fernando H Gregorio, Gustavo González, Juan E Cousseau, Taneli Riihonen, and Risto Wichman. Patch Antenna Design for Full-Duplex Transceivers. In *2017 European Conference on Networks and Communications (EuCNC)*, pages 1–5. IEEE, 2017.

[108] T Nguyen and T Karacolak. Planar Patch Antenna System With High Isolation for Full-Duplex Applications. *Electronics Letters*, 55(25):1326–1329, 2019.

[109] Yang Cai, Liu Yang, Yingsong Zhang, and Zuping Qian. Millimeter Wave Low-Profile Relay Antennas for 5G Full Duplex Self-Interference Suppression. In *2017 IEEE International Conference on Signal Processing, Communications and Computing (ICSPCC)*, pages 1–4. IEEE, 2017.

[110] Haq Nawaz, Ahmad Umar Niazi, Muhammad Abdul Basit, and Muhammad Usman. Single Layer, Differentially Driven, LHCP Antenna With Improved Isolation for Full Duplex Wireless Applications. *IEEE Access*, 7:169796–169806, 2019.

[111] Jaegeun Ha, Mohamed A Elmansouri, Prathap Valale Prasannakumar, and Dejan S Filipovic. Monostatic Co-polarized Full-Duplex Antenna With Left-or Right-Hand Circular Polarization. *IEEE Transactions on Antennas and Propagation*, 65(10): 5103–5111, 2017.

[112] Jie Wu, Mingjian Li, and Nader Behdad. A Wideband, Unidirectional Circularly Polarized Antenna for Full-Duplex Applications. *IEEE Transactions on Antennas and Propagation*, 66(3):1559–1563, 2018.

[113] Jie Wu, Yu Jian Cheng, Mingjian Li, and Nader Behdad. Circularly-Polarized, Unidirectional Antennas for Simultaneous Transmit and Receive (STAR) Applications. In *2017 IEEE International Symposium on Antennas and Propagation & USNC/URSI National Radio Science Meeting*, pages 2183–2184. IEEE, 2017.

[114] Di Wu, Yu-Xiang Sun, Bo Wang, and Ruina Lian. A Compact, Monostatic, Co-Circularly Polarized Simultaneous Transmit And Receive (STAR) Antenna With High Isolation. *IEEE Antennas and Wireless Propagation Letters*, 2020.

[115] Allan Pen, Marc Le Roy, Raafat Lababidi, Denis Le Jeune, André Perennec, Jean-Luc Issler, Kevin Elis, Adrien Gay, and Jean-Hervé Corre. Broadside FD Antenna Topologies for Nanosat Intersatellite Link. In *2020 18th IEEE International New Circuits and Systems Conference (NEWCAS)*, pages 242–245. IEEE, 2020.

[116] Mohammad Ranjbar Nikkhah, Jie Wu, Hung Luyen, and Nader Behdad. A Concurrently-Dual-Polarized, Simultaneous Transmit and Receive (STAR) Antenna. *IEEE Transactions on Antennas and Propagation*, 2020.

[117] Ziheng Zhou, Yue Li, Jiadong Hu, Yijing He, Zhijun Zhang, and Pai-Yen Chen. Monostatic Copolarized Simultaneous Transmit and Receive (STAR) Antenna by Integrated Single-Layer Design. *IEEE Antennas and Wireless Propagation Letters*, 18(3):472–476, 2019.

[118] Yi-Ming Zhang and Jia-Lin Li. Analyses and Full-Duplex Applications of Circularly Polarized OAM Arrays Using Sequentially Rotated Configuration. *IEEE Transactions on Antennas and Propagation*, 66(12):7010–7020, 2018.

[119] Prafulla Deo, Dariush Mirshekar-Syahkal, Gan Zheng, Arpan Pal, and Amit Mehta. Broadband Antenna for Passive Self-Interference Suppression in Full-Duplex Communications. In *2018 IEEE Radio and Wireless Symposium (RWS)*, pages 243–245. IEEE, 2018.

[120] Prafulla Deo, Dariush Mirshekar-Syahkal, and Gan Zheng. EBG Enhanced Broadband Dual Antenna Configuration for Passive Self-Interference Suppression in Full-Duplex Communications. In *2018 15th European Radar Conference (EuRAD)*, pages 461–464. IEEE, 2018.

[121] Gregory Makar, Nghi Tran, and Tutku Karacolak. A High-Isolation Monopole Array With Ring Hybrid Feeding Structure for In-Band Full-Duplex Systems. *IEEE Antennas and Wireless Propagation Letters*, 16:356–359, 2016.

[122] N Raymondi, M Seredich, T Karacolak, NH Tran, and DHN Nguyen. Compact and Power-Efficient 5 GHz Full-Duplex Design Utilizing the 180° Ring Hybrid Coupler. In *2017 International Conference on Recent Advances in Signal Processing, Telecommunications & Computing (SigTelCom)*, pages 170–174. IEEE, 2017.

[123] Trevor Snow, Caleb Fulton, and William J Chappell. Multi-Antenna Near Field Cancellation Duplexing for Concurrent Transmit and Receive. In *2011 IEEE MTT-S International Microwave Symposium*, pages 1–4. IEEE, 2011.

[124] Donghyun Lee and Byung-Wook Min. 2 x 2 MIMO In-Band Full-Duplex Radio Front-End With 50 dB Self-Interference Cancellation in 90 MHz Bandwidth. In *2017 IEEE MTT-S International Microwave Symposium (IMS)*, pages 670–672. IEEE, 2017.

[125] Donghyun Lee and Byung-Wook Min. 1-TX and 2-RX In-Band Full-Duplex Radio Front-End With 60 dB Self-Interference Cancellation. In *2015 IEEE MTT-S International Microwave Symposium*, pages 1–4. IEEE, 2015.

[126] Elie G Tianang and Dejan S Filipovic. A Dipole Antenna System for Simultaneous Transmit and Receive. In *2015 IEEE International Symposium on Antennas and Propagation & USNC/URSI National Radio Science Meeting*, 2015.

[127] Camille Jouvaud, David Dassonville, and Patrick Rosson. High Self-Interference Mitigation Achieved Thanks to Significant Antenna Isolation and Advanced RF Frontend for In-Band Full-Duplex Communications. In *2019 49th European Microwave Conference (EuMC)*, pages 1072–1075. IEEE, 2019.

[128] Kang Luo, Wei-Ping Ding, Yong-Jin Hu, and Wen-Quan Cao. Design of Dual-Feed Dual-Polarized Microstrip Antenna With High Isolation and Low Cross Polarization. *Progress in Electromagnetics Research*, 36:31–40, 2013.

[129] Koffi Gbafa, A Diallol, Philippe Le Thuc, and Robert Staraj. Tx/Rx Antenna System for Full-Duplex Application. In *2018 IEEE International Symposium on*

Antennas and Propagation & USNC/URSI National Radio Science Meeting, pages 1571–1572. IEEE, 2018.

[130] Koffi Gbafa, Aliou Diallo, Philippe Le Thuc, and Robert Staraj. High Isolated MIMO Antenna System for Full-Duplex 5G Applications. In *2019 IEEE Conference on Antenna Measurements & Applications (CAMA)*, pages 49–52. IEEE, 2019.

[131] Ehab A Etellisi, Mohamed A Elmansouri, and Dejan S Filipovic. Co-Channel Simultaneous Transmit and Receive with 3-Element Array Antenna. In *2019 International Applied Computational Electromagnetics Society Symposium (ACES)*, pages 1–2. IEEE, 2019.

[132] A Mohammad, Karthik Sundaresan, Sampath Rangarajan, Xinyu Zhang, and Sanaz Barghi. The Case for Antenna Cancellation for Scalable Full-Duplex Wireless Communications. *ACM Hotnets, Cambridge, MA, USA*, 2011.

[133] Ehsan Aryafar, Mohammad Amir Khojastepour, Karthikeyan Sundaresan, Sampath Rangarajan, and Mung Chiang. MIDU: Enabling MIMO Full Duplex. In *Proceedings of the 18th annual international conference on Mobile computing and networking*, pages 257–268, 2012.

[134] Jie Wu, Cong Wang, and Yong Xin Guo. Dual-Band Co-Aperture Planar Array Antenna Constituted of Segmented Patches. *IEEE Antennas and Wireless Propagation Letters*, 19(2):257–261, 2019.

[135] Ariunzaya Batgerel and Soon Young Eom. High-Isolation Microstrip Patch Array Antenna For Single Channel Full Duplex Communications. *IET Microwaves, Antennas & Propagation*, 9(11):1113–1119, 2015.

[136] Yi-Ming Zhang and Jia-Lin Li. Differential-Series-Fed Dual-Polarized Traveling-Wave Array for Full-Duplex Applications. *IEEE Transactions on Antennas and Propagation*, 68(5):4097–4102, 2019.

[137] Dejan S Filipovic, Mohamed Elmansouri, and Ehab A Etellisi. On wideband Simultaneous Transmit and Receive (STAR) With a Single Aperture. In *2016 IEEE International Symposium on Antennas and Propagation (APSURSI)*, pages 1075–1076. IEEE, 2016.

[138] Elias A Alwan, Alexander Hovsepian, and John L Volakis. Ultra-Wideband Dual Polarization Arrays With Collocated Elements for High Isolation Simultaneous Transmit and Receive Systems. In *2016 IEEE International Symposium on Phased Array Systems and Technology (PAST)*, pages 1–3. IEEE, 2016.

[139] Mohamed A Elmansouri, Andrew J Kee, and Dejan S Filipovic. Wideband Antenna Array for Simultaneous Transmit and Receive (STAR) Applications. *IEEE Antennas and Wireless Propagation Letters*, 16:1277–1280, 2016.

[140] Alexander Hovsepian, Elias A Alwan, and John L Volakis. Wideband Scanning Array of Spiral Antennas for Simultaneous Transmit and Receive (STAR). In *2017 IEEE International Symposium on Antennas and Propagation & USNC/URSI National Radio Science Meeting*, pages 487–488. IEEE, 2017.

[141] Alexander Hovsepian, Satheesh Bojja Venkatakrishnan, Elias A Alwan, and John L Volakis. Wideband Beam Steering Using a 4-Arm Spiral Array for Simultaneous Transmit and Receive (STAR) Operation. In *2018 IEEE International Symposium on Antennas and Propagation & USNC/URSI National Radio Science Meeting*, pages 1915–1916. IEEE, 2018.

[142] Alexander Hovsepian, Elias A Alwan, and John L Volakis. A Wideband, Scanning Array of Four-Arm Spiral Elements for Simultaneous Transmit and Receive. *IEEE Antennas and Wireless Propagation Letters*, 19(4):537–541, 2020.

[143] Ehab A Etellisi, Mohamed A Elmansouri, and Dejan S Filipovic. Wideband Monostatic Simultaneous Transmit and Receive (STAR) Antenna. *IEEE Transactions on Antennas and Propagation*, 64(1):6–15, 2015.

[144] Ehab A Etellisi, Mohamed A Elmansouri, and Dejan S Filipovic. Wideband Monostatic Co-Polarized Co-Channel Simultaneous Transmit and Receive Broadside Circular Array Antenna. *IEEE Transactions on Antennas and Propagation*, 67(2):843–852, 2018.

[145] KE Kolodziej, PT Hurst, AJ Fenn, and LI Parad. Ring Array Antenna With Optimized Beamformer for Simultaneous Transmit and Receive. In *Proceedings of the 2012 IEEE International Symposium on Antennas and Propagation*, pages 1–2. IEEE, 2012.

[146] KE Kolodziej and BT Perry. Vehicle-Mounted Star Antenna Isolation Performance. In *2015 IEEE International Symposium on Antennas and Propagation & USNC/URSI National Radio Science Meeting*, pages 1602–1603. IEEE, 2015.

[147] KE Kolodziej, JG McMichael, and BT Perry. Simultaneous Transmit and Receive Antenna Isolation Improvement in Scattering Environments. In *2014 IEEE Antennas and Propagation Society International Symposium (APSURSI)*, pages 2228–2229. IEEE, 2014.

[148] Ehab A Etellisi, Mohamed A Elmansouri, and Dejan S Filipovic. Wideband Simultaneous Transmit and Receive (STAR) Bi-Layer Circular Array. In *2015 IEEE International Symposium on Antennas and Propagation & USNC/URSI National Radio Science Meeting*, pages 2227–2228. IEEE, 2015.

[149] Ehab A Etellisi, Mohamed A Elmansouri, and Dejan S Filipović. Wideband Simultaneous Transmit and Receive (STAR) Circular Array System. In *2016 IEEE International Symposium on Phased Array Systems and Technology (PAST)*, pages 1–5. IEEE, 2016.

[150] Ehab A Etellisi, Mohamed A Elmansouri, and Dejan Filipovic. Broadband Full-Duplex Monostatic Circular-Antenna Arrays: Circular Arrays Reaching Simultaneous Transmit and Receive Operation. *IEEE Antennas and Propagation Magazine*, 60(5):62–77, 2018.

[151] Ruina Lian, Ting-Yen Shih, Yingzeng Yin, and Nader Behdad. A High-Isolation, Ultra-Wideband Simultaneous Transmit and Receive Antenna With Monopole-Like

Radiation Characteristics. *IEEE Transactions on Antennas and Propagation*, 66 (2):1002–1007, 2017.

[152] Di Wu, Yuzhang Zang, Hung Luyen, Mingjian Li, and Nader Behdad. A Compact, Low-Profile Simultaneous Transmit and Receive Antenna With Monopole-Like Radiation Characteristics. *IEEE Antennas and Wireless Propagation Letters*, 18 (4):611–615, 2019.

[153] Ahmed H Abdelrahman and Dejan S Filipovic. Antenna System for Full-Duplex Operation of Handheld Radios. *IEEE Transactions on Antennas and Propagation*, 67(1):522–530, 2018.

[154] Ahmed H Abdelrahman and Dejan S Filipovic. Full Duplex Antenna Subsystem for Handheld Radios. In *2017 IEEE International Symposium on Antennas and Propagation & USNC/URSI National Radio Science Meeting*, pages 1891–1892. IEEE, 2017.

[155] Libin Sun, Yue Li, Zhijun Zhang, and Zhenghe Feng. Compact Co-Horizontally Polarized Full-Duplex Antenna with Omnidirectional Patterns. *IEEE Antennas and Wireless Propagation Letters*, 18(6):1154–1158, 2019.

[156] Hyeong-Seok Jang, Won-Gyu Lim, Wang-Ik Son, Sung-Yong Cha, and Jong-Won Yu. Microstrip Patch Array Antenna with High Isolation Characteristic. *Microwave and Optical Technology Letters*, 54(4):973–976, 2012.

[157] William F Moulder, Bradley T Perry, and Jeffrey S Herd. Wideband Antenna Array for Simultaneous Transmit and Receive (STAR) Applications. In *2014 IEEE Antennas and Propagation Society International Symposium (APSURSI)*, pages 243–244. IEEE, 2014.

[158] Elie G Tianang, Mohamed A Elmansouri, and Dejan S Filipovic. High Isolation Diplexer-Free Dual-Polarized Array for Geostationary Satellites. In *2018 IEEE-APS Topical Conference on Antennas and Propagation in Wireless Communications (APWC)*, pages 737–740. IEEE, 2018.

[159] Prathap Valale Prasannakumar, Mohamed A Elmansouri, and Dejan S Filipovic. High-Directivty Broadband Simultaneous Transmit and Receive (STAR) Antenna System. In *2018 IEEE International Symposium on Antennas and Propagation & USNC/URSI National Radio Science Meeting*, pages 387–388. IEEE, 2018.

[160] Ehab A Etellisi, Mohamed A Elmansouri, and Dejan S Filipovic. Wideband Dual-Mode Monostatic Simultaneous Transmit and Receive Antenna System. In *2016 IEEE International Symposium on Antennas and Propagation (APSURSI)*, pages 1821–1822. IEEE, 2016.

[161] Ehab A Etellisi, Mohamed A Elmansouri, and Dejan S Filipović. In-Band Full-Duplex Multimode Lens-Loaded Eight-Arm Spiral Antenna. *IEEE Transactions on Antennas and Propagation*, 66(4):2084–2089, 2018.

[162] Mohamed A Elmansouri, Jaegeun Ha, and Dejan Filipovic. Multioctave Antenna Array for Simultaneous Transmit and Receive Applications. In *2018 International*

Applied Computational Electromagnetics Society Symposium (ACES), pages 1–2. IEEE, 2018.

[163] Andrew Kee, Mohamed Elmansouri, and Dejan S Filipovic. Circularly Polarized PIFA Array for Simultaneous Transmit and Receive Applications. In *2017 IEEE International Symposium on Antennas and Propagation & USNC/URSI National Radio Science Meeting*, pages 2303–2304. IEEE, 2017.

[164] Won-Gyu Lim, Hyeong-Seok Jang, and Jong-Won Yu. UHF RFID Antenna Structure with High Isolation Characteristic. In *Asia-Pacific Microwave Conference 2011*, pages 1822–1825. IEEE, 2011.

[165] Randy Cacciola, Eric Holzman, Lincoln Carpenter, and Steve Gagnon. Impact of Transmit Interference on Receive Sensitivity in a Bi-Static Active Array System. In *2016 IEEE International Symposium on Phased Array Systems and Technology (PAST)*, pages 1–5. IEEE, 2016.

[166] Mohamed A Elmansouri and Dejan S Filipovic. Realization of Ultra-Wideband Bistatic Simultaneous Transmit and Receive Antenna System. In *2016 IEEE International Symposium on Antennas and Propagation (APSURSI)*, pages 2115–2116. IEEE, 2016.

[167] Hang Xu, Hai Zhou, Steven Gao, Hanyang Wang, and Yujian Cheng. Multimode Decoupling Technique With Independent Tuning Characteristic for Mobile Terminals. *IEEE Transactions on Antennas and Propagation*, 65(12):6739–6751, 2017.

[168] Jian-Hui Xun, Ling-Feng Shi, Wei-Rong Liu, and Dong-Jin Xin. A Self-Interference Suppression Structure for Collinear Dipoles. *IEEE Antennas and Wireless Propagation Letters*, 18(10):2100–2104, 2019.

[169] Kei Iwamoto, Mikko Heino, Katsuyuki Haneda, and Hiroyuki Morikawa. Design of an Antenna Decoupling Structure for an Inband Full-Duplex Collinear Dipole Array. *IEEE Transactions on Antennas and Propagation*, 66(7):3763–3768, 2018.

[170] K Iwamoto, M Heino, K Haneda, and H Morikawa. Antenna Decoupling Structure For a Single-Frequency Full-Duplex Planar Dipole Array. In *2015 International Conference on Electromagnetics in Advanced Applications (ICEAA)*, pages 1123–1126. IEEE, 2015.

[171] Mohammad Alibakhshikenari, Mohsen Khalily, Bal Singh Virdee, Chan Hwang See, Raed A Abd-Alhameed, and Ernesto Limiti. Mutual-Coupling Isolation Using Embedded Metamaterial EM Bandgap Decoupling Slab for Densely Packed Array Antennas. *IEEE Access*, 7:51827–51840, 2019.

[172] Jung-Dong Park, Muhibur Rahman, and Hsiang Nerng Chen. Isolation Enhancement of Wide-Band MIMO Array Antennas Utilizing Resistive Loading. *IEEE Access*, 7:81020–81026, 2019.

[173] Shun-Hui Zhu, Xue-Song Yang, Jian Wang, Nian-Sheng Nie, and Bing-Zhong Wang. Mutual Coupling Reduction of±45° Dual-Polarized Closely Spaced MIMO Antenna by Topology Optimization. *IEEE Access*, 8:29089–29098, 2020.

[174] Muhammad Irshad Khan, Muhammad Irfan Khattak, Saeed Ur Rahman, Abdul Baseer Qazi, Ahmad Abdeltawab Telba, and Abdelrazik Sebak. Design and Investigation of Modern UWB-MIMO Antenna with Optimized Isolation. *Micromachines*, 11(4):432, 2020.

[175] Habib Ullah, Saeed Ur Rahman, Qunsheng Cao, Ijaz Khan, and Hamid Ullah. Design of swb mimo antenna with extremely wideband isolation. *Electronics*, 9(1): 194, 2020.

[176] Mikko Heino, Sathya N Venkatasubramanian, Clemens Icheln, and Katsuyuki Haneda. Design of Wavetraps for Isolation Improvement in Compact In-Band Full-Duplex Relay Antennas. *IEEE Transactions on Antennas and Propagation*, 64(3): 1061–1070, 2015.

[177] Dani Korpi, Mikko Heino, Clemens Icheln, Katsuyuki Haneda, and Mikko Valkama. Compact Inband Full-Duplex Relays With Beyond 100 dB Self-Interference Suppression: Enabling Techniques and Field Measurements. *IEEE Transactions on Antennas and Propagation*, 65(2):960–965, 2016.

[178] Yi-Ming Zhang, Shuai Zhang, Jia-Lin Li, and Gert Frølund Pedersen. A Wavetrap-Based Decoupling Technique for 45° Polarized MIMO Antenna Arrays. *Ieee Transactions on Antennas and Propagation*, 68(3):2148–2157, 2019.

[179] Yiming Zhang, Shuai Zhang, and Gert Frølund Pedersen. A Simple and Wideband Decoupling Method for Antenna Array Applications. In *2020 International Workshop on Antenna Technology (iWAT)*, pages 1–4. IEEE, 2020.

[180] John AM Lyon, MAH Ibrahim, Constantine John Digenis, Alan Geetran Cha, Nicolaos Georgiou Alexopoulos, DR Brundage, and William Walter Parker. Electromagnetic Coupling Reduction Techniques. Technical report, 1968.

[181] Prathap Valale Prasannakumar, Mohamed A Elmansouri, Ljubodrag B Boskovic, Maxim Ignatenko, and Dejan S Filipovic. Wideband Quasi-Monostatic Simultaneous Transmit and Receive Reflector Antenna. *IEEE Transactions on Antennas and Propagation*, 68(4):2630–2637, 2019.

[182] Mohamed Elmansouri, Prathap Valaleprasannakumar, Elie Tianang, Ehab Etellisi, and Dejan Filipovic. Single and Dual-Polarized Wideband Simultaneous Transmit and Receive Antenna System. In *2017 IEEE International Symposium on Antennas and Propagation & USNC/URSI National Radio Science Meeting*, pages 1105–1106. IEEE, 2017.

[183] Prathap Valale Prasannakumar, Mohamed A Elmansouri, and Dejan S Filipovic. Wideband Decoupling Techniques for Dual-Polarized Bi-Static Simultaneous Transmit and Receive Antenna Subsystem. *IEEE Transactions on Antennas and Propagation*, 65(10):4991–5001, 2017.

[184] Mahmoud A Abdalla and Ahmed M Abdelraheem. Compact Transmit Receive Hybrid Electromagnetic Isolation in Antenna Array Transceiver System for Full Duplex Applications. *IET Microwaves, Antennas & Propagation*, 11(3):417–425, 2016.

[185] Mohammad Alibakhshikenari, Bal Singh Virdee, I Chan H See, Raed Abd-Alhameed, Francisco Falcone, Aurora Andújar, Jaume Anguera, and Emesto Limiti. Study on Antenna Mutual Coupling Suppression Using Integrated Metasurface Isolator For SAR and MIMO Applications. In *2018 48th European Microwave Conference (EuMC)*, pages 1425–1428. IEEE, 2018.

[186] Mohammad Alibakhshikenari, Mohsen Khalily, Bal Singh Virdee, Chan Hwang See, Raed A Abd-Alhameed, and Ernesto Limiti. Mutual Coupling Suppression Between Two Closely Placed Microstrip Patches Using EM-Bandgap Metamaterial Fractal Loading. *IEEE access*, 7:23606–23614, 2019.

[187] Ibrahim Mohamed, Mahmoud Abdalla, and Abd El-Aziz Mitkees. Perfect Isolation Performance Among Two-Element MIMO Antennas. *AEU-International Journal of Electronics and Communications*, 107:21–31, 2019.

[188] Ibrahim S Mohamed, Mahmoud A Abdalla, and Abdel-Azez A Mitkees. Extreme Suppression for Mutual Coupling by Means of Miniaturized Uniplanar Electromagnetic Bandgap. In *2018 IEEE International Symposium on Antennas and Propagation & USNC/URSI National Radio Science Meeting*, pages 167–168. IEEE, 2018.

[189] Mohamed F El-Sewedy, Mahmoud A Abdalla, and Ahmed Abdelraheem. Isolation Enhancement of MIMO Antennas Using Bilateral CEBG Structures. In *2018 IEEE International Symposium on Antennas and Propagation & USNC/URSI National Radio Science Meeting*, pages 1535–1536. IEEE, 2018.

[190] Mohammad Habib Ullah, Md Rezwanul Ahsan, Wan Nor Liza Wan Mahadi, Tarik Abdul Latef, and Md Jasim Uddin. Isolation Improvement of Dual Feed Patch Antenna by Assimilating Metasurface Ground. *Microwave and Optical Technology Letters*, 57(6):1406–1409, 2015.

[191] Ibrahim Mohamed, Mahmoud Abdalla, and Abd El-Aziz Mitkees. TX/RX Radar Array Antennas With Small Correlation. *AEU-International Journal of Electronics and Communications*, 101:128–137, 2019.

[192] Diqun Lu, Lu Wang, Erfu Yang, and Gang Wang. Design of High-Isolation Wideband Dual-Polarized Compact MIMO Antennas With Multiobjective Optimization. *IEEE Transactions on Antennas and Propagation*, 66(3):1522–1527, 2017.

[193] Haoran Xing, Xinyan Wang, Zhenbin Gao, Xing An, Hong-xing Zheng, Mengjun Wang, and Erping Li. Efficient Isolation of an MIMO Antenna Using Defected Ground Structure. *Electronics*, 9(8):1265, 2020.

[194] Young-Jun Kim, Gunhark Noh, Han Lim Lee, and Sungwook Yu. Dual-Polarized Multi-Channel 24 GHz Radar Sensor Antenna for High Channel-to-Channel Isolation. *Sensors*, 20(18):5233, 2020.

[195] Si-Jia Li, Jun Gao, Xiangyu Cao, Zhao Zhang, and Di Zhang. Broadband and High-Isolation Dual-Polarized Microstrip Antenna With Low Radar Cross Section. *IEEE Antennas and Wireless Propagation Letters*, 13:1413–1416, 2014.

[196] Sathya N Venkatasubramanian, Linsheng Li, Anu Lehtovuori, Clemens Icheln, and Katsuyuki Haneda. Impact of Using Resistive Elements for Wideband Isolation Improvement. *IEEE Transactions on Antennas and Propagation*, 65(1):52–62, 2016.

[197] Yi-Feng Cheng and Kwok-Keung M Cheng. Compact Wideband Decoupling and Matching Network Design for Dual-Antenna Array. *IEEE Antennas and Wireless Propagation Letters*, 19(5):791–795, 2020.

[198] Luyu Zhao, Lap K Yeung, and Ke-Li Wu. A Coupled Resonator Decoupling Network for Two-Element Compact Antenna Arrays in Mobile Terminals. *IEEE Transactions on Antennas and Propagation*, 62(5):2767–2776, 2014.

[199] Shin-Chang Chen, Yu-Shin Wang, and Shyh-Jong Chung. A Decoupling Technique for Increasing the Port Isolation Between Two Strongly Coupled Antennas. *IEEE Transactions on Antennas and Propagation*, 56(12):3650–3658, 2008.

[200] Yi-Feng Cheng and Kwok-Keung M Cheng. A Novel Dual-Band Decoupling and Matching Technique for Asymmetric Antenna Arrays. *IEEE Transactions on Microwave Theory and Techniques*, 66(5):2080–2089, 2018.

[201] Min Li, Lijun Jiang, and Kwan Lawrence Yeung. A Novel Wideband Decoupling Network for Two Antennas Based on the Wilkinson Power Divider. *IEEE Transactions on Antennas and Propagation*, 2020.

[202] Huan Meng and Ke-Li Wu. An LC Decoupling Network for Two Antennas Working at Low Frequencies. *IEEE Transactions on Microwave Theory and Techniques*, 65 (7):2321–2329, 2017.

[203] Rashid Ahmad Bhatti, Soongyu Yi, and Seong-Ook Park. Compact Antenna Array with Port Decoupling for LTE-Standardized Mobile Phones. *IEEE Antennas and Wireless Propagation Letters*, 8:1430–1433, 2009.

[204] Xinyi Tang, Koen Mouthaan, and Jacob C Coetzee. Dual-Band Decoupling and Matching Network Design for Very Closely Spaced Antennas. In *2012 42nd European Microwave Conference*, pages 49–52. IEEE, 2012.

[205] Mohammed M Albannay, Jacob C Coetzee, Xinyi Tang, and Koen Mouthaan. Dual-Frequency Decoupling for Two Distinct Antennas. *IEEE Antennas and Wireless Propagation Letters*, 11:1315–1318, 2012.

[206] Cheng-Hsun Wu, Chia-Lin Chiu, and Tzyh-Ghuang Ma. Very Compact Fully Lumped Decoupling Network for a Coupled Two-Element Array. *IEEE Antennas and Wireless Propagation Letters*, 15:158–161, 2015.

[207] Cheng-Hsun Wu, Guan-Ting Zhou, Yi-Lung Wu, and Tzyh-Ghuang Ma. Stub-Loaded Reactive Decoupling Network for Two-Element Array Using Even-Odd Analysis. *IEEE Antennas and Wireless Propagation Letters*, 12:452–455, 2013.

[208] Linsheng Li, Sathya Venkatasubramanian, Anu Lehtovuori, Clemens Icheln, Mikko Heino, and Katsuyuki Haneda. T-Shaped Decoupling Network for Wideband Isolation Improvement Between Two Strongly Coupled Antennas. In *2015 Loughborough Antennas & Propagation Conference (LAPC)*, pages 1–4. IEEE, 2015.

[209] Andrew T Wegener and William J Chappell. Simultaneous Transmit and Receive With a Small Planar Array. In *2012 IEEE/MTT-S International Microwave Symposium Digest*, pages 1–3. IEEE, 2012.

[210] Andrew T Wegener. Broadband Near-Field Filters for Simultaneous Transmit and Receive in a Small Two-Dimensional Array. In *2014 IEEE MTT-S International Microwave Symposium (IMS2014)*, pages 1–3. IEEE, 2014.

[211] Andrew T Wegener and William J Chappell. Coupled Antenna Scheme Using Filter Design Techniques and Tunable Resonators to Show Simultaneous Transmit and Receive. In *2013 IEEE MTT-S International Microwave Symposium Digest (MTT)*, pages 1–4. IEEE, 2013.

[212] Andrew T Wegener and William J Chappell. High Isolation in Antenna Arrays for Simultaneous Transmit and Receive. In *2013 IEEE International Symposium on Phased Array Systems and Technology*, pages 593–597. IEEE, 2013.

[213] Xian Qi Lin, Hui Li, Sailing He, and Yong Fan. A Decoupling Technique for Increasing the Port Isolation Between Two Closely Packed Antennas. In *Proceedings of the 2012 IEEE International Symposium on Antennas and Propagation*, pages 1–2. IEEE, 2012.

[214] Andrew T Wegener and William J Chappell. Simultaneous Transmit and Receive with a Small Planar Array. In *2012 IEEE/MTT-S International Microwave Symposium Digest*, pages 1–3. IEEE, 2012.

[215] Tolga Dinc and Harish Krishnaswamy. A T/R Antenna Pair with Polarization-Based Reconfigurable Wideband Self-Interference Cancellation for Simultaneous Transmit and Receive. In *2015 IEEE MTT-S International Microwave Symposium*, pages 1–4. IEEE, 2015.

[216] American Federal Communications Comission (FCC). Electronic Code of Federal Regulations (eCFR), Part 15, Subpart F–Ultra-Wideband Operation. `https://www.ecfr.gov/cgi-bin/text-idx?SID=01e27c97abc21e453f5107d0fd384a59&mc=true&node=sp47.1.15.f&rgn=div6`, April 2003. (Last checked on 11/02/2020).

[217] Rf-lambda circulators and isolators. `https://www.rflambda.com/search_circulator.jsp`. (Last checked on 11/02/2020).

[218] Ernest J Wilkinson. An N-way Hybrid Power Divider. *IRE Transactions on microwave theory and techniques*, 8(1):116–118, 1960.

[219] Bassem Henin and Amin Abbosh. Planar Wideband In-Phase Power Divider Using Three-Line Coupled Structure. *Microwave and Optical Technology Letters*, 56(4): 1010–1012, 2014.

[220] H Zhu, A Abbosh, and L Guo. Ultra-Wideband Unequal In-Phase Power Divider Using Three-Line Coupled Structure. *Electronics letters*, 50(15):1081–1082, 2014.

[221] Trung-Sinh Dang, Chang-Woo Kim, and Sang-Woong Yoon. Ultra-Wideband Power Divider Using Three Parallel-Coupled Lines and One Shunt Stub. *Electronics letters*, 50(2):95–96, 2014.

[222] He Zhu and AM Abbosh. Compact Ultra-Wideband In-Phase Power Divider Using Three-Line Coupled Structure. In *2014 IEEE Antennas and Propagation Society International Symposium (APSURSI)*, pages 820–821. IEEE, 2014.

[223] Ziqiang Yang, Bangyu Luo, Jun Dong, and Tao Yang. Ultra-Wideband Power Divider Employing Coupled Line and Short-Ended Stub. *Microwave and Optical Technology Letters*, 58(3):713–715, 2016.

[224] Pratik Mondal and Susanta Kumar Parui. Multi-Mode Resonator-Based Ultra-Wideband Power Divider. *Microwave and Optical Technology Letters*, 58(10):2419–2422, 2016.

[225] Wei-Qiang Liu, Feng Wei, Chun-Hui Pang, and Xiao-Wei Shi. Design of a Compact Ultra-Wideband Power Divider. In *2012 International Conference on Microwave and Millimeter Wave Technology (ICMMT)*, volume 2, pages 1–3. IEEE, 2012.

[226] Chunlin Zhuge, Kaijun Song, and Yong Fan. Ultra-Wideband (UWB) Power Divider Based on Signal Interference Techniques. *Microwave and Optical Technology Letters*, 54(4):1028–1030, 2012.

[227] Sai Wai Wong and Lei Zhu. Ultra-Wideband Power Divider with Good In-Band Splitting and Isolation Performances. *IEEE microwave and wireless components letters*, 18(8):518–520, 2008.

[228] SW Wong and L Zhu. Ultra-Wideband Power Dividers with Good Isolation and Improved Sharp Roll-Off Skirt. *IET microwaves, antennas & propagation*, 3(8): 1157–1163, 2009.

[229] Sai Wai Wong and L. Zhu. Ultra-wideband power dividers with good isolation and sharp roll-off skirt. In *2008 Asia-Pacific Microwave Conference*, pages 1–4, 2008. doi: 10.1109/APMC.2008.4958422.

[230] Meili Weng, Yaoliang Song, and Junding Zhao. Design of Compact Microstrip UWB Power Divider Using Square Ring Multiple-Mode Resonator. In *2015 Asia-Pacific Microwave Conference (APMC)*, volume 1, pages 1–3. IEEE, 2015.

[231] Osama Ahmed and Abdel-Razik Sebak. A Modified Wilkinson Power Divider/Combiner for Ultrawideband Communications. In *2009 IEEE Antennas and Propagation Society International Symposium*, pages 1–4. IEEE, 2009.

[232] Bo Zhou, Hao Wang, and Weixing Sheng. A Novel UWB Wilkinson Power Divider. In *The 2nd International Conference on Information Science and Engineering*, pages 1763–1765. IEEE, 2010.

[233] AM Abbosh. Planar Ultra Wideband Inphase Power Divider. *Microwave and Optical Technology Letters*, 51(5):1185–1188, 2009.

[234] Rong-Cang Han, Ru-Ying Sun, and Shao-Hua Shi. A Wideband Planar Hybrid Coupler Using Coupled-Line Power Divider and Broadband Phase Shifter. In *2017 Sixth Asia-Pacific Conference on Antennas and Propagation (APCAP)*, pages 1–3. IEEE, 2017.

[235] Seymour B Cohn. A Class of Broadband Three-Port TEM-Mode Hybrids. *IEEE Transactions on Microwave Theory and Techniques*, 16(2):110–116, 1968.

[236] Björn Deutschmann and Arne F Jacob. Compact Ultra-Broadband Power Dividers with Integrated Resistors. In *2018 48th European Microwave Conference (EuMC)*, pages 620–623. IEEE, 2018.

[237] Nikolay Drobotun, Dmitry Yanchuk, and Evgeny Khoroshilov. Compact Planar Ultra-Wideband Power Dividers with Frequency Range Up to 67 GHz for Multichannel Receivers. In *2016 46th European Microwave Conference (EuMC)*, pages 198–201. IEEE, 2016.

[238] VN Fedorov, ND Malyutin, and NB Drobotun. Analysis and Experimental Research of Ultrawideband Divider-Combiner of Pico-and Nanosecond Pulses. In *2018 Ural Symposium on Biomedical Engineering, Radioelectronics and Information Technology (USBEREIT)*, pages 355–358. IEEE, 2018.

[239] F Trenz, M Hofmann, R Weigel, G Fischer, and D Kissinger. Compact 2–28 GHz Planar Multi-Octave Bandwidth Wilkinson Power Dividers. In *2014 IEEE MTT-S International Microwave Symposium (IMS2014)*, pages 1–4. IEEE, 2014.

[240] Oguzhan Kizilbey, Suheyb Bozdemir, and Binboga Siddik Yarman. 2–10 GHz Multisection 2-Way Wilkinson Power Divider with Enhanced Port Match and Isolation. In *2017 IEEE 18th Wireless and Microwave Technology Conference (WAMICON)*, pages 1–4. IEEE, 2017.

[241] Chun Tong Chiang and Boon-Kuan Chung. Ultra Wideband Power Divider Using Tapered Line. *Progress In Electromagnetics Research*, 106:61–73, 2010.

[242] B Mencia-Oliva, AM Pelaez-Perez, P Almorox-Gonzalez, and JI Alonso. New Technique for the Design of Ultra-Broadband Power Dividers Based on Tapered Lines. In *2009 IEEE MTT-S International Microwave Symposium Digest*, pages 493–496. IEEE, 2009.

[243] Sandi Ibrahimpašić and Moamer Hasanović. Multi-Section Wilkinson Power Splitter with Tuned Quarter-Wave Transformers to Compensate for Different Velocities in Even and Odd Mode. In *Annual Review of Progress in Applied Computational Electromagnetics*, volume 26, 2010.

[244] K Rajkamal and I Govardhani. Miniaturized Ultra Wideband Planar Wilkinson Power Divider. *International Journal of Pure and Applied Mathematics*, 117(18 Special Issue):135–140, 2017.

[245] Enric Miralles, Bernhard Schönlinner, Volker Ziegler, and Frank Ellinger. Fast Design Method and Validation of Very Wideband Tapered Wilkinson Divider. In *2015 European Microwave Conference (EuMC)*, pages 119–122. IEEE, 2015.

[246] Jia-Chi Samuel Chieh and Anh-Vu Pham. Development of a Wide Bandwidth Wilkinson Power Divider on Multilayer Organic Substrates. *Microwave and Optical Technology Letters*, 52(7):1606–1609, 2010.

[247] Jia-Chi Samuel Chieh and Anh-Vu Pham. Development of a Broadband Wilkinson Power Combiner on Liquid Crystal Polymer. In *2009 Asia Pacific Microwave Conference*, pages 2068–2071. IEEE, 2009.

[248] B Mishra, A Rahman, S Shaw, M Mohd, S Mondal, and PP Sarkar. Design of an Ultra-Wideband Wilkinson Power Divider. In *2014 First International Conference on Automation, Control, Energy and Systems (ACES)*, pages 1–4. IEEE, 2014.

[249] Lei Chang, Cheng Liao, Ling-Lu Chen, Wenbin Lin, Xuan Zheng, and Yan-Liang Wu. Design of an Ultra-Wideband Power Divider Via the Coarse-Grained Parallel Micro-Genetic Algorithm. *Progress In Electromagnetics Research*, 124:425–440, 2012.

[250] J Arzola, C Miller, and RM Henderson. 40 GHz Laminate Power Divider Circuits Using Integrated Resistors. In *2015 IEEE MTT-S International Microwave Symposium*, pages 1–3. IEEE, 2015.

[251] Bo Zhou. Broadband and Compact LTCC Power Divider. *Electronics Letters*, 51 (23):1939–1941, 2015.

[252] H Wang, X Tang, Y Liu, and Y Cao. Analysis and Design of Ultra-Wideband Power Divider by Micro-Genetic Algorithm. *Journal of Electromagnetic Waves and Applications*, 26(10):1341–1349, 2012.

[253] Reza Nemati, Shokrollah Karimian, and Nasser Masoumi. An Optimized Approach for Design of Three-Section Wilkinson Power Divider. In *2018 9th International symposium on Telecommunications (IST)*, pages 575–580. IEEE, 2018.

[254] Huang Sen, Xie Xiaoqiang, and Yan Bo. A Serrated Microstrip Lines Wilkinson Power Divider. In *2012 International Conference on Microwave and Millimeter Wave Technology (ICMMT)*, volume 4, pages 1–3. IEEE, 2012.

[255] Weijuan Chen, Shulan Li, Zehai Wu, and Yuanan Liu. Wideband Power Divider Based on Klopfenstein Tapered Line. In *2019 International Conference on Microwave and Millimeter Wave Technology (ICMMT)*, pages 1–3. IEEE, 2019.

[256] Ammar H Ali, Raed A Abd-Alhameed, James M Noras, and Mark B Child. An Ultra Wide Band Power Divider for Antenna Array Feeding Network. In *2016 Loughborough Antennas & Propagation Conference (LAPC)*, pages 1–4. IEEE, 2016.

[257] PC Goodman. A Wideband Stripline Matched Power Divider. In *1968 G-MTT International Microwave Symposium*, pages 16–20. IEEE, 1968.

[258] In Bok Kim, Ki Hyuk Kwon, Seung Bok Kwon, Wahab Mohyuddin, Hyun Chul Choi, and Kang Wook Kim. Ultra-Wideband Multi-Section Power Divider on Suspended Stripline. In *2017 IEEE MTT-S International Microwave Symposium (IMS)*, pages 427–430. IEEE, 2017.

[259] Muhammad Zairil Bin Muhammad Nor, Sharul Kamal Abdul Rahim, Mursyidul Idzam bin Sabran, and Mohd Subri Bin Abdul Rani. Wideband Planar Wilkinson Power Divider Using Double-Sided Parallel-Strip line Technique. *Progress In Electromagnetics Research*, 36:181–193, 2013.

[260] PO Afanasiev, VA Sledkov, and MB Manuilov. A Novel Design of Ultra-Wideband Strip-Line Power Divider for 2–18 GHz. In *2013 IX Internatioal Conference on Antenna Theory and Techniques*, pages 323–325. IEEE, 2013.

[261] BM Schiffman. A New Class of Broad-Band Microwave 90-Degree Phase Shifters. *IRE Transactions on Microwave Theory and Techniques*, 6(2):232–237, 1958.

[262] JL Ramos Quirarte and J Piotr Starski. Novel Schiffman Phase Shifters. *IEEE transactions on microwave theory and techniques*, 41(1):9–14, 1993.

[263] Yun-Peng Lyu, Lei Zhu, and Chong-Hu Cheng. Design and Analysis of Schiffman Phase Shifter Under Operation of its Second Phase Period. *IEEE Transactions on Microwave Theory and Techniques*, 66(7):3263–3269, 2018.

[264] Yong-Xin Guo, Zhen-Yu Zhang, and Ling Chuen Ong. Improved Wide-Band Schiffman Phase Shifter. *IEEE Transactions on Microwave Theory and Techniques*, 54(3):1196–1200, 2006.

[265] Zheng Zhang, Yong-Chang Jiao, Shun-Feng Cao, Xiao-Ming Wang, and Fu-Shun Zhang. Modified Broadband Schiffman Phase Shifter Using Dentate Microstrip and Patterned Ground Plane. *Progress In Electromagnetics Research*, 24:9–16, 2011.

[266] Seungyeoup Rhee. Broadband Schiffman Phase Shifter Using Coupled Suspended Lines with Tuning Septums. *Microwave and Optical Technology Letters*, 55(5):1036–1038, 2013.

[267] Partha Kumar Deb, Tamasi Moyra, and Bidyut Kumar Bhattacharyya. Design of Compact Wideband 90° Schiffman Phase Shifter Incorporating CSRR. *Electromagnetics*, 40(3):207–216, 2020.

[268] BM Schiffman. Multisection Microwave Phase-Shift Network (Correspondence). *IEEE Transactions on Microwave Theory and Techniques*, 14(4):209–209, 1966.

[269] VALERY PETROVICH Meschanov, IRINA VADIMOVNA Metelnikova, VD Tupikin, and GEORGIEVNA GALINDA Chumaevskaya. A New Structure of Microwave Ultrawide-Band Differential Phase Shifter. *IEEE transactions on microwave theory and techniques*, 42(5):762–765, 1994.

[270] JP Shelton and JA Mosko. Synthesis and Design of Wide-Band Equal-Ripple TEM Directional Couplers and Fixed Phase Shifters. *IEEE Transactions on Microwave Theory and Techniques*, 14(10):462–473, 1966.

[271] AP Krenitskii, VP Meshchanov, and LV Shikova. Synthesis of Ultrawideband Differential Phase Shifters Based on coupled Transmission Lines. *Journal of Communications Technology and Electronics*, 52(7):736–742, 2007.

[272] VI Alekseev, AN Anufriev, VP Meshchanov, VV Semenchuk, and LV Shikova. New Structure of Ultrawideband Fixed Phase Shifters Based on Stepped Coupled Transmission Lines with Stubs. *Journal of Communications Technology and Electronics*, 62(5):535–541, 2017.

[273] Qingxiang Dong, Yongle Wu, Yana Zheng, Weimin Wang, and Yuanan Liu. A Compact Single-Layer Ultra-Wideband Phase Shifter Using Weakly Coupled Lines. *IEEE Access*, 7:12575–12583, 2019.

[274] Po-Sheng Huang and Hsin-Chia Lu. Improvement of the Phase Shifter in 90° Power Splitter for UWB Applications. *IEEE microwave and wireless components letters*, 22(12):621–623, 2012.

[275] L Guo, H Zhu, and AM Abbosh. Planar UWB Phase Shifter Using Parallel Coupled Lines Combined with Short-Ended Stubs and Impedance Transformer. In *2015 Asia-Pacific Microwave Conference (APMC)*, volume 2, pages 1–3. IEEE, 2015.

[276] L Guo, H Zhu, and A Abbosh. Wideband Phase Shifter with Wide Phase Range Using Parallel Coupled Lines and L-Shaped Networks. *IEEE Microwave and Wireless Components Letters*, 26(8):592–594, 2016.

[277] Qiang Liu, Yuanan Liu, Junyu Shen, Shulan Li, Cuiping Yu, and Yinghua Lu. Wideband Single-Layer 90° Phase Shifter Using Stepped Impedance Open Stub and Coupled-Line With Weak Coupling. *IEEE Microwave and Wireless Components Letters*, 24(3):176–178, 2014.

[278] Amin M Abbosh. Ultra-Wideband Phase Shifters. *IEEE Transactions on Microwave Theory and Techniques*, 55(9):1935–1941, 2007.

[279] Amin Abbosh, Marek Bialkowski, and David Thiel. Tunable Ultra Wideband Phase Shifter Using Liquid Crystal Polymer. In *2009 Asia Pacific Microwave Conference*, pages 2076–2079. IEEE, 2009.

[280] Yawei Wang, Zhongwu Yu, Jiangang Liang, Xiangjun Gao, and Li Zhu. Ultra-Wideband 45° Phase Shifter Based on Multi-Section Broadside Coupling Structure. In *2016 IEEE International Conference on Microwave and Millimeter Wave Technology (ICMMT)*, volume 1, pages 336–338. IEEE, 2016.

[281] Soufiane Tebache, Adel Belouchrani, Farid Ghanem, and Ali Mansoul. Compact 45° Phase Shifter Based on Coupled Tapered Transition for UWB Applications. In *2017 5th International Conference on Electrical Engineering-Boumerdes (ICEE-B)*, pages 1–4. IEEE, 2017.

[282] Amin M Abbosh. Ultra-Wideband Phase Shifter Using Broadside-Coupled Coplanar Waveguide Structure. *Microwave and Optical Technology Letters*, 54(1):114–116, 2012.

[283] Amin M Abbosh. Broadband Fixed Phase Shifters. *IEEE microwave and wireless components letters*, 21(1):22–24, 2010.

[284] Somayeh Khajepour, Shahrooz Asadi, Mohammad Saeid Ghaffarian, and Gholamreza Moradi. Design of Novel Wideband Reflective Phase Shifters with Wide Range of Phase Applications. *AEU-International Journal of Electronics and Communications*, 71:30–36, 2017.

[285] Somayeh Khajepour, Shahrooz Asadi, and Gholamreza Moradi. Reflective Phase Shifter Based on Wideband Multi-Section Hybrid Coupler in Slot-Coupled Structure. *Microwave and Optical Technology Letters*, 59(3):567–573, 2017.

[286] Jun Wang, Zhongxiang Shen, and Lei Zhao. UWB 90° Phase Shifter Based on Broadside Coupler and T-Shaped Stub. *Electronics Letters*, 52(25):2048–2050, 2016.

[287] Siti Zuraidah Ibrahim, Marek E Bialkowski, and Amin M Abbosh. Ultrawideband Quadrature Power Divider Employing Double Wireless Via. *Microwave and Optical Technology Letters*, 54(2):300–305, 2012.

[288] Soufiane Tebache, Farid Ghanem, Adel Belouchrani, and Ali Mansoul. Frequency Independent 180° Phase Shifter Based on UWB Coupled Sections. *Microwave and Optical Technology Letters*, 59(12):3185–3189, 2017.

[289] L Guo and A Abbosh. Phase Shifters with Wide Range of Phase and Ultra-Wideband Performance Using Stub-Loaded Coupled Structure. *IEEE Microwave and Wireless Components Letters*, 24(3):167–169, 2014.

[290] L Guo and A Abbosh. Ultra-Wideband Phase Shifter Using Broadside-Coupled Microstrip Coplanar Waveguide. In *2013 Asia-Pacific Microwave Conference Proceedings (APMC)*, pages 951–953. IEEE, 2013.

[291] Y Wang, ME Bialkowski, and AM Abbosh. Double Microstrip-Slot Transitions for Broadband ±90° Microstrip Phase Shifters. *IEEE microwave and wireless components letters*, 22(2):58–60, 2012.

[292] Mohammad Karim Alizadeh, Hossein Shamsi, Mohammad Bagher Tavakoli, and Hadi Aliakbarian. Single-Layer Wideband Differential Phase Shifter Using High-Order Multimode Resonator Structure. *AEU-International Journal of Electronics and Communications*, 115:153023, 2020.

[293] Yun-Peng Lyu, Lei Zhu, and Chong-Hu Cheng. Ultra-Wideband (UWB) Phase Shifter on Multimode Resonator: Concept, Theory, and Design. In *2018 IEEE MTT-S International Wireless Symposium (IWS)*, pages 1–4. IEEE, 2018.

[294] Yun-Peng Lyu, Lei Zhu, and Chong-Hu Cheng. A New Design of Ultrawideband Single-Layer 90° Phase Shifter in the View of Group Delay. *IEEE Microwave and Wireless Components Letters*, 29(6):376–378, 2019.

[295] Yun-Peng Lyu, Lei Zhu, and Chong-Hu Cheng. Wideband Phase Shifters With Miniaturized Size on Multiple Series and Shunt Resonators: Proposal and Synthetic Design. *IEEE Transactions on Microwave Theory and Techniques*, 2020.

[296] Yun-Peng Lyu, Lei Zhu, and Chong-Hu Cheng. Single-Layer Broadband Phase Shifter Using Multimode Resonator and Shunt $\lambda/4$ Stubs. *IEEE Transactions on Components, Packaging and Manufacturing Technology*, 7(7):1119–1125, 2017.

[297] Xiu-Hua Jin, Xiao-Dong Huang, and Chong-Hu Cheng. Microstrip Stepped-Impedance Ring All-Pass Filter and Wideband 90° Phase Shifter. *International Journal of RF and Microwave Computer-Aided Engineering*, 24(2):191–195, 2014.

[298] Sai Ho Yeung, Quan Xue, and Kim Fung Man. Broadband 90° Differential Phase Shifter Constructed Using a Pair of Multisection Radial Line Stubs. *IEEE transactions on microwave theory and techniques*, 60(9):2760–2767, 2012.

[299] Sai Ho Yeung, Zicong Mei, Tapan Kumar Sarkar, and Magdalena Salazar-Palma. Design and Testing of a Single-Layer Microstrip Ultrawideband 90 Differential Phase Shifter. *IEEE microwave and wireless components letters*, 23(3):122–124, 2013.

[300] Dimitrios E Anagnostou, Matt Morton, John Papapolymerou, and Christos G Christodoulou. A 0–55-GHz Coplanar Waveguide to Coplanar Strip Transition. *IEEE Transactions on Microwave Theory and Techniques*, 56(1):1–6, 2008.

[301] Shau-Gang Mao, Chieh-Tsao Hwang, Ruey-Beei Wu, and Chun Hsiung Chen. Analysis of Coplanar Waveguide-to-Coplanar Stripline Transitions. *IEEE Transactions on Microwave Theory and Techniques*, 48(1):23–29, 2000.

[302] Yunfeng Dong, Tom K Johansen, and Vitaliy Zhurbenko. Ultra-Wideband Coplanar Waveguide-to-Asymmetric Coplanar Stripline Transition From DC to 165 GHz. *International Journal of Microwave and Wireless Technologies*, 10(8):870–876, 2018.

[303] Yunfeng Dong, Tom K Johansen, Vitaliy Zhurbenko, and Peter Jesper Hanberg. Coplanar Transitions Based on Aluminum Nitride Interposer Substrate for Terabit Transceivers. In *2017 47th European Microwave Conference (EuMC)*, pages 620–623. IEEE, 2017.

[304] S Kim, S Jeong, Y-T Lee, D-H Kim, J-S Lim, K-S Seo, and S Nam. Ultra-Wideband (from DC to 110 GHz) CPW to CPS Transition. *Electronics Letters*, 38(13):622–623, 2002.

[305] Young-Gon Kim and Kang Wook Kim. Design of an Ultra-Wideband Transition From Double-Sided Parallel Stripline to Coplanar Waveguide. *International Journal of Antennas and Propagation*, 2013, 2013.

[306] Young-Gon Kim, Sun-Young Song, and Kang Wook Kim. A Pair of Ultra-Wideband Planar Transitions for Phase Inversion Applications. *IEEE microwave and wireless components letters*, 20(9):492–494, 2010.

[307] Kokkadan Jacob Nelson, Arimpoorpallan Ouseph Lindo, Chandroth Karuvandi Aanandan, Pezholil Mohanan, and Kesavath Vasudevan. Broadband Vertical Transitions Between Double-Sided Parallel-Strip Line and Coplanar Waveguide. *Progress In Electromagnetics Research*, 75:119–124, 2018.

[308] Xiu Yin Zhang, Jian-Xin Chen, and Quan Xue. Broadband Transition Between Double-Sided Parallel-Strip Line and coplanar Waveguide. *IEEE microwave and wireless components letters*, 17(2):103–105, 2007.

[309] Young-Gon Kim, Dong-Sik Woo, Kang Wook Kim, and Young-Ki Cho. A new ultra-wideband microstrip-to-cps transition. In *2007 IEEE/MTT-S International Microwave Symposium*, pages 1563–1566. IEEE, 2007.

[310] Jung Seok Lee, Gwan Hui Lee, Wahab Mohyuddin, Hyun Chul Choi, and Kang Wook Kim. Design of an Ultra-Wideband Microstrip-to-Slotline Transition on Low-Permittivity Substrate. *Electronics*, 9(8):1329, 2020.

[311] Gwan Hui Lee, Dong Hwi Kim, Wahab Mohyuddin, Sachin Kumar, Hyun Chul Choi, and Kang Wook Kim. Wideband Bended CPS-to-Microstrip Transition for Millimeter-Wave Antenna-Detector Module. *Microwave and Optical Technology Letters*, 62(5):1991–1996, 2020.

[312] Qi Jiang, Calvin Domier, and NC Luhmann. A Wideband Low Loss Planar Microstrip-to-CPS Balun. In *2012 Asia Pacific Microwave Conference Proceedings*, pages 1205–1207. IEEE, 2012.

[313] Gwan Hui Lee, Wahab Mohyuddin, Hyun Chul Choi, and Kang Wook Kim. Asymmetric Ultra-Wideband Microstrip-to-Coplanar Stripline Transition. *IEEE Microwave and Wireless Components Letters*, 28(5):386–388, 2018.

[314] Mrinal Kanti Mandal and Zhi Ning Chen. Compact Ultra-Wideband Microstrip-to-Coplanar Stripline Transitions. In *IEEE MTT-S International Microwave and RF Conference*, pages 1–4. IEEE, 2013.

[315] Young-Ho Suh and Kai Chang. A Wideband Coplanar Stripline to Microstrip Transition. *IEEE Microwave and wireless components letters*, 11(1):28–29, 2001.

[316] J Chramiec and BJ Janiczak. Design of Impedance-Transforming Microstrip-Balanced Stripline Tapered Transitions. *Electronics Letters*, 29(1):3–4, 1993.

[317] Sang-Gyu Kim and Kai Chang. Ultrawide-Band Transitions and New Microwave Components Using Double-Sided Parallel-Strip Lines. *IEEE Transactions on Microwave Theory and Techniques*, 52(9):2148–2152, 2004.

[318] TW Eubanks and K Chang. Low-Loss Ultra-Wideband Double-Sided Parallel-Strip Line Transition and Power Divider. *Electronics letters*, 46(1):93–94, 2010.

[319] Lei Fang and Rashaunda Henderson. Broadband Conductor-Backed Coplanar Waveguide to Double-Sided Parallel Strip Line Transition at Millimeter wave. In *2017 Texas Symposium on Wireless and Microwave Circuits and Systems (WMCS)*, pages 1–4. IEEE, 2017.

[320] MM Zinieris, R Sloan, and LE Davis. A Broadband Microstrip-to-Slotline Transition. *Microwave and optical technology letters*, 18(5):339–342, 1998.

[321] Nai-Biao Wang, Yong-Chang Jiao, Li Zhang, Yue Song, and Fu-Shun Zhang. A Simple Low-Loss Broadband 1–14 GHz Microstrip-to-Slotline Transition. *Microwave and Optical Technology Letters*, 51(9):2236–2239, 2009.

[322] J-L Li, W Shao, and X-S Yang. An Ultra-Wideband Microstrip-to-Slotline Transition. *Journal of Electromagnetic Waves and Applications*, 26(14-15):1889–1896, 2012.

[323] Rainee Simons and RAINEE N Simons. *Coplanar Waveguide Circuits, Components, and Systems*, volume 15. Wiley Online Library, 2001.

[324] Xiao-Ping Chen and Ke Wu. Low-Loss Ultra-Wideband Transition Between Conductor-Backed Coplanar Waveguide and Substrate Integrated Waveguide. In *2009 IEEE MTT-S International Microwave Symposium Digest*, pages 349–352. IEEE, 2009.

[325] Zamzam Kordiboroujeni and Jens Bornemann. New wideband Transition From Microstrip Line to Substrate Integrated Waveguide. *IEEE Transactions on Microwave Theory and Techniques*, 62(12):2983–2989, 2014.

[326] Farzaneh Taringou, David Dousset, Jens Bornemann, and Ke Wu. Substrate-Integrated Waveguide Transitions to Planar Transmission-Line Technologies. In *2012 IEEE/MTT-S International Microwave Symposium Digest*, pages 1–3. IEEE, 2012.

[327] Abdelnasser A Eldek. Design of Ultra Wideband Microstrip 180 Degree Phase Shifter. *Microwave and Optical Technology Letters*, 50(7):1841–1844, 2008.

[328] Abdelnasser A Eldek. Microstrip 180 Degree Phase Shifter for Ultra Wideband Applications. In *2008 IEEE Antennas and Propagation Society International Symposium*, pages 1–4. IEEE, 2008.

[329] Abdelnasser A Eldek. Wideband 180° Phase Shifter Using Microstrip-CPW-Microstrip Transition. *Progress In Electromagnetics Research*, 2:177–187, 2008.

[330] Ka Wai Wong, Leung Chiu, and Quan Xue. Wideband Parallel-Strip Bandpass Filter Using Phase Inverter. *IEEE microwave and wireless components letters*, 18 (8):503–505, 2008.

[331] Nathan Marchand. Transmission Line Conversion Transformers. *Electron*, 17(12): 142–145, 1944.

[332] Tim Canning, Jeff R Powell, and Steve C Cripps. Optimal Design Of Broadband Microwave Baluns Using Single-layer Planar Circuit Technology. *IEEE transactions on microwave theory and techniques*, 62(5):1183–1191, 2014.

[333] Hai Ta, Alexander Stameroff, and Anh-Vu Pham. Development Of A Defected Ground Structure Wide Bandwidth Balun On Multilayer Organic Substrate. In *2010 Asia-Pacific Microwave Conference*, pages 1641–1644. IEEE, 2010.

[334] Chi Van Pham, Binh Pham, Anh-Vu Pham, and Robert E Leoni. A 46: 1 Bandwidth Ratio Balun On Multilayer Organic Substrate. In *2015 IEEE MTT-S International Microwave Symposium*, pages 1–3. IEEE, 2015.

[335] Xing Lan, Flavia Fong, Mark Kintis, Keith Kono, Derrick Yamauchi, Wen-Ben Luo, and David Farkas. An Ultra-wideband Balun Using Multi-metal GaAs MMIC Technology. *IEEE Microwave and Wireless Components Letters*, 20(8):474–476, 2010.

[336] Keng-Chih Lin and Yi-Cheng Lin. A Simple Printed Compensated Balun For Enhanced Ultra-wideband Performances. *IEEE microwave and wireless components letters*, 24(1):5–7, 2013.

[337] Hsiao-Wei Chin, Lih-Tyng Hwang, Fa-Shian Chang, Shun-Min Wang, and Pei-Shuo Li. Design Of An IPD Ultra Wideband Marchand Balun Using A Phase Compensation Line. In *2015 Asia-Pacific Microwave Conference (APMC)*, volume 2, pages 1–3. IEEE, 2015.

[338] Zhan Xu and Leonard MacEachern. Optimum Design of Wideband Compensated and Uncompensated Marchand Baluns With Step Transformers. *IEEE transactions on microwave theory and techniques*, 57(8):2064–2071, 2009.

[339] Srikanth Itapu, Mohammad Almalkawi, and Vijay Devabhaktuni. A 0.8–8 GHz Multi-Section Coupled Line Balun. *Electronics*, 4(2):274–282, 2015.

[340] Mahmoud Al Basraoui and Prasad N Shastry. Wideband Planar Log-Periodic Balun. *International Journal of RF and Microwave Computer-Aided Engineering: Co-sponsored by the Center for Advanced Manufacturing and Packaging of Microwave, Optical, and Digital Electronics (CAMPmode) at the University of Colorado at Boulder*, 11(6):343–353, 2001.

[341] Chu-Yu Chen and Shu-Hao Ye. A Symmetric Log-Periodic Balun for Ultra-Wideband Application. *Microwave and Optical Technology Letters*, 50(4):947–948, 2008.

[342] Andy M Morishita, Ryan C Gough, Jonathan H Dang, Aaron T Ohta, and Wayne A Shiroma. A Liquid-Metal Reconfigurable Log-Periodic Balun. In *2014 IEEE MTT-S International Microwave Symposium (IMS2014)*, pages 1–3. IEEE, 2014.

[343] W Shao and J-L Li. A Compact Log-Periodic Branch-Line Balun with an Octave Bandwidth. *Journal of Electromagnetic Waves and Applications*, 25(14-15):2033–2042, 2011.

[344] Zhi Kuang Cai, Bo Zhou, Peiqi Chen, Lingxuan Huang, Ninglin Wang, and Xuan Ni. Miniaturized and Folded Multisection Quadrature Hybrid for UWB Applications. *Progress In Electromagnetics Research*, 79:129–133, 2018.

[345] Sangeetha Velan and Malathi Kanagasabai. A Compact Single Layer Branch-Line Coupler for Ultra-Wideband (UWB) Applications. *International Journal of Microwave and Wireless Technologies*, 9(3):505, 2017.

[346] Xinyi Tang, Koen Mouthaan, and Jacob C Coetzee. Tunable Decoupling and Matching Network for Diversity Enhancement of Closely Spaced Antennas. *IEEE Antennas and Wireless Propagation Letters*, 11:268–271, 2012.

[347] Kevin Khee-Meng Chan, Adrian Eng-Choon Tan, and Karumudi Rambabu. Decade Bandwidth Circularly Polarized Antenna Array. *IEEE transactions on antennas and propagation*, 61(11):5435–5443, 2013.

[348] Mauro Anselmi, Massimiliano Pingue, Antonio Manna, Roberto Flamini, and Luigi Cosmi. Design and Realization of 3 dB hybrid stripline coupler in 0.5–18.0 GHz. In *2014 44th European Microwave Conference*, pages 464–467. IEEE, 2014.

[349] Carl Pfeiffer, Thomas Steffen, and Boris Tomasic. Millimeter-Wave Ultra-Wideband PCB 180° Hybrid for 12-67 GHz. *Progress In Electromagnetics Research*, 92:213–221, 2020.

[350] Carl Pfeiffer, Thomas Steffen, and Boris Tomasic. UWB Millimeter-Wave 180° Hybid Couplers. In *2019 IEEE International Symposium on Antennas and Propagation and USNC-URSI Radio Science Meeting*, pages 967–968. IEEE, 2019.

[351] M Nakajima and Hiroaki Tanabe. A Design Technique for Raising Upper Frequency Limit of Wide-Band 180° Hybrids. In *1996 IEEE MTT-S International Microwave Symposium Digest*, volume 2, pages 879–882. IEEE, 1996.

[352] Slawomir Gruszczynski, Krzysztof Wincza, and Krzysztof Sachse. Design of Compensated Coupled-Stripline 3-dB Directional Couplers, Phase Shifters, and Magic-T's—Part II: Broadband Coupled-Line Circuits. *IEEE transactions on microwave theory and techniques*, 54(9):3501–3507, 2006.

[353] Tianjun Lin, Sijia Gu, and Tuami Lasri. 2-20 GHz Non-Uniform Coupler for Six-Port Reflectometer. In *2017 IEEE Topical Conference on Wireless Sensors and Sensor Networks (WiSNet)*, pages 15–18. IEEE, 2017.

[354] Benito Lopez-Berrocal, Jose de Oliva-Rubio, Enrique Marquez-Segura, Alvaro Moscoso-Martir, Inigo Molina-Fernandez, and Peter Uhlig. High Performance 1.8-18 GHz 10-dB Low Temperature Co-Fired Ceramic Directional Coupler. *Progress In Electromagnetics Research*, 104:99–112, 2010.

[355] FC De Ronde. A New Class of Microstrip Directional Couplers. In *G-MTT 1970 International Microwave Symposium*, pages 184–189. IEEE, 1970.

[356] Marek Edward Bialkowski and Yifan Wang. Wideband Microstrip 180° Hybrid Utilizing Ground Slots. *IEEE Microwave and Wireless Components Letters*, 20(9): 495–497, 2010.

[357] Khairul Huda Yusof, Norhudah Seman, and Mohd Haizal Jamaluddin. Analysis of Wideband Ground-Slotted 180° Hybrid Design. In *2012 IEEE Asia-Pacific Conference on Applied Electromagnetics (APACE)*, pages 205–209. IEEE, 2012.

[358] MA Ashraf, ZO Al-Hekail, MA Alkanhal, and A Sebak. Design of a Slot-Coupled Ultra-Wideband 180° Hybrid Coupler. In *2012 15 International Symposium on Antenna Technology and Applied Electromagnetics*, pages 1–4. IEEE, 2012.

[359] Steffen Scherr, Serdal Ayhan, Grzegorz Adamiuk, Philipp Pahl, and Thomas Zwick. Ultrawide Bandwidth-Hybrid-Coupler in Planar Technology. *International Journal of Microwave Science and Technology*, 2014, 2014.

[360] Yasmine Abdalla and Hany Hammad. Ultra-Wideband Compact Slot-Coupled 180° Hybrid Based on Ultra-Wideband Wilkinson Power Divider. In *2014 44th European Microwave Conference*, pages 231–234. IEEE, 2014.

[361] Masayoshi Aikawa and Hiroyo Ogawa. A New MIC Magic-T Using Coupled Slot Lines. *IEEE Transactions on Microwave Theory and Techniques*, 28(6):523–528, 1980.

[362] B Henin and A Abbosh. Wideband Hybrid Using Three-Line Coupled Structure and Microstrip-Slot Transitions. *IEEE microwave and wireless components letters*, 23(7):335–337, 2013.

[363] Lu Fan, Chien-Hsun Ho, Sridhar Kanamaluru, and Kai Chang. Wide-Band Reduced-Size Uniplanar Magic-T, Hybrid-Ring, and de Ronde's CPW-Slot Couplers. *IEEE Transactions on Microwave Theory and Techniques*, 43(12):2749–2758, 1995.

[364] Chien-Hsun Ho, Lu Fan, and Kai Chang. Broad-Band Uniplanar Hybrid-Ring and Branch-Line Couplers. *IEEE transactions on microwave theory and techniques*, 41 (12):2116–2125, 1993.

[365] Marco A Llamas, Miquel Ribo, David Girbau, and Lluis Pradell. A Rigorous Multimodal Analysis and Design Procedure of a Uniplanar 180° Hybrid. *IEEE transactions on microwave theory and techniques*, 57(7):1832–1839, 2009.

[366] M-H Murgulescu, P Legaud, E Moisan, E Penard, M Goloubkoff, and I Zaquine. New Small Size, Wideband 180° Ring Couplers: Theory and Experiment. In *1994 24th European Microwave Conference*, volume 1, pages 670–674. IEEE, 1994.

[367] M-H Murgulescu, E Moisan, P Legaud, E Penard, and I Zaquine. New Wideband, $0.67\lambda_g$ Circumference 180° Hybrid Ring Coupler. *Electronics Letters*, 30(4):299–300, 1994.

[368] Wenjie Feng, Quan Xue, and Wenquan Che. Compact Planar Magic-T Based on the Double-Sided Parallel-Strip Line and the Slotline Coupling. *IEEE transactions on microwave theory and techniques*, 58(11):2915–2923, 2010.

[369] Young-Gon Kim, Sun-Young Song, and Kang Wook Kim. A Compact Wideband Ring Coupler Utilizing a Pair of Transitions for Phase Inversion. *IEEE microwave and wireless components letters*, 21(1):25–27, 2011.

[370] Leung Chiu, Quan Xue, and Chi Hou Chan. A Compact Wideband Parallel-Strip 180° Hybrid Coupler. *Microwave and Optical Technology Letters*, 50(12):3271–3274, 2008.

[371] Amin M Abbosh and Marek E Bialkowski. Design of Compact Directional Couplers for UWB Applications. *IEEE Transactions on Microwave Theory and Techniques*, 55(2):189–194, 2007.

[372] Marek E Bialkowski, Siti Zuraidah Ibrahim, and Amin M Abbosh. Wideband Performance of 3 dB Microstrip-Slot Coupler Using Different Substrates. *Microwave and Optical Technology Letters*, 53(7):1618–1624, 2011.

[373] Design of Ultra Wideband 3 dB Quadrature Microstrip-Slot Coupler, author=Abbosh, AM and Bialkowski, ME, journal=Microwave and Optical Technology Letters, volume=49, number=9, pages=2101–2103, year=2007, publisher=Wiley Online Library.

[374] Dyg Norkhairunnisa ABANG Zaidel, Sharul Kamal Abdul Rahim, Norhudah Seman, Tharek Abdul Rahman, Raimi Dewan, Siti Fatimah Ausordin, and Peter S Hall. Mountain-Shaped Coupler for Ultra Wideband Applications. *Radioengineering*, 22(3):745–750, 2013.

[375] Muhammad A Ashraf, Abdel Razik Sebak, Zeyad O Al-Hekail, and Majeed A Alkanhal. Parametric Analysis of Multi Section slot Coupled Quadrature Coupler. In *2012 25th IEEE Canadian Conference on Electrical and Computer Engineering (CCECE)*, pages 1–4. IEEE, 2012.

[376] Marek E Bialkowski, Norhudah Seman, and Mook Seng Leong. Design of a Compact Ultra Wideband 3 dB Microstrip-Slot Coupler with High Return Losses and Isolation. In *2009 Asia Pacific Microwave Conference*, pages 1334–1337. IEEE, 2009.

[377] Nor Salehah binti Muklas, Sharul Kamal Abdul Rahim, and Norhudah Seman. Ultra Wideband Coupler Design for Butler Matrix Application. In *The 17th Asia Pacific Conference on Communications*, pages 506–511. IEEE, 2011.

[378] SNAM Ghazali, N Seman, RC Yob, MKA Rahim, and SKA Rahim. Design and Cross-Section Analysis of Wideband Rectangular-Shaped Directional Coupler. In *2011 IEEE International RF & Microwave Conference*, pages 161–165. IEEE, 2011.

[379] Dyg NA Zaidel, Sharul KA Rahim, Norhudah Seman, Tharek A Rahman, and A Abdulrahman. Low Cost and Compact Directional Coupler for Ultrawideband Applications. *Microwave and Optical Technology Letters*, 54(3):670–674, 2012.

[380] Osama MH Ahmed, Abdel-Razik Sebak, and Tayeb A Denidni. A Novel Butterfly-Shaped Multilayer Backward Microstrip Hybrid Coupler for Ultrawideband Applications. *Microwave and Optical Technology Letters*, 54(10):2231–2237, 2012.

[381] DNA Zaidel, SKA Rahim, N Seman, CL Chew, and NH Khamis. A Design of Octagon-Shaped 3-dB Ultra Wideband Coupler Using Multilayer Technology. *Microwave and Optical Technology Letters*, 55(1):127–130, 2013.

[382] Dyg Norkhairunnisa Abang Zaidel, Sharul Kamal Abdul Rahim, Norhudah Seman, Ashraf Abdulrahman Adam, Tharek Abdul Rahman, and Peter S Hall. Compact UWB Multilayer 3 dB Directional Coupler Design and Analysis on Coupler Performances. *Microwave and Optical Technology Letters*, 55(9):2214–2219, 2013.

[383] A Moscoso-Martir, JG Wanguemert-Perez, I Molina-Fernandez, and E Marquez-Segura. Slot-Coupled Multisection Quadrature Hybrid for UWB Applications. *IEEE Microwave and Wireless Components Letters*, 19(3):143–145, 2009.

[384] Alvaro Moscoso-Martir, Inigo Molina-Fernandez, and Alejandro Ortega-Monux. High Performance Multi-Section Corrugated Slot-Coupled Directional Couplers. *Progress In Electromagnetics Research*, 134:437–454, 2013.

[385] Muhammad A Ashra, Abdel Razik Sebak, Zeyad O Al-Hekail, and Majeed A Alkanhal. B4. Analysis and Design of Single Section and Three-Section Ultra-Wideband Quadrature Hybrid Couplers. In *2012 29th National Radio Science Conference (NRSC)*, pages 37–44. IEEE, 2012.

[386] Andreas Oborovski, Maximilian Hofmann, Robert Weigel, and Dietmar Kissinger. Multi-Octave Planar Microwave Slot-Coupled Directional Coupler Up to 28 GHz with Novel Phase Velocity Compensation. In *2014 44th European Microwave Conference*, pages 77–80. IEEE, 2014.

[387] Ying Wang, Guang Hua, and Jing Du. Design of Ultra-Wideband Magic-T Using Microstrip/Slot Coupler and Phase Shifter. In *2015 Asia-Pacific Microwave Conference (APMC)*, volume 1, pages 1–3. IEEE, 2015.

[388] AM Abbosh and ME Bialkowski. Design of a UWB Planar 180° Hybrid Exploiting Microstrip-Slot Transitions. *Microwave and optical technology letters*, 49(6):1343–1346, 2007.

[389] Parisa Safaie, Masoud Movahhedi, and Ali Ghafoorzadeh-Yazdi. A Systematic Method to Design Desired Wideband 180° Couplers. In *2019 27th Iranian Conference on Electrical Engineering (ICEE)*, pages 1245–1248. IEEE, 2019.

[390] Roger Jacques and Didier Meignant. Novel Wide Band Microstrip Balun. In *1981 11th European Microwave Conference*, pages 839–843. IEEE, 1981.

[391] Benjamin Sewiolo, Marcus Hartmann, Benjamin Waldmann, and Robert Weigel. An Ultra-Wideband Coupled-Line Balun Using Patterned Ground Shielding Structures. In *2008 IEEE Radio and Wireless Symposium*, pages 459–462. IEEE, 2008.

[392] A Abbosh. Ultra-wideband Quasi-Yagi Antenna Using Dual-Resonant Driver and Integrated Balun of Stepped Impedance Coupled Structure. *IEEE transactions on antennas and propagation*, 61(7):3885–3888, 2013.

[393] Juan-Jose Sanchez-Martinez and Enrique Márquez-Segura. Generalized Analytical Design of Broadband Planar Baluns Based on Wire-Bonded Multiconductor Transmission Lines. *Progress In Electromagnetics Research*, 134:169–187, 2013.

[394] J Rogers and R Bhatia. A 6 to 20 GHz Planar Balun Using a Wilkinson Divider and Lange Couplers. In *1991 IEEE MTT-S International Microwave Symposium Digest*, pages 865–868. IEEE, 1991.

[395] Christian Zietz, Gunnar Armbrecht, and Ilona Rolfes. A Compact Ultra-Wideband Double Balun Feeding Network on a Single Layer PCB. In *Proceedings of the Fourth European Conference on Antennas and Propagation*, pages 1–5. IEEE, 2010.

[396] Zhen-Yu Zhang, Yong-Xin Guo, Ling Chuen Ong, and MYW Chia. A New Wide-Band Planar Balun on a Single-Layer PCB. *IEEE Microwave and Wireless Components Letters*, 15(6):416–418, 2005.

[397] Peng Wu, Yong Zhang, Yu-Liang Dong, and Qin Zhang. A Novel Ka-Band Planar Balun Using Microstrip-CPS-Microstrip Transition. *IEEE microwave and wireless components letters*, 21(3):136–138, 2011.

[398] Zhenhua Chen, Bing Yu, Yong Zhou, Fayu Wan, and Junxiang Ge. 75–110 GHz Integrated Active Sextupler Module. In *2015 IEEE International Wireless Symposium (IWS 2015)*, pages 1–4. IEEE, 2015.

[399] Xueqing Meng, Bo Wu, Zhi-Xiang Huang, and Xian-Liang Wu. Compact 30: 1 Bandwidth Ratio Balun for Printed Balanced Antennas. *Progress In Electromagnetics Research*, 64:125–132, 2016.

[400] Sean Sengele, Brad Baker, Jonathan Holmes, Glenn Hopkins, Jared Walker, and Kenneth Reigle. An Ultra Wideband, 1–20 Ghz Balun in an Electrically Small Conducting Enclosure. In *2015 IEEE International Symposium on Antennas and Propagation & USNC/URSI National Radio Science Meeting*, pages 1390–1391. IEEE, 2015.

[401] J-S Lim, U-H Park, Y-C Jeong, K-S Choi, D Ahn, S Oh, and J-J Koo. 800–5000 MHz Ultra-Wideband CPW Balun. *Electronics Letters*, 42(18):1037–1039, 2006.

[402] Mohammad S Mahani and Ramesh Abhari. A Planar Ultra Wide Band Single Layer Microstrip Balun Operating From 200 Mhz to 10 Ghz. In *2012 IEEE/MTT-S International Microwave Symposium Digest*, pages 1–3. IEEE, 2012.

[403] Farshid Tamjid, Chris M Thomas, and Aly E Fathy. A Compact Wideband Balun Design Using Double-sided Parallel Strip Lines With Over 9: 1 Bandwidth. *International Journal of RF and Microwave Computer-Aided Engineering*, 30(11): e22425, 2020.

[404] Leung Chiu and Quan Xue. A Parallel-Strip Balun for Wideband Frequency Doubler. *International Journal of Microwave Science and Technology*, 2013, 2013.

[405] L Chiu, TY Yum, Q Xue, and CH Chan. A Wideband Compact Parallel-Strip 180° Wilkinson Power Divider for Push-Pull Circuitries. *IEEE microwave and wireless components letters*, 16(1):49–51, 2005.

[406] Binh L Pham, Hai H Ta, Anh-Vu Pham, Robert E Leoni, and Yehuda Leviatan. 23: 1 Bandwidth Ratio Quasi-Lumped Component Balun on a Multilayer Organic Substrate. *IET Microwaves, Antennas & Propagation*, 10(5):561–567, 2016.

[407] Zhongpu Li and Jinxian Liu. Design of a Novel Ultra Wide Band Balance Microstrip Balun. In *2015 2nd International Conference on Information Science and Control Engineering*, pages 694–696. IEEE, 2015.

[408] AM Abbosh and Marek E Bialkowski. An UWB Planar Out-of-Phase Power Divider Employing Parallel Stripline-Microstrip Transitions. *Microwave and optical technology letters*, 49(4):912–914, 2007.

[409] AM Abbosh, Marek E Bialkowski, and J Mazierska. An UWB Planar Out-of-Phase Power Divider Employing Microstrip-Slot and Parallel Stripline-Microstrip Transitions. In *2006 Asia-Pacific Microwave Conference*, pages 905–908. IEEE, 2006.

[410] Q Li, X-W Shi, F Wei, and J-G Gong. A Novel Planar 180 Out-of-Phase Power Divider for UWB Application. *Journal of Electromagnetic Waves and Applications*, 25(1):161–167, 2011.

[411] Long Xiao, Hao Peng, and Tao Yang. Ultra-Wideband Four-Way In-Phase Multilayer Power Divider with High Isolation. *Progress In Electromagnetics Research*, 49:31–37, 2014.

[412] Long Xiao and Tao Yang. UWB Multilayer Power Divider with High Isolation. *Progress In Electromagnetics Research*, 50:57–63, 2014.

[413] King Zeng and Xiaojun Bi. Slotline-Based Balun with Wide Bandwidth and High Isolation. In *2018 IEEE International Conference on Integrated Circuits, Technologies and Applications (ICTA)*, pages 40–41. IEEE, 2018.

[414] Long Xiao, Hao Peng, Tao Yang, and Jun Dong. Power Divider Based on Stepped-Impedance Slotline. *Progress In Electromagnetics Research*, 50:147–154, 2014.

[415] Bing Xiao, J Hong, and B Wang. A Novel UWB Out-of-Phase Four-Way Power Divider. *ACES Journal-Applied Computational Electromagnetics Society*, 26(10): 863, 2011.

[416] Hao Peng, Ziqiang Yang, Yu Liu, Tao Yang, and Ke Tan. An Improved UWB Non-Coplanar Power Divider. *Progress In Electromagnetics Research*, 138:31–39, 2013.

[417] Long Xiao, Hao Peng, and Tao Yang. Compact Ultra-Wideband In-Phase Multilayer Power Divider. *Progress In Electromagnetics Research*, 48:33–37, 2014.

[418] He Zhu, Zhiqun Cheng, and Y Jay Guo. Design of Wideband In-Phase and Out-of-Phase Power Dividers Using Microstrip-to-Slotline Transitions and Slotline Resonators. *IEEE Transactions on Microwave Theory and Techniques*, 67(4):1412–1424, 2019.

[419] Ummee T Ahmed and Amin M Abbosh. Design of Wideband Single-Layer In-Phase Power Divider Using Microstrip to Slotline Coupled Structure. *Microwave and Optical Technology Letters*, 57(4):789–791, 2015.

[420] Kaijun Song, Yu Zhu, Qi Duan, Maoyu Fan, and Yong Fan. Extremely Compact Ultra-Wideband Power Divider Using Hybrid Slotline/Microstrip-Line Transition. *Electronics Letters*, 51(24):2014–2015, 2015.

[421] UT Ahmed and AM Abbosh. Extremely Wideband In-Phase Power Divider Using Modified Wilkinson Design. *Microwave and Optical Technology Letters*, 57(8):1799–1802, 2015.

[422] UT Ahmed and AM Abbosh. In-Phase Power Divider With Three Octaves Band Using Microstrip to Slotline Transitions and Loosely Coupled Microstrip Lines. In *2015 Asia-Pacific Microwave Conference (Apmc)*, volume 2, pages 1–3. IEEE, 2015.

[423] Phong Thanh Nguyen, Amin Abbosh, and Stuart Crozier. Ultra-Wideband Balun Using Microstrip to Slotline Transitions. In *2012 IEEE Asia-Pacific Conference on Antennas and Propagation*, pages 309–310. IEEE, 2012.

[424] Kaijun Song and Quan Xue. Novel Ultra-Wideband (UWB) Multilayer Slotline Power Divider With Bandpass Response. *IEEE Microwave and Wireless Components Letters*, 20(1):13–15, 2009.

[425] Ya-Li Yao, Fu-Shun Zhang, Min Liang, and Mao-Ze Wang. Planar Wideband Balun With Novel Slotline T-Junction Transition. *Progress In Electromagnetics Research*, 64:73–79, 2016.

[426] Yu Zhu, Kaijun Song, Maoyu Fan, and Yong Fan. Wideband Single-Ended-to-Balanced Power Divider With Intrinsic Common-Mode Suppression. *IEEE Microwave and Wireless Components Letters*, 30(4):379–382, 2020.

[427] Kaijun Song, Yuxia Mo, Quan Xue, and Yong Fan. Wideband Four-Way Out-of-Phase Slotline Power Dividers. *IEEE Transactions on Industrial Electronics*, 61(7): 3598–3606, 2013.

[428] Long Xiao, Hao Peng, and Tao Yang. The Design of a Novel Compact Ultra-Wideband (UWB) Power Divider. *Progress In Electromagnetics Research*, 44:43–46, 2014.

[429] UL Rohde, AK Poddar, S Pegwal, V Madhavan, SK Koul, M Abegaonkar, and MA Silaghi. Ultra Wide Band Balun/180° Power Divider Using Microstrip-Slotline-Microstrip Transition. In *2015 IEEE MTT-S International Microwave and RF Conference (IMaRC)*, pages 400–404. IEEE, 2015.

[430] Saurabh Pegwal, Mahesh P Abegaonkar, and Shiban K Koul. Ultrawideband Doubly Tapered Slot Antenna (DTSA) With Integrated Balun as a Feed for Time-domain Target Detection. *Microwave and Optical Technology Letters*, 59(10):2415–2421, 2017.

[431] Kaijun Song and Quan Xue. Ultra-wideband Out-of-Phase Power Divider Using Multilayer Microstrip-Slotline Coupling Structure. *Microwave and Optical Technology Letters*, 52(7):1591–1594, 2010.

[432] Bing Xiao, Heming Yao, Min Li, Jing-Song Hong, and Kwan L Yeung. Flexible Wideband Microstrip-Slotline-Microstrip Power Divider and its Application to Antenna Array. *IEEE Access*, 7:143973–143979, 2019.

[433] L Guo, A Abbosh, and H Zhu. Ultra-Wideband In-Phase Power Divider Using Stepped-Impedance Three-Line Coupled Structure and Microstrip-to-slotline Transitions. *Electronics letters*, 50(5):383–384, 2014.

[434] He Zhu, Jing-Yu Lin, and Y Jay Guo. Wideband Filtering Out-of-Phase Power Dividers Using Slotline Resonators and Microstrip-to-Slotline Transitions. In *2019 IEEE MTT-S International Microwave Symposium (IMS)*, pages 919–922. IEEE, 2019.

[435] Ummee T Ahmed and Amin M Abbosh. Wideband Out-of-Phase Power Divider Using Microstrip to Slotline Transitions, Coupled Lines, and Shunt Open-Ended Stubs. *Microwave and Optical Technology Letters*, 57(9):2216–2218, 2015.

[436] A Wideband Microstrip Balun Structure, author=Wu, Peng and Xue, Quan, booktitle=2014 IEEE MTT-S International Microwave Symposium (IMS2014), pages=1–3, year=2014, organization=IEEE.

[437] Peng Wu, Shaowei Liao, and Quan Xue. A Wideband Microstrip Dual Balun Structure. In *2015 IEEE MTT-S International Microwave Symposium*, pages 1–3. IEEE, 2015.

[438] P Wu, Z Wang, and Y Zhang. Wideband Planar Balun Using Microstrip to CPW and Microstrip to CPS Transitions. *Electronics letters*, 46(24):1611–1613, 2010.

[439] Yufu Li and XiaoXing Yin. Design of Output-Input Inversed Polarity Pulse Power Divider for Ultra-Wideband Communications. *Wireless Communications and Mobile Computing*, 2018, 2018.

[440] Mao-Ze Wang, Fu-Shun Zhang, Jian Sun, Ke Chen, and Bin Wen. Design of Several Power Dividers Using CPW-to-Microstrip Transition. *Progress In Electromagnetics Research*, 41:125–134, 2013.

[441] Ali K Horestani and Zahra Shaterian. Ultra-Wideband Balun and Power Divider Using Coplanar Waveguide to Microstrip Transitions. *AEU-International Journal of Electronics and Communications*, 95:297–303, 2018.

[442] Zahra Shaterian and Ali Karami Horestani. Ultra-Wideband Multi-Section Wilkinson Power Divider. *Microwave and Optical Technology Letters*, 2020.

[443] AM Abbosh. Ultra Wideband Inphase Power Divider for Multilayer Technology. *IET microwaves, antennas & propagation*, 3(1):148–153, 2009.

[444] AM Abbosh. Multilayer Inphase Power Divider for UWB Applications. *Microwave and Optical Technology Letters*, 50(5):1402–1405, 2008.

[445] Ramesh Garg, Inder Bahl, and Maurizio Bozzi. *Microstrip Lines and Slotlines*. Artech house, 2013.

[446] Jeffrey B Knorr. Slot-Line Transitions (Short Papers). *IEEE transactions on Microwave Theory and Techniques*, 22(5):548–554, 1974.

[447] Victor H Rumsey, Nicholas Declaris, and Henry G Booker. Frequency independent antennas. 1966.

[448] Y. Mushiake. *Self-Complementary Antennas: Principle of Self-Complementarity for Constant Impedance*. Springer London, 2012. ISBN 9781447110033.

[449] DH Werner and PL Werner. Frequency-Independent Features of Self-Similar Fractal Antennas. *Radio Science*, 31(6):1331–1343, 1996.

[450] C Puente, J Romeu, R Pous, X Garcia, and F Benitez. Fractal Multiband Antenna Based on the Sierpinski Gasket. *Electronics Letters*, 32(1):1–2, 1996.

[451] Xianhua Yang, J Chiochetti, D Papadopolous, and L Susman. Fractal Antenna Elements and Arrays. *Applied microwave and wireless*, 11:34–46, 1999.

[452] Warsha Balani, Mrinal Sarvagya, Tanweer Ali, Manohara Pai MM, Jaume Anguera, Aurora Andujar, and Saumya Das. Design Techniques of Super-Wideband Antenna–Existing and Future Prospective. *IEEE Access*, 7:141241–141257, 2019.

[453] Renato Cicchetti, Emanuela Miozzi, and Orlandino Testa. Wideband and UWB Antennas for Wireless Applications: A Comprehensive Review. *International Journal of Antennas and Propagation*, 2017, 2017.

[454] Yingsong Li, Wenxing Li, Qiubo Ye, and Raj Mittra. A Survey of Planar Ultra-Wideband Antenna Designs and Their Applications. In *Forum for Electromagnetic Research Methods and Application Technologies (FERMAT)*, volume 1, pages 1–16, 2014.

[455] R Chernobrovkin, I Ivanchenko, V Pischikov, and N Popenko. UWB Equiangular Spiral Antenna for 7.5–40 GHz. *Microwave and optical technology letters*, 54(9): 2190–2194, 2012.

[456] Roman Kubacki, Mirosław Czyżewski, and Dariusz Laskowski. Enlarged Frequency Bandwidth of Truncated Log-Periodic Dipole Array Antenna. *Electronics*, 9(8): 1300, 2020.

[457] Muhammad Hamza and Wasif T Khan. Hybrid Utilization of Loading Techniques and Cavity Groove for Performance Enhancement of the UWB (2–18 GHz) Spiral Antenna. *International Journal of Antennas and Propagation*, 2018, 2018.

[458] Dinesh Kumar Raheja, Sachin Kumar, and Binod Kumar Kanaujia. Compact Quasi-Elliptical-Self-Complementary Four-Port Super-Wideband MIMO Antenna With Dual Band Elimination Characteristics. *AEU-International Journal of Electronics and Communications*, 114:153001, 2020.

[459] Shrivishal Tripathi, Akhilesh Mohan, and Sandeep Yadav. Hexagonal Fractal Ultra-Wideband Antenna Using Koch Geometry with Bandwidth Enhancement. *IET Microwaves, Antennas & Propagation*, 8(15):1445–1450, 2014.

[460] Sarthak Singhal and Amit Kumar Singh. Asymmetrically CPW-Fed Circle Inscribed Hexagonal Super Wideband Fractal Antenna. *Microwave and Optical Technology Letters*, 58(12):2794–2799, 2016.

[461] Sarthak Singhal and Amit Kumar Singh. Modified Star-Star Fractal (MSSF) Super-Wideband Antenna. *Microwave and Optical Technology Letters*, 59(3):624–630, 2017.

[462] Xiao-Feng Bai, Shun-Shi Zhong, and Xian-Ling Liang. Leaf-Shaped Monopole Antenna With Extremely Wide Bandwidth. *Microwave and Optical Technology Letters*, 48(7):1247–1250, 2006.

[463] PJ Gibson. The Vivaldi Aerial. In *1979 9th European Microwave Conference*, pages 101–105. IEEE, 1979.

[464] Constantine A Balanis. *Antenna Theory: Analysis and Design*. John wiley & sons, 2016.

[465] Kevin Khee-Meng Chan, Adrian Eng-Choon Tan, and Karumudi Rambabu. Decade Bandwidth Circularly Polarized Antenna Array. *IEEE transactions on antennas and propagation*, 61(11):5435–5443, 2013.

[466] BAL-0026 Broadband Balun. `https://www.markimicrowave.com/baluns/bal-0026.aspx`. (Accessed on 03/02/2021).

[467] PD-0126 2-Way Wilkinson Microwave/RF Power Divider / Combiner. `https://www.markimicrowave.com/power-dividers/pd-0126.aspx`. (Accessed on 03/02/2021).

DOCTORAT BRETAGNE LOIRE / MATHSTIC

ENSTA Bretagne

UBO Université de Bretagne Occidentale

Titre : Systèmes d'antennes Ultra-Large-Bande pour Applications In-Band Full-Duplex.

Mot clés : Ultra-Large-Bande, In-Band Full-Duplex, annulation de l'auto-interférence, transitions microruban-ligne fente, antennes Vivaldi.

Résumé : La technologie In-Band Full-Duplex a pour objectif d'augmenter l'efficacité spectrale des liaisons sans-fils en permettant à deux systèmes de communiquer simultanément dans la même bande de fréquence. Dans cette configuration In-Band Full-Duplex, le principal défi consiste à annuler ou réduire les signaux d'auto-interférence, qui se couplent de l'émetteur vers son propre récepteur. Divers circuits d'annulation d'auto- interférence peuvent alors être mis en œuvre : au niveau de l'antenne, de l'étage analogique et/ou numérique. Les techniques classiques d'annulation d'auto-interférence sont majoritairement dédiées aux systèmes à bande étroite et peu de travaux ont été menés pour étendre leurs performances à un fonctionnement en large-bande et encore moins en Ultra-Large-Bande. Dans ce travail, nous nous focalisons sur l'étude des techniques d'annulation compatibles avec un fonctionnement Ultra-Large-Bande et sur leurs mises en œuvre. Les systèmes antennaires proposés sont basés sur une technique d'annulation en champ proche qui utilise quatre antennes et deux baluns. Les avantages des systèmes développés sont multiples, ils proposent tous une bande passante extrêmement large tout en maintenant un niveau d'annulation d'auto-interférence au moins supérieur à 55-60 dB sur cette bande avec des configurations permettant soit d'en augmenter la solidité mécanique, soit d'obtenir une double polarisation ou encore avec une alimentation innovante des antennes.

Title: Wideband Antenna Systems for In-Band Full-Duplex Applications.

Keywords: Ultra-Wideband, In-band Full-Duplex, Self-Interference Cancellation, Microstrip-to-Slotline Transitions, Vivaldi Antennas.

Abstract: In-band full-duplex technology aims to mitigate the scarcity of spectral resources by allowing two radios to communicate simultaneously in the same frequency band. The main challenge for full-duplex radios is to cancel the self-interference signals, which couple from the transmitter of one radio to its own receiver, by implementing various self-interference cancellation circuity at the antenna, analog, and digital stages of the radio front-end. Conventional self-interference cancellation techniques were dedicated for narrowband systems and little work has been conducted to extend their performance for wideband operation. Thus, in this work, we focus on studying the wideband potential of the available cancellation techniques and implementing wideband full-duplex systems based on those techniques. The implemented systems are based on the near-field cancellation technique which uses four antennas and two baluns. The systems' merits vary from extremely wide bandwidth to higher mechanical solidity and dual-polarization, but they all can maintain a decent amount of cancellation.